

Polydiketopyrrolopyrroles: Synthesis, Doping and Applications towards Thermoelectrics and Bioelectronics

DISSERTATION

zur Erlangung des akademischen Grades
eines Doktors der Naturwissenschaften (Dr. rer. nat.) in der
Bayreuther Graduiertenschule für Mathematik und Naturwissenschaften (BayNAT)
der Universität Bayreuth

vorgelegt von

Gert Krauss

geboren in Waldshut-Tiengen

Bayreuth, 2022

Die vorliegende Arbeit wurde in der Zeit von April 2017 bis Juni 2021 in Bayreuth am Lehrstuhl für Makromolekulare Chemie I der Universität Bayreuth unter der Betreuung von Herrn Prof. Dr. Mukundan Thelakkat angefertigt.

Vollständiger Abdruck der von der Bayreuther Graduiertenschule für Mathematik und Naturwissenschaften (BayNAT) der Universität Bayreuth genehmigten Dissertation zur Erlangung des akademischen Grades eines Doktors der Naturwissenschaften (Dr. rer. nat.).

Dissertation eingereicht am: 25.02.2022

Zulassung durch das Leitungsgremium: 01.03.2022

Wissenschaftliches Kolloquium: 23.06.2022

Amtierender Direktor: Herr Prof. Dr. Hans Keppler

Prüfungsausschuss:

Prof. Dr. Mukundan Thelakkat (Gutachter)

Prof. Dr. Markus Retsch (Gutachter)

Prof. Dr. Birgit Weber (Vorsitz)

Prof. Dr. Andreas Greiner

Contents

SUMMARY	X
ZUSAMMENFASSUNG	XII
1. INTRODUCTION	1
1.1 Organic Semiconductors	1
1.1.1 Second Generation π -Conjugated Polymers	3
1.1.2 Synthetic Approaches toward 2 nd Generation Conjugated Polymers	8
1.1.3 Synthesis of DPP and Thiophene Monomers	11
1.2 Doping of Conjugated Polymers	13
1.2.1 Charge Transport in Conjugated Polymers	13
1.2.2 Chemical Doping	14
1.3 Organic Mixed Ion-Electron Conductors for Organic Electrochemical Transistors	18
1.4 Organic Thermoelectrics	25
REFERENCES	32
2. OBJECTIVE OF THE THESIS	39
3. OVERVIEW OF THE THESIS	41
4. INDIVIDUAL CONTRIBUTIONS TO JOINT PUBLICATIONS	48
4.1. "Polydiketopyrrolopyrroles Carrying Ethylene Glycol Substituents as Efficient Mixed Ion-Electron Conductors for Biocompatible Organic Electrochemical Transistors"	48
4.2. "HOMO-Homo Electron Transfer: An Elegant Strategy for p-Type Doping of Polymer Semiconductors toward Thermoelectric Applications"	49
4.3. "Highly Efficient Doping of Conjugated Polymers using Multielectron Acceptor Salts"	49
4.4. "Principles of Structural Design of Conjugated Polymers Showing Excellent Charge Transport toward Thermoelectrics and Bioelectronics Applications (Annex)"	50
5. POLYDIKETOPYRROLOPYRROLES CARRYING ETHYLENE GLYCOL SUBSTITUENTS AS EFFICIENT MIXED ION-ELECTRON CONDUCTORS FOR BIOCOMPATIBLE ORGANIC ELECTROCHEMICAL TRANSISTORS	51
6. HOMO-HOMO ELECTRON TRANSFER: AN ELEGANT STRATEGY FOR P-TYPE DOPING OF POLYMER SEMICONDUCTORS TOWARD THERMOELECTRIC APPLICATIONS	96
7. HIGHLY EFFICIENT DOPING OF CONJUGATED POLYMERS USING MULTIELECTRON ACCEPTOR SALTS	130
8. ANNEX: PRINCIPLES OF STRUCTURAL DESIGN OF CONJUGATED POLYMERS SHOWING EXCELLENT CHARGE TRANSPORT TOWARD THERMOELECTRICS AND BIOELECTRONICS APPLICATIONS"	175
9. EIDESSTATTLICHE VERSICHERUNGEN UND ERKLÄRUNGEN	229

Herzlichen Dank!

an all diejenigen, die mich während der letzten Jahre begleitet haben und damit direkt oder indirekt zum Gelingen dieser Doktorarbeit beigetragen haben. Mit und durch Euch ist diese Zeit schön geworden, hat Früchte getragen und einige lebenslange Freundschaften hervorgebracht.

Allen voran danke ich meinem Betreuer Prof. Dr. Mukundan Thelakkat für die Aufnahme in seinen Arbeitskreis, für das Vertrauen in mich und die fortwährende Forderung, Förderung und Unterstützung. Danke auch für einen ideal ausgestatteten Arbeitsplatz, zahllose wissenschaftliche Diskussionen und persönliche Gespräche.

Für das mehr als gute Arbeitsklima, Hilfsbereitschaft bei der Arbeit und im Privaten, danke ich der gesamten MC I. Besonderer Dank geht an Christina Wunderlich und Petra Weiss, deren Türen immer offenstehen, die einen stets mit einem Lächeln im Gesicht begrüßen und auf die immer Verlass ist.

Dem Baracken-Team Dominic Rosenbach, Alexander Krimalowski und Jannik Petry danke ich für die gemeinsame Zeit in der wir zusammengewachsen sind, für das familiäre Klima in der B6 und ungezählte schöne Erinnerungen in und außerhalb der Uni, auf dem Fahrrad, beim Wandern oder beim Gärtnern.

Philip Schmode und Florian Meichsner im fachlichen für Zusammenarbeit an der OECT-Front, GPC-Messungen, Diskussionen und vieles mehr. Für all die schönen Wanderungen oder Radtouren und insgesamt dafür, dass wir Freunde geworden sind.

Danke an Andreas Frank, Eva Fürsattel, Säge, Basti Klose und Simon Gumbel für die kulinarischen Abende im Kaffeezimmer, auf dem Dach und auch mal in Kulmbich.

Adrian Hochgesang danke ich für seine fachliche Expertise, eine immerzu perfekte Zusammenarbeit zu jeder Tages- und Nachtzeit und an Feiertagen und für die spaßige Zeit an der Glovebox und im Reinraum.

Ein besonderer Dank gilt Tina Weller, die mich schon im Masterstudium unter ihre Fittiche nahm, mir viele Arbeitstechniken im Labor beibrachte und mir in den ersten Zügen der Doktorarbeit eine wichtige Mentorin war. David Heinrich danke ich für viele hilfreiche Gespräche beim Mittagskaffee, Tipps und Kniffen im Labor, Korrekturlesen von Masterarbeit und Publikationen.

Martina Fried, Jutta Failner und Sandra Ganzleben danke ich für synthetische Unterstützung und die Bereitstellung von frisch destillierten Lösungsmitteln. Alexander Kern und Jonas Mayer dafür, dass sie sich zuverlässig um IT, Reinraum und diverse Messgeräte kümmern, immer einen schlaun Rat parat haben.

I thank John Mohanraj and Mahima Goel for the good work we did together, fruitful scientific discussions, help at the glove box, at measurements and during writing and correction of manuscripts; and altogether for a nice time to look back on.

Steffen Trippmacher und Prof. Dr. Georg Papastavrou danke ich dafür, dass sie uns unkompliziert ermöglicht haben QCM-Messungen an Ihren Instrumenten durchzuführen. Dr. Sahar Salehi danke ich für die tadellose und außergewöhnlich zügige Durchführung von Zelltests.

Nicht zuletzt danke ich meinen Eltern und meinem Bruder für die fortwährende Unterstützung und den Glauben an mich. Meinen engsten Wegbegleitern Niklas, Any, Simon, Kevin und Basti: Ihr wart immer für mich da, habt für Ausgleich gesorgt, wir haben unvergessliche Reisen gemacht, uns gemeinsam zum Sport motiviert, gelacht, geweint und sind gemeinsam erwachsen geworden.

Danke, dass Ihr das Leben außerhalb der Uni schön macht und mir Rückhalt gebt. Ohne Euch wäre ich heute nicht dort, wo ich bin.

*Too many think that the grass
is greener somewhere else.
But the grass is greener
where you water it.*

Summary

Organic semiconductors (OSCs) based on polydiketopyrrolopyrrole polymers (PDPPs) are well-known for their excellent charge carrier properties and stability. They offer firm handles for chemical functionalization and many subunits of the molecule can be tuned almost deliberately. In the present thesis, this chemical versatility of PDPPs was exploited to answer specific scientific questions and deduce design principles for the use of PDPPs in bioelectronic applications. Furthermore, OSCs like PDPPs often need to be doped to adjust their electrical properties to fit desired specifications. Chemical doping is a pivotal tool to tune e.g., the charge carrier density and the electrical conductivity of OSCs, but recently considerable drawbacks of this conventional molecular doping strategy were identified. We therefore proposed a novel doping concept, proved its practicality, and studied it in detail.

In the first chapter, we designed a series of four PDPPs with a systematically increasing content of ethylene glycol (EG) substituents. Thereby for the first time, the basic functionality of the thiophene flanked DPP backbone i.e., a pronounced hole-transport behavior was combined with a fine-tuned hydrophilic character. The concept was to gradually increase the hydrophilic character of the polymers to improve the compatibility with water and solvated ions, ultimately leading to different mixed ion-electron conduction properties. It was successfully shown that the compatibility with water and ions indeed follows the intended behavior and mixed conduction was observed at higher EG contents. It was shown that the polymers with higher EG content perform well in organic electrochemical transistor (OECT) devices, both under sodium chloride solution as well as when a cell-growth medium is used as the electrolyte. This was the first report of OECT operation using a cell growth medium. The transistor devices were tested under steady operation for over 1200 consecutive measurement cycles, underlining the stability of the PDPP. Cell viability tests confirmed the absence of cytotoxicity of the polymer. Ultimately, the combination of stable operation and operation in a cell-growth medium and the non-toxic character demonstrates the potential for application in bioelectronic applications.

Today to increase and tune the electrical conductivity of organic semiconductors, molecular doping is the strategy of choice. Conventional molecular doping usually demands high molar doping ratios up to several tenths of percent of dopant. High molar doping ratios, however, are always accompanied by side-effects: large amounts of foreign molecules within the semiconducting polymer matrix disturb the polymer morphology and therefore, hinder charge transport. Moreover, the ionization efficiency itself suffers from high doping levels and undesired charge trapping and scattering can occur. To combat these limitations, in the second chapter we have developed a new strategy to elegantly dope polymer semiconductors by using an oxidized hole-transport material (HTM) as the active dopant. The operative point of this concept is that, after the electron transfer from the oxidized HTM to the neutral polymer has occurred, the dopant becomes a HTM which does not hamper or even assists

charge transport. The doping process was studied via different methods using a PDPP as organic semiconductor and the thermoelectric behavior of the doped materials was measured. This concept was then extended in the third chapter, where we studied whether oxidized HTMs in higher oxidative state yield advantages over e.g., singly oxidized HTMs. The anticipation that the required molar doping amount can be reduced even further by using multielectron acceptors, rather than one-electron acceptors was proven. The work also compared the often-discussed role of the host polymer's polarity on the doping process by parallelly using two PDPPs as OSC which explicitly only differ in their side chains (EG vs. alkyl). By comparing mono, di and tetra cationic HTM dopants, it was shown that the charge carrier density of systems doped with the various dopants is directly linked to the valency of the introduced dopant. Thereby, the tetra cationic HTM dopant afforded unusually high doping efficiencies of ca. 20 % at only 5 % molar doping ratio in the more polar host OSC.

To conclude, my research work produced guidelines for the design of active materials for operationally stable and non-toxic MIECs to be used in bioelectronics, based on a DPP polymer structure. Furthermore, a novel highly efficient new doping method was established and assessed in detail, rendering strongly increased charge carrier densities and electrical conductivities possible, at unprecedentedly low doping levels.

Zusammenfassung

Organische Halbleiter auf Basis von Polydiketopyrrolopyrrol-Polymeren (PDPPs) sind bekannt für ihre hervorragenden Ladungstransporteigenschaften und ihre Stabilität. Weiterhin bieten sie Angriffspunkte zur chemischen Funktionalisierung und viele Struktureinheiten des Moleküls lassen sich gezielt modifizieren. In der vorliegenden Arbeit wurde diese chemische Vielseitigkeit von PDPPs genutzt, um spezifische wissenschaftliche Fragestellungen zu beantworten und Designprinzipien für den Einsatz von PDPPs in bioelektronischen Anwendungen abzuleiten. In vielen Anwendungen müssen organische Halbleiter, wie z.B. PDPPs, dotiert werden, um ihre elektrischen Eigenschaften an gewünschte Spezifikationen anzupassen. Chemisches Dotieren ist ein zentrales Werkzeug, um z.B. die Ladungsträgerdichte oder die elektrische Leitfähigkeit zu beeinflussen, jedoch wurden in der Vergangenheit erhebliche Nachteile dieser konventionellen molekularen Dotierstrategie identifiziert. Wir haben daher ein neuartiges Dopingkonzept vorgeschlagen, dessen Praxistauglichkeit bewiesen und eingehend untersucht.

Im ersten Kapitel wurde eine Reihe von vier PDPPs mit systematisch zunehmendem Gehalt an Ethylenglykol (EG)-Substituenten entworfen und hergestellt. Dabei wurde erstmals die grundlegende Funktionalität des Thiophen-flankierten DPP-Rückgrats, d.h. ein ausgeprägtes Lochtransportverhalten, mit einem fein abgestimmten hydrophilen Charakter kombiniert. Das Konzept bestand darin, den hydrophilen Charakter der Polymere schrittweise zu erhöhen. Dadurch konnte die Kompatibilität mit Wasser und solvatisierten Ionen verbessert werden, was letztendlich zu unterschiedlichen Mischleitungs-Eigenschaften führte. Es wurde erfolgreich gezeigt, dass die Kompatibilität mit Wasser und Ionen tatsächlich dem beabsichtigten Verhalten folgt, und Mischleitung wurde bei höheren EG-Gehalten beobachtet. Es wurde gezeigt, dass die Polymere mit höherem EG-Gehalt in organischen elektrochemischen Transistoren (OECT) gut funktionieren, sowohl unter Natriumchloridlösung als auch bei Verwendung eines Zellwachstumsmediums als Elektrolyt. Dies stellte den ersten Bericht über den Betrieb von OECTs unter Verwendung eines Zellwachstumsmediums in der Literatur dar. Die Transistoren wurden über 1200 aufeinanderfolgende Messzyklen im Dauerbetrieb getestet, was die Stabilität des PDPP unterstreicht. Zelltests schlossen die Zytotoxizität des Polymers aus. Letztendlich demonstriert die Kombination aus einem stabilen Betrieb und dem Betrieb in einem Zellwachstumsmedium, sowie dem ungiftigen Charakter das Potenzial für die Anwendung in bioelektronischen Anwendungen.

Um die elektrische Leitfähigkeit organischer Halbleiter zu erhöhen und einzustellen, ist heutzutage die molekulare Dotierung die Strategie der Wahl. Herkömmliches molekulares Dotieren erfordert gewöhnlich hohe molare Anteile des eingesetzten Dotanten bis hin zu mehreren zehn Prozent des Dotierungsmittels. Solch hohe molare Dotierungsverhältnisse sind jedoch immer mit Nebenwirkungen verbunden: große Mengen an Fremdmolekülen innerhalb

der Polymermatrix stören dessen Morphologie und behindern so den Ladungstransport. Darüber hinaus leidet die Ionisationseffizienz selbst unter hohen Dotierungsniveaus, und es kann zu unerwünschtem Ladungseinfang und -streuung kommen. Um diese Nachteile zu überwinden, haben wir im zweiten Kapitel eine neuartige Strategie entwickelt, um polymere Halbleiter zu dotieren, indem wir ein oxidiertes Lochtransportmaterial (HTM) als Dotierungsmittel einsetzen. Der Kern dieses Konzepts ist, dass nach erfolgtem Elektronentransfer vom oxidierten HTM zum neutralen Polymer auch das Dotierungsmittel selbst zum Lochtransporter wird. Dieser behindert den Ladungstransport nicht, sondern vermag ihn gar zu unterstützen. Der Dotierungsprozess wurde mit verschiedenen Methoden unter Verwendung eines PDPP als Halbleiter untersucht und das thermoelektrische Verhalten der dotierten Materialien untersucht. Dieses Konzept wurde später im dritten Kapitel erweitert, worin wir untersuchten, ob oxidierte HTMs in höheren Oxidationsstufen Vorteile gegenüber beispielsweise einfach oxidierten HTMs bieten. Die Erwartung, dass die erforderliche molare Menge des Dotierungsmittels durch Verwendung von Multielektronen-Akzeptoren anstelle von Einelektronen-Akzeptoren noch weiter reduziert werden kann, wurde bestätigt. Die Arbeit verglich auch die häufig diskutierte Rolle der Polarität des Wirtspolymers auf den Dotierungsprozess, indem zwei PDPPs direkt miteinander verglichen wurden, die sich explizit nur in ihren Seitenketten (EG vs. alkyl) unterschieden. Der Vergleich von mono-, di- und tetrakationischen Dotierungsmitteln zeigte, dass die Ladungsträgerdichte der mit den verschiedenen Dotierungsmitteln dotierten Systemen, direkt mit der Wertigkeit des eingebrachten Dotierungsmittels verknüpft ist. Dabei lieferte das tetrakationische Dotierungsmittel ungewöhnlich hohe Ionisierungseffizienzen von ca. 20 % bei nur 5 % molarem Dotierungsverhältnis im polaren Wirtpolymer.

Zusammenfassend brachte meine Forschungsarbeit Design-Prinzipien zur Gestaltung aktiver Materialien für betriebsstabile und ungiftige MIECs zur Verwendung in der Bioelektronik auf der Grundlage einer DPP-Polymerstruktur hervor. Darüber hinaus wurde ein neuartiges hocheffizientes Dotierungsverfahren etabliert und im Detail untersucht, welches stark erhöhte Ladungsträgerdichten und elektrische Leitfähigkeiten bei beispiellos niedrigen Dotierungsniveaus ermöglicht.

1. Introduction

Owing to the advancements in the various fields of polymer chemistry, new applications involving polymer materials and their engineering evolved during the last few decades. In science and technology, medicine and also our everyday life, established technologies have been replaced or improved and novel possibilities arose owing to the synthetical availability of functional polymers. This was possible because polymers offer an unforeseen freedom for obtaining a plethora of desired properties. Spanning from mechanical properties which can e.g., be flexible foils in packaging applications or sturdy casings for appliances, over insulating polymers in construction many physical properties can be tuned as desired. In the coatings technology for instance in the automotive sector, thin polymer layers in the thickness of only 100 μm , equal to the diameter of a human hair, ensure an appealing appearance along with protection of the substrate against weathering and corrosion over decades. All these manifold functions, which are by far not listed exhaustively, are today only accomplishable through synthetic polymers.

The present work evolves around fields where electrically active polymers are necessary; especially conjugated polymers with semiconducting properties, combined with the merits of common plastics. They constitute an ingenious family of materials with attractive potential applications. Within the framework of this dissertation, these polymers open up the capability for purposeful interaction between biological systems and electrical signals, as captured by the field of bioelectronics. The second application concerns itself with the direct conversion of thermal energy into electrical power, which is possible *via* polymer based thermoelectric materials. The following chapter briefly introduces the chemistry and physics of organic semiconductors, their special properties, as well as the two respective topics of the present dissertation.

1.1 Organic Semiconductors

The discovery of electrically conductive polymers in 1977 marked the begin of a new era of technical innovations.^[1] Until then, plastics were regarded as insulators, *i.e.* incapable of carrying electrical current and, in fact, this property which is distinctively different from metallic materials was desired in many places where plastics were used. By discovering the synthetic metals, as they were referred to as at the time, a paradigm shift was set in motion. Soon after the invention of electrically conductive polyacetylene (PAC), numerous other conjugated polymers have followed along. Some of the most important ones were polyaniline (PANI)^[2], polypyrrole (PPy)^[3], poly(*p*-phenylene) (PPP)^[4], poly(*p*-phenylene-vinylene) (PPV)^[5] or polythiophenes (PTh)^[6,7], and their structures are depicted overleaf in *Figure 1*. Some of these structures have been described long before the landmark work of Shirakawa *et al.* in

1977, but their potential remained unrecognized. But by the now increasing scientific interest in conductive polymers, these early organic semiconductors (OSCs) became valuable model systems for fundamental studies, thus helping to understand this new class of materials.

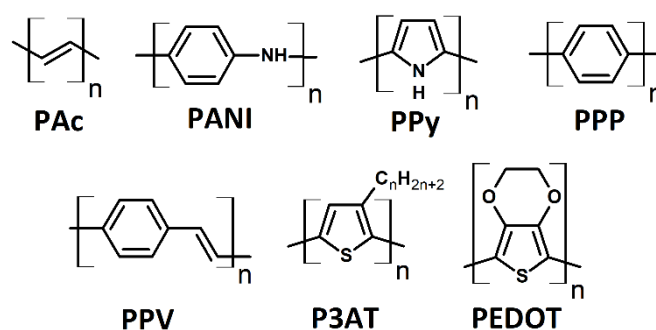


Figure 1 – Examples for 1st generation conjugated polymers: Polyacetylene (PAC), polyaniline (PANI), polypyrrole (PPy), poly(p-phenylene) (PPP), poly(p-phenylene-vinylene), poly(3-alkylthiophene) (P3AT), poly(3,4-ethylenedioxythiophene) (PEDOT).

These early conjugated polymers rapidly advanced and further processable materials like the polyalkylthiophenes (P3AT) and poly(3,4-ethylenedioxythiophene) (PEDOT) were developed. PEDOT can be acid-doped with either toluene sulfonic acid or polystyrene sulfonate (PSS) and in its doped form, PEDOT/PSS, it is a widely used and commercially available conducting polymer. With optimized procedures extremely high electrical conductivities beyond 6000 S cm⁻¹ can be reached.^[8] It is among the highest efficient organic thermoelectric materials, reaching a room-temperature figure of merit of $zT = 0.42$,^[9] and is already employed in prototype technical applications.^[10] The most important derivative of P3ATs is the poly(3-hexylthiophene) P3HT which is the best studied conjugated polymer today. Owing to its neat structure and the rather simple possibility for the controlled synthesis of regioregular P3HT *via* the Kumada Catalyst-Transfer Polymerization,^[11,12] it became a representative model system for studying fundamental charge transport properties or doping mechanisms of conjugated polymers.^[13–15]

Today, almost half a century later, the laboratory curiosities from the 1980s matured into an abundance of applications which have found their way into the consumer market and our everyday life. The reasons for this are manifold: OSCs can be tailored to fulfil specific requirements such as light absorption or emission, or a tunable electrical conductivity. They unite these abilities with the benefits of conventional plastics like being light weight, mechanically flexible, non-toxic, based on earth abundant materials and allowing for low-energy processing methods. This resulted in well-known applications for OSCs, such as the multibillion-dollar market for organic light emitting diodes (OLEDs). Today, OLEDs are ubiquitously used in televisions, smart phones, smart watches, and other displays.^[16,17] Photovoltaic energy generation contributes greatly to combating the global energy crisis by sustainably generating clean energy, *i.e.* without the emission of greenhouse gasses. In the last few years, organic photovoltaic (OPV) materials based on OSCs have entered the commercial market.^[18,19] Through the development of new polymer structures which can be

tailored to specific requirements, new fields of applications are on the verge of being broken into. Great advances have been made in the fields of bioelectronics and organic thermoelectrics.^[20,21] Bioelectronic devices allow for the transduction of signals from the biological world into measurable electrical data, which is an ever growing task in the frontier areas between medicine, biology and chemistry. Organic thermoelectric generators (TEGs) constitute another new area of research. TEGs can convert temperature gradients into electrical energy and are indispensable components in the innovation of many modern devices and may also contribute to providing clean energy by harvesting wasted heat. Where an autonomous power supply is required e.g., for so called smart-devices and the internet of things, TEGs could fulfil this need. Where large amounts of energy are lost by heat, TEGs can help to harvest this energy.

1.1.1 Second Generation π -Conjugated Polymers

All the devices listed above requiring modern OSCs are constituted by conjugated polymers as active materials. Many of the early conjugated polymers like the ones shown in *Figure 1* have the drawback of being insoluble in virtually any organic solvent, thus aggravating their processing, the scope of their application and impede a comprehensive characterization. The development of new conjugated polymers allows for the distinction between the 1st generation conjugated polymers like the ones discussed before, and a 2nd generation of conjugated polymers. By introducing solubilizing side chains, the solubility in organic solvents or compatibility with water and additives can be established and the processability is enhanced drastically. By designing more complex monomer structures and implementing the push-pull concept in donor-acceptor copolymers,^[22,23] the optoelectronic properties of the resulting polymers can be accurately tuned. The central idea in push-pull systems is to covalently combine donor units (D) with acceptor moieties (A) in an alternating manner, which leads to orbital overlap and a decrease in the materials absorption energy. This was a breakthrough, especially for OPV, where low band gap polymers were needed urgently to improve light harvesting, both as donor materials as well as acceptor materials. Consequently, the 2nd generation conjugated polymers offer a high degree of freedom for careful molecular design and for establishing structure property relationships. Some most important donor and acceptor structural units for this novel type of polymers are given in *Figure 2* below.

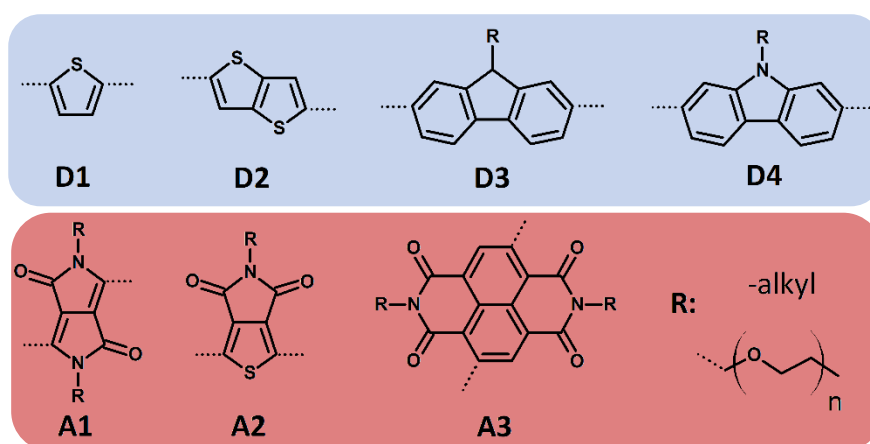


Figure 2 – Donor (blue) - and acceptor (red) motifs of important 2nd generation conjugated polymers. D1: thiophene (Th), D2: thieno[3,2-b]thiophene (TT, thienothiophene), D3: fluorene, D4: carbazole. A1: 2,5-dialkylpyrrolo[3,4-c] pyrrole-1,4-dione (DPP), A2: 5-alkyl-4H-thieno[3,4-c]pyrrole-4,6-dione (TPD), A3: naphthalenediimide (NDI).

R: solubilizing side chain can be either a linear- or branched alkyl chain or oligo ethylene glycol.

The building blocks of 2nd generation conjugated polymers consist of annulated heterocycles, which are substituted with side chains R. These side chains can either be linear or branched alkyl substituents and have the function of imparting solubility to the polymer. The aliphatic alkyl chains can be partially or fully replaced by oligoethylene glycol (OEG) moieties, which further expands the solubility. But more important, it improves the compatibility with additives^[24] or water^[25] and increases the polymer's polarity and dielectric constant.^[26] The fused heterocycles are the polymer backbone and the choice of the heteroatoms and functional groups like carbonyl functions controls the nature of preferred majority charge carriers. Electron rich cores (D1 – D4) primarily result in hole transport materials, whereas electron deficient cores (A1 – A3) establish electron transport materials. Sterical demands and electrostatic interactions between individual substituents of different electronegativity dictate the geometric conformation between the monomer units. Thereby, their orbital overlap is influenced, which directly affects the charge transport along the polymer chains. In total, a variety of parameters in the molecular design arise, which allow for tuning of macroscopic material properties. By means of the preferred majority charge carriers, the materials can be divided into p- and n-type polymers, for hole and electron transport, respectively.

In the following, the structural variation and its consequences on physical properties are discussed using one typical example of the PDPP copolymer.

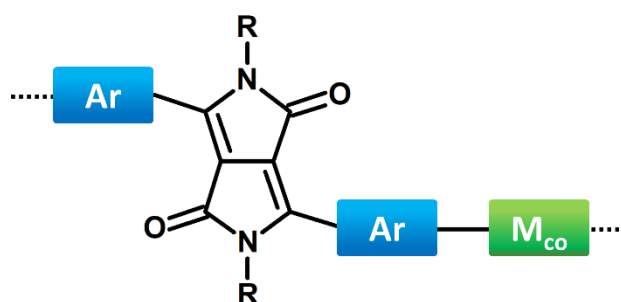


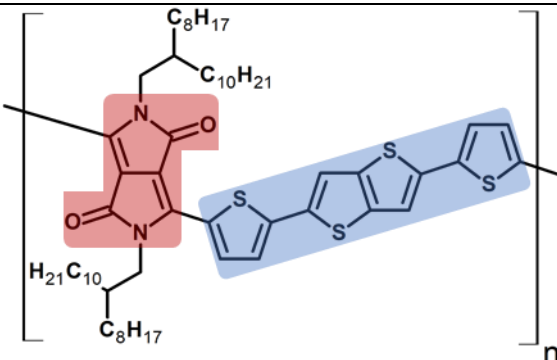
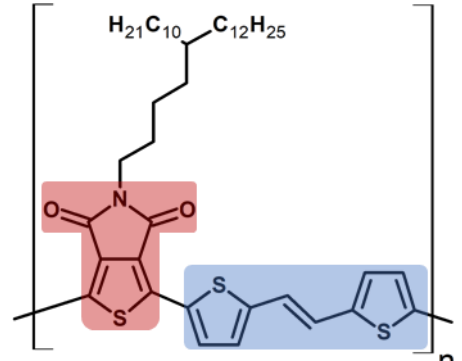
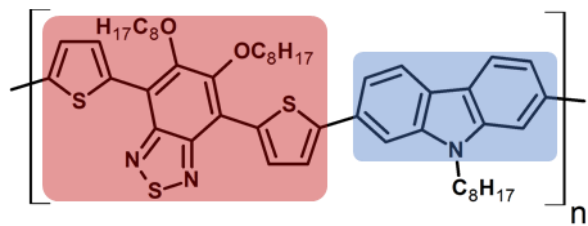
Figure 3 – Schematic of the generic diketopyrrolopyrrole copolymer repeating unit, including the DPP core substituted with R, being either alkyl, or oligo ethylene glycol chains, the aryl flanking units (Ar) and the comonomer M_{co} .

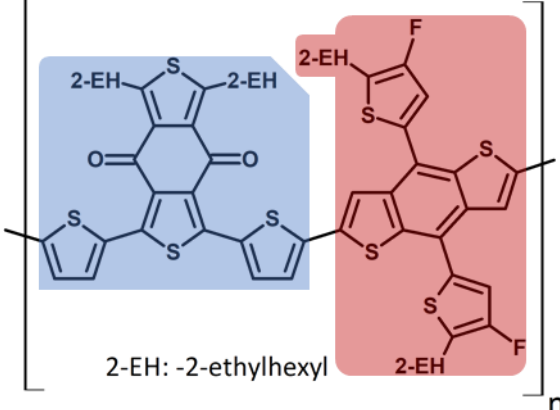
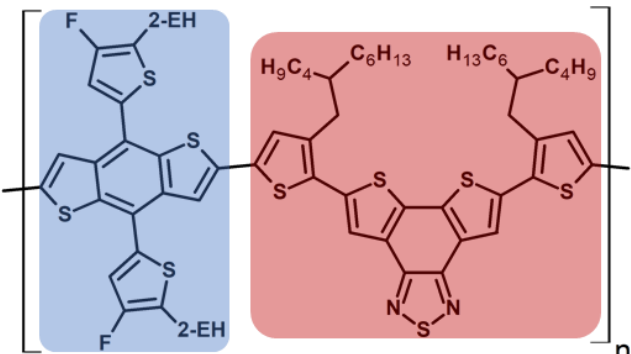
These design principles are now applied, and their validity is demonstrated on diketopyrrolopyrrole (DPP) polymers, as one of the most important class of 2nd generation conjugated polymers. PDPPs are characterized by a very high thermal and photostability and are for instance well suited materials for OPV applications.^[27,28] The DPP-core is adaptable to fit different purposes. The generic structure of PDPP copolymers is shown schematically in *Figure 3* above, including the DPP core, substituents (R), flanking units (Ar) and a comonomer (M_{co}) and the respective roles of the moieties are explained in the following. By varying the flanking units from thiophene [T] to phenyl [Ph], 2-pyridyl [Py] and 2-pyrazyl [Pz], the mode of operation can be adjusted from p-type over ambipolar transport to n-type transport.^[29,30] More in particular, the influences of the individual molecular motifs on some selected resulting properties, like charge transport or molecular orientation have been extensively studied by Mueller *et al.* Upon employing thiophene- or 2-pyridyl flanking units, the planarization of the backbone is facilitated. This leads to remarkably low band gaps with an optical absorption onset up to 1100 nm for the thiophene flanked DPP using thiophene as the comonomer.^[31] The reason for this can be briefly explained by the dihedral angles between the DPP core and the flanking unit, and between the flanking unit and the co-monomer. For thiophene and 2-pyridyl, low dihedral angles are possible because the both thiophen-sulfur, as well as the pyridyl-nitrogen can align with the carboxyl-oxygen of the DPP core and lock in *via* noncovalent interactions. This planarization assists the crystalline order, leads to a tighter π - π stacking and enhanced coherence length.^[29] In the case of a phenyl-ring the hydrogen-atoms of the phenyl ring are sterically hindered by the carboxyl group of the DPP core, which causes a distortion and, therefore, a larger twist along the backbone.^[31] Macroscopically, this can be observed *via* relatively lower band gaps and higher charge carrier mobilities in thiophene and pyridyl flanked PDPPs, compared to phenyl flanked derivatives, both, in the bulk as well as in thin films. Aside from the mode of charge transport (p- or n-type) the choice of building blocks also influences the molecular order in the polymer. Controlling the orientation of the polymer with respect to the substrate e.g., by the different aryl flanking units and comonomers is desired, as the charge transport is differently oriented in different applications: in field effect transistors the charge transport happens at the interface between

dielectric and polymer, laterally between the electrodes. In diode assemblies like organic solar cells, the charge transport occurs vertically to the substrate. For PDPPs it was found, that thiophene flanking-units tend to orient the polymer in an edge-on fashion *i.e.*, the polymer's backbone standing perpendicular with respect to the substrate. On the contrary, pyridyl flanked derivatives align in a face-on manner *i.e.*, the polymer backbone lying flat on the substrate; this preference is alleviated in poorly oriented phenyl-flanked PDPPs. When varying the electron withdrawing effect in the co-monomer the orientation and the mode of operation can be further fine-tuned. In the case of thiophene as comonomer, this is e.g. possible *via* alkoxylation or perfluorination.^[29] Further aspects of the structure-property relationships from molecular design principles toward macroscopic properties are examined and explained more elaborately in this thesis. By optimizing the side chain R in e.g., moving the branching point away from the backbone the crystallinity, and thus, the charge transport can be improved considerably.^[32] When the hydrocarbon chain is substituted by OEG chains, the polymer becomes swellable in water.^[33,34] Aside from the aforementioned applications in OPVs, outstanding charge transport properties are reached when copolymerizing thiophene-flanked DPP with thienothiophene TT. High hole mobilities of $\mu_h^{OFET} = 10 \text{ cm}^2 \text{ V}^{-1}\text{s}^{-1}$ were reported for the resulting polymer PDPP[T]₂-TT.^[35] In addition to this, the DPP based polymers show promising results as the active material in TEGs,^[36] as mixed ion electron conductors (MIEC) for bioelectronic applications and are the central subject of this work.^[34,37]

The versatility of combining the D and A units leading to a wide variety of D-A copolymers with entirely different optical and electronic properties. This versatility is depicted using some prominent examples in *Table 1* below. The donor part is marked blue, and the acceptor part is marked red in these structures.

Table 1: Selected D-A copolymers used in solar cell applications. The *name* refers to the abbreviated description as used by the original authors. λ_{\max} : optical absorption maximum, $\mu_{\text{h}}^{\text{OFET}}$: reported hole mobility measured using organic field effect transistors.

Structure Name	λ_{\max}	$\mu_{\text{h}}^{\text{OFET}}$	Ref.
 <p>PDPP-DTT</p>	822 nm	$10.5 \text{ cm}^2\text{V}^{-1}\text{s}^{-1}$	[35]
 <p>PTPD-TVT</p>	480 nm	$1.7 \cdot 10^{-2} \text{ cm}^2\text{V}^{-1}\text{s}^{-1}$	[38]
 <p>PB PDTBT</p>	404, 579 nm	$1 \cdot 10^{-4} \text{ cm}^2\text{V}^{-1}\text{s}^{-1}$	[39]

Structure Name	λ_{\max}	$\mu_{\text{h}}^{\text{OFET}}$	Ref.
 <p>2-EH: -2-ethylhexyl</p> <p>PM6</p>	575, 613 nm	n.a.	[40]
 <p>2-EH: -2-ethylhexyl</p> <p>D18</p>	584 nm	$1.6 \cdot 10^{-3} \text{ cm}^2\text{V}^{-1}\text{s}^{-1}$	[41]

Almost all of the D-A copolymers shown above function as donor components in a polymer solar cell and some of them deliver power conversion efficiencies above 15% in combination with non-fullerene acceptor molecules.^[35,38–41]

1.1.2 Synthetic Approaches toward 2nd Generation Conjugated Polymers

Polymerizations can be divided into two different types, which are either based on the chain-growth or on the step-growth mechanism. In chain growth-reactions, the polymerization proceeds by the addition of a monomer unit to an initiator or to a preexisting reactive chain end at a time. The polymerization continues until all monomer is consumed or the reaction is terminated by other means, like the intentional termination or when side reactions prevail. In step-growth reactions however, the polymer is stepwise formed by bifunctional monomer units capable of reacting with one another.^[42] Thereby, sequentially new larger monomers are formed which have the same reactivity as the initial ones, and every reaction step requires the same activation. Possible mechanisms for step-growth polyreactions are for instance polyadditions, where the underlying chemical reaction is an addition between functionality A

and B, for example in the synthesis of polyurethanes from a diisocyanate and a diol. The other reaction type for a step-growth polyreaction are polycondensations, where the underlying chemical reaction is a condensation *i.e.*, a reaction where two molecules merge under the loss of a small molecule, often water or HCl.^[43] Polycondensations are e.g. used in the production of polyesters, polyamides, or in the synthesis of conjugated polymers *via* one of the cross coupling reactions to form the C-C bonds. The reactions of interest here are Suzuki, Sonogashira, Heck and Stille coupling reactions. In the Stille cross-coupling polycondensation, the coupling between dibrominated and distannylated monomers according to *Figure 4* below takes place, and details regarding this reaction type are elaborated in the next section.

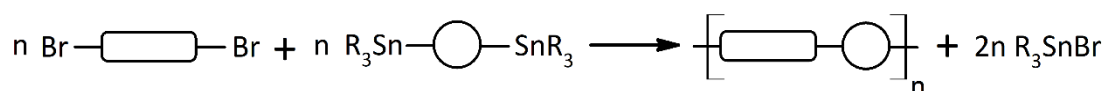


Figure 4 – Schematic Stille cross-coupling polycondensation reaction, R: alkyl.

An important peculiarity of polycondensations is that only at very high conversions high molecular weights or degrees of polymerization X_n , respectively, are obtained. This can be expressed by the Carothers equation (*equation 1*) below:^[44]

$$X_n = \frac{1+r}{r+1-2rp} \quad (\text{equation 1})$$

$$r = \frac{N_A}{N_B} \quad \& \quad r \leq 1 \quad (\text{equation 2})$$

X_n : degree of polymerization, p : conversion, r : stoichiometric ratio of reactants,
 $N_{A/B}$: number of molecules of the monomer A/B.

Moreover, the stoichiometric ratio of monomers r limits the maximum achievable degree of polymerization which rapidly decays when r deviates from 1, even when the reaction has proceeded to full conversion. Aside from weighing errors or residual monomer impurities, side reactions like oxygen mediated homocouplings between two A-A or two B-B monomers are possible in transition metal catalyzed cross coupling polycondensations and may lead to a imbalanced stoichiometric ratio.^[45,46] The error from a deviation of the stoichiometric ratio from $r = 1$ can be excluded by using bifunctional monomers from the type A-B, where the Carothers equation reduces to *equation 3*.

$$X_N = \frac{1}{1-p} \quad (\text{equation 3})$$

Thereby, the degree of polymerization is only limited by the conversion until which the reaction is driven to. However, the synthetic effort toward asymmetrically functionalized monomers is considerably higher and, more importantly, a strategic variation of the comonomers is virtually impossible. In summary, successful polycondensations necessitate the use of highly pure monomers and accurate experimental procedures in order to obtain polymers of reasonable molecular weights. A clear advantage is the possibility of a purposeful variation of the building blocks within the resulting copolymers. This renders

polycondensations using A-A / B-B monomers an ideal toolkit for synthesizing novel 2nd generation conjugated polymers and studying their structure property relationships.

For the synthesis of PDPPs and many other conjugated polymers, step growth polymerizations are the standard synthetic method, particularly the class of palladium catalyzed cross-coupling polycondensations. Most commonly Suzuki- and Stille cross-coupling reactions are employed. Because Stille cross-coupling polycondensation reactions were utilized to synthesize all the polymers in the present work, this type of reaction is discussed in the following. The C-C bond formation in Stille cross-coupling reactions is accomplished using dibrominated (A-A) and distannylated (B-B) monomers following the catalytic cycle shown below. Other cross-coupling reactions proceed analogously, but utilize differently activated C-C bonds, for instance by borylation in Suzuki cross-couplings.

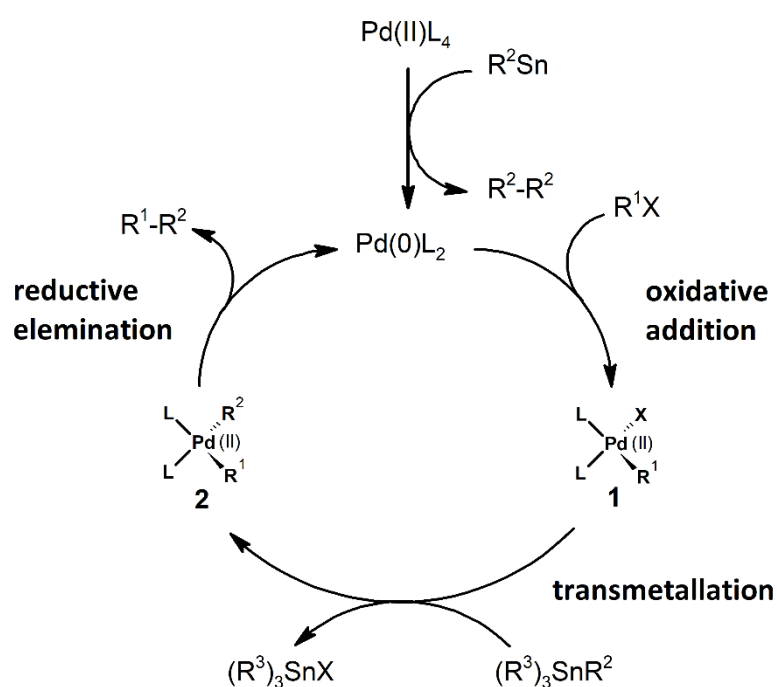


Figure 5 – General catalytic cycle of the Palladium catalyzed Stille cross-coupling reaction involving the three fundamental steps of oxidative addition of the organohalide to the metal center, transmetallation of the coupling partner from Sn to Pd and subsequent reductive elimination of the coupling product and recovery of the catalyst. R¹, R²: aryl, alkenyl, alkynyl, alkyl. R³: alkyl. X: I, Br, F, OTf.

The Stille cross-coupling reactions proceed in the following three fundamental steps:^[47]

1. Oxidative addition of the aryl halide R¹-X to the catalytically active metal species Pd^{±0}, forming complex 1.
2. Transmetallation of R² from tin to the palladium catalyst and transfer of the halide X to tin, formation of complex 2.
3. Reductive elimination of the substrates under formation of the C-C bond and recovery of the catalyst.

The tendency for the transmetallation of Rⁿ from tin to palladium decreases with the substituent's electronegativity following sp > sp² > sp³, or simpler: alkyl << aryl. Therefore, the

substituents R^3 are usually methyl or butyl, and R^2 is the desired aromatic comonomer which is transmetalated selectively. The advantage of the Stille cross-coupling over other transition metal catalyzed cross-coupling reactions is the tolerance of most functional groups^[48], as a drawback the high toxicity of organic tin compounds is to be mentioned. Used catalysts are $[Pd_2(dba)_3]$, $Pd(PPh_3)_4$ or $Pd[(o\text{-tol})_3P]_2$ and common solvents as dimethyl formamide or chlorobenzene are mostly used, but also aqueous systems and ionic liquids like $EMIM \cdot BF_4$ have been reported.^[49] If the chosen reactants are bifunctional, the cross-coupling will proceed as a step-growth polymerization and it is termed as cross-coupling polycondensation.

1.1.3 Synthesis of DPP and Thiophene Monomers

The aryl flanked diketopyrrolopyrrole (DPP) structure has been known for decades and was originally developed for the use as a colorant.^[50] Figure 6 below shows the so called succinate route which is today the established route for the synthesis of DPP derivatives.^[51] The mechanism is exemplarily given for the thiophene flanked DPP.^[52,53] Diethyl succinate **1** is first deprotonated at the α -position by a strong base, e.g. sodium *tert*-butoxide. After a rearrangement, the double bond attacks the cyano-function of the flanking unit and the intermediate imine **2** is formed. The same process is repeated on the remaining α -carbon and the resulting intermediate **3** expels one equivalent of ethanol after the intramolecular nucleophilic attack at the carbonyl-carbon, thus forming the first lactam-ring. This repeats itself once more and the final DPP-core **4** is afforded.

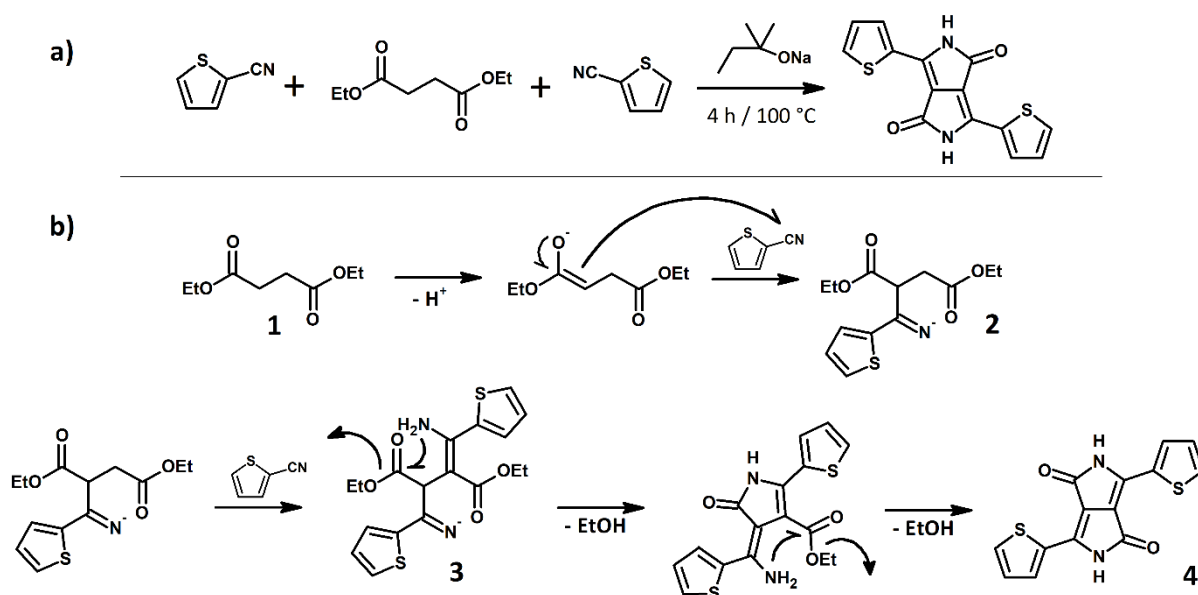


Figure 6 – a) Reaction scheme for the synthesis of thiophene flanked DPP starting from thiophene-2-carbonitrile and diethyl succinate (top). b) Corresponding reaction mechanism (bottom).

The resulting crude product is insoluble in any common organic solvent and must be equipped with solubilizing side chains. In the past, exclusively branched alkyl chains were used for this purpose^[54,55] but more recently, the substitution with hydrophilic oligoethylene glycol (OEG) chains has increasingly emerged. Thereby, the scope of application of DPP based and other

conjugated polymers could be extended toward new applications like bioelectronics^[34] where fully hydrophobic polymers are not desired. The use of polar OEG groups furthermore improves the miscibility with polar additives like dopants^[24], which is beneficial for thermoelectric materials^[56] or high-mobility organic field effect transistors.^[57]

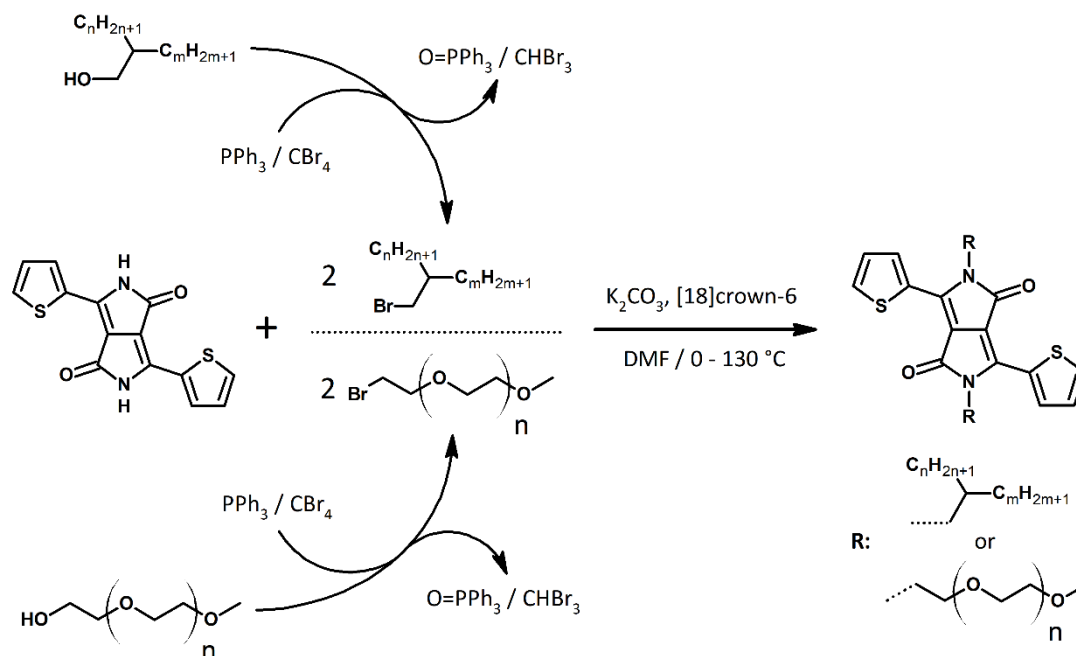


Figure 7 – Side chain functionalization of the DPP core on the example of DPP[T]₂ using either a brominated branched alkyl chain (top) which is previously obtained *via* an Appel reaction, or a brominated linear oligoethylene glycol chain which also is previously synthesized using an Appel reaction.

Figure 7 above shows the synthetic approach toward alkyl and OEG substituted DPPs, respectively. In both cases, the corresponding bromide is required as substitution partner, which is conveniently accessible from its alcohol by an Appel reaction. First, the amino function in the DPP-core is deprotonated by a weak base e.g., potassium carbonate, and is then subjected to a nucleophilic substitution with the respective bromide. The reaction proceeds smoothly in most cases; only when introducing OEG substituents, care must be taken. The OEG bromide must be added in the cold as it is prone to elimination of HBr at elevated temperatures. This side reaction should be excluded, as it disturbs the reaction considerably because firstly, the required reactant (OEG-Br) decomposes and, secondly, the formed acid can lead to hydrolysis of the DPP's lactam ring.^[58] Finally, in order to transform the DPP into a monomer which is polymerizable in Stille cross coupling polycondensation, it needs to be dibrominated. This is carried out using *N*-bromosuccinimide according to the reaction scheme below.

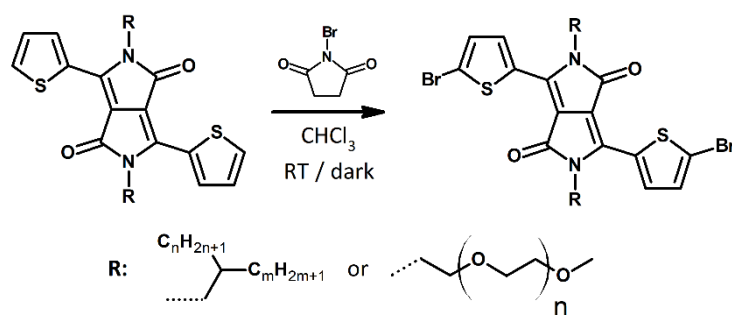


Figure 8 – Bromination of the alkyl- or OEG functionalized DPP[T]₂ core using N-bromosuccinimide.

The comonomers for dibrominated DPPs in Stille cross coupling polycondensations are bis-stannylated donor monomers, which are for instance accessible *via* the lithiation of 2,5-dibromo-3,4-ethylenedioxythiophene or in a one-pot procedure *via* a metathesis reaction with trimethyltin chloride after lithiation of the neat OEG-substituted thiophene unit (Figure 9).

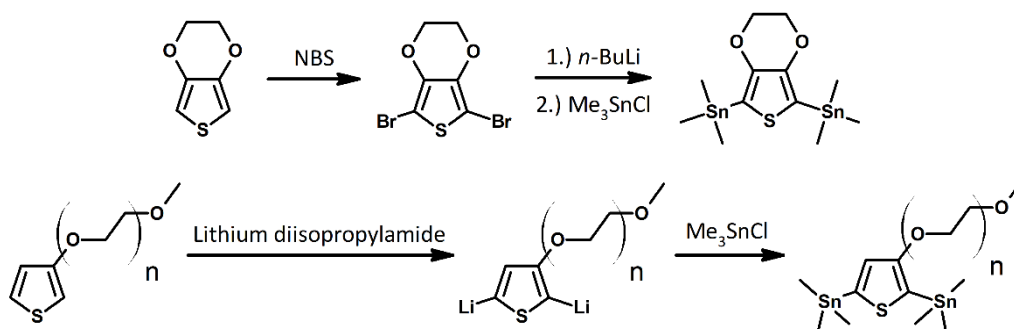


Figure 9 – Stannylation of 3,4-ethylenedioxythiophene over the brominated intermediate (top), stannylation of 3-oligoethylene substituted thiophene after lithiation with lithium diisopropylamide (bottom).

It must be noted that although the stannylated thiophene compounds are obtained *via* less reaction steps, they pose a greater synthetic challenge than the synthesis of the DPP comonomers. Especially the purification of the stannylated products is difficult, as they often feature high boiling temperatures and the trialkyltin moieties are sensitive toward silica gel. This aggravates both, the distillation even under high vacuum, and column chromatography. As highly pure monomers are crucial for the success of step-growth polymerizations this has to be kept in mind.

1.2 Doping of Conjugated Polymers

1.2.1 Charge Transport in Conjugated Polymers

The charge transport in conjugated polymers at room temperature and above is dominated by the hopping-transport mechanism, whereas only at lower temperatures (< 40 K) a band-like transport as known from inorganic conductors predominates.^[59,60] In the case of electron (e⁻) transport, the charge carriers move through the lowest unoccupied molecular orbitals (LUMOs) of the OSC, hole (h⁺) transport proceeds through vacant states in the highest occupied molecular orbital (HOMO) of the OSC. According to the hopping mechanism, charge

carriers (e^-/h^+) can propagate throughout the density of states (DOS) of the semiconductor *via* discrete hopping events between localized states which are spatially and energetically separated. For a successful hopping event, an electron must take up a sufficient amount of energy for instance by thermal excitation, to overcome the energetic barrier between the two discrete states.^[61] In disordered materials like conjugated polymers, the hopping rate w_{ij} between two sites i and j depends on both, the spatial distance, and the energetic difference between the respective states as well as of the overlap of their wavefunctions and is described by *equation 4* according to the Miller-Abrahams model.^[61]

$$w_{ij} = v_0 \exp(-2\gamma r_{ij}) \cdot \begin{cases} \exp\left(-\frac{\epsilon_j - \epsilon_i}{k_B T}\right) & , \epsilon_j > \epsilon_i \\ 1 & , \epsilon_j \leq \epsilon_i \end{cases} \quad (\text{equation 4})$$

with v_0 : hopping attempt frequency, r_{ij} : jump distance, γ : inverse localization radius of the electron's wavefunction, ϵ_{ij} : energy of the state i/j , k_B : Boltzmann constant.

If the hopping event is "uphill" in energy, the rate is temperature activated with the required activation energy being the energetic difference between the two states. *Vice versa*, downward jumps are independent of the available thermal energy. Care needs to be taken, since in real OSCs additional defect states are present which arise from e.g., trace impurities, kinks in the polymer chain or crystal lattice faults. These defects may act as trap states, which strongly bind electrons, hindering them from further partaking in charge transport. The trapped electrons can either be liberated thermally (shallow traps) or are trapped irreversibly (deep traps). The charge carrier mobility following the thermally activated hopping is consequently thermally activated as well and can be written as ^[62]

$$\mu = \mu_0 \exp\left(-\left[\frac{2\sigma}{3k_B T}\right]^2\right) \quad (\text{equation 5})$$

Where μ_0 : mobility pre-factor and σ : width of the Gaussian density of states.

showing that the carrier mobility follows an Arrhenius type behavior. The macroscopic electrical conductivity is ultimately described by the correlation in *equation 6*:

$$\sigma = N \cdot e \cdot \mu \quad (\text{equation 6})$$

With N : charge carrier density, e : elemental charge and μ : charge carrier mobility.

The relationship shows that the variables dictating the electric conductivity are the charge carrier density and the aforementioned mobility, which both are influenced by doping which is elaborated further in the following section.

1.2.2 Chemical Doping

Organic semiconductors like conjugated polymers intrinsically contain a very low amount of mobile charge carriers, which are however essential for contributing to an electric current. The concentration of charge carriers in an OSC can for instance be increased by the injection from an electrode, photoexcitation or doping with chemical additives.^[61] For numerous applications, the method of choice for tuning the charge carrier density of an active material

is the addition of molecular dopants, e.g. in organic solar cells^[63], thermoelectric generators^[36] or in organic field effect transistors (OFETs).^[64] Thereby, the electrical conductivities can be tuned over several orders of magnitude, as exemplarily demonstrated on P3HT: it comprises an electrical conductivity in the range of $10^{-5} \text{ S cm}^{-1}$ in the pristine state, which increases to *ca.* 1 S cm^{-1} after the addition of 10 mol% of the common dopant tetracyanoquinodimethane (F₄TCNQ).^[65] By chemical doping, the charge carrier density is increased after the dopant reduces (n-type doping) or oxidizes (p-type doping) the OSC. In n-type doping an electron is added to the OSCs LUMO, and *vice versa*, an electron is removed from the OSCs HOMO in p-type doping.^[66,67]

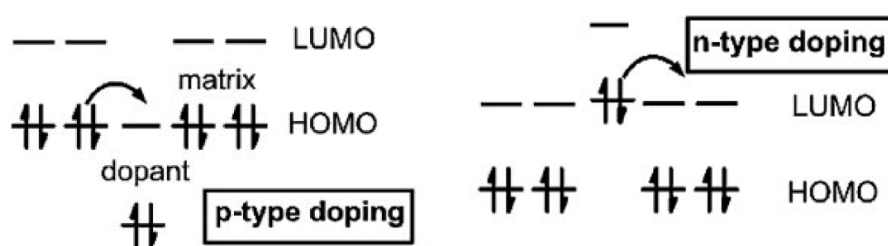


Figure 10 – Schematic illustration of the doping process for p-type (left) and n-type doping (right). In p-type doping, the dopant receives an electron from the OSC matrix, during n-type doping an electron is donated to the host polymers LUMO. Adapted from literature.^[67]

By introducing additional charge carriers not only the carrier density is increased, but also low lying trap states are filled, thus leading to a disproportional increase in charge carrier mobility already at very low doping ratios ($< 1 \text{ mol } \%$).^[68] Further doping leads to a shift of the materials Fermi level toward the LUMO (n-doping) or HOMO (p-doping), thereby reducing the distance between Fermi and transport level^[69], which further raises the charge carrier mobility and, ultimately, increases the electrical conductivity. Therefore, chemical doping is a powerful tool to tune electrical properties of a given OSC. Depending on the sterical demands and energetic conditions of host polymer and dopant, the doping can proceed following two different mechanisms, which are the integer charge transfer and the formation of charge transfer complexes (CPX).^[70] The two ways are explained on the example of p-doping in the following paragraph. If the electron affinity (EA) of the dopant is equal or lower than the ionization potential (IP) of the OSC, the charge transfer can proceed in the form of a redox reaction with e.g., conventional oxidizing agents like elemental Iodine, NOPF₆ or F₄TCNQ. Lewis-acids like Iron(III)chloride can also be capable of accepting an electron from the OSC.^[70] The chemical structures of some important p-dopants are shown below in *Figure 11*:

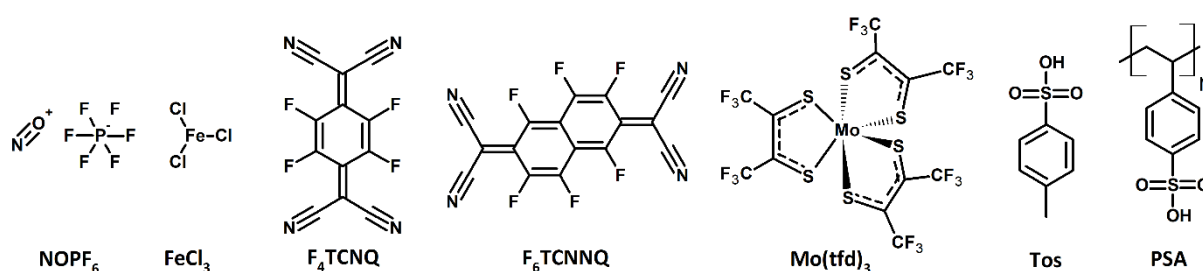


Figure 11 – Examples of common molecular p-type dopant structures. Nitrosonium hexafluorophosphate (NOPF_6), Iron(III)chloride (FeCl_3), tetracyanoquinodimethane (F_4TCNQ), tetracyanonaphthoquinodimethane (F_6TCNNQ), Molybdenum tris(1,2-bis(trifluoromethyl)ethane-1,2-dithiolene) ($\text{Mo}(\text{tfd})_3$), toluenesulfonic acid (Tos), polystyrene sulfonic acid (PSA).

The second case comprises the hybridization of the frontier orbitals of OSC and dopant with the subsequent formation of a charge transfer complex, which can provide mobile charge carriers by thermal activation.^[71] A noteworthy peculiarity of the charge transfer complex formation is the circumstance, that it can occur even when the thermodynamic driving force for a integer charge transfer is not given, *i.e.* if the dopant's electron affinity is lower than the OSC's ionization potential (in the case of p-doping). A necessary condition for the formation of charge transfer complexes is an adequate overlap of the frontier orbitals of OSC and dopant.^[72] This is mainly the case in planar dopants which can intercalate very well into the (crystal) lattice of the host polymer, but almost impossible for sterically demanding dopants like for instance molybdenum tris(1,2-bis(trifluoromethyl)ethane-1,2-dithiolene) complexes (*cf.* Figure 11 above).

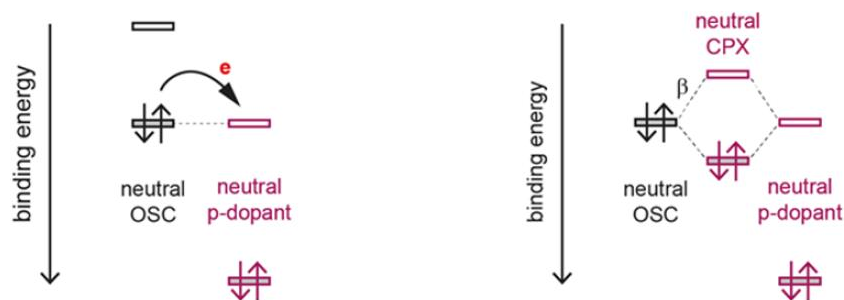


Figure 12 – Schematic illustration of the two possible doping pathways, *i.e.* integer charge transfer between OSC and dopant (left), or hybridization of OSC and dopant frontier orbitals and formation of a charge transfer complex (CPX). Adapted from Literature.^[71]

If a conjugated polymer can be protonated at some position of its conjugated backbone, this poses another mechanism for p-doping, and it is referred to as acid-doping. The most prominent example for an acid doped conjugated polymer is PEDOT, which is mixed with either toluenesulfonic acid (Tos) or polystyrene sulfonate (PSS). The obtained materials PEDOT:Tos or PEDOT:PSS are commercially established hole conductors^[10] which can reach very high electrical conductivities beyond 6000 S cm^{-1} using optimized preparation procedures.^[8]

The biggest drawback of classical chemical doping as explained above is the dramatic decrease of the doping efficiency with increasing doping concentration. As described earlier, a certain amount of dopant is necessary to fill deep lying traps to move the Fermi level toward the transport level.^[68] But with increasing molar doping ratios (MDR) it becomes more probable that free charge carriers are captured by electrostatic attraction of ionized dopants, which are increasingly dispersed within the matrix.^[73] A further complication brought about by high molar doping ratios is the disturbance of the polymer morphology upon accommodating an excess amount of dopant molecules, which reduces the charge carrier mobility. Still additionally, an increasing density of ionized molecules within the polymer matrix offers scattering centers for charge carriers which, too, decreases the overall charge carrier mobility and forbidding a further increase of the electrical conductivity. Altogether, the doping efficiency rapidly deteriorates from the order of $\eta_{\text{dop}} \approx 50\%$ for ultralow molar doping ratios below $10^{-3}\%$ to below $\eta_{\text{dop}} \approx 5\%$ when the MDR exceeds 5 – 10 mol%.^[70,71] In light of commonly very high employed MDRs in the range up to 40 %, the poor exploitation of the doping process is obvious. Aside from the classical doping procedures entailing these causal difficulties, there are several reports describing another approach. By admixing partially oxidized electron-rich molecules into polymers or small molecule OSCs, the electrical conductivity of the host material can be enhanced. This idea was originally described in the context of Perovskite solar cells, where the hole transport material spiro-OMeTAD has been oxidized using Lithium bis(trifluoromethane)sulfonimide (LiTFSI). The thereby obtained dicationic spiro-OMeTAD(TFSI)₂ served as p-dopant for neutral spiro-OMeTAD.^[74] In a similar fashion, the monocationic radical salt tris(4-bromophenylammoniumyl) hexachloroantimonate ("Magic Blue") has recently been used to p-dope PDPP-based polymers and other conjugated polymers.^[75] In both cases, a single electron transfer could be achieved, leading to an increased charge carrier density and electrical conductivity. The concept of transferring an electron from a partially occupied HOMO (SOMO) of an OSC to a neutral small molecule OSC or polymer semiconductor is fully studied and explained in detail in this thesis.

1.3 Organic Mixed Ion-Electron Conductors for Organic Electrochemical Transistors

Organic mixed ion-electron conductors (OMIECs) are organic semiconductors which are capable of transporting both, electrical charges (electrons/holes) and ions.^[76] MIECs can be realized in electron rich p-type or electron deficient n-type materials, similar to the differentiation in OSCs. Necessary for mixed conduction are on the one hand conventional semiconducting properties for the electronic contribution and, additionally, the material must readily incorporate (hydrated) ions.^[77] The semiconducting properties can be established by employing a conjugated polymer backbone and the contribution for the ionic conductivity is today mostly established by equipping the polymer with polar moieties such as ionic groups ($R-COO^-H^+$, $R-SO_3^-H^+$, $R-SO_3^-M^+$, $R-N^+R'_3X^-$)^[78] or hydrophilic oligo ethylene glycol side chains.^[79] But there are also reports of side chain-free MIECs, if for example a sufficient polarity or hydrophilicity is provided by the backbone itself.^[80] One important application of OMIECs is the organic electrochemical transistor (OECT), where mixed conduction is required in order to fulfil the working principle, which is elucidated in the following paragraph.

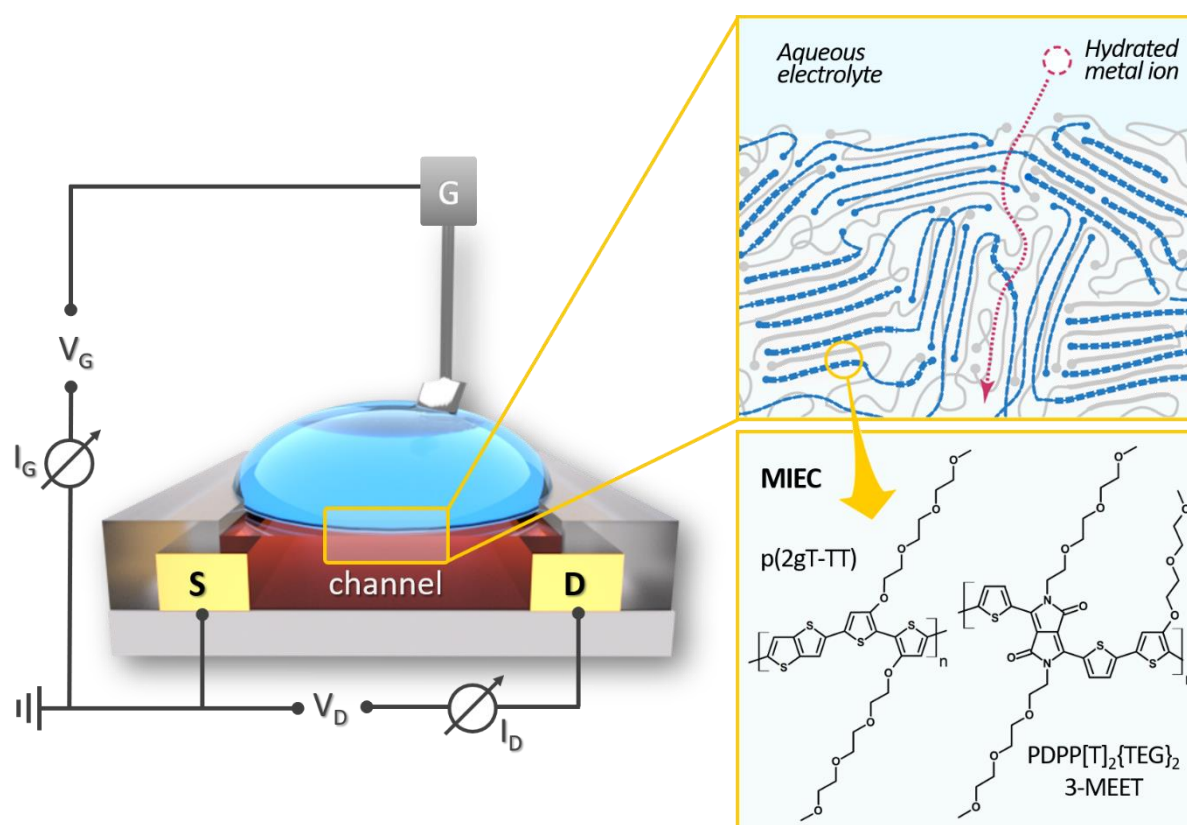


Figure 13 – Schematic OECT device structure (left) comprising source (S), drain (D) and gate (G) electrodes drawn in gold, the active channel material (red), as well as the electrolyte solution drop on top. The magnification of the active channel/electrolyte interface (top right) illustrates the permeation of hydrated ions into the bulk of the MIEC, and below, two exemplary MIEC materials are shown. Adapted from literature.^[81–83]

The device structure as shown in *Figure 13* above comprises the following parts, which are the gate, source and drain electrodes as well as the active material and an electrolyte. Source and drain electrodes are typically patterned from gold.^[83] The gate-electrode usually is a non-

polarizable Ag/AgCl electrode, because it can provide large amounts of charges. This is necessary due to the high volumetric capacitances of the MIECs which is in direct contact with both the source and drain electrodes as well as with the electrolyte. By applying a gate voltage, an electrical field forms, leading to the injection of dissolved ions, for instance Na^+ or Ca^{2+} , along with their hydration shell into the bulk of the polymer. This so-called electrochemical doping process is controlled by the gate voltage V_G and directly triggers the modulation of the capacity of the whole film and a considerable degree of swelling. The charges introduced by the ions are compensated by the OSC, thus increasing the polymers electrical conductivity *via* the created charges on the polymer backbone.^[84] As a result, an applied drain voltage V_D can give rise to a drain current I_D , which represents the output parameter. Because an OECT is normally used as a transducing entity between the surrounding biological medium and an electrical signal, the measure for this transducing quality is given in terms of the transconductance g_m . It is defined according to *equation 7* below and represents the change of drain current per change of gate voltage.^[85]

$$g_m = \frac{\partial I_D}{\partial V_G} \quad (\text{equation 7})$$

The transconductance is empirically accessible from the first derivative of the transfer curve of the transistor measurement and depends on a number of other parameters. It can be alternatively written as *equation 8*:

$$g_m = \frac{Wd}{L} \cdot \mu C^* \cdot (V_G - V_{Th}) \quad (\text{equation 8})$$

Where W : channel width, d : film thickness, L : channel length, μ : OECT-charge carrier mobility, C^* : volumetric capacitance, V_G : gate-voltage and V_{Th} : threshold-voltage.

This formulation emphasizes that the transconductance is depending on the channel geometry (expressed by the term Wd/L) and the biasing-conditions ($V_G - V_{Th}$). The second term (μC^*) however, cannot be manipulated by the device architecture or the operating conditions, as it is constituted by material parameters *i.e.*, the OECT-charge carrier mobility μ as well as the volumetric capacitance C^* . This renders the μC^* product as an useful figure of merit for the comparison of different mixed conductors.^[77] The μC^* product can be determined experimentally by plotting the transconductance g_m *vs.* the product of the geometric term and the biasing conditions ($Wd/L \cdot (V_G - V_{Th})$) and fitting the relationship linearly; the slope corresponds to μC^* .^[86] In addition to the previously discussed essential requirements for mixed conduction, a material must fulfill a number of other criteria in order to qualify for an MIEC for the application in bioelectronic devices. Those are a low ionization potential, enabling the transistor to be switched on and off at low potentials, *i.e.* $V_{Th} \ll 1 \text{ V}$.^[87] This is necessary for the operation in aqueous media, where a breakdown of the electrolyte would occur beyond *ca.* 1 V. Furthermore, the device is ought to be operated in contact with biological structures or living cells, which also do not tolerate higher potentials. Next, the material must provide sufficient stability in aqueous electrolyte regarding chemical inertia and mechanical durability *i.e.*, dissolution or delamination of the film. The degree of swellability

has to be controlled, as a too little swelling hampers the ion penetration into the bulk, whereas a very pronounced swelling may hamper the charge transport properties of the MIEC.^[88] It has to be noted, that μ and C^* are *a priori* contradictory quantities, as the charge carrier mobility profits from high order and crystallinity. The volumetric capacitance, however, depends on a facile ion-uptake and swelling, which generally reduces the degree of order on the molecular scale. Further conditions with regard to the application of MIECs are the absence of toxicity and, preferably, mechanical flexibility to favor the interaction with soft biological tissues.^[89] All of these manifold requirements can be met by PDPPs after careful molecular design. Some interesting PDPPs, and other examples for p-type MIECs from 2nd generation conjugated polymers are shown below.

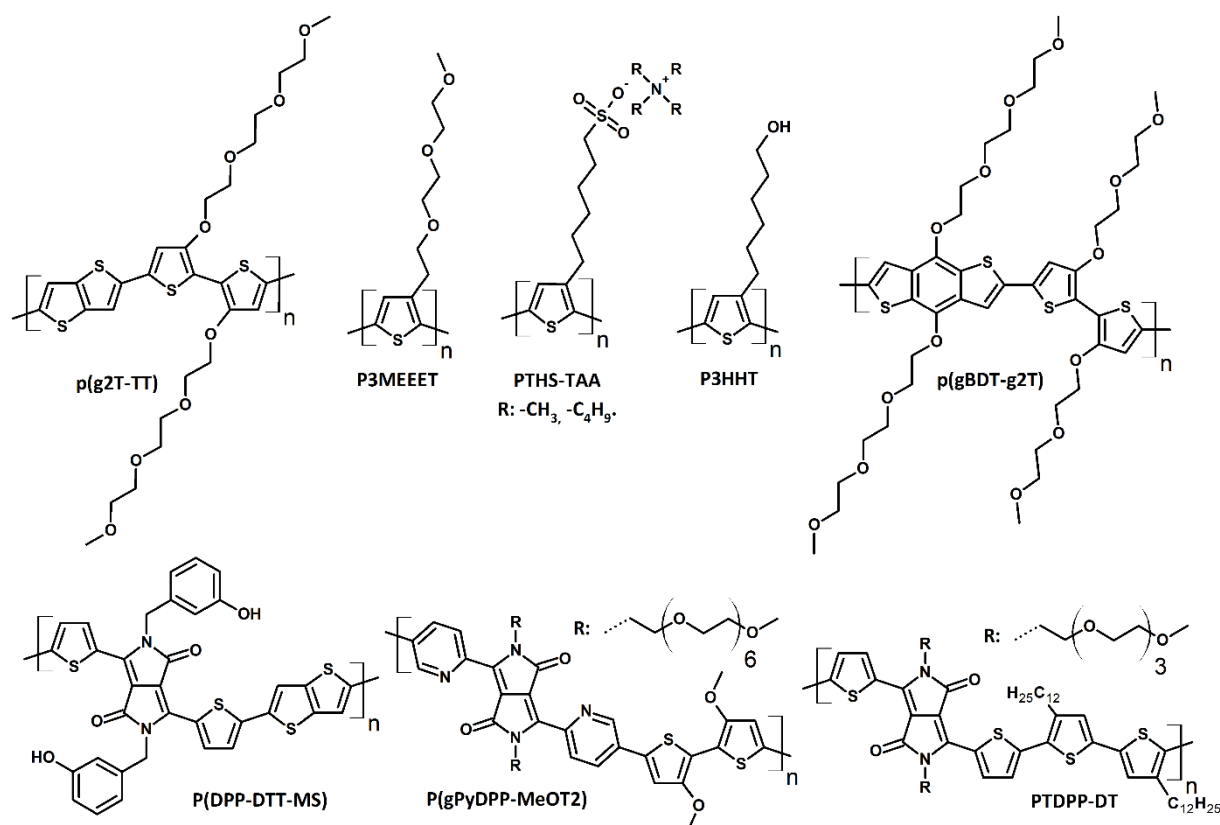


Figure 14 – Important modern p-type MIEC materials for the use in accumulation mode OECT operation, compiled from literature. Top row: thiophene based copolymers p(g2T-TT)^[82], P3MEEET^[88], PTHS-TAA (TAA: tetra alkylamine)^[90,91], P3HHT^[92], p(gBDT-g2T)^[93], P(DPP-DPP-MS)^[94], P(gPyDPP-MeOT2)^[34], PTDPP-DT^[95,96].

Figure 14 displays only materials which are operated in accumulation mode *i.e.*, where the transistor is in the OFF state without an applied potential, and ions are injected into the polymer by electrochemical gating, rendering the active layer conducting. In these p-type materials, a negative gate voltage leads to the injection of anions into the bulk of the polymer film, thus increasing its capacitance and modulating its electrical conductivity. In contrast, depletion mode materials are already conductive and in the ON state without an applied gate voltage, like for example the PEDOT:PSS discussed in the previous chapter. These types of materials are dedoped by applying a gate voltage, thus turning the transistor off. In a p-type depletion-mode material a positive gate potential depletes the material from conductivity-

enhancing counter anions, thus decreasing the materials conductivity.^[97] Compared with depletion mode materials, accumulation mode materials have the advantage of a drastically lower power consumption, because only a drain current is flowing when the transistor is actually in the ON state. When considering the materials in *Figure 14*, it is conspicuous that many polymers are based on polythiophenes which carry miscellaneous oligo ethylene glycol substituents. This is due to the fact that this strategy allows for reaching the required properties with rather simple chemical tools. Polythiophenes are known to be good hole transport materials and owing to well established synthetic approaches, a plethora of polymer architectures and functionalizations are accessible.^[14,98] Glycol moieties can be easily introduced to establish the water compatibility and the swellability within the material. This led to the development of today's champion material p(2gT-TT) where thienothiophene (TT) is copolymerized with TEG substituted bithiophene (g2T), leading to a μC^* product of $240 \text{ F cm}^{-1}\text{V}^{-1}\text{s}^{-1}$.^[82] The polymer P3MEEET similarly features a polythiophene backbone which is equipped with TEG, spaced by an ethyl group from the backbone. The spacer-length (without, methyl or ethyl) allows for tuning of the crystallinity in the solid state and swelling under aqueous conditions, and the best performance is obtained for the ethyl spaced derivative achieving a figure of merit of $\mu C^* = 11 \text{ F cm}^{-1}\text{V}^{-1}\text{s}^{-1}$.^[88] A different way of facilitating the necessary compatibility with water and ions is the employment of polyelectrolytes; this concept is realized in PTHS based polymers. Depending on the size of the counterion, the volumetric capacitance and maximum attained transconductance are modulated, with the highest values being obtained for the smallest trimethylammonium cation.^[90,91] When replacing the TEG side-chain in the polythiophene with a hydroxy-terminated hexyl chain, the swellability without an applied doping potential is drastically reduced, as e.g. compared to p(2gT-TT) which already swells considerably in the unbiased state, *i.e.* passively. The concomitant reduction of the charge transport properties is similarly alleviated, thus leading to a μC^* product of $35 \text{ F cm}^{-1}\text{V}^{-1}\text{s}^{-1}$.^[92] A distinctively different backbone structure is found in p(gBDT-g2T), where the TEG equipped bithiophene (g2T) is copolymerized with TEG substituted benzodithiophene (gBDT). By attaching oxygen atoms directly to the benzyl core, the OECT could be operated at low potentials as the threshold voltage decreased to -0.5 V , but no figure of merit was determined in the original work.^[93] Compared to thiophene-based polymers, DPP-based MIEC materials are scarcely reported and the most important ones are also shown in the bottom row of *Figure 14* above. The polymer P(DPP-DTT-MS) is obtained by printing a water-soluble precursor polymer, carrying ionic moieties on side of the pendant phenol-substituents. The solubilizing moieties are cleaved by UV light, forming the insoluble MIEC which achieves a figure of merit of $22 \text{ F cm}^{-1}\text{V}^{-1}\text{s}^{-1}$.^[94] The water-compatibility in the polymer P(gPyDPP-MeOT2) is established by attaching hexa- and heptaethylene glycol side-chains to the DPP core, which is adjoined by 2-pyridyl flanking units and copolymerized with methoxy-substituted bithiophene. The resulting polymer offered a good operational stability in OECT operation, but no figure of merit was given.^[34] In the DPP derivative PTDPP-DT the water-compatibility is once more introduced by OEG substituents. An increased OECT

performance was obtained when the used electrolyte contained the large tetrafluoroborate anion, resulting in a high μC^* product of $559 \text{ F cm}^{-1}\text{V}^{-1}\text{s}^{-1}$. This high figure of merit, is however reduced to $149 \text{ F cm}^{-1}\text{V}^{-1}\text{s}^{-1}$ when standard NaCl solution is used as the electrolyte.^[95] Another study of this polymer similarly revealed a successful operation in OECTs using the ionic liquid diethylmethyl(2-methoxyethyl) ammonium bis(trifluoromethylsulfonyl)imide (DEME · TFSI) as the electrolyte, but no figure of merit was determined.^[96] In a recent study of three thiophene-flanked EG substituted PDPPs copolymerized with either TT, bithiophene or methoxy-substituted bithiophene the role of polaron-delocalization on the mixed conduction properties was investigated. It was found that a higher polaron delocalization favors the OECT performance and a high figure of merit of $\mu C^* = 342 \text{ F cm}^{-1}\text{V}^{-1}\text{s}^{-1}$ was measured for the bithiophene-derivative p(gDPP-T2).^[33] These examples show that after careful molecular design different classes of conjugated polymers can be tailored for the specific application as MIEC.

Although p-type materials have been more extensively studied in the context of organic mixed conductors, n-type materials are of importance, especially for the interaction with biological systems such as DNA or for direct monitoring of glucose. Some n-type materials have been synthesized and studied and *Figure 15* below shows these MIECs, developed as n-type OECT materials.

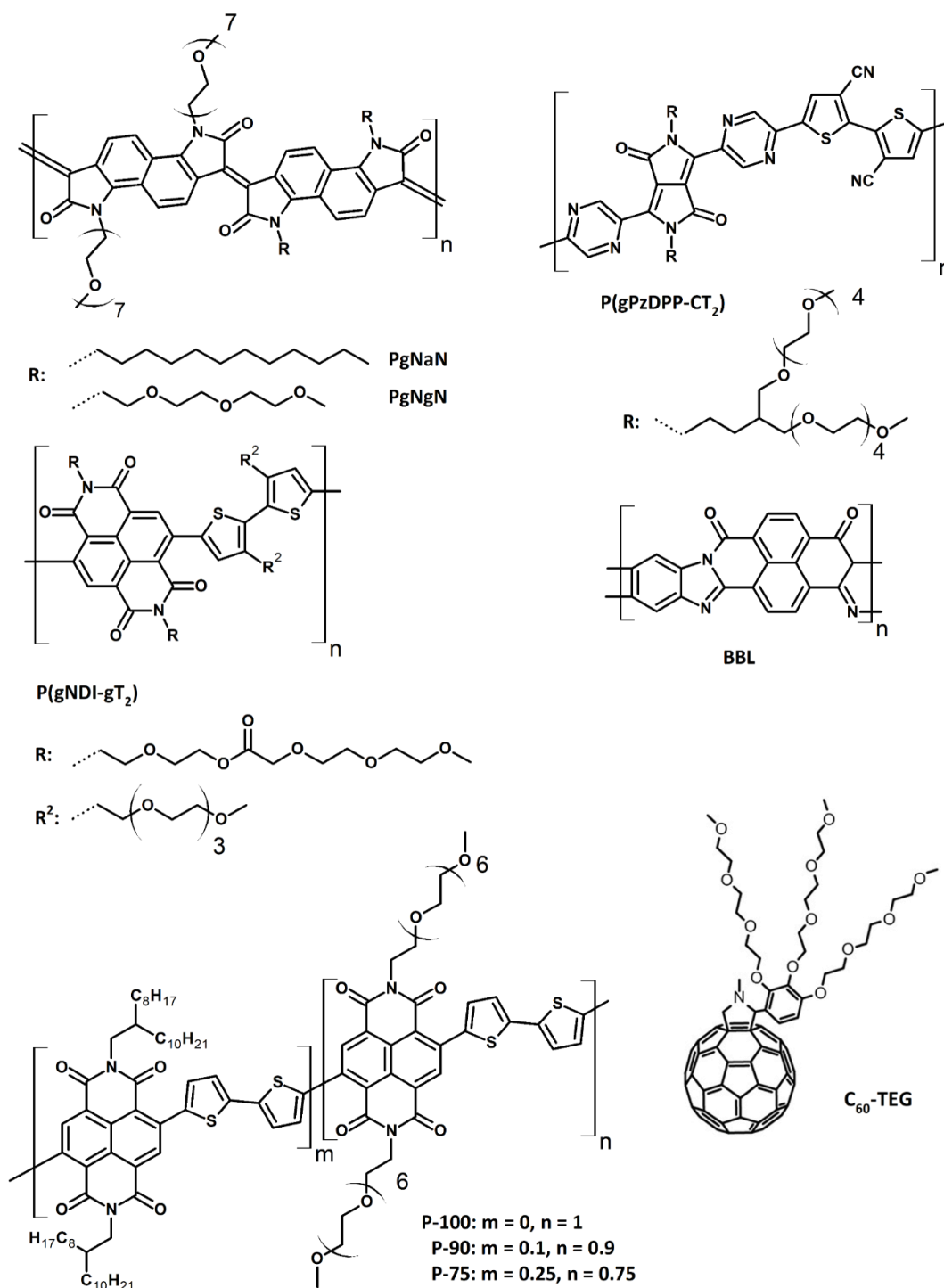


Figure 15 – Important modern n-type MIEC materials for the use in accumulation mode OECT operation, compiled from literature. PgNaN and PgNgN^[99], P(gPzDPP-CT₂)^[100], P(gNDI-gT₂)^[101], BBL^[80], P-100, P-90, P-75^[102], C₆₀-TEG^[103].

Following the universally accepted design principles, electron deficient building blocks were used in all the n-type OECT materials reported. The polymer based on poly(naphthylidene diimide) (PNDI), p(gNDI-gT₂) reached a maximum transconductance of $g_m = 21.7 \mu\text{S}$ at a gate Voltage of $V_G = 0.5 \text{ V}$, with an on-off-ratio of $3.2 \cdot 10^3$. A stable operation over two hours was reported.^[101] Other PNDI-based copolymers with a varying content of the glycolic substituted comonomer (P-100, P-90, P-75) were also investigated, and the derivative carrying 90 mol %

of the oligoethylene-glycol substituted NDI has shown the best OECT performance in this series. The authors reported a transconductance of $1.09 \mu\text{S}$ resulting in a figure of merit of $\mu C^* = 0.05 \text{ F cm}^{-1}\text{V}^{-1}\text{s}^{-1}$.^[102] Very recently, the novel DPP based n-type copolymer P(gPzDPP-CT₂) with mixed conduction properties was developed, in which the DPP-core is flanked with pyrazine moieties and branched oligoethylene glycol units serve as solubilizing side chains. A maximum transconductance of $29.5 \mu\text{S}$ at a gate voltage of *ca.* 0.5 V , as well as a figure of merit of $\mu C^* = 1.72 \text{ F cm}^{-1}\text{V}^{-1}\text{s}^{-1}$ were reported by the authors.^[100] Recently, two polymers based on the isoindigo motif, PgNaN and PgNgN were published as n-type OECT material. The polymers exhibited transconductance values of *ca.* $g_m = 180$ and $3 \mu\text{S}$ ($V_G = 0.4 \text{ V}$) for PgNaN and PgNgN, respectively. The authors reported figure of merits of $\mu C^* = 0.662$ and $0.037 \text{ F cm}^{-1}\text{V}^{-1}\text{s}^{-1}$ for PgNaN and PgNgN, respectively.^[99] The ladder-type conjugated n-type polymer poly(benzimidazobenzophenanthroline) BBL exhibited a transconductance value of $g_m = 9.7 \text{ mS}$ at gate voltages between $V_G = 0.6 - 0.7 \text{ V}$ and a stable operation over one hour was reported.^[80] Finally, the electron acceptor material C₆₀ was modified with oligoethylene side-chains, leading to the material 2-(2,3,4-tris(methoxytriglycol) phenyl) [60]fulleropyrrolidine (C₆₀-TEG), in order to make it viable as MIEC. Transconductance values of $g_m = 4.1 \mu\text{S}$ at $V_G = 0.8 \text{ V}$ were reached and a μC^* product of $7 \text{ F cm}^{-1}\text{V}^{-1}\text{s}^{-1}$ was reported.^[103]

A common complication of materials as the ones discussed above is that their compatibility with aqueous media is so pronounced that, in fact, they tend to delaminate or even dissolve during operation under water. In order to prevent this damaging and maintain stable operation, the polymers can be crosslinked. This is typically achieved *via* the addition of (3-glycidyloxypropyl)trimethylsiloxane (GOPS) to the polymer solution during sample preparation, followed by a thermal crosslinking step. On the one hand, this stabilizes materials which would otherwise dissolve or delaminate and enables their use as MIECs, but on the other hand, it complicates the processing and can decrease the device performance.^[91,104,105] Therefore, polymer systems which do not necessitate any crosslinking additives are desired. Apart from the employed polymer, the choice of electrolyte, particularly the size of injected ions, has a profound impact on the OECT performance. With increasing ion size at constant charge, the transconductance increases,^[106] albeit on at the expense of the switching speed, as the diffusion is hindered the larger the size.

1.4 Organic Thermoelectrics

Organic thermoelectrics are another novel uprising application of conjugated polymers. The principle of thermoelectrics and the manifold reasons for the use of OSCs in this application are explained in the following sections.

Thermoelectric (TE) materials are capable of converting heat gradients into electrical energy, and thereby enable scavenging of waste heat which would otherwise be lost irreversibly.^[107] The generation of electricity *via* TE materials has numerous advantages, which can be fully exploited according to the desired use case. These cases of application are essentially divided into two sectors: waste heat recovery^[108] or energy harvesting for the powering of small consumers for instance in the field of the internet of things (IoT), wearable body-heat powered devices^[109] or as heat flux sensors.^[110] Most important for waste heat recovery is the possibility to harvest thermal energy at high temperatures, which is advantageous for obtaining a high figure of merit, ultimately leading to improved efficiencies. The reason for this is that the highest attainable efficiency of a heat engine is described by Carnot-cycles according to *equation 9* below:^[111]

$$\eta_C = \frac{T_h - T_c}{T_h} \quad (\text{equation 9})$$

with η_C : Carnot-efficiency, $T_{h/c}$: hot/cold side temperature in [K].

According to which the theoretical efficiency scales with the average temperature of the process. This particularly qualifies inorganic TE materials for this task, as they typically withstand high temperatures well beyond 200 °C for prolonged periods, unlike most organic materials. In the second field *i.e.*, the powering of small electrical consumers, optimized organic TE (OTE) materials can fulfil the respective requirements. These are a high design freedom for accessing complex geometric structures, along with mechanical flexibility to enable the OTE materials to be applied in combination with textiles, or even in direct contact with the human skin. Because the produced electrical power is relatively smaller than in the aforementioned high-temperature applications, it is here possible to reliably provide modest powers in the range of microwatts at the desired location.^[112] This goes hand in hand with the possibility for cheap and environmentally friendly low-temperature processing of the materials, biocompatibility and the absence of toxic or hazardous elements. For these reasons, OTE materials have the potential to improve everyday devices and enter the vast market for consumer electronics.

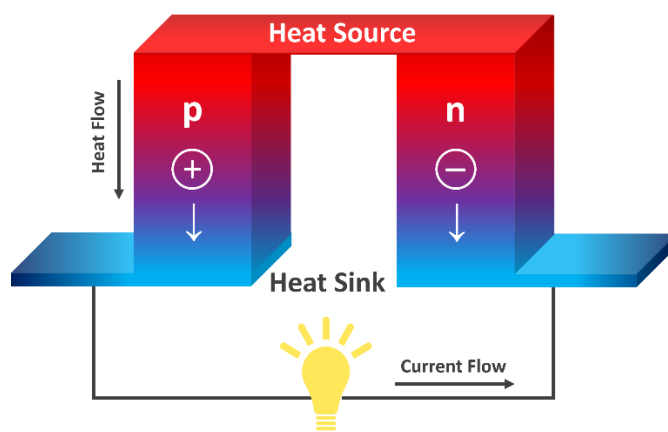


Figure 16 – Schematic of a thermocouple, constituting the smallest working unit of a thermoelectric generator (TEG). Here, a p-type and a n-type leg are positioned thermally in parallel, and electrical in series. Thereby, the applied temperature gradient drives holes and electrons, respectively, from the hot to the cold side, thus causing an external electrical current. Adapted from literature.^[113]

Figure 16 above shows the schematic structure of a thermocouple, which is the smallest unit of a TEG. It consists of a p-type and a n-type leg which are connected thermally in parallel and electrical in series. After applying a thermal gradient, the respective majority charge carriers (holes or electrons) are driven toward the cold side. Thereby, an electrical field is formed and an external voltage is created.^[114] The underlying principle traces back to Thomas Johann Seebeck, after whom the most important parameter in the field of thermoelectrics is termed: the Seebeck coefficient. In TE materials, it is a measure for the obtained voltage per unit temperature difference *i.e.*, $S = dV/dT$.^[108,115] The quality or efficiency of the generated electricity is measured by the dimensionless figure of merit zT which is defined according to equation 10 below.^[108]

$$zT = \frac{S^2 \sigma T}{\kappa} \quad (\text{equation 10})$$

Where zT : figure of merit, S : Seebeck coefficient, σ : electrical conductivity, T : average operating temperature, κ : thermal conductivity.

For OTE materials one often finds the power factor PF in the literature, which is similar to the figure of merit zT , but does not consider the thermal conductivity. It is defined as equation 11:

$$PF = S^2 \sigma T \quad (\text{equation 11})$$

This simplification is reasonable for polymers, because among most polymers the thermal conductivity is both, rather low and relatively constant within this material class. The relationships from equation 10 and equation 11 above show that an optimized TE material must have a high Seebeck coefficient as well as a high electrical conductivity. The thermal conductivity, however, needs to be low. Furthermore, it is apparent that the zT value scales with the operational temperature. Therefore, inorganic materials which can be operated at elevated temperatures, effortlessly reach higher zT values than organic conjugated polymers.

In accordance to the Wiedemann-Franz-Law, the thermal conductivity of a material consists of a phonon- and electron contribution and can be written as:^[116]

$$\kappa_{tot} = \kappa_{phon} + \kappa_{el} = \kappa_{phon} + L\sigma T \quad (\text{equation 12})$$

with κ_{tot} : total thermal conductivity, $\kappa_{phon/el}$: phonon / electron contribution to the thermal conductivity, L : Lorenz-number, σ : electrical conductivity, T : absolute temperature.

In amorphous and semi-crystalline polymers the phonon contribution to the total thermal conductivity is negligible due to the absence of a continuous crystal lattice^[117] and the electronic contribution scales with the charge carrier density. The absolute values of thermal conductivities of most polymeric materials lie in the range of 0.15 – 0.3 W m⁻¹K⁻¹, which is orders of magnitude less than that of semi-metals or other inorganic semiconductors.^[116–118] The remaining parameters in *equation 10* i.e., the Seebeck coefficient and the electrical conductivity require more attention in order to obtain an optimized OTE material. Within broad boundaries, the electrical conductivity of conjugated polymers can be tuned fairly deliberately by chemical doping. However, the adjustment of the electrical conductivity by doping must be carried out very cautious because the Seebeck coefficient is interrelated with the charge carrier density in a tradeoff-relationship. From *equation 13* below it can be seen, that the Seebeck coefficient decays with an increasing charge carrier density.^[119]

$$S = \frac{8\pi^2 k_B^2}{3eh^2} m^* T \left(\frac{\pi}{3n} \right)^{\frac{2}{3}} \quad (\text{equation 13})$$

Where S : Seebeck coefficient, k_B : Boltzmann constant, e : elemental charge, h : Planck constant, m^* : electron effective mass, T : absolute temperature, n : charge carrier density.

The bulk electrical conductivity σ however, scales proportionally with the charge carrier density according to *equation 6* discussed earlier. This tradeoff-relationship results in a physical dilemma which is visualized in *Figure 17* below.

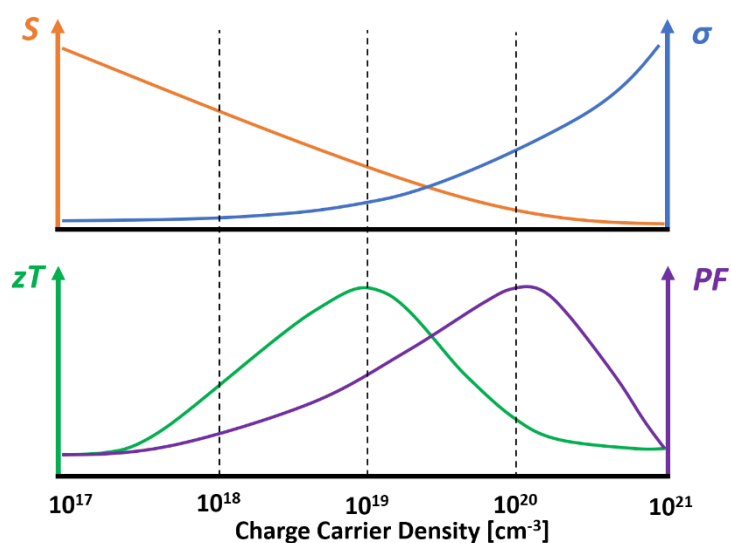


Figure 17 – Illustration of the compiled interrelations of the thermoelectric parameters, where the Seebeck coefficient progresses inversely to the electrical conductivity (top) with respect to the charge carrier density. Resulting figure of merit (zT) and power factor (PF) with respect to the charge carrier density (bottom). Not drawn to scale, adapted from literature.^[120,121]

This emphasizes that *via* targeted chemical doping of a given conjugated polymer, its charge carrier density can be tuned toward an optimum point, where the product of $S^2\sigma$ has a maximum. A further optimization of the power factor or figure of merit by doping is hindered and thus, further parameters must be exploited. Another aspect that results from *equation 6* is that a high charge carrier mobility improves the electrical conductivity as well. Thereby, the charge carrier concentration remains unchanged, and consequently the Seebeck coefficient is not affected adversely. The requirements to the materials for efficient OTEs are in summary a low thermal conductivity, which is readily given in OSCs. Moreover, a careful optimization of the charge carrier density is required and further improvements of the zT value can from there on be achieved by employing conjugated polymers exhibiting high charge carrier mobilities.

In the beginning of this section, it was mentioned that organic TE materials compete with inorganic TE materials. But advantages and drawbacks of either one of the material classes are easily distinguishable, whereof specific applications for the respective material class arise. As briefly discussed above, inorganic TE materials are well suitable for stationary high-temperature applications. The leading cause is on the one hand simply the superior thermal stability, which allows for high operating temperatures. On the other hand, the brittleness of inorganic TE materials restricts the resulting devices from application where pronounced thermal cycling occurs, as fatigue cracking of a TE leg causes failure of the whole TEG device. They are moreover much heavier than their organic counterparts, which impedes the use in mobile applications like the automotive sector. Lastly, they have virtually no mechanical flexibility and consist of heavy metals (mainly bismuth, tellurium, lead, antimony *etc.*)^[108,122] which are toxic or hazardous. Therefore, a widespread application and distribution of these

toxic elements, especially on consumer basis is not possible or at least obsolete with respect to environmental aspects. Accordingly, the use in direct contact with the human body is restricted, too. Yet, the stationary application of inorganic TE materials for harvesting large amounts of waste heat, for instance in thermal power plants, technical furnaces *etc.* is highly reasonable. This is an ideal use case for inorganic materials, as high temperatures can be harvested under constant conditions and an appropriate disposal of the hazardous materials can be ensured after the life cycle of the device is expired. The predestined applications for organic TE materials are, as previously touched, those where small electrical consumers must be locally supplied with energy. Examples for this are all wearable devices or health monitor sensors, which become increasingly important and will find their way into our everyday lives in the near future.^[123,124] The human body provides a large amount of unused heat, which lies in the range of 50 W m^{-2} in rest, and up to 500 W m^{-2} under physical exercise. Consequently, already at modest power conversion efficiencies of 2 – 5 %, electrical powers in the range of milliwatts can be tapped, which is sufficient for powering the aforementioned devices.^[9,125] Clear advantages of polymeric TE materials are all those, which render synthetic polymers useful for most applications where they are already established today: environmentally friendly large scale production and processing at low temperatures or even at room temperature from solution or the complete absence of hazardous elements and a reduced weight. As the polymers can be deposited on unproblematic substrates like paper,^[126,127] their disposal, e.g. by feeding it into thermal power plants without toxic emissions is safe and makes OTE materials highly attractive.

In order to yield reasonable efficiencies, a TE material should exhibit a figure of merit of $zT \approx 1$ to reach a power generation efficiency of at least 5 % at temperature differences between hot and cold side of 100 – 200 K. This relationship is visualized by plotting *equation 14* as depicted in *Figure 18* below:^[128,129]

$$\eta_p = \frac{T_h - T_c}{T_h} \cdot \left(\frac{\sqrt{1 - zT} - 1}{\sqrt{1 + zT} + \frac{T_c}{T_h}} \right) \quad (\text{equation 14})$$

with η_p : power conversion efficiency, $T_{h/c}$: hot/cold side temperature, zT material figure of merit.

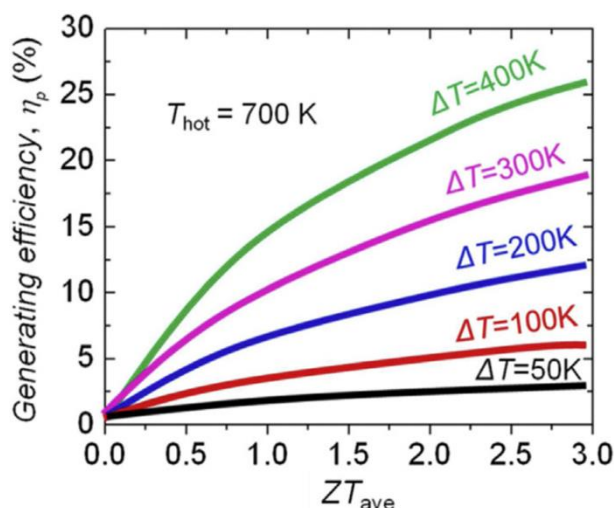


Figure 18 – Power generation efficiencies in dependence of the average figure of merit zT of a given materials and different temperature gradients. Adapted from literature.^[129]

Among inorganic TE materials bismuth telluride (Bi_2Te_3) is the most common and commercially available material for room temperature applications; it reaches a figure of merit of $zT \approx 1$ and is regarded as the benchmark material for organic thermoelectrics. The today best OTE material was achieved with an optimized processing method using PEDOT:PSS, reaching a figure of merit of $zT = 0.42$, which lies well in the range of the inorganic benchmark material.^[9] Further important examples for conjugated polymers as p-type TE materials are displayed in below in *Figure 19*:

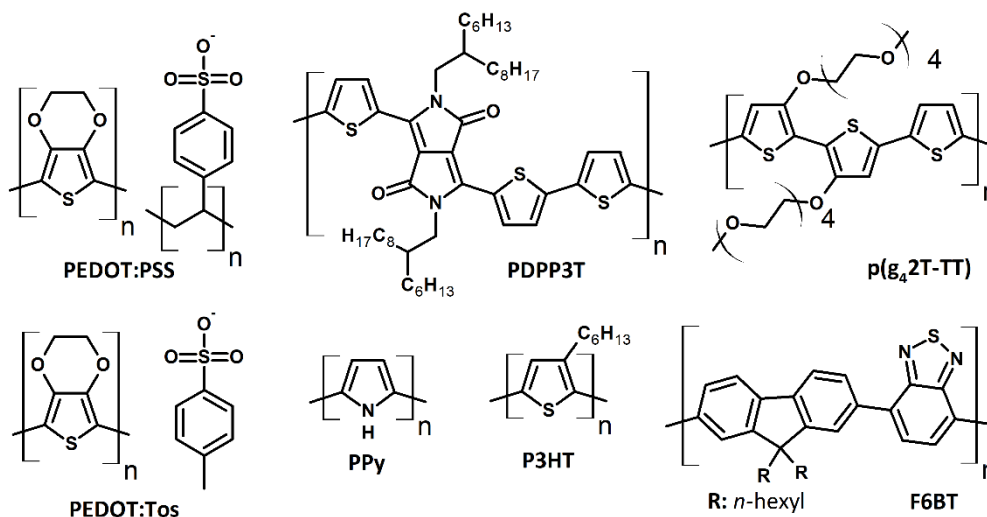


Figure 19 – Selected important p-type conjugated polymers for the use as organic thermoelectric materials, compiled from literature. PEDOT:PSS: poly(styrene sulfonic acid) doped poly(3,4-ethylenedioxythiophene), PDPPP3T: thiophene-flanked diketopyrrolopyrrole-thiophene copolymer, p(g42T-TT): tetraethylene glycol substituted bithiophene-thiophene copolymer, PEDOT:Tos: toluenesulfonic acid doped poly(3,4-ethylenedioxythiophene), PPy: polypyrrole, P3HT: poly(3-hexylthiophene), F6BT: Poly(9,9-di-*n*-hexylfluorene-*alt*-benzothiadiazole) copolymer.

Naturally, some of the early conjugated polymers like polypyrrole or omnipresent p-type conjugated polymers like P3HT, PEDOT or polyfluorene derivatives were studied as organic TE materials in the past. Nevertheless, only PEDOT and a few 2nd generation conjugated polymers

have asserted themselves as good OTE materials to date; their basic parameters are described below. When electrochemically polymerized in the presence of boron trifluoride, polypyrrole (PPy) reached a power factor of $PF = 1.75 \mu\text{W m}^{-1}\text{K}^{-2}$ in free standing films.^[130] Films of P3HT are reported to reach similar power factors in the range of $PF \approx 0.1 - 20 \mu\text{W m}^{-1}\text{K}^{-2}$ when doped with the strong oxidant nitrosonium hexafluorophosphate or iron(III) bis(trifluoromethane)sulfonimide (TFSI).^[131,132] Interestingly, by the introduction of oligoethylene glycol side chains to a polythiophene backbone, e.g. as in p(g₄2T-TT), the power factor is maintained around $2 \mu\text{W m}^{-1}\text{K}^{-2}$ when doped with the common dopant F₄TCNQ.^[24] In the polyfluorene derivative F6BT, where hexyl substituted fluorene was copolymerized with benzothiadiazole a power factor of $PF = 1.7 \mu\text{W m}^{-1}\text{K}^{-2}$ was measured when doped with iron(III) chloride.^[133] When moving to the DPP based 2nd generation conjugated polymer PDPP3T a much higher power factor of $PF = 276 \mu\text{W m}^{-1}\text{K}^{-2}$ could be observed, also after doping with iron(III)chloride.^[36] Finally, using the popular p-type conjugated polymer PEDOT either doped using poly(styrenesulfonic acid) or toluenesulfonic acid high figures of merit in the range of $zT = 0.25 - 0.42$ were reached using optimized processing methods.^[9,125] These examples altogether emphasize, that the use of modern and purposefully tailored materials is required to reach appreciable performances, able to compete with the inorganic counterpart and thus allow for a wide application of OTE materials.

References

- [1] H. Shirakawa, E. J. Louis, A. G. MacDiarmid, C. K. Chiang, A. J. Heeger, *J. Chem. Soc., Chem. Commun.* **1977**, 0, 578–580.
- [2] J.-C. Chiang, A. G. MacDiarmid, *Synthetic Metals* **1986**, 13, 193–205.
- [3] A. F. Diaz, K. K. Kanazawa, G. P. Gardini, *J. Chem. Soc., Chem. Commun.* **1979**, 635–636.
- [4] P. Kovacic, A. Kyriakis, *Tetrahedron Letters* **1962**, 3, 467–469.
- [5] R. A. Wessling, *Journal of Polymer Science: Polymer Symposia* **1985**, 72, 55–66.
- [6] W. Steinkopf, R. Leitsmann, K. H. Hofmann, *Justus Liebigs Annalen der Chemie* **1941**, 546, 180–199.
- [7] T. Yamamoto, K. Sanechika, A. Yamamoto, *Journal of Polymer Science: Polymer Letters Edition* **1980**, 18, 9–12.
- [8] X. Wang, X. Zhang, L. Sun, D. Lee, S. Lee, M. Wang, J. Zhao, Y. Shao-Horn, M. Dincă, T. Palacios, K. K. Gleason, *Sci Adv* **2018**, 4, eaat5780.
- [9] G.-H. Kim, L. Shao, K. Zhang, K. P. Pipe, *Nature Mater* **2013**, 12, 719–723.
- [10] A. Elschner, S. Kirchmeyer, W. Lovenich, U. Merker, K. Reuter, *PEDOT: Principles and Applications of an Intrinsically Conductive Polymer*, CRC Press, **2010**.
- [11] A. Yokoyama, R. Miyakoshi, T. Yokozawa, *Macromolecules* **2004**, 37, 1169–1171.
- [12] E. E. Sheina, J. Liu, M. C. Iovu, D. W. Laird, R. D. McCullough, *Macromolecules* **2004**, 37, 3526–3528.
- [13] M. Surin, Ph. Leclère, R. Lazzaroni, J. D. Yuen, G. Wang, D. Moses, A. J. Heeger, S. Cho, K. Lee, *Journal of Applied Physics* **2006**, 100, 033712.
- [14] S. Ludwigs, Ed., *P3HT Revisited – From Molecular Scale to Solar Cell Devices*, Springer-Verlag, Berlin Heidelberg, **2014**.
- [15] P. Pingel, D. Neher, *Phys. Rev. B* **2013**, 87, 115209.
- [16] S.-J. Zou, Y. Shen, F.-M. Xie, J.-D. Chen, Y.-Q. Li, J.-X. Tang, *Materials Chemistry Frontiers* **2020**, 4, 788–820.
- [17] “Bloomberg LED & OLED Market Report. Accessed on 07/04/2021,” can be found under <https://www.bloomberg.com/press-releases/2019-06-03/global-led-oled-displays-and-lighting-products-market-expected-to-reach-us-95936-mn-by-2025-qy-research>, **2019**.
- [18] Heliatek GmbH, “Commercial OPV with 13.2 % conversion efficiency,” **2016**.
- [19] Heliatek GmbH, “Heliasol 436-2000, OPV with 20 years of output guarantee,” can be found under <https://www.heliatek.com/de/produkte/heliasol/>, **2021**.
- [20] B. D. Paulsen, K. Tybrandt, E. Stavrinidou, J. Rivnay, *Nat. Mater.* **2019**, DOI 10.1038/s41563-019-0435-z.
- [21] M. Lindorf, K. A. Mazzio, J. Pflaum, K. Nielsch, W. Brütting, M. Albrecht, *J. Mater. Chem. A* **2020**, 8, 7495–7507.
- [22] E. Bundgaard, F. C. Krebs, *Solar Energy Materials and Solar Cells* **2007**, 91, 954–985.
- [23] Y.-J. Cheng, S.-H. Yang, C.-S. Hsu, *Chemical Reviews* **2009**, 109, 5868–5923.
- [24] R. Kroon, D. Kiefer, D. Stegerer, L. Yu, M. Sommer, C. Müller, *Advanced Materials* **2017**, 29, 1700930.
- [25] C.-C. Wang, H. Tsai, H.-H. Shih, S. Jeon, Z. Xu, D. Williams, S. Iyer, T. C. Sanchez, L. Wang, M. Cotlet, H.-L. Wang, *ACS Appl. Mater. Interfaces* **2010**, 2, 738–747.
- [26] S. Torabi, F. Jahani, I. Van Severen, C. Kanimozhi, S. Patil, R. W. A. Havenith, R. C. Chiechi, L. Lutsen, D. J. M. Vanderzande, T. J. Cleij, J. C. Hummelen, L. J. A. Koster, *Advanced Functional Materials* **2015**, 25, 150–157.
- [27] W. Li, W. S. C. Roelofs, M. Turbiez, M. M. Wienk, R. A. J. Janssen, *Advanced Materials* **2014**, 26, 3304–3309.

- [28] Y. Zou, D. Gendron, R. Neagu-Plesu, M. Leclerc, *Macromolecules* **2009**, *42*, 6361–6365.
- [29] C. J. Mueller, E. Gann, C. R. Singh, M. Thelakkat, C. R. McNeill, *Chem. Mater.* **2016**, *28*, 7088–7097.
- [30] X. Yan, M. Xiong, J.-T. Li, S. Zhang, Z. Ahmad, Y. Lu, Z.-Y. Wang, Z.-F. Yao, J.-Y. Wang, X. Gu, T. Lei, *J. Am. Chem. Soc.* **2019**, *141*, 20215–20221.
- [31] C. J. Mueller, C. R. Singh, M. Fried, S. Huettner, M. Thelakkat, *Adv. Funct. Mater.* **2015**, *25*, 2725–2736.
- [32] I. Meager, R. S. Ashraf, S. Mollinger, B. C. Schroeder, H. Bronstein, D. Beatrup, M. S. Vezie, T. Kirchartz, A. Salleo, J. Nelson, I. McCulloch, *J. Am. Chem. Soc.* **2013**, *135*, 11537–11540.
- [33] M. Moser, A. Savva, K. Thorley, B. D. Paulsen, T. C. Hidalgo, D. Ohayon, H. Chen, A. Giovannitti, A. Marks, N. Gasparini, A. Wadsworth, J. Rivnay, S. Inal, I. McCulloch, *Angewandte Chemie International Edition* **2021**, *60*, 7777–7785.
- [34] A. Giovannitti, R. B. Rashid, Q. Thiburce, B. D. Paulsen, C. Cendra, K. Thorley, D. Moia, J. T. Mefford, D. Hanifi, D. Weiyuan, M. Moser, A. Salleo, J. Nelson, I. McCulloch, J. Rivnay, *Adv. Mater.* **2020**, 1908047.
- [35] J. Li, Y. Zhao, H. S. Tan, Y. Guo, C.-A. Di, G. Yu, Y. Liu, M. Lin, S. H. Lim, Y. Zhou, H. Su, B. S. Ong, *Scientific Reports* **2012**, *2*, 754.
- [36] I. H. Jung, C. T. Hong, U.-H. Lee, Y. H. Kang, K.-S. Jang, S. Y. Cho, *Scientific Reports* **2017**, *7*, 44704.
- [37] M. Moser, A. Savva, K. Thorley, B. D. Paulsen, T. C. Hidalgo, D. Ohayon, H. Chen, A. Giovannitti, A. Marks, N. Gasparini, A. Wadsworth, J. Rivnay, S. Inal, I. McCulloch, *Angewandte Chemie International Edition* **n.d.**, *n/a*, DOI <https://doi.org/10.1002/anie.202014078>.
- [38] Y. R. Cheon, Y. J. Kim, J. Ha, M.-J. Kim, C. E. Park, Y.-H. Kim, *Macromolecules* **2014**, *47*, 8570–8577.
- [39] R. Qin, W. Li, C. Li, C. Du, C. Veit, H.-F. Schleiermacher, M. Andersson, Z. Bo, Z. Liu, O. Inganäs, U. Wuerfel, F. Zhang, *J. Am. Chem. Soc.* **2009**, *131*, 14612–14613.
- [40] G. Liu, J. Jia, K. Zhang, X. Jia, Q. Yin, W. Zhong, L. Li, F. Huang, Y. Cao, *Advanced Energy Materials* **2019**, *9*, 1803657.
- [41] Q. Liu, Y. Jiang, K. Jin, J. Qin, J. Xu, W. Li, J. Xiong, J. Liu, Z. Xiao, K. Sun, S. Yang, X. Zhang, L. Ding, *Science Bulletin* **2020**, *65*, 272–275.
- [42] S. Koltzenburg, M. Maskos, O. Nuyken, *Polymer Chemistry*, Springer-Verlag, Berlin Heidelberg, **2017**.
- [43] S. Koltzenburg, M. Maskos, O. Nuyken, *Polymere: Synthese, Eigenschaften und Anwendungen*, Springer Spektrum, Berlin, **2014**.
- [44] M. D. Lechner, K. Gehrke, E. H. Nordmeier, *Makromolekulare Chemie: Ein Lehrbuch für Chemiker, Physiker, Materialwissenschaftler und Verfahrenstechniker*, Springer Spektrum, **2014**.
- [45] G. H. L. Heintges, R. A. J. Janssen, *RSC Adv.* **2019**, *9*, 15703–15714.
- [46] K. H. Hendriks, W. Li, G. H. L. Heintges, G. W. P. van Pruissen, M. M. Wienk, R. A. J. Janssen, *J. Am. Chem. Soc.* **2014**, *136*, 11128–11133.
- [47] D. Steinborn, *Grundlagen der metallorganischen Komplexkatalyse*, Teubner, Wiesbaden, **2007**.
- [48] D. Milstein, J. K. Stille, *J. Am. Chem. Soc.* **1978**, *100*, 3636–3638.
- [49] T. N. Mitchell, in *Metal-Catalyzed Cross-Coupling Reactions*, John Wiley & Sons, Ltd, **2004**, pp. 125–161.
- [50] M. Groteklaes, in *Römpp, Diketopyrrolopyrrol-Pigmente*, Thieme, Stuttgart, **2006**.
- [51] A. C. Rochat, L. Cassar, A. Iqbal, *Preparation of Pyrrolo-(3, 4-c) Pyrroles*, **1986**, 459949.

- [52] A. Iqbal, M. Jost, R. Kirchmayr, J. Pfenninger, A. Rochat, O. Wallquist, *Bulletin des Sociétés Chimiques Belges* **1988**, *97*, 615–644.
- [53] C. J. H. Morton, R. Gilmour, D. M. Smith, P. Lightfoot, A. M. Z. Slawin, E. J. MacLean, *Tetrahedron* **2002**, *58*, 5547–5565.
- [54] C. B. Nielsen, M. Turbiez, I. McCulloch, *Advanced Materials* **2013**, *25*, 1859–1880.
- [55] W. Li, K. H. Hendriks, M. M. Wienk, R. A. J. Janssen, *Acc. Chem. Res.* **2016**, *49*, 78–85.
- [56] A. I. Hofmann, R. Kroon, L. Yu, C. Müller, *J. Mater. Chem. C* **2018**, *6*, 6905–6910.
- [57] S.-F. Yang, Z.-T. Liu, Z.-X. Cai, M. J. Dyson, N. Stingelin, W. Chen, H.-J. Ju, G.-X. Zhang, D.-Q. Zhang, *Adv. Sci.* **2017**, *4*, 1700048.
- [58] K. P. C. Vollhardt, N. E. Schore, *Organic Chemistry: Structure and Function*, Freeman, New York; Basingstoke, **2011**.
- [59] V. Coropceanu, J. Cornil, D. A. da Silva Filho, Y. Olivier, R. Silbey, J.-L. Brédas, *Chem. Rev.* **2007**, *107*, 926–952.
- [60] N. Karl, *Synthetic Metals* **2003**, *133–134*, 649–657.
- [61] A. Köhler, H. Bässler, *Electronic Processes in Organic Semiconductors*, Wiley-VCH, Weinheim, **2015**.
- [62] H. Bässler, *Physica Status Solidi B* **1993**, *175*, 15–56.
- [63] Y. Zhang, H. Zhou, J. Seifert, L. Ying, A. Mikhailovsky, A. J. Heeger, G. C. Bazan, T.-Q. Nguyen, *Advanced Materials* **2013**, *25*, 7038–7044.
- [64] Y. Hu, Z. D. Rengert, C. McDowell, M. J. Ford, M. Wang, A. Karki, A. T. Lill, G. C. Bazan, T.-Q. Nguyen, *ACS Nano* **2018**, *12*, 3938–3946.
- [65] H. Méndez, G. Heimel, S. Winkler, J. Frisch, A. Opitz, K. Sauer, B. Wegner, M. Oehzelt, C. Röthel, S. Duhm, D. Többens, N. Koch, I. Salzmann, *Nature Communications* **2015**, *6*, 8560.
- [66] K. Walzer, B. Maennig, M. Pfeiffer, K. Leo, *Chem. Rev.* **2007**, *107*, 1233–1271.
- [67] B. Lüssem, M. Riede, K. Leo, *Physica Status Solidi A* **2013**, *210*, 9–43.
- [68] S. Olthof, S. Mehraeen, S. K. Mohapatra, S. Barlow, V. Coropceanu, J.-L. Brédas, S. R. Marder, A. Kahn, *Phys. Rev. Lett.* **2012**, *109*, 176601.
- [69] V. I. Arkhipov, P. Heremans, E. V. Emelianova, G. J. Adriaenssens, H. Bässler, *Appl. Phys. Lett.* **2003**, *82*, 3245–3247.
- [70] B. Lüssem, C.-M. Keum, D. Kasemann, B. Naab, Z. Bao, K. Leo, *Chem. Rev.* **2016**, *116*, 13714–13751.
- [71] I. Salzmann, G. Heimel, M. Oehzelt, S. Winkler, N. Koch, *Acc. Chem. Res.* **2016**, *49*, 370–378.
- [72] H. Méndez, G. Heimel, A. Opitz, K. Sauer, P. Barkowski, M. Oehzelt, J. Soeda, T. Okamoto, J. Takeya, J.-B. Arlin, J.-Y. Balandier, Y. Geerts, N. Koch, I. Salzmann, *Angewandte Chemie International Edition* **2013**, *52*, 7751–7755.
- [73] M. L. Tietze, L. Burtone, M. Riede, B. Lüssem, K. Leo, *Phys. Rev. B* **2012**, *86*, 035320.
- [74] B. Tan, S. R. Raga, A. S. R. Chesman, S. O. Fürer, F. Zheng, D. P. McMeekin, L. Jiang, W. Mao, X. Lin, X. Wen, J. Lu, Y.-B. Cheng, U. Bach, *Advanced Energy Materials* **2019**, *9*, 1901519.
- [75] A. I. Hofmann, R. Kroon, S. Zokaei, E. Järsvall, C. Malacrida, S. Ludwigs, T. Biskup, C. Müller, *Adv. Electron. Mater.* **2020**, *6*, 2000249.
- [76] J. Rivnay, S. Inal, B. A. Collins, M. Sessolo, E. Stavrinidou, X. Strakosas, C. Tassone, D. M. Delongchamp, G. G. Malliaras, *Nat Commun* **2016**, *7*, 11287.
- [77] S. Inal, G. G. Malliaras, J. Rivnay, *Nat Commun* **2017**, *8*, 1767.
- [78] W. Lee, J. H. Seo, H. Y. Woo, *Polymer* **2013**, *54*, 5104–5121.
- [79] B. D. Paulsen, K. Tybrandt, E. Stavrinidou, J. Rivnay, *Nature Materials* **2020**, *19*, 13–26.

- [80] H. Sun, M. Vagin, S. Wang, X. Crispin, R. Forchheimer, M. Berggren, S. Fabiano, *Advanced Materials* **2018**, *30*, 1704916.
- [81] J. Rivnay, R. M. Owens, G. G. Malliaras, *Chem. Mater.* **2014**, *26*, 679–685.
- [82] A. Giovannitti, D.-T. Sbircea, S. Inal, C. B. Nielsen, E. Bandiello, D. A. Hanifi, M. Sessolo, G. G. Malliaras, I. McCulloch, J. Rivnay, *Proceedings of the National Academy of Sciences* **2016**, *113*, 12017–12022.
- [83] G. Krauss, F. Meichsner, A. Hochgesang, J. Mohanraj, S. Salehi, P. Schmode, M. Thelakkat, *Adv. Funct. Mater.* **2021**, 2010048.
- [84] J. Rivnay, S. Inal, A. Salleo, R. M. Owens, M. Berggren, G. G. Malliaras, *Nat Rev Mater* **2018**, *3*, 17086.
- [85] J. T. Friedlein, R. R. McLeod, J. Rivnay, *Organic Electronics* **2018**, *63*, 398–414.
- [86] J. Rivnay, P. Leleux, M. Ferro, M. Sessolo, A. Williamson, D. A. Koutsouras, D. Khodagholy, M. Ramuz, X. Strakosas, R. M. Owens, C. Benar, J.-M. Badier, C. Bernard, G. G. Malliaras, *Science Advances* **2015**, *1*, e1400251.
- [87] P. Schmode, D. Ohayon, P. M. Reichstein, A. Savva, S. Inal, M. Thelakkat, *Chem. Mater.* **2019**, *31*, 5286–5295.
- [88] P. Schmode, A. Savva, R. Kahl, D. Ohayon, F. Meichsner, O. Dolynchuk, T. Thurn-Albrecht, S. Inal, M. Thelakkat, *ACS Appl. Mater. Interfaces* **2020**, *12*, 13029–13039.
- [89] D. Khodagholy, T. Doublet, P. Quilichini, M. Gurfinkel, P. Leleux, A. Ghestem, E. Ismailova, T. Hervé, S. Sanaur, C. Bernard, G. G. Malliaras, *Nature Communications* **2013**, *4*, 1575.
- [90] S. Inal, J. Rivnay, P. Leleux, M. Ferro, M. Ramuz, J. C. Brendel, M. M. Schmidt, M. Thelakkat, G. G. Malliaras, *Advanced Materials* **2014**, *26*, 7450–7455.
- [91] M. M. Schmidt, M. ElMahmoudy, G. G. Malliaras, S. Inal, M. Thelakkat, *Macromolecular Chemistry and Physics* **2017**, *219*, 1700374.
- [92] T. Nicolini, J. Surgailis, A. Savva, A. D. Scaccabarozzi, R. Nakar, D. Thuau, G. Wantz, L. J. Richter, O. Dautel, G. Hadziioannou, N. Stingelin, *Advanced Materials* **2021**, *33*, 2005723.
- [93] C. B. Nielsen, A. Giovannitti, D.-T. Sbircea, E. Bandiello, M. R. Niazi, D. A. Hanifi, M. Sessolo, A. Amassian, G. G. Malliaras, J. Rivnay, I. McCulloch, *Journal of the American Chemical Society* **2016**, *138*, 10252–10259.
- [94] B. Schmatz, A. W. Lang, J. R. Reynolds, *Adv. Funct. Mater.* **2019**, *29*, 1905266.
- [95] X. Wu, Q. Liu, A. Surendran, S. E. Bottle, P. Sonar, W. L. Leong, *Advanced Electronic Materials* **2021**, *7*, 2000701.
- [96] Q. Liu, K. Kanahashi, K. Matsuki, S. Manzhos, K. Feron, S. E. Bottle, K. Tanaka, T. Nanseki, T. Takenobu, H. Tanaka, P. Sonar, *Advanced Electronic Materials* **2020**, *6*, 1901414.
- [97] E. Zeglio, O. Inganäs, *Advanced Materials* **2018**, *30*, 1800941.
- [98] J. Mei, Z. Bao, *Chem. Mater.* **2014**, *26*, 604–615.
- [99] X. Chen, A. Marks, B. D. Paulsen, R. Wu, R. B. Rashid, H. Chen, M. Alsufyani, J. Rivnay, I. McCulloch, *Angewandte Chemie International Edition* **2021**, *60*, 9368–9373.
- [100] J. Shi, P. Li, X.-Y. Deng, J. Xu, Z. Huang, Y. Lei, Y. Wang, J.-Y. Wang, X. Gu, T. Lei, *Chem. Mater.* **2022**, *34*, 864–872.
- [101] A. Giovannitti, C. B. Nielsen, D.-T. Sbircea, S. Inal, M. Donahue, M. R. Niazi, D. A. Hanifi, A. Amassian, G. G. Malliaras, J. Rivnay, I. McCulloch, *Nat Commun* **2016**, *7*, 13066.
- [102] A. Giovannitti, I. P. Maria, D. Hanifi, M. J. Donahue, D. Bryant, K. J. Barth, B. E. Makdah, A. Savva, D. Moia, M. Zetek, P. R. F. Barnes, O. G. Reid, S. Inal, G. Rumbles, G. G. Malliaras, J. Nelson, J. Rivnay, I. McCulloch, *Chemistry of Materials* **2018**, *30*, 2945–2953.
- [103] C. G. Bischak, L. Q. Flagg, K. Yan, C.-Z. Li, D. S. Ginger, *ACS Appl. Mater. Interfaces* **2019**, *11*, 28138–28144.

- [104] A. Håkansson, S. Han, S. Wang, J. Lu, S. Braun, M. Fahlman, M. Berggren, X. Crispin, S. Fabiano, *J. Polym. Sci. Part B: Polym. Phys.* **2017**, *55*, 814–820.
- [105] S. Zhang, P. Kumar, A. S. Nouas, L. Fontaine, H. Tang, F. Cicoira, *APL Materials* **2015**, *3*, 014911.
- [106] C. Cendra, A. Giovannitti, A. Savva, V. Venkatraman, I. McCulloch, A. Salleo, S. Inal, J. Rivnay, *Adv. Funct. Mater.* **2019**, *29*, 1807034.
- [107] L. E. Bell, *Science* **2008**, *321*, 1457–1461.
- [108] L. B. Kong, T. Li, H. H. Hng, F. Boey, T. Zhang, S. Li, *Waste Energy Harvesting: Mechanical and Thermal Energies*, Springer-Verlag, Berlin Heidelberg, **2014**.
- [109] L. Francioso, C. D. Pascali, in *Thermoelectric Energy Conversion*, John Wiley & Sons, Ltd, **2017**, pp. 205–232.
- [110] G. Gromov, in *Thermoelectric Energy Conversion*, John Wiley & Sons, Ltd, **2017**, pp. 233–282.
- [111] H. D. Baehr, *Thermodynamik: Grundlagen und technische Anwendungen*, Springer-Verlag, Berlin Heidelberg, **2002**.
- [112] M. Mukaida, K. Kirihaara, Q. Wei, *ACS Appl. Energy Mater.* **2019**, *2*, 6973–6978.
- [113] M. Goel, C. D. Heinrich, G. Krauss, M. Thelakkat, *Macromol. Rapid Commun.* **2019**, *40*, 1800915.
- [114] O. Bubnova, X. Crispin, *Energy Environ. Sci.* **2012**, *5*, 9345–9362.
- [115] H. J. Goldsmid, *Introduction to Thermoelectricity*, Springer-Verlag, Berlin Heidelberg, **2016**.
- [116] H. Kuchling, *Taschenbuch der Physik*, Carl Hanser Verlag, München, **2011**.
- [117] G. W. Ehrenstein, *Polymer-Werkstoffe: Struktur - Eigenschaften - Anwendung*, Carl Hanser Verlag, **2011**.
- [118] Z. Guo, D. Lee, Y. Liu, F. Sun, A. Sliwinski, H. Gao, P. C. Burns, L. Huang, T. Luo, *Phys. Chem. Chem. Phys.* **2014**, *16*, 7764–7771.
- [119] G. J. Snyder, E. S. Toberer, *Nature Mater* **2008**, *7*, 105–114.
- [120] D. J. Paul, in *Thermoelectric Materials and Devices*, **2016**, pp. 83–108.
- [121] C. Wood, *Rep. Prog. Phys.* **1988**, *51*, 459–539.
- [122] K. Koumoto, T. Mori, Eds. , *Thermoelectric Nanomaterials: Materials Design and Applications*, Springer-Verlag, Berlin Heidelberg, **2013**.
- [123] W. Gao, S. Emaminejad, H. Y. Y. Nyein, S. Challa, K. Chen, A. Peck, H. M. Fahad, H. Ota, H. Shiraki, D. Kiriya, D.-H. Lien, G. A. Brooks, R. W. Davis, A. Javey, *Nature* **2016**, *529*, 509–514.
- [124] J. Kim, A. S. Campbell, B. E.-F. de Ávila, J. Wang, *Nat Biotechnol* **2019**, *37*, 389–406.
- [125] O. Bubnova, Z. U. Khan, A. Malti, S. Braun, M. Fahlman, M. Berggren, X. Crispin, *Nature Mater* **2011**, *10*, 429–433.
- [126] Q. Wei, M. Mukaida, K. Kirihaara, Y. Naitoh, T. Ishida, *RSC Adv.* **2014**, *4*, 28802–28806.
- [127] A. K. Menon, O. Meek, A. J. Eng, S. K. Yee, *Journal of Applied Polymer Science* **2017**, *134*, DOI 10.1002/app.44060.
- [128] J. Yang, T. Caillat, *MRS Bulletin* **2006**, *31*, 224–229.
- [129] X. Zhang, L.-D. Zhao, *Journal of Materiomics* **2015**, *1*, 92–105.
- [130] M. Li, C. Luo, J. Zhang, J. Yang, J. Xu, W. Yao, R. Tan, X. Duan, F. Jiang, *Surfaces and Interfaces* **2020**, *21*, 100759.
- [131] Y. Xuan, X. Liu, S. Desbief, P. Leclère, M. Fahlman, R. Lazzaroni, M. Berggren, J. Cornil, D. Emin, X. Crispin, *Phys. Rev. B* **2010**, *82*, 115454.
- [132] Q. Zhang, Y. Sun, W. Xu, D. Zhu, *Energy Environ. Sci.* **2012**, *5*, 9639–9644.

- [133] A. Liang, X. Zhou, W. Zhou, T. Wan, L. Wang, C. Pan, L. Wang, *Macromolecular Rapid Communications* **2017**, *38*, 1600817.
- [134] B. H. Lee, G. C. Bazan, A. J. Heeger, *Adv. Mater.* **2016**, *28*, 57–62.
- [135] Y. Kim, S. Chung, K. Cho, D. Harkin, W.-T. Hwang, D. Yoo, J.-K. Kim, W. Lee, Y. Song, H. Ahn, Y. Hong, H. Sirringhaus, K. Kang, T. Lee, *Adv. Mater.* **2019**, *31*, 1806697.
- [136] H. Yan, J. G. Manion, M. Yuan, F. P. García de Arquer, G. R. McKeown, S. Beaupré, M. Leclerc, E. H. Sargent, D. S. Seferos, *Adv. Mater.* **2016**, *28*, 6491–6496.
- [137] H. Hase, I. Salzmann, in *Handbook of Organic Materials for Electronic and Photonic Devices (Second Edition)* (Ed.: O. Ostroverkhova), Woodhead Publishing, **2019**, pp. 349–383.
- [138] J. Hynynen, D. Kiefer, L. Yu, R. Kroon, R. Munir, A. Amassian, M. Kemerink, C. Müller, *Macromolecules* **2017**, *50*, 8140–8148.
- [139] Y. Karpov, T. Erdmann, M. Stamm, U. Lappan, O. Guskova, M. Malanin, I. Raguzin, T. Beryozkina, V. Bakulev, F. Günther, S. Gemming, G. Seifert, M. Hamsch, S. Mannsfeld, B. Voit, A. Kiriy, *Macromolecules* **2017**, *50*, 914–926.
- [140] H. Li, E. Plunkett, Z. Cai, B. Qiu, T. Wei, H. Chen, S. M. Thon, D. H. Reich, L. Chen, H. E. Katz, *Advanced Electronic Materials* **2019**, *5*, 1800618.
- [141] Y. Xuan, X. Liu, S. Desbief, P. Leclère, M. Fahlman, R. Lazzaroni, M. Berggren, J. Cornil, D. Emin, X. Crispin, *Phys. Rev. B* **2010**, *82*, 115454.
- [142] D. Kiefer, R. Kroon, A. I. Hofmann, H. Sun, X. Liu, A. Giovannitti, D. Stegerer, A. Cano, J. Hynynen, L. Yu, Y. Zhang, D. Nai, T. F. Harrelson, M. Sommer, A. J. Moulé, M. Kemerink, S. R. Marder, I. McCulloch, M. Fahlman, S. Fabiano, C. Müller, *Nature Mater* **2019**, *18*, 149–155.
- [143] G. Chauhan, R. Srivastava, A. Kumar, O. Rana, P. C. Srivastava, M. N. Kamalasanan, *Organic Electronics* **2012**, *13*, 394–398.
- [144] I. E. Jacobs, E. W. Aasen, J. L. Oliveira, T. N. Fonseca, J. D. Roehling, J. Li, G. Zhang, M. P. Augustine, M. Mascall, A. J. Moulé, *J. Mater. Chem. C* **2016**, *4*, 3454–3466.
- [145] F. Deschler, D. Riedel, A. Deák, B. Ecker, E. von Hauff, E. Da Como, *Synthetic Metals* **2015**, *199*, 381–387.
- [146] J. Euvrard, A. Revaux, P.-A. Bayle, M. Bardet, D. Vuillaume, A. Kahn, *Organic Electronics* **2018**, *53*, 135–140.
- [147] V. I. Arkhipov, E. V. Emelianova, P. Heremans, H. Bässler, *Phys. Rev. B* **2005**, *72*, 235202.
- [148] W. H. Nguyen, C. D. Bailie, E. L. Unger, M. D. McGehee, *J. Am. Chem. Soc.* **2014**, *136*, 10996–11001.
- [149] W. Zhang, F. Zhang, B. Xu, Y. Li, L. Wang, B. Zhang, Y. Guo, J. M. Gardner, L. Sun, L. Kloo, *ACS Appl. Mater. Interfaces* **2020**, *12*, 33751–33758.
- [150] M. Goel, M. Siegert, G. Krauss, J. Mohanraj, A. Hochgesang, D. C. Heinrich, M. Fried, J. Pflaum, M. Thelakkat, *Adv. Mater.* **2020**, *32*, 2003596.
- [151] B. Meng, J. Liu, L. Wang, *Polym. Chem.* **2020**, *11*, 1261–1270.
- [152] B. Meng, H. Song, X. Chen, Z. Xie, J. Liu, L. Wang, *Macromolecules* **2015**, *48*, 4357–4363.
- [153] I. Salzmann, G. Heimel, S. Duhm, M. Oehzelt, P. Pingel, B. M. George, A. Schnegg, K. Lips, R.-P. Blum, A. Vollmer, N. Koch, *Phys. Rev. Lett.* **2012**, *108*, 035502.
- [154] G. A. Olah, G. K. S. Prakash, Q. Wang, X. Li, in *Encyclopedia of Reagents for Organic Synthesis*, American Cancer Society, **2004**.
- [155] C. Lambert, G. Nöll, *J. Am. Chem. Soc.* **1999**, *121*, 8434–8442.
- [156] Y. Su, X. Wang, X. Zheng, Z. Zhang, Y. Song, Y. Sui, Y. Li, X. Wang, *Angew. Chem. Int. Ed.* **2014**, *53*, 2857–2861.
- [157] S. Amthor, B. Noller, C. Lambert, *Chemical Physics* **2005**, *316*, 141–152.

- [158] C. Kvarnström, A. Petr, P. Damlin, T. Lindfors, A. Ivaska, L. Dunsch, *J Solid State Electrochem* **2002**, *6*, 505–512.
- [159] K. Gräf, M. A. Rahim, S. Das, M. Thelakkat, *Dyes and Pigments* **2013**, *99*, 1101–1106.
- [160] D. J. Myers, J. Osteryoung, *Anal. Chem.* **1973**, *45*, 267–271.
- [161] W. Zhang, L. Wang, Y. Guo, B. Zhang, V. Leandri, B. Xu, Z. Li, J. M. Gardner, L. Sun, L. Kloo, *Chem. Commun.* **2020**, *56*, 1589–1592.
- [162] A. Fediai, F. Symalla, P. Friederich, W. Wenzel, *Nat Commun* **2019**, *10*, 4547.
- [163] M. Schwarze, C. Gaul, R. Scholz, F. Bussoletti, A. Hofacker, K. S. Schellhammer, B. Nell, B. D. Naab, Z. Bao, D. Spoltore, K. Vandewal, J. Widmer, S. Kera, N. Ueno, F. Ortman, K. Leo, *Nature Mater* **2019**, *18*, 242–248.
- [164] H. Matsui, D. Kumaki, E. Takahashi, K. Takimiya, S. Tokito, T. Hasegawa, *Phys. Rev. B* **2012**, *85*, 035308.
- [165] J. O. Oelerich, F. Jansson, A. V. Nenashev, F. Gebhard, S. D. Baranovskii, *J. Phys.: Condens. Matter* **2014**, *26*, 255801.
- [166] B. Hartenstein, H. Bässler, *Journal of Non-Crystalline Solids* **1995**, *190*, 112–116.
- [167] P. M. Borsenberger, H. Bässler, *J. Chem. Phys.* **1991**, *95*, 5327–5331.
- [168] Z. Hawash, L. K. Ono, Y. Qi, *Adv. Mater. Interfaces* **2018**, *5*, 1700623.
- [169] J. A. Röhr, X. Shi, S. A. Haque, T. Kirchartz, J. Nelson, *Phys. Rev. Applied* **2018**, *9*, 044017.
- [170] S.-J. Yoo, J.-H. Lee, J.-H. Lee, J.-J. Kim, *Appl. Phys. Lett.* **2013**, *102*, 183301.
- [171] D. Kiefer, A. Giovannitti, H. Sun, T. Biskup, A. Hofmann, M. Koopmans, C. Cendra, S. Weber, L. J. Anton Koster, E. Olsson, J. Rivnay, S. Fabiano, I. McCulloch, C. Müller, *ACS Energy Lett.* **2018**, *3*, 278–285.
- [172] J. Liu, L. Qiu, R. Alessandri, X. Qiu, G. Portale, J. Dong, W. Talsma, G. Ye, A. A. Sengrian, P. C. T. Souza, M. A. Loi, R. C. Chiechi, S. J. Marrink, J. C. Hummelen, L. J. A. Koster, *Adv. Mater.* **2018**, *30*, 1704630.
- [173] J. Liu, G. Ye, H. G. O. Potgieser, M. Koopmans, S. Sami, M. I. Nugraha, D. R. Villalva, H. Sun, J. Dong, X. Yang, X. Qiu, C. Yao, G. Portale, S. Fabiano, T. D. Anthopoulos, D. Baran, R. W. A. Havenith, R. C. Chiechi, L. J. A. Koster, *Advanced Materials* **2021**, *33*, 2006694.

2. Objective of the Thesis

Conjugated polymers based on diketopyrrolopyrrole derivatives are advantageous for different applications owing to their excellent properties. Some of the most noteworthy ones are their pronounced and tunable light absorption or their excellent light, thermal and chemical stability, enabling their use in solar cells. For the application in bioelectronics or thermoelectrics, however, some additional properties are desired. These are for the former case, water compatibility or swellability in aqueous media, respectively. Moreover, a very low oxidation potential and of course, biocompatibility of the polymer. For the latter *i.e.*, thermoelectrics, good charge transport mobilities are required along with facile doping possibilities and naturally, thermal durability. Before the start of this dissertation project, different variations of PDPPs were tested as the active materials in organic solar cells, thin film transistors *etc.* But despite the abovementioned capabilities of DPP based polymers, which are highly promising for thermoelectric and bioelectronic applications, they were unexplored and not established in these fields. This thesis deals with structural variation of PDPPs, their p-doping using the novel concept of HOMO-HOMO doping as well as their applications in thermoelectrics and bioelectronics.

Therefore, one aim was to design suitable mixed-conducting PDPP derivatives for bioelectronic applications and test them in OECTs. We decided to employ a thiophene flanked DPP as the workhorse structure for the p-type polymers, as the individual motifs within the molecule can be chosen deliberately, enabling us to systematically study structure-property relations. It was previously recognized that these PDPPs can exhibit sufficiently good hole transport properties, however no mixed conduction properties were known for DPP polymers. Thus, we set our focus on tuning the hydrophilicity, which is a necessary condition for mixed conduction properties. We studied this by increasing the content of ethylene glycol moieties within the polymer to see if a mixed conductor and thus, an OECT material can be obtained. Furthermore, we identified the possibility for gaining a reduced oxidation potential by purposefully using the comonomers EDOT and 3-MEET which are known to entail this property in their homopolymers. It was anticipated that by using 3-MEET, a further increased ethylene glycol content within the final copolymer can assist the mixed conduction properties. The materials would then be first characterized comprehensively by means of chemical and electronic properties and, if proven to be viable for the use as MIEC, further tested in OECT devices. Furthermore, their cycling stability and absence of toxicity versus biological cells must be ensured in order to provide stable and biocompatible MIEC polymers.

In the case of the application as thermoelectric materials, some scientific reports were published during the course of this dissertation, where different PDPP derivatives were employed as the active material for thermoelectric devices. These works pointed to the circumstance, that new ways for effective p-doping of the conjugated polymer have a pivotal role in the further optimization of the thermoelectric materials. We therefore set on to

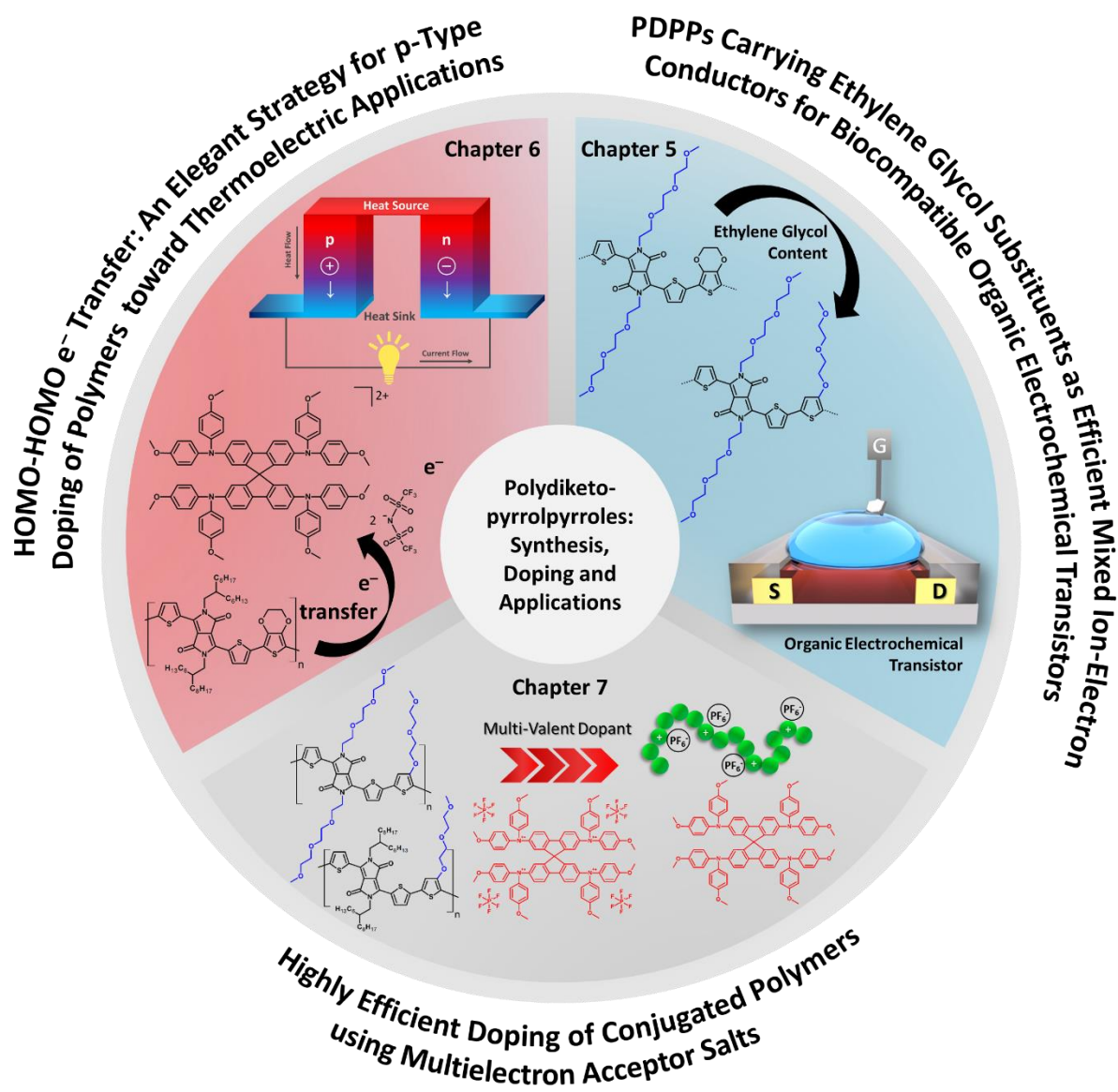
develop a new concept for the effective p-type doping of polymers, addressing the issue that conventional dopants introduce species to the doped polymer system, which can't actively participate, or even hamper the charge transport after doping. Our first approach was motivated by the idea to dope a prototypical hole transport polymer (PDPP[T]₂-EDOT) by an oxidized hole transport material [Spiro-OMeTAD]²⁺(TFSI⁻)₂. After complete charge transfer between polymer and dopant, the reduced dopant should not hinder the charge transport or may even assist it, as it is a hole transport material as well. This concept should be proven by characterizing the systems regarding their electronic and optoelectronic properties, and the performance in thermoelectric devices needs to be evaluated.

In an extensive consecutive study, this concept was expanded to further, or respectively, more highly oxidized hole transport dopants. The question arose, whether the doping efficacy scales with the oxidation state of the used dopant and if benefits can be gained thereby, as compared with conventional redox dopants like NOPF₆ or the single electron acceptor Magic Blue. In this work, also the often-discussed influence of the polymer's polarity on the doping process was studied by using two very similar polymers, which specifically only differ in the side-chain structure; one being completely hydrophobic, the other one carrying two triethylene glycol chains.

3. Overview of the Thesis

The thesis is focused on the purposeful design of diketopyrrolopyrrole-based conjugated polymers for the use as mixed conductors in bioelectronic devices as well as doped p-type semiconductors as thermoelectric materials. In all chapters, the polymer structures were constructed around a thiophene-flanked DPP core, as this central motif allows for the chemical stability, charge transport properties and chemical flexibility required for the intended applications. Chemical flexibility in this regard allows for the choice of different substituents and comonomers, in order to strategically tune the properties of the resulting polymers. A particular focus lied on introducing ethylene glycol (EG) substituents in a targeted manner, to improve and investigate the compatibility with water and polar species such as water and ions (**Chapter 5**). Here, four PDPPs with increasing EG content (0 – 52 wt.% EG) were synthesized and tested as mixed conductors. The second scientific question is centered around doping. It concerns itself with testing a novel HOMO-HOMO doping method for conjugated polymers and uses the doped materials in thermoelectric materials (**Chapter 6**). Here, we studied if an oxidized small molecule hole transport material (HTM), [Spiro-OMeTAD]²⁺(TFSI⁻)₂, is capable of doping a p-type polymer efficiently. For this, a prototypical PDPP derivative, PDPP[T]₂-EDOT, was synthesized and mixed with [Spiro-OMeTAD]²⁺(TFSI⁻)₂, and the resulting electronic and thermoelectric properties were investigated. Finally, this new HOMO-HOMO doping-concept was extended in a comprehensive way by synthesizing different multi-electron acceptor salts and verifying the doping efficiency of these radical cation salts varying in their capability to accept electrons. (**Chapter 7**). Thus, four dopants of which one was a conventional redox-dopant, but the others were singly, doubly and four-fold oxidized HTMs were compared. As host-polymers, two PDPP derivatives were chosen which mainly differ in their EG content, so that additionally the influence of the host's polarity and dielectric constant on the doping process could be studied. This establishes the universal nature of the novel doping concept.

A graphical overview over the contents of the three chapters are given, which are elaborated further below.



Chapter 5: Polydiketopyrrolopyrroles Carrying Ethylene Glycol Substituents as Efficient Mixed Ion-Electron Conductors for Biocompatible Organic Electrochemical Transistors

PDPPs are a comparatively less studied material class in the field of bioelectronics and systematic studies regarding structure-property relationships were lacking in the literature. A key-aspect of efficient mixed conductors is the *a priori* controversial interplay of swellability and charge transport. In this work, four PDPPs with increasing EG content and two different comonomers, EDOT and 3-MEET were studied and design rules for efficient DPP-based MIECs could be deduced.

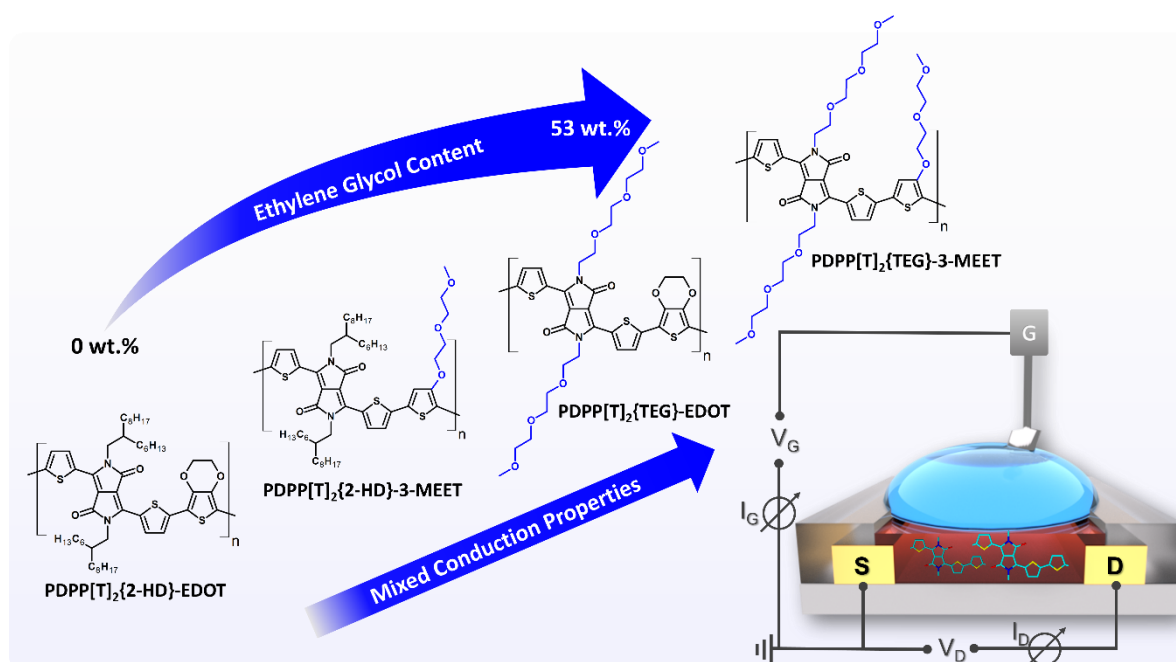


Figure 20 - Graphical Overview over chapter 5, adapted from Reference.^[83] Four p-type DPP-based polymers with increasing content of ethylene glycol and concomitantly increasing mixed conduction properties, allowing for the application in an organic electrochemical transistor devices (bottom right corner).

After the basic chemical characterization of the molecular weight distributions and thermal properties of the synthesized polymers, first the charge transport properties in the dry state were determined, which clarified that the substitution pattern has no systematic influence on the charge carrier mobility. Moreover, the oxidizability in the dry state was unaffected by substituent and comonomer, which allows for the conclusion that these properties are mostly dictated by the polymer backbone. The oxidizability in the wet/swollen state, as probed by spectroelectrochemical experiments however, exhibited a clear dependence on the EG content. The polaron formation was observable at lower doping potentials in the two polymers with the highest EG content. In addition, the EG content was tightly linked to the volumetric capacitance, which was up to two orders of magnitude higher for the two more hydrophilic polymers, as compared to the ones with the least EG contents. When measuring the swelling *via* electrochemical quartz crystal microbalance with dissipation monitoring measurements (E-QCMD), this trend was confirmed, as only the two polymers with the highest degrees of EG substitution showed an appreciable swelling. Ultimately, in the OECT devices the two less hydrophilic materials showed no mixed conduction at all, but beyond 40 wt.% EG content the materials could be successfully employed as OECT materials. The transconductances and threshold potentials of both OECT materials were in the same range, the polymer with the highest EG content however, showed a higher figure of merit (μC^* product). At the end, the operational stability of the polymers was tested, and the best polymer retained 97 % of its initial drain current after 1200 consecutive measurement cycles. Next, in a joint work, the tolerance of the two working OECT materials toward a cell-growth medium as the electrolyte was tested, as compared to the standard aq. sodium chloride solution. No differences could be observed compared with the sodium chloride solution. The

polymers were also subjected to in-vitro cytotoxicity tests, where no toxicity at all was detected. In conclusion I have systematically synthesized four novel DPP based polymers and studied the influence of the degree of EG substitution on the mixed conduction properties. At the end, a well performing polymer was identified, which operates stably in an OECT without any adverse toxic effects or the need for additives such as crosslinkers.

Chapter 6: HOMO-Homo Electron Transfer: An Elegant Strategy for p-Type Doping of Polymer Semiconductors toward Thermoelectric Applications

Conventional p-doping of organic semiconductors (OSCs) predominantly employs electron acceptors like F₄TCNQ and others, as discussed earlier. The common disadvantage of this doping strategy is the very high required amount of dopant of up to 30-50 mol%, owing to poor doping efficiencies which also drastically decrease with an increased dopant content. The dopant molecules distributed across the polymer matrix, ionized or pristine, do not assist, but usually even hamper the charge transport. Therefore, we picked up the idea of using a small molecule radical cation salt, [Spiro-OMeTAD]²⁺(TFSI)⁻₂ which itself is a hole transporter as the dopant. The DPP based polymer PDPP[T]₂-EDOT served as the matrix, and the doubly oxidized [Spiro-OMeTAD]²⁺ having singly occupied MOs (SOMOs) was tested as the dopant. The schematic below shows the structures of the used polymer as well as the oxidized hole transport material *i.e.*, the dopant and illustrates the doping process of electrons being transferred from the polymer HOMO to partially occupied MOs of the doubly oxidized [Spiro-OMeTAD]²⁺.

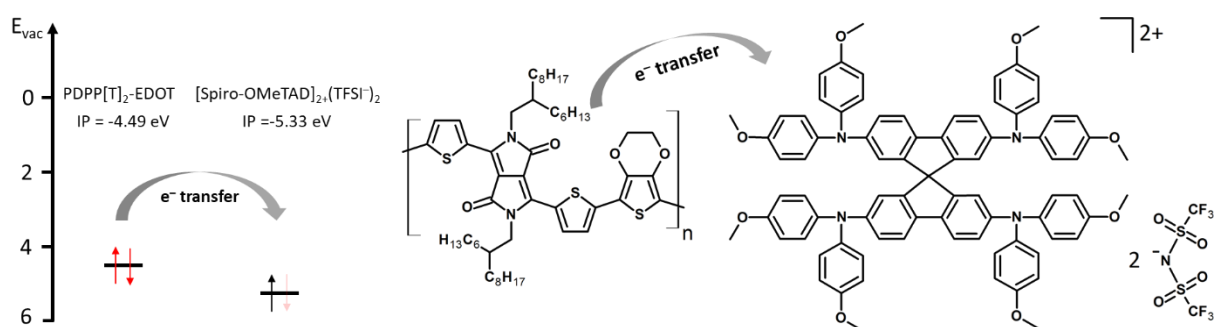


Figure 21 – Left: illustration of the electron transfer between the polymer HOMO and the dopants singly occupied MOs. Right: Polymer-dopant system used to demonstrate the feasibility of doping of a hole-transport polymer PDPP[T]₂-EDOT with the oxidized hole-transport material [Spiro-OMeTAD]²⁺(TFSI)⁻₂.

To start with, the electronic parameters of the pure polymer, pure dopant and neutral dopant-precursor were determined, above all their Fermi levels and the ionization potentials. Next, doped films of polymer and oxidized HTM were prepared and a progressively shifted Fermi level of the doped polymer films toward the pristine polymer's HOMO proved the successful doping. By using UV/Vis/NIR absorption spectroscopy, a progressive extinction of the polymer's main absorption with the simultaneous formation of polaronic absorption features could be observed upon addition of the new dopant. As a result, it was affirmed that the

oxidized HTM, [Spiro-OMeTAD]²⁺(TFSI⁻)₂ dopes the p-type polymer PDPP[T]₂-EDOT. To our big surprise, the electrical conductivity increased by four orders of magnitude from 10⁻⁴ S cm⁻¹ to 1 S cm⁻¹ at moderate doping levels below 5 mol%. The thermoelectric parameters demonstrated the common dependencies *i.e.*, a decrease of the Seebeck coefficient from *ca.* 500 μV K⁻¹ in the undoped films down to *ca.* 100 μV K⁻¹ upon increasing the charge carrier concentration and a shift of Fermi level towards valence band maximum. A maximum power factor of 0.07 μW m⁻¹K⁻² was achieved at the doping level of 4 mol%. In conclusion, the new method of doping a p-type polymer with the oxidized HTM [Spiro-OMeTAD]²⁺(TFSI⁻)₂ is a successful and to date unprecedented strategy.

Chapter 7: Highly Efficient Doping of Conjugated Polymers using Multielectron Acceptor Salts

In the previous chapter, a novel doping strategy for conjugated polymers was demonstrated for the first time using a doubly charged HTM as electron acceptor. This concept was extended and studied more thoroughly in this chapter using multielectron acceptors, which can accept more than two electrons. The core issue was to study if oxidized HTM-dopants in higher oxidative states entail advantages as compared to dopants in lower oxidation states. Furthermore, the implications of the newly presented doping method on the electronic properties, as opposed to a conventional redox dopant (nitrosonium hexafluorophosphate) were investigated. Finally, we addressed the popular question of the role of the polymer polarity on the doping process. The studied polymer systems were based on two almost identical PDPPs, which only differ in their side-chain structure: one carries TEG-substituents (hydrophilic) at the DPP core and the other one long branched alkyl chains (hydrophobic). The dopants which were compared are the aforementioned redox dopant NOPF₆, the singly oxidized HTM (*tris*(4-bromophenyl)ammonium hexachloroantimonate, “Magic Blue”), the doubly oxidized [Spiro-OMeTAD]²⁺(PF₆⁻)₂ as well as the four-fold oxidized [Spiro-OMeTAD]⁴⁺(PF₆⁻)₄. Here the last two dopants were newly synthesized for this study.

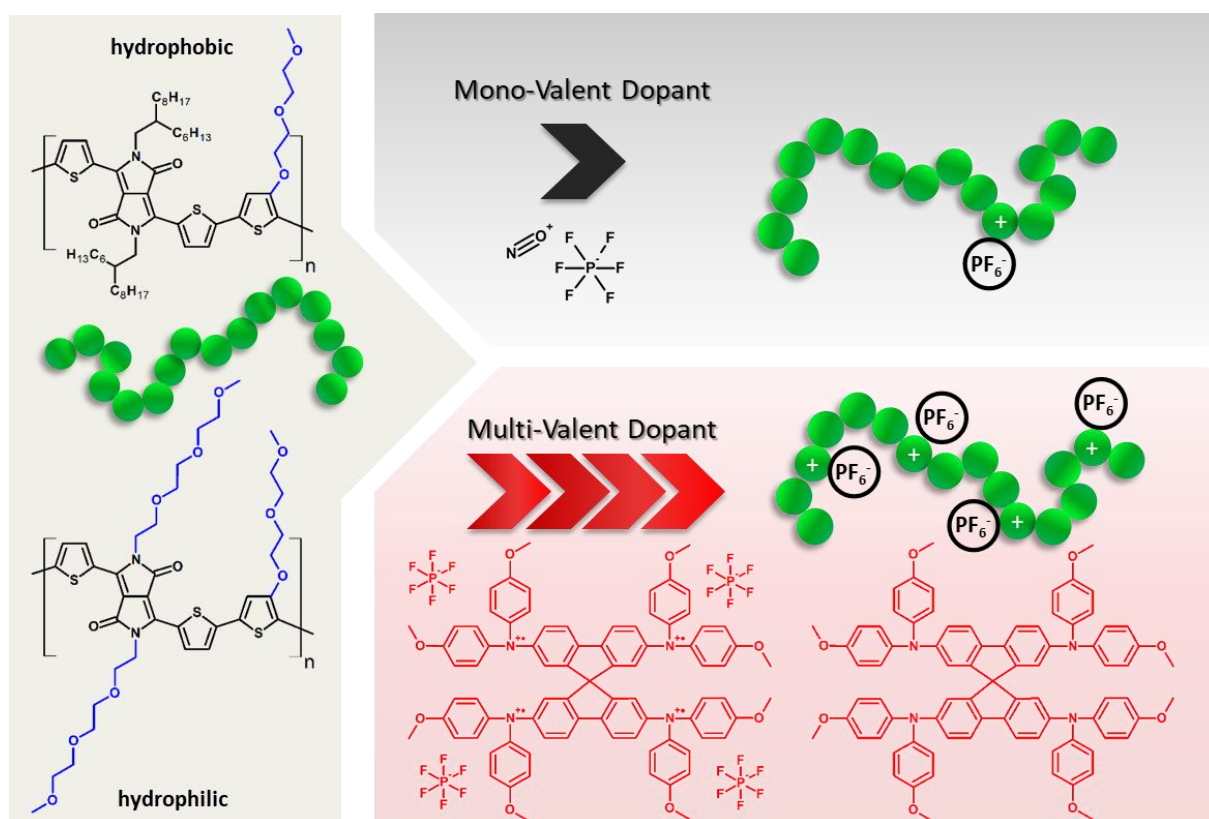


Figure 22 – Hydrophobic and hydrophilic polymers and schematic of the doping process using either mono valent dopants (top) imparting one charge at a time, or multi valent dopants (bottom) as exemplarily shown by the tetra cationic dopant $[\text{Spiro-OMeTAD}]^{4+}(\text{PF}_6^-)_4$ imparting multiple charges per used dopant molecule; additionally, the reduced dopant remains within the doped polymer without hindering the charge transport.

First, all the materials were characterized separately, and special attention was paid to their electronic properties. We then monitored the doping process by means of optical absorption spectroscopy in solution. This qualitatively revealed that the formation of polaron absorptions and ground state bleaching, respectively, scales with the oxidation state of the dopants. Because the electrical conductivity is often the macroscopic property of interest when doping an OSC, the conductivities of doped films were measured both at room temperature and temperature dependent to access the activation energies for charge transport. In the ultra-low doping regime below 1 mol%, no differences between the dopants were observable, regardless of the host polymer. Beyond 1 mol% dopant however, drastic differences became obvious. The two- and four-fold oxidized HTM caused a drastic improvement of the electrical conductivity, whereas almost no change was observed for both single electron acceptors. This was the case in both polymers, but in the more polar polymer the differences were more pronounced and the final conductivities at 5 mol% dopant were distinctively higher, than in the more hydrophobic polymer. The activation energy measurements also revealed drastic differences and clarified the different doping mechanisms between conventional redox-doping and the newly presented way *via* oxidized HTMs. After the addition of NO^+PF_6^- , the activation energy instantly dropped monotonically and approached 0 meV at higher doping levels. This is explained with the Fermi level moving towards the transport level by the increased charge carrier density as a result of increased doping. For the HTM-dopants,

however, the activation energy remained constant over the whole doping range up to 2 mol%. This indicates an unchanged distance between Fermi and transport level due to the redistribution of electrons between HTM dopant and polymer. On measuring the charge carrier density, exactly the doubled and quadrupled carrier density was found in doped polymers, for the doubly and four-fold oxidized dopants respectively, as compared to the singly oxidized HTM at 5 mol% dopant. This was perfectly observable in the hydrophilic polymer. Regarding the charge carrier mobility, it surprisingly turned out that the HTM dopants irrespective of the host polymer resulted in neither advantages nor disadvantages. Finally, regarding the doping efficiency, it became clear that the doping efficiency scaled with the increasing oxidation state of the dopant, especially at higher dopant concentrations. At the highest dopant ratio of 5 mol%, the four-fold oxidized [Spiro-OMeTAD]⁴⁺(PF₆⁻)₄ exhibited an efficiency of *ca.* 20 %, whereas the doping efficiency of NOPF₆ had already deteriorated to 3 % at the same concentration. To conclude, we have synthesized novel oxidized HTMs and comprehensively tested and investigated them as dopants for two p-type polymers. We could demonstrate that the highest oxidized dopant results in the most facile increase of charge carrier density and electrical conductivity, while retaining the highest doping efficiency within the series. By using the four-fold oxidized dopant, the required dopant amounts necessary to increase the conductivity by four orders of magnitude from 10⁻⁵ to *ca.* 0.2 S cm⁻¹ could be reduced to just 5 mol%. A higher polarity of the host polymer assists the doping process due to a better miscibility of the charged species or better accessibility of the dopant to the backbone. Improved shielding of coulombically bound charges due to a slightly increased dielectric constant, as introduced by the TEG-substitutes contributes to this advantage. Thus, multivalent oxidized HTMs facilitate an advantageous charge carrier generation, as compared to lower oxidized variants or conventional redox dopants like NOPF₆. This is manifested especially at higher dopant concentrations of > 2 mol%, but overall, the required dopant ratios are drastically reduced to single-digit molar dopant ratios, which is a big step toward highly efficient doping without the necessity of using excess dopant amounts.

4. Individual Contributions to Joint Publications

The following section specifies the individual contributions to joint publications of the authors.

4.1. “Polydiketopyrrolopyrroles Carrying Ethylene Glycol Substituents as Efficient Mixed Ion-Electron Conductors for Biocompatible Organic Electrochemical Transistors”
Published as *Advanced Functional Materials* **2021**, 31, 2010048 by **Gert Krauss**, Florian Meichsner, Adrian Hochgesang, John Mohanraj, Sahar Salehi, Philip Schmode and Mukundan Thelakkat.

I synthesized the monomers and polymers and performed the chemical and thermal characterization of all the materials. Furthermore, I determined the oxidation potentials *via* differential pulse polarography measurements in thin films and conducted the spectroelectrochemical measurements and processed and evaluated all the data. I fabricated and measured OFET devices to calculate the charge carrier mobilities in the dry state and fabricated and measured OECT devices to calculate and determine all the OECT-related parameters, including the cycling tests and the transient response time measurements. Finally, I curated and plotted all the data in the publication and wrote the manuscript, except the cytotoxicity paragraph (*vide infra*).

Florian Meichsner prepared and measured samples for the active and passive swelling *via* electrochemical Quartz-Crystal Microbalance measurements and evaluated the measurements. He also prepared the samples for the cell-compatibility tests.

Adrian Hochgesang performed the electrochemical impedance spectroscopy measurements, processed the measured data, calculated the volumetric capacitances, and wrote the respective experimental description in the manuscript. He further assisted with the device cycling experiments.

John Mohanraj measured ultraviolet photoelectron spectroscopy of the polymers and calculated the ionization potentials and wrote the corresponding experimental description in the manuscript.

Sahar Salehi conducted the cytotoxicity tests and wrote the corresponding paragraphs in the manuscript.

Philip Schmode assisted me with the OECT device fabrication and measurement, helped with the evaluation of the measured OECT data as well as the E-QCMD measurements. He corrected and proof-read the manuscript and aided with scientific discussions.

Mukundan Thelakkat supervised the project and corrected the final manuscript.

4.2. “HOMO-Homo Electron Transfer: An Elegant Strategy for p-Type Doping of Polymer Semiconductors toward Thermoelectric Applications”

Published as *Advanced Materials* **2020**, 32, 2003596 by Mahima Goel, Marie Siegert, **Gert Krauss**, John Mohanraj, Adrian Hochgesang, David C. Heinrich, Martina Fried, Jens Pflaum and Mukundan Thelakkat.

Mahima Goel prepared thin film samples conducted absorption spectroscopy measurements, doping studies and measured the electrical conductivities. She also wrote the manuscript.

Marie Siegert measured thermoelectric parameters and the temperature dependent electrical conductivity and contributed to the thermoelectric part of manuscript.

I synthesized the monomers and polymer and conducted their chemical and thermal characterization. I measured the spectroelectrochemical behavior of the pure polymer and absorption spectra of the doped polymer solution. Moreover, I was involved in scientific discussions and corrected the manuscript.

John Mohanraj performed the X-ray photoelectron spectroscopy experiments for the determination of the dopant composition and measured ultraviolet photoelectron spectroscopy for the determination of the electronic parameters of dopant and polymer.

Adrian Hochgesang measured the charge carrier mobility and charge carrier densities *via* electrochemical impedance spectroscopy and Mott-Schottky measurements, respectively.

David C. Heinrich assisted Mahima Goel with data analysis.

Martina Fried synthesized the dopant.

Jens Pflaum and Mukundan Thelakkat supervised the project and corrected the final manuscript.

4.3. “Highly Efficient Doping of Conjugated Polymers using Multielectron Acceptor Salts” Submitted for publication in *Macromolecular Rapid Communications* by **Gert Krauss**, Adrian Hochgesang, John Mohanraj and Mukundan Thelakkat.

Gert Krauss and Adrian Hochgesang contributed equally to the conceptualization and planning of the research project, writing of the manuscript and supplementary information. Further, the determination of the charge carrier densities *via* absorption spectroscopy and impedance measurements was done together.

I synthesized and chemically characterized the used monomers and polymers. Further, I prepared the samples and performed optical absorption measurements and spectroelectrochemical absorption measurements, including the evaluation of the obtained results. I moreover prepared and measured devices for the determination of the electrical conductivities at room temperature and temperature dependent for the calculation of the

activation energies. Finally, I processed and plotted all the data and prepared all the figures in the submitted manuscript.

Adrian Hochgesang synthesized and characterized the used dopants, prepared samples, measured and calculated the charge carrier densities of NOPF₆-doped films *via* Mott-Schottky measurements as well as the zero-field mobilities of the neutral dopant precursors. He fabricated devices for and measured the electrical permittivity. Furthermore, he prepared devices for ultraviolet photoelectron spectroscopy measurements of the dopants, polymers, and doped polymers.

John Mohanraj performed and evaluated X-ray photoelectron spectroscopy measurements of the dopants for the determination of their chemical composition and corrected the manuscript.

Mukundan Thelakkat supervised the project and corrected the manuscript.

4.4. “Principles of Structural Design of Conjugated Polymers Showing Excellent Charge Transport toward Thermoelectrics and Bioelectronics Applications (Annex)”
Review Published as *Macromolecular Rapid Communications* **2019**, 1800915 by Mahima Goel, David Heinrich, **Gert Krauss** and Mukundan Thelakkat.

Mahima Goel wrote the paragraph concerning the design rules and stability issues in n-type materials (section 3) and the synthetic principles for D-A and A-A n-type polymers. She also contributed the general introduction to thermoelectrics (section 4).

David Heinrich contributed the section 2, reviewing the charge carrier transport in organic semiconductor polymers and section 5, reviewing the literature for conjugated polymers for bioelectronics.

I contributed the introduction (section 1) as well as section 3, focusing on the design rules and synthetic strategies toward p-type materials, the non-covalent interactions, and the planarization by fused aromatic building blocks. I wrote the p-type thermoelectric polymer and doping strategy part in section 4.

Mukundan Thelakkat outlined the contents and concept of review, supervised the preparation of the review, and corrected the final manuscript.

5. Polydiketopyrrolopyrroles Carrying Ethylene Glycol Substituents as Efficient Mixed Ion-Electron Conductors for Biocompatible Organic Electrochemical Transistors

Published as “Polydiketopyrrolopyrroles Carrying Ethylene Glycol Substituents as Efficient Mixed Ion-Electron Conductors for Biocompatible Organic Electrochemical Transistors” in *Advanced Functional Materials* **2021**, 31, 2010048 by Gert Krauss, Florian Meichsner, Adrian Hochgesang, John Mohanraj, Sahar Salehi, Philip Schmode and Mukundan Thelakkat.

G. Krauss, F. Meichsner, A. Hochgesang, J. Mohanraj, P. Schmode, Prof. M. Thelakkat
Applied Functional Polymers, Macromolecular Chemistry I, University of Bayreuth,
Universitätsstr. 30, Bayreuth, 95440, Germany
E-mail: mukundan.thelakkat@uni-bayreuth.de

S. Salehi
University of Bayreuth, Department of Biomaterials,
Prof.-Rüdiger-Bormann-Str. 1, Bayreuth, 95447, Germany

Prof. M. Thelakkat
Bavarian Polymer Institute (BPI), University of Bayreuth,
Universitätsstr. 30, Bayreuth, 95440, Germany

Keywords: Bioelectronics, Conjugated Polymers, Biosensors, Organic Electronics, Structure-Property-Relationship.

Abstract

Herein, we present a comprehensive investigation of four Polydiketopyrrolopyrroles (PDPPs) with increasing ethylene glycol (EG) content and varying nature of comonomer and deduce guidelines for the design of efficient mixed ion-electron conductors (MIECs). The studies in NaCl electrolyte-gated organic electrochemical transistors (OECTs) reveal that a high amount of EG on the DPP moiety is essential for MIEC. The PDPP containing 52 wt.% EG exhibits a high volumetric capacitance of 338 Fcm^{-3} (at 0.8 V), a high hole mobility in aqueous medium ($0.13 \text{ cm}^2\text{V}^{-1}\text{s}^{-1}$) and a μC^* product of $45 \text{ Fcm}^{-1}\text{V}^{-1}\text{s}^{-1}$. OECTs using this polymer retained 97 % of its initial drain-current after 1200 cycles (90 min of continuous operation). In cell-growth medium, the OECT-performance was fully maintained as in NaCl electrolyte. In vitro cytotoxicity and cell viability assays reveal the excellent cell compatibility of these novel systems, showing no toxicity after 24 h of culture. Due to the excellent OECT performance with a considerable cycling stability for 1200 cycles and an outstanding cell compatibility, these PDPPs render themselves viable for in vitro and in vivo bioelectronics.

1. Introduction

Conjugated polymers have become ubiquitous in many kinds of electronic applications, such as light emitting diodes^[1,2], solar cells^[3-5], field effect transistors^[6] or thermoelectrics^[7-10], and naturally they also found their way into the field of organic bioelectronics.^[11] In bioelectronic devices, mixed ion-electron conductors (MIECs) are required as the active materials to transport both electrical charges and ions. MIECs are capable of operating under very low gate voltages and they incorporate ions from a surrounding electrolyte upon electrochemical doping. The main application for MIECs are organic electrochemical transistors (OECTs). An OECT always acts as a transducing entity between its biologic environment and the resulting electrical output. The quality of this property is expressed in terms of the transconductance g_m (**equation 1**), i.e. the change in drain-current per unit change in gate voltage. The transconductance can be determined from **equation 2** below, where the so called μC^* -product can be derived as a geometry and bias independent figure of merit, which gives a direct measure for the MIEC properties.^[12]

$$g_m = \frac{\partial I_D}{\partial V_G} \quad (\text{equation 1})$$

where g_m : transconductance, I_D : drain-current and V_G : gate-voltage.

$$g_m = \frac{W \cdot d}{L} \cdot \mu C^* \cdot (V_{Th} - V_G) \quad (\text{equation 2})$$

where W : channel width, d : film thickness, L : channel length, μ : OECT-charge carrier mobility, C^* : volumetric capacitance, V_{Th} : threshold-voltage and V_G : gate voltage.

It is obvious that a combination of both, a high charge carrier mobility (μ), and a high volumetric capacitance (C^*) is required to achieve very good mixed conduction properties in a material. These two properties require a precise tuning of the chemical structures via careful molecular design. Alongside with the good charge and ion transport capabilities, the materials must be water-compatible in a way that they swell moderately but do not dissolve or delaminate in the aqueous environment. Obviously, the polymer needs to be biocompatible and the transistors must switch on and off at low threshold-voltages, i.e. $V_{Th} \ll 1$ V, to avoid breakdown of the aqueous electrolyte and degradation of the biological environment.

Different MIECs based on conjugated polymers have been tested and evaluated in OECTs. The most-studied material is a doped system based on a poly(3,4-ethylenedioxythiophene):polystyrene sulfonate (PEDOT:PSS) dispersion, which operates under depletion mode. However, the use of PEDOT:PSS dispersions limits the scope of tailoring different properties such as the swelling, degree of doping and processing.^[13] Moreover, post-processing methods like cross linking are required to prevent dissolution in water, which adversely affect the device parameters.^[14,15] Additionally, the need for MIECs working in the accumulation mode prompted the development of a wide variety of novel systems such as conjugated polyelectrolytes and their copolymers^[16,17] as well as polar conjugated polymers carrying ethylene glycol substituents.^[18,19] Thus the structural features need to fulfil a variety of conditions such as mode of operation, easy oxidizability at low

voltages, fast ion transport and water-compatibility as well as good charge carrier mobility in doped and swollen state to make a conjugated polymer suitable as MIEC. To determine design principles of efficient MIECs and consequently, to understand their structure-property relationships, a systematic tailoring of the chemical structures in a series of systems is still required.

Other than the above-mentioned classes of MIECs based on polythiophenes, there are only very few reports of OECTs using the second-generation conjugated polymers, based on donor-acceptor structures as p-type MIECs.^[20,21] Donor-acceptor copolymers, especially those incorporating diketopyrrolopyrrole (DPP) moieties as acceptor units can exhibit high charge carrier mobilities and their synthetic strategies to tune the chemical structures over a wide range are well established.^[22,23] We as well as others have earlier shown that the flanking units, solubilizing side-chains and comonomers can be adjusted deliberately to attain the desired type of charge transport and alignment.^[23-24] For example, the majority charge carriers (n- or p-type), the oxidation potential as well as the solubility can be varied. Also, PDPPs are known for their good chemical, thermal and light-stability. Lastly, by adaptation of chemical structures, PDPPs can be made biocompatible as well as decomposable^[25] and therefore, envisioning bioelectronics from PDPPs can be very promising. Yet, to date the PDPPs were rarely studied as materials for MIECs or in OECTs. The group of McCulloch et al.^[26] incorporated lysine side-chain moieties in a conventional PDPP and showed the advantages for neural cell adhesion and growth, but no OECT results were reported. Later Schmatz et al.^[27] reported the technological relevance of printing a highly soluble PDPP carrying photocleavable solubilizing moieties using green solvents for OECT applications. Further, Giovannitti et al.^[28] studied a pyridine-flanked PDPP, copolymerized with bithiophene or 3,3'-dimethoxy-2,2'-bithiophene in OECTs and reported the advantage of using such conjugated polymers with high ionization energies to avoid undesired non-capacitive faradaic reactions such as oxygen reduction. Very recently, Moser et al. have reported the influence of the polymer microstructures on the polaron delocalization and the resulting performance in OECTs using glycol substituted PDPPs using three different co-monomers, thieno[3,2-b]thiophene, bithiophene and dimethoxy-bithiophene.^[29] The groups of Wu et al.^[30] and Liu et al.^[31] have also reported on the advantages of using ionic liquid electrolytes along with a glycol substituted PDPP, copolymerized with dodecyl substituted bithiophene. These reports motivated us to address the fundamental design principles required for an efficient and biocompatible p-type MIEC based on hydrophilic PDPPs carrying ethylene glycol (EG) substituents.

Here, we focussed on the systematic molecular design to obtain polymers which do not necessitate the use of any cross linkers or any post-deposition efforts to stabilize the polymer film against dissolution. We designed and synthesized four PDPP derivatives with increasing content of ethylene glycol substituent from zero to 52 wt% and varied the location of the same (either on the DPP core or on the comonomer) to establish a structure-property relationship.

After studying the basic material properties on thin films such as hole mobility in organic field-effect transistors (OFETs) and ionization energies (using UPS) in the dry state, we characterized them comprehensively in the aqueous environment by spectroelectrochemical absorption spectroscopy (SEC) and electrochemical quartz-crystal microbalance with dissipation monitoring (E-QCMD) and finally in OECT devices. The OECT performance was assessed in both sodium chloride solution, as well as a standardized cell-growth medium (Dulbecco's Modified Eagle Medium, DMEM) as the electrolyte. The necessity of a high EG content (40-50 wt.%) and the location of the EG substituent (on the DPP core) for high performance is established. Further, we studied the cycling stability of the materials and could show that the devices retain up to 82 – 97 % of their initial drain current after 1200 simulated measurement cycles. Finally, the in vitro cytotoxicity and cell viability assays reveal the high cell compatibility and their potential for in vivo applications. The high cycling stability of the OECT in the electrolyte medium and equal performance in the cell growth medium, as well as the absence of toxicity in contact with fibroblast cells is highly promising towards real biosensors. Thus, for the first time, we report a systematic and comprehensive study for a second-generation donor-acceptor conjugated polymer based on PDPPs in the context of biosensors. We also provide a valuable understanding of the MIEC properties and biocompatibility of this family of polymers and deduce design rules for high performing DPP-based MIEC materials.

2. Results and Discussion

2.1. Synthesis and Material Characterization

Four polymers with increasing EG content were designed, synthesized and studied in detail. In **Figure 1**, the chemical structures of the four polymers are depicted as PDPP[T]₂{2-HD}-EDOT, PDPP[T]₂{2-HD}-3-MEET, PDPP[T]₂{TEG}-EDOT, PDPP[T]₂{TEG}-3-MEET. The synthesis and charge transport properties for the reference polymer without any EG substituent was reported by us earlier^[32], whereas all the other three are novel polymers. All the polymers have a thiophene [T]₂-flanked diketopyrrolopyrrole core in common, resulting in materials with hole-transport properties.^[33] The abbreviation {2-HD} denotes the alkyl substituent 2-hexyldecyl, and the abbreviation {TEG} represents triethylene glycol substituents on the DPP core. The comonomers 3,4-ethylenedioxythiophene (EDOT) and 3-[2-(2-methoxyethoxy)ethoxy]thiophene (3-MEET), carrying direct ethylene glycol substitution at the thiophen ring without a spacer were chosen in order to keep the oxidation potential of the final polymers as low as possible.^[19,33] Materials with a low oxidation potential are desirable in OECTs to achieve low threshold-voltages, which is essential for the application of biosensors in aqueous media to avoid electrochemical degradation of water or living cells. The polymers are designed to have an increasing amount of polar EG content from 0 wt.% in PDPP[T]₂{2-HD}-EDOT to 12.8 wt% in PDPP[T]₂{2-HD}-3-MEET, 40.3 wt % in PDPP[T]₂{TEG}-EDOT, and 52.3 wt.% in PDPP[T]₂{TEG}-3-MEET. Further, PDPP[T]₂{2-HD}-3-MEET carries the EG substituent only on the comonomer (3-MEET), whereas PDPP[T]₂{TEG}-3-MEET contains ethylene glycol chains both on the DPP-core, as well as on the co-monomer 3-MEET. This

should allow us a comprehensive and systematic study of the influence of ethylene glycol substituents – both, the content and the location – on mixed-ion-electron conduction and biocompatibility in PDPPs.

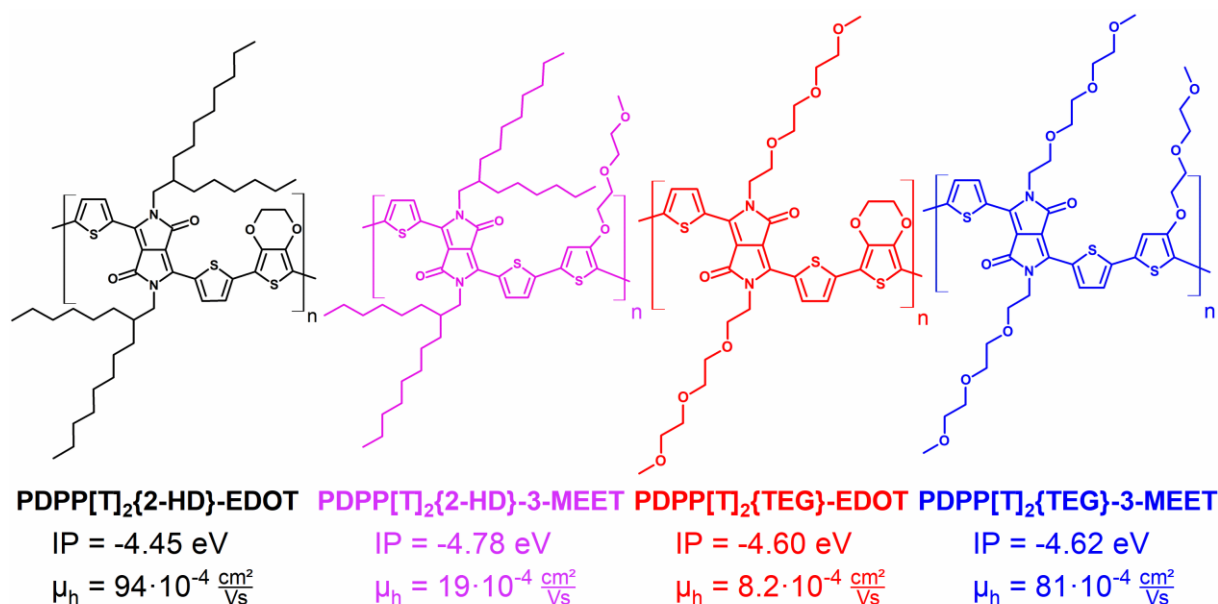


Figure 1 – Structures of the studied polymers. Ionization potentials (IP) taken from UPS measurements, hole-mobility (μ_h) values from OFET-measurements, extracted from the saturation regime. The EG content varies from zero to 12.8 to 40.3 and 52.3 wt% from left to right.

The DPP-core was synthesized following a published protocol^[34] and the synthetic route is shown in **Figure S1**. This DPP-core was substituted with either the alkyl-swallow tails or the TEG-chains by nucleophilic substitution with the respective alkyl- or TEG-bromide. The comonomers, EDOT^[32,35] as well as 3-MEET^[19,36] were synthesized after published procedures and stannylated (**Figure S2 and S3**). All polymerizations were conducted using conventional Stille Cross Coupling polycondensation conditions in chlorobenzene at 180 °C and full experimental details are given in the supporting information. Gel-permeation chromatography (GPC) showed number average molecular weights between 9 kg mol⁻¹ and 25 kg mol⁻¹, corresponding to a degree of polymerization of 15 – 28. It should be noted that PDPP[T]₂{TEG}-EDOT is insoluble in chloroform, thus 1,1,1,3,3,3-hexafluoro isopropanol was used as eluent vs. poly(methyl methacrylate) calibration, the other polymers were measured using chloroform as eluent vs. polystyrene calibration, explaining the different molecular weight value.

First, fundamental material characterization on thin films in the solid state under dry conditions was carried out, and the results are summarized in Table 1. The thermal stability was measured using thermogravimetric analysis (**Figure S4**). All polymers exhibit excellent thermal stabilities beyond 300 °C. The polymers carrying branched alkyl-side chains on the DPP-core decompose at slightly higher temperatures (402 and 371 °C for PDPP[T]₂{2-HD}-EDOT and PDPP[T]₂{2-HD}-3-MEET, respectively) than the ones bearing TEG-chains at the DPP-core (328 and 337 °C for PDPP[T]₂{TEG}-EDOT and PDPP[T]₂{TEG}-3-MEET, respectively) (Table 1). Since conventional DSC measurements did not reveal any phase transitions, the polymers

were studied via flash differential scanning calorimetry (Flash-DSC) at scan rates between 50 Ks⁻¹ – 1000 Ks⁻¹ (**Figure S5**). Only for the two polymers bearing branched alkyl side-chains on the DPP core, melting was observed at 348 °C (for PDPP[T]₂{2-HD}-EDOT) and at 248 °C (for PDPP[T]₂{2-HD}-3-MEET), showing that the substitution of EDOT with 3-MEET decreases the melting-temperature by 100 °C. The polymers carrying TEG-chains at the DPP-core did not show thermal transitions in the temperature range between 30 °C and 450 °C.

Table 1. Polymer data overview

Polymer	Molecular weight [kg mol ⁻¹] ^{a)}	Thermal stability [°C] ^{c)}	T _m [°C] ^{d)}	T _c [°C] ^{d)}	μ _h [cm ² V ⁻¹ s ⁻¹] ^{e)}	I _{ON/OFF} ^{e)}	IP ^{f)} [eV]	Oxidation potential [V] ^{g)}
PDPP[T] ₂ {2-HD}-EDOT	46	402	348	311	9.4 · 10 ⁻³	1.5 · 10 ⁵	-4.45	0.78
PDPP[T] ₂ {2-HD}-3-MEET	18	371	248	227	1.9 · 10 ⁻³	4.5 · 10 ²	-4.78	0.61
PDPP[T] ₂ {TEG}-EDOT	9 ^{b)}	328	n.d.	n.d.	8.2 · 10 ⁻⁴	3.4 · 10 ²	-4.60	0.24
PDPP[T] ₂ {TEG}-3-MEET	22	337	n.d.	n.d.	8.1 · 10 ⁻³	2.1 · 10 ³	-4.62	0.27

^{a)} Number average molecular weight determined by GPC using chloroform vs. PS-calibration; ^{b)} measured with 1,1,1,3,3,3-hexafluoro isopropanol as eluent vs. PMMA-calibration; ^{c)} Thermogravimetry, 5% wt. loss, heating rate 10 Kmin⁻¹; ^{d)} Determined by flash differential scanning calorimetry at 400 K/s; ^{e)} OFET mobility, extracted from the saturation regime of annealed films; ^{f)} Determined via ultraviolet photoelectron spectroscopy; ^{g)} Determined by differential pulse polarography in thin films on platinum coated ITO glass in acetonitrile with 1 M tetrabutylammonium hexafluoro phosphate as supporting electrolyte.

Hole-mobilities were determined from OFET-measurements using bottom-gate bottom-contact geometry with channel lengths between 5 μm and 20 μm. **Figure S6** shows the output- and transfer characteristics of the four polymers. All polymers exhibited good hole-transport characteristics with hole mobilities ranging from 0.0008 to 0.009 cm²V⁻¹s⁻¹. The highest hole mobilities were measured for PDPP[T]₂{2-HD}-EDOT (0.009 cm²V⁻¹s⁻¹) and PDPP[T]₂{TEG}-3-MEET (0.008 cm²V⁻¹s⁻¹), whereas the other two polymers exhibited hole mobilities of 0.002 cm²V⁻¹s⁻¹ (PDPP[T]₂{2-HD}-3-MEET) and 0.0008 cm²V⁻¹s⁻¹ (PDPP[T]₂{TEG}-EDOT). We did not observe any considerable dependencies of the charge carrier mobilities on the substitution pattern. However, on comparing the two polymers carrying TEG on the DPP core, PDPP[T]₂{TEG}-EDOT and PDPP[T]₂{TEG}-3-MEET, containing 40 and 52 wt.% EG, respectively, the hole mobility of the latter is one order of magnitude larger than in the former. As explained in the OECT section later, we like to note here that the interdependence of morphology, swelling and charge transport in electrolyte medium determines the OECT performance. But this can be very complex and differ from that in the dry state.

The ionization potential (IP) values of PDPP[T]₂{2-HD}-EDOT, PDPP[T]₂{TEG}-EDOT, PDPP[T]₂{2-HD}-3-MEET, PDPP[T]₂{TEG}-3-MEET polymers determined from ultraviolet photoelectron spectroscopy (UPS) measurements are -4.45, -4.60, -4.78 and -4.62 eV,

respectively, and the spectra are depicted in **Figure S7**. This indicates that the comonomers EDOT and 3-MEET have similar influences on alternating donor-acceptor polymers in determining their oxidizability. And in dry solid state, we could not infer any dependence of the nature of the side chain on the ionization potential. Additionally, differential pulse polarography measurements (**Figure S8**) of thin films in acetonitrile were conducted to estimate any influence of the side chains on the oxidation potential in a polar liquid environment. The values are given in Table 1. Obviously, in these measurements an influence of the hydrophilic character of the side chains has been observed. In general, the oxidation potentials decrease with increasing ethylene glycol content. This is in agreement with the general observation that a substitution of branching alkyl chain with linear TEG group on DPP core reduces the torsion angle between the donor and acceptor units and improve interchain π - π interactions, which in consequence, reduce the IP value.^[37-39] Thus, it is to be noted, that the UPS values differ from differential pulse polarography data due to differences in the stabilization of radical cations formed during the oxidation in the measurement environment.

The material characterization in solid state using UPS and OFET indicate that these polymers have sufficient hole transport mobilities and low ionization potentials, which make them interesting for further tests in aqueous media to evaluate their suitability for application in OECTs. From here onwards, all further measurements were carried out in aqueous electrolyte media, if not stated differently, since this is the required environment for OECT applications.

2.2. Spectroelectrochemical Absorption Measurements

After the basic characterization in the dry state, we went on to study properties in the swollen state with and without applied doping potentials, which are more relevant for the function of OECTs. To begin with, the oxidation behavior in aqueous medium was studied using spectroelectrochemical absorption measurements (SEC). In this technique, the polymer film is stepwise biased (100 mV steps) and the concomitant changes in the vis-NIR absorption spectrum are monitored. Thereby, the electrochemical doping can be observed by the appearance of polaron-absorption features with the simultaneous decrease of the ground state absorption. The measured SEC curves are shown in **Figure S9** and the difference plots in **Figure 2** (a-d) obtained by subtracting the absorption spectrum of the pristine sample (at 0 V) from those of the electrochemically doped ones. All four polymers could be oxidized at low potentials (300 – 400 mV) and a distinct arisal of polaron absorptions along with a concomitant ground state bleaching (GSB) could be observed with increased doping potential. It is clearly observable that the polymers PDPP[T]₂{2-HD}-EDOT and PDPP[T]₂{2-HD}-3-MEET show a distinctively different oxidation behavior compared to the polymers PDPP[T]₂{TEG}-EDOT and PDPP[T]₂{TEG}-3-MEET.

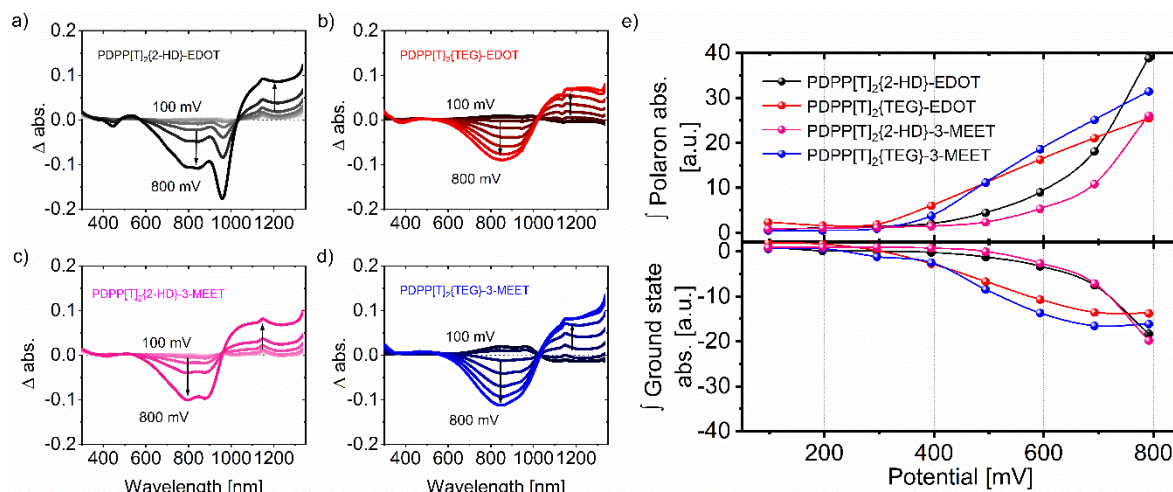


Figure 2 – Spectroelectrochemical Vis/NIR absorption measurements. Difference absorption spectra of a) PDPP[T]₂{2-HD}-EDOT, b) PDPP[T]₂{TEG}-EDOT, c) PDPP[T]₂{2-HD}-3-MEET, d) PDPP[T]₂{TEG}-3-MEET, e) integrals of the polaron absorption (top) and of the ground state bleaching (bottom) with increasing doping potential.

For instance, the intensity of both, the polaron absorption (1040 – 1300 nm) and the GSB (500 – 1040 nm), is more pronounced for the TEG-substituted PDPPs for the whole range of doping potentials of 300 – 700 mV, than with the alkyl substituted ones. This shows that the polymers bearing triethylene glycol chains at the DPP-core are more easily oxidized in aqueous environment, than the two polymers carrying hydrophobic alkyl moieties at a given potential. A quantitative way to assess the changes comparatively is shown in Figure 2 e), where the integral of the polaron absorption (1040 – 1300 nm) and the pristine absorption peak (550 – 1040 nm) corresponding to GSB are plotted versus the applied voltage. The TEG-substituted polymers exhibit a higher onset potential (400 mV), than the two with alkyl-substituents (300 mV) for the polaron formation. When comparing the slopes of the polaron- or GSB plot in the linear range of 300 – 600 mV, it is obvious that the polymers carrying TEG substituents in DPP core exhibit a higher slope than the other two indicating more pronounced and faster oxidation.

Thus, the SEC measurements show that the two polymers carrying TEG chains at the DPP core, are more easily oxidized in water. Regarding the onset of oxidation, it appears to be irrelevant whether the co-monomer is EDOT or 3-MEET, which is in accordance with the ionization potential values discussed above (Table 1). The difference in polaron formation observed in SEC measurements in polar solvents can be correlated with oxidation potentials obtained from differential pulse polarography measurements (also in polar solvents) and not with the ionization potentials obtained from UPS measurements in the solid state.

This is the case, because in UPS measurements the intrinsic properties of the material in the dry solid state are probed. However, in spectroelectrochemical absorption spectroscopy and differential pulse polarography the situation is different: the polymer film is submerged in an aqueous electrolyte (SEC) or polar organic electrolyte (differential pulse polarography). The

polarons are stabilized by solvated counterions which must penetrate through the film in order to compensate for the charges. This diffusion is controlled by the hydrophilic character as well as the swellability of the polymer. Where charges can easily be compensated by counterions from the electrolyte, the polarons are stabilized and the process is less hindered, resulting in an easier oxidation. Similar observations have been reported for other p-type TEG-substituted conjugated polymers.^[40] The drastic differences seen in the SEC measurements indicate further, that the amount of polaronic species also depends on the percentage of ethylene glycol per repeating unit within the polymer, and not only on the position of the oxidation potential. This is shown by correlating the polaron content in the SEC measurements with the ethylene glycol content in the various polymers (**Figure 3 b**). The formation of polaronic species scales linearly with the weight fraction of ethylene glycol per repeating unit.

2.3 Capacitance and Swelling

Since both, the water absorption as well as the ion injection are controlled by the ethylene glycol moieties in these polymers, we first proceeded to measure the volumetric capacitances C^* using electrochemical impedance spectroscopy (EIS). The spectra are shown in **Figure S10** and a detailed description of the calculation of C^* is discussed in the corresponding section of the supporting information. Figure 3 a) shows the extracted volumetric capacitances of the four polymers up to a potential of 0.8 V. In the most hydrophobic polymer PDPP[T]₂{2-HD}-EDOT (0 wt.% ethylene glycol), virtually no increase of the capacitance can be observed upon biasing the material. But already in PDPP[T]₂{2-HD}-3-MEET which carries one ethylene-glycol chain per repeating unit (12 wt.% EG), the capacitance is slightly increased from 0.2 to 8 Fcm⁻³ at 0.8 V. Both of the polymers bearing two- and three ethylene glycol side chains per repeating unit (PDPP[T]₂{TEG}-EDOT (40 wt.% EG) and PDPP[T]₂{TEG}-3-MEET (52 wt.% EG)), however, show a tremendous increase of the volumetric capacitance reaching values of 167 Fcm⁻³ and 338 Fcm⁻³ at an oxidation potential of 0.8 V, respectively. To illustrate this trend, the volumetric capacitances of the polymers are displayed with their corresponding amounts of ethylene glycol in Figure 3 b). We find an empirical relationship, where the capacitance of the polymers scales with the degree of ethylene glycol substitution following a power law. In this context, it is interesting to mention that Giovannitti et al. studied the influence of an increasing ethylene glycol content in an n-type polymer, poly(naphthalene-1,4,5,8-tetracarboxylic-diimide-bithiophene) on the volumetric capacitance and charge carrier mobility and could show that a minimum EG content of 50 % was necessary for OECT operation.^[41]

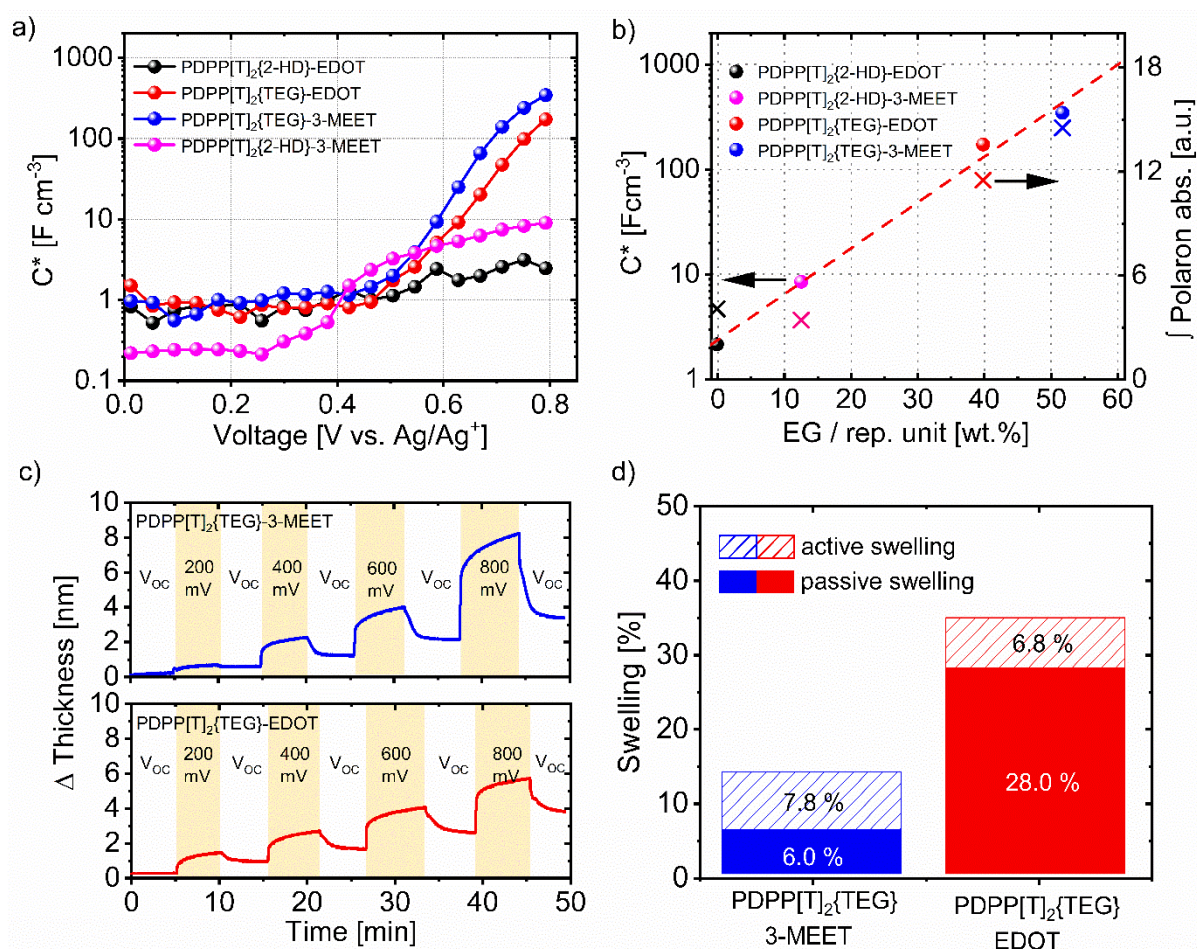


Figure 3 – a) Voltage dependent volumetric capacitance (C^*) measurement extracted from EIS, b) correlation of the max. attained capacitance at 0.8 V with the ethylene glycol content within the polymer and the corresponding integral of the polaron absorption at 500 mV. c) Thickness variation as a function of the different applied potentials in E-QCMD measurement of PDPP[T]₂{TEG}-3-MEET (blue) and PDPP[T]₂-EDOT (red). Sequentially, an increasing doping potential is applied followed by the open circuit potential. d) comparison of the passive-, active and total swelling after applying 0.8 V.

To understand the interdependence of swelling and capacitance, we measured the passive (**Figure S11**) and the active (**Figure 3 c-d**, **Figure S12**) swelling-behavior of the polymers using electrochemical quartz crystal microbalance with dissipation monitoring (E-QCMD) analysis. In this measurement, the polymer is deposited onto a metallized quartz crystal resonator, which is excited to its eigenfrequency. This frequency depends on the mass deposited on the crystal. Upon water-uptake and ion migration after exposure to an aqueous electrolyte, the polymer gains weight, leading to a reduced oscillation frequency and from this dissipation, the mass uptake can be derived by QCMD (passive swelling). If the polymer is additionally biased with a doping potential, the mass exchange between an electrically active film and an electrolyte can be monitored, as the film undergoes electrochemical (de-)doping (E-QCMD, active swelling). The (E)-QCMD experiments were carried out on 60 - 100 nm thick polymer films with 0.1 M aq. NaCl solution as the electrolyte, further experimental details are given in the supporting information. In the passive swelling experiments, the two polymers carrying

hydrophobic alkyl substituents on the DPP-core (PDPP[T]₂{2-HD}-EDOT and PDPP[T]₂{2-HD}-3-MEET) showed a negligible swelling of 0 and 3 %. However, for the both polymers bearing TEG-side chains at the DPP core (PDPP[T]₂{TEG}-3-MEET and PDPP[T]₂{TEG}-EDOT) a degree of passive swelling of 6 and 28 %, respectively, was measured (Figure S11-S12). To study the influence of the degree of oxidation on the swelling, pulsed E-QCMD studies were conducted on the both polymers, which have shown passive swelling. After equilibration of the films in the electrolyte, different doping potentials were applied for 5 minutes each and the concomitant changes in the film thicknesses were monitored. After each doping step, the system was relaxed to the open circuit potential for five minutes, followed by the next potential step. The corresponding plots are shown in Figure 3 c) where the degree of swelling follows the applied doping potential. At low doping potentials (200 mV), the increase in film thickness lies in the range of 1 nm for both polymers, which is in line with the results from the spectroelectrochemical absorption measurements (Figure 2), where no oxidation could be detected below 200 mV doping potential. When increasing the applied potential beyond 400 mV, the polymer containing 52 wt.% ethylene glycol swells distinctively stronger than the polymer with 40 wt.% ethylene glycol, as to be expected from the higher volumetric capacitance and the SEC-measurements. It is further apparent that after removing the doping potential, the films are not returning to their initial thicknesses. This originates from water, introduced via the hydration shell of attracted ions which remains incorporated in the film without continuous biasing. At the highest doping potential of 800 mV, PDPP[T]₂{TEG}-3-MEET and PDPP[T]₂{TEG}-EDOT showed an active swelling of 8.2 nm (7.8 %) and 5.6 nm (6.8 %), respectively. The total swelling consisting of the sum of passive and the active swelling is illustrated for both the two polymers in Figure 3 d), amounting to 14 and 35%, respectively. Beyond the observation that an EG content of up to 13 wt.% is not sufficient to enable passive swelling at all, there is no clear correlation between the passive water uptake and the EG content. The passive swelling behavior depends on a variety of factors such as the crystallinity and morphology and developing a profound understanding of these interdependencies requires further intensive work. More importantly, however, the active swelling behavior which is pivotal for the intended application in OECT devices, increases with the EG content, explaining the improved volumetric capacitance from PDPP[T]₂{TEG}-EDOT to PDPP[T]₂{TEG}-3-MEET as discussed above. Thus, the polymer PDPP[T]₂{TEG}-3-MEET containing 52 wt.% of EG shows the highest active swelling of 7.8 % and the highest volumetric capacitance of 338 Fcm⁻³ at an oxidation potential of 0.8 V.

2.4 Organic Electrochemical Transistors

Since SEC-measurements have shown that the polymers can be oxidized in aqueous electrolyte at very low voltages (< 400 mV), E-QCMD measurements confirm the swellability of the two most hydrophilic polymers, and their charge storage ability changes substantially under applied potential, we systematically studied the performance in thin-film OECTs. The systematic variation of ethylene glycol content may allow a structure-property correlation of mixed ion conduction properties using the OECT-data. For this, OECTs were fabricated, using a parylene lift off method and interdigitated electrodes with varying channel-widths between $5\ \mu\text{m}$ and $15\ \mu\text{m}$ and W/L ratios varying from $5 \cdot 10^{-4}$ to $1.5 \cdot 10^{-3}$. Compared to planar devices, the used interdigitated devices augment the measured drain current and transconductance, making the OECT more sensitive for small gate voltage changes. **Figure 4** shows the OECT characteristics and a schematic of measurement setup along with the image of an interdigitated microelectrodes. The film thicknesses were between $48\ \text{nm}$ and $65\ \text{nm}$ and further details regarding the device fabrication are given in the supporting information.

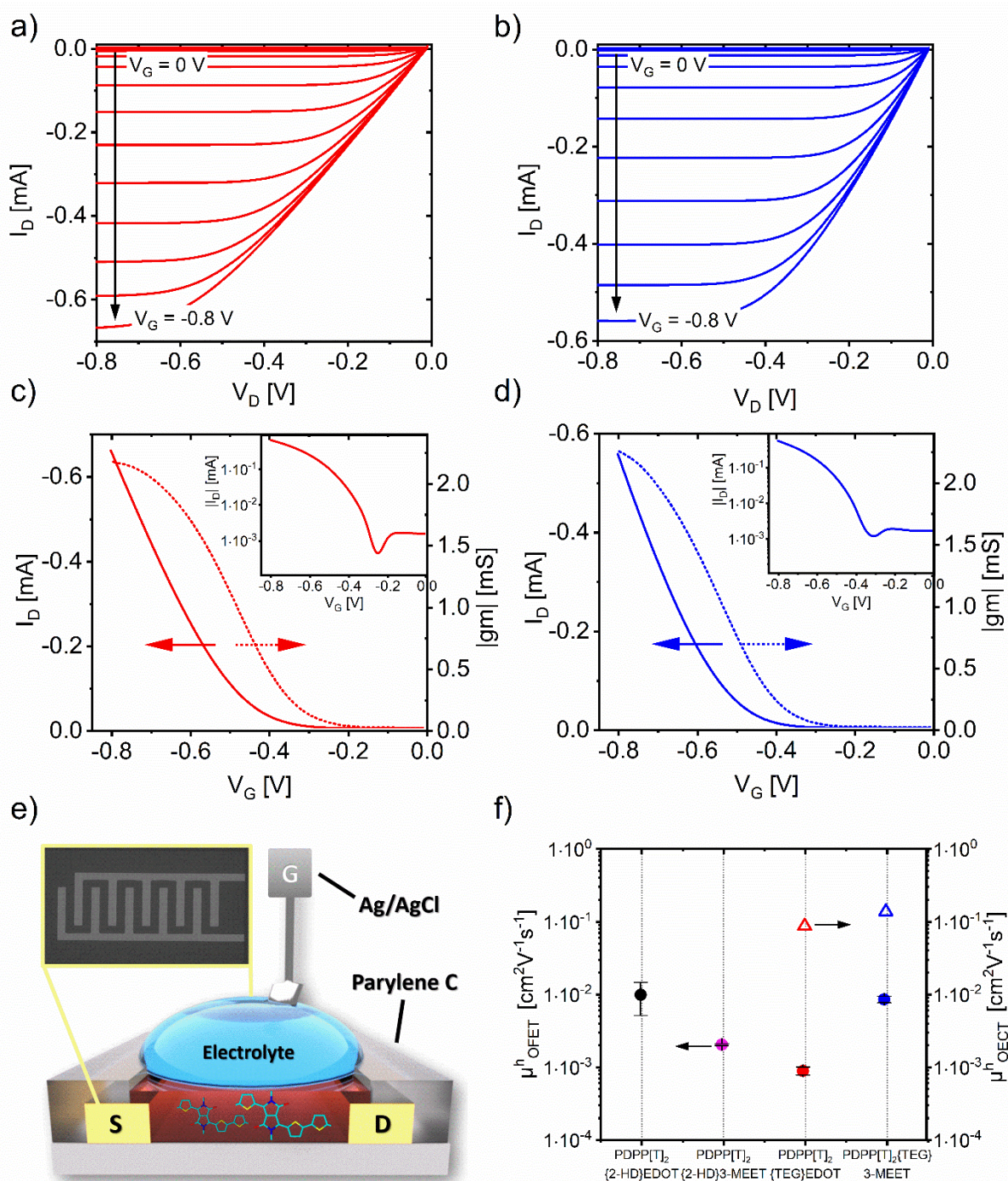


Figure 4 – OECT-plots of the measurement using 0.1 M NaCl as electrolyte. Output curves of a) PDPP[T]₂{TEG}-EDOT and b) PDPP[T]₂{TEG}-3-MEET. Transfer curves with the corresponding transconductance progressions and inset showing the ON/OFF ratio for c) PDPP[T]₂{TEG}-EDOT and d) PDPP[T]₂{TEG}-3-MEET. e) OECT setup, with a schematic device structure and micrograph of an interdigitated electrode. f) comparison of the OECT- and OFET mobilities of the various polymers.

Table 2. OECT parameters of the polymers using 0.1 M NaCl_{aq.} solution as the electrolyte.

Polymer	V_{Th} [V] ^{a)}	g_m [mS] ^{a)}	d [nm] ^{b)}	C^* [Fcm ⁻³] ^{c)}	wt.% Ethylene glycol per rep. unit	μC^* [Fcm ⁻¹ V ⁻¹ s ⁻¹]	μ_{OECT} [cm ² V ⁻¹ s ⁻¹] ^{d)}
PDPP[T] ₂ {2-HD}-EDOT	-	-	38	2	0 wt.%	-	-
PDPP[T] ₂ {2-HD}-3-MEET	-	-	41	8	12.8 wt.%	-	-
PDPP[T] ₂ {TEG}-EDOT	-0.38	1.4	40	167	40.3 wt.%	14	0.084
PDPP[T] ₂ {TEG}-3-MEET	-0.36	1.9	56	338	52.3 wt.%	45	0.133

^{a)} From OECT-measurements; ^{b)} measured with profilometer; ^{c)} from EIS measurements at -0.8 V; ^{d)} calculated from the figure of merit (μC^*) and volumetric capacitance C^* ; ^{e)} as determined from QCMD measurements using 0.1 M NaCl solution.

2.4.1. Operation with Aqueous Sodium Chloride Electrolyte

In a first set of experiments, we employed a 0.1 m NaCl aqueous solution as the electrolyte. With the most hydrophobic polymer (PDPP[T]₂{2-HD}-EDOT) without any EG substituent and PDPP[T]₂{2-HD}-3-MEET with an ethylene glycol content of 13 wt.%, no OECT behavior was observed even up to a gate voltage of 1V. However, both the polymers PDPP[T]₂{TEG}-EDOT and PDPP[T]₂{TEG}-3-MEET with 40 wt.% and 52 wt.% ethylene glycol, respectively, exhibited well-defined output characteristics even at very low gate voltages of about -0.3 V with high I_{DS} currents reaching the range of 0.6 – 0.7 mA at a gate voltage of -0.8 V. In Figure 4 a)-d), output- and transfer characteristics of these polymers are shown. For the polymers, PDPP[T]₂{TEG}-EDOT, having 40 wt.% EG and PDPP[T]₂{TEG}-3-MEET with 52 wt.% EG content, the threshold-voltage of $V_{Th} = -0.32$ V and -0.37 V, respectively, were measured. In terms of the transconductance, the polymer with 52 wt.% EG content a higher value ($g_m = 1.9$ mS at $V_G = -0.8$ V) compared to the polymer with 40 wt.% EG content ($g_m = 1.4$ mS at $V_G = -0.8$ V) was reached. When normalized to the film-thickness, the transconductances amount to 394 and 340 Scm⁻¹ for PDPP[T]₂{TEG}-3-MEET and PDPP[T]₂{TEG}-EDOT, respectively. Even though the maximum drain-currents and threshold-voltages are similar, an increased amount of ethylene glycol leads to an improvement in transconductance by 50 Scm⁻¹. Because the increasing EG content manifested a higher volumetric capacitance as discussed above, we were interested in the impact of the EG content on ion transport within the polymer. We have therefore measured the transient response times of the OECTs by applying square-wave potentials to both, the gate and the source-drain electrodes and concomitantly measuring the temporal response in the drain current. In **Figure S16** the tim- dependent measurements are shown and it is found, that the ion transport in the polymer containing 52 wt.% EG is distinctively faster ($\tau_{90} = 6$ ms), than in the one containing 40 wt.% EG ($\tau_{90} = 11$ ms). The figure of merit (μC^*) extracted from fitting the linear regime of the linear plot of transconductance vs. the geometric parameter $WdL^{-1}(V_{Th}-V_G)$ (**Figure S13**). Both polymers exhibit very high

transconductance values; for the most polar polymer PDPP[T]₂{TEG}-3-MEET, a three times higher figure of merit of $\mu C^* = 45 \text{ F cm}^{-1} \text{ V}^{-1} \text{ s}^{-1}$ was obtained, compared to PDPP[T]₂{TEG}-EDOT ($14 \text{ F cm}^{-1} \text{ V}^{-1} \text{ s}^{-1}$). From the values of the volumetric capacitance measured by EIS at 0.8 V, 338 F cm^{-3} and 167 F cm^{-3} for PDPP[T]₂{TEG}-3-MEET and PDPP[T]₂{TEG}-EDOT, respectively, the OECT-mobility μ_{OECT} were calculated as $\mu_{\text{OECT}} = 0.084$ and $0.133 \text{ cm}^2 \text{ V}^{-1} \text{ s}^{-1}$, respectively. These values are similar to those of other PDPPs reported in aqueous media in the literature such as p(gPyDPP-MeOT2) ($\mu C^* = 57 \text{ F cm}^{-1} \text{ V}^{-1} \text{ s}^{-1}$), whereas p(gDPP-TT) ($\mu C^* = 125 \text{ F cm}^{-1} \text{ V}^{-1} \text{ s}^{-1}$) and p(gDPP-T2) ($\mu C^* = 342 \text{ F cm}^{-1} \text{ V}^{-1} \text{ s}^{-1}$) exhibit improved parameters due to the presence of other comonomers (TT and T2) which favor polaron delocalization and hence improved μ_{OECT} values.^[29]

Comparing the hole mobility in the dry state, as obtained by OFET-measurements with the OECT-mobility in the swollen state (Figure 4 f), allows for conclusions to be drawn about the influence of the swelling on the charge transport. The fact that the polymer PDPP[T]₂{TEG}-3-MEET with the highest ethylene-glycol content of 52 wt.% EG showed one order of magnitude higher OFET-hole mobilities ($0.008 \text{ cm}^2 \text{ V}^{-1} \text{ s}^{-1}$) as compared to PDPP[T]₂{TEG}-EDOT with 40 wt.% EG ($0.0008 \text{ cm}^2 \text{ V}^{-1} \text{ s}^{-1}$) in dry state and that the charge carrier mobility in the wet state, μ_{OECT} for the former (with higher active swelling of 7.8 %), lies very similar to the latter indicates that the charge transport can suffer upon very high swelling. In other terms, the higher degree of active swelling in the former does not facilitate an improved charge carrier mobility in OECT devices. This indicates the need for a control of swelling, if $\mu_{\text{OECT}} C^*$ product is to be improved further. This also suggests that an increased ethylene glycol content leads to both, an increased volumetric capacitance, as discussed earlier, along with a higher degree of swelling, which shows an extreme interdependency towards the charge transport in OECTs. This also makes it clear that an uncontrolled high degree of swelling is not required for the OECT performance.

2.4.2. Cycling Stability

Since long-term cycling stability is a crucial requirement for the successful repeated use of a material in devices, especially in everyday applications, we were curious to study the cyclability of our OECT materials. To do so, we subjected the OECT devices to 3 x 400 simulated measurement-cycles comprising of 30 minutes of continuous operation in each cycle under a particular gate voltage (three sets of cycles in the saturation regime corresponding to specific V_D and V_G were selected) and monitored the change in the device's output parameter, i.e. the drain current. The measurements were conducted consecutively and on the same device and therefore, the measurements at the highest gate voltage of $V_G = -0.7 \text{ V}$ reflect an overall cycling for a time span of 1.5 hours or 1200 cycles. Details regarding the exact procedure are given in the supporting information and the cycling-plots of are displayed in **Figure 5** below. Both polymers with 40 and 52 wt.% EG content show no deterioration of the drain current at long-term operation in the first 400 cycles under $V_G = -0.5 \text{ V}$, which is highly promising. On further cycling at higher gate potential ($V_G = -0.6 \text{ V}$), for the next 400 cycles, they retain 87 and

91 % of their initial drain currents. Even after another 400 cycles ($V_G = -0.7$ V), the 97 and 82 % drain current are maintained. We assume that these small differences on stability after prolonged cycling can be arising out of the differences in the comonomers of the polymers; 3-MEET compared to EDOT since this is the only difference between the two polymers. The fact that there is only a very small decrease in drain current even after 1200 cycles at high gate voltages speaks for polydiketopyrrolopyrrole systems for applications in biosensors.

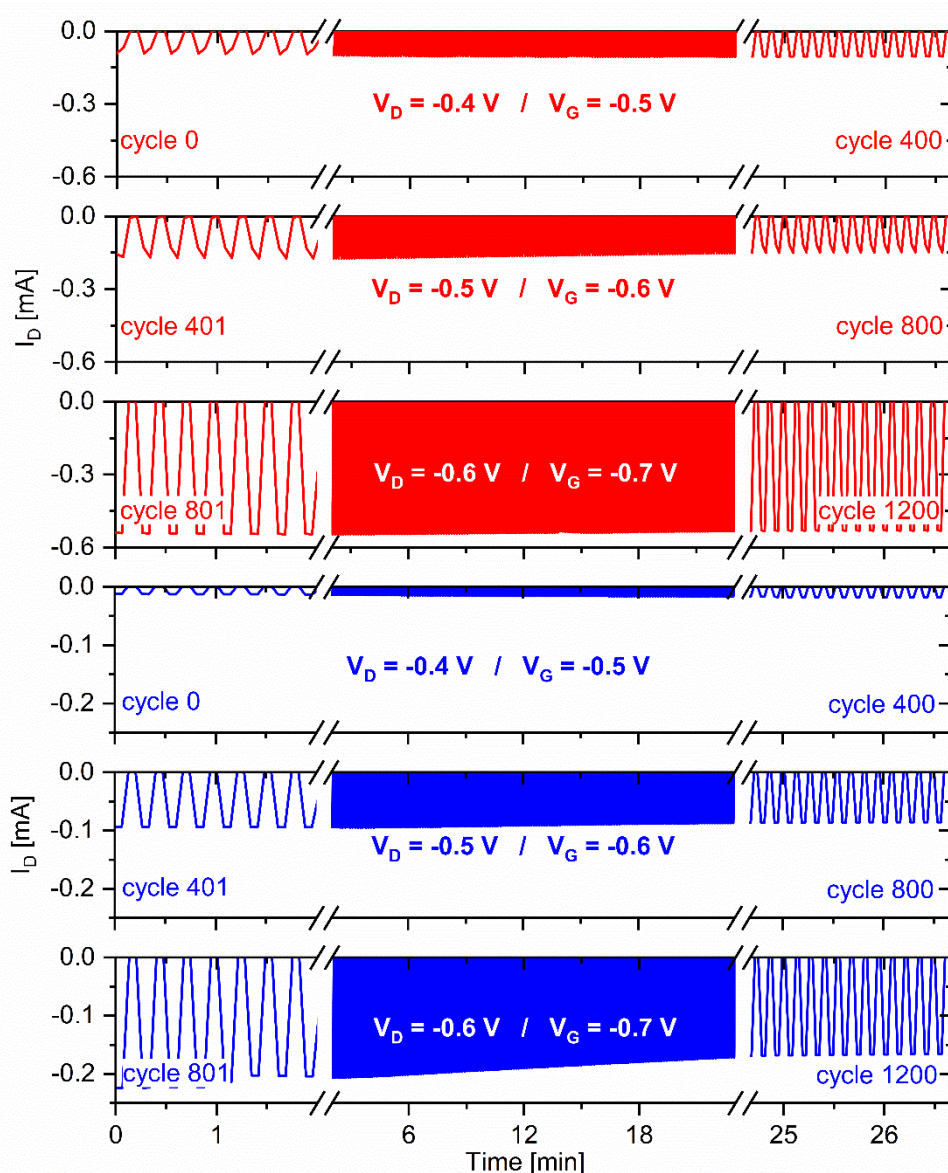


Figure 5 – Long-term cycling tests of the polymers PDPP[T]₂{TEG}-EDOT (red) and PDPP[T]₂{TEG}-3-MEET (blue) at different applied source-drain and gate voltages using aq. 0.1 M NaCl as the electrolyte. With a simulated cycle consisting of 2 s of applied gate and drain potential, followed by 2 s of bias free conditions, the same samples were subjected to 3 x 400 cycles with increasing potentials.

2.4.3. Operation in a Cell-Growth Medium

Up to here, we achieved an appreciable performance of the two polymers in OECT devices using sodium chloride solution as the electrolyte. We now wanted to extend our work into a more realistic regime of operation, and thus, tried to replace the NaCl electrolyte solution with

a commonly used cell culture medium. For this, we chose the standardized commercial DMEM as the electrolyte. DMEM contains different inorganic salts such as NaCl (6.4 gL^{-1}), NaHCO_3 (3.7 gL^{-1}) etc., amino acids, vitamins, D-glucose (4.5 gL^{-1}) as major ingredients. By using DMEM instead of $0.1 \text{ m NaCl}_{\text{aq}}$, the OECT-performance was evaluated for both the polymers, containing 40 and 52 wt.% of ethylene glycol. The output- and transfer characteristics are shown in **Figure 6 a)-b)** and **Figure S14**. Both the systems showed very low threshold-voltages in the range of -0.34 to -0.37 V , which is comparable to the values observed in sodium chloride solution. Similarly, the transconductance-values were also maintained in the range between 2.1 and 1.8 mS (or 326 to 368 Scm^{-1} , normalized to the film thickness). The excellent performance of these two polymers in a standardized cell-growth medium without any loss in transconductance and maintaining a very low threshold potential is highly promising towards real biosensing applications in in vitro and in vivo bioelectronics.

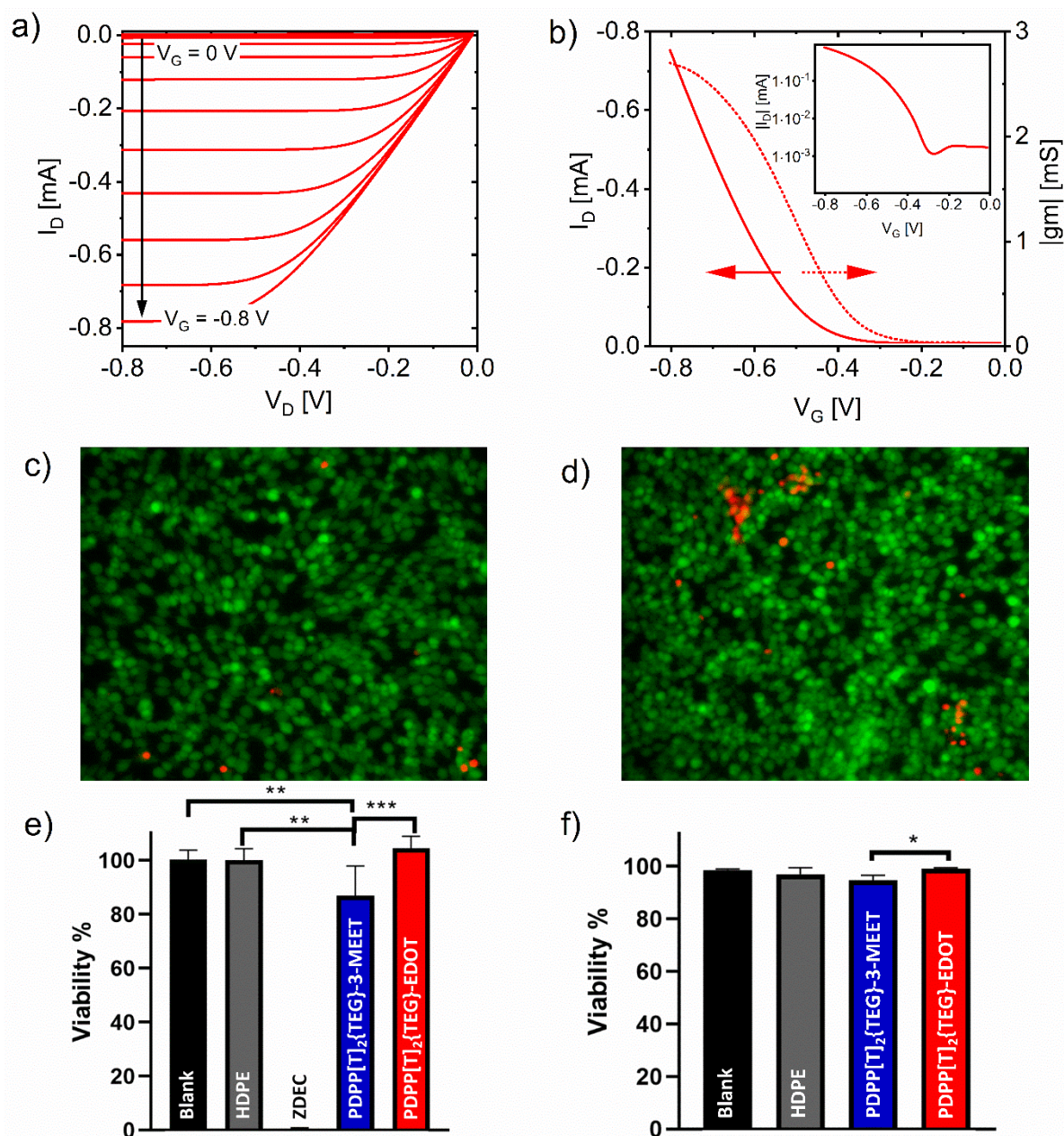


Figure 6 – a) OECT- output and b) transfer curves with the corresponding transconductance-progressions of PDPP[T]₂{TEG}-EDOT using DMEM as electrolyte. Qualitative and quantitative measurements of the cytotoxicity effect of the polymers on fibroblasts cells. c) - d) Fluorescent images of cells taken after live dead assay, where calcein AM (green) represents live cells, and ethidium homodimer (red) represents dead cells in contact with c) PDPP[T]₂{TEG}-EDOT and d) PDPP[T]₂{TEG}-3-MEET. e) - f) quantitative measurement of cell viability using e) CellTiter-Blue® Cell Viability Assay and f) live dead assay. Blank (cells with no contact to materials), HDPE (negative control), and ZDEC (positive control). Data are presented as the mean ± standard deviation; *** P value < 0.001, ** P value < 0.01 and * P value < 0.05.

2.4.4. In-vitro cytotoxicity tests

Next, we conducted in vitro cytotoxicity tests based on the ISO 10993-5:2009 standard. The indirect contact (agar test, **Figure S15**) and extract tests (**Figure 6 c) - f)** allow studying the interaction of any leachable byproducts or dissolved polymers with the cell monolayer without

direct contact of the material. We observed normal morphology of fibroblast cells after being incubated with polymeric films while they had agar layer as an interface (Figure S15). Their morphology was comparable with negative control (HDPE) and Blank (cells with no materials contact) while the positive control clearly showed changes in morphology from adherent and spread cells to the round shape cells. Cells exposed to a polyurethane film containing Zinc-diethyldithiocarbamate (ZDEC) as the positive control, clearly were less spread compared to cells in the negative and blank control and detachment of the cell monolayer could be observed. Live dead staining and fluorescent imaging, after extract test, also confirmed that the confluent cell monolayer was intact and the normal morphology of cells was preserved while cells in contact with positive control (ZDEC) did not survive and few dead cells were imaged (Figure 6 and S15). Quantitative analysis of CellTiter-Blue[®] assay (Figure 6 e) and live dead assay (Figure 6 f) confirmed high viability percentage of cells for both PDPP[T]₂{TEG}-EDOT and PDPP[T]₂{TEG}-3-MEET. Interestingly, despite the high viability of the cells in contact with both of them, after analyzing the live dead images, a significant difference was measured in viability of the cells in contact with PDPP[T]₂{TEG}-EDOT (99%) in comparison with PDPP[T]₂{TEG}-3-MEET (94%). This observation was also confirmed by CellTiter-Blue assay[®]. However, we can clearly observe that in none of the extract and agar test, after 24 h of culture, any cytotoxic response was detected: the morphology of fibroblasts was preserved and the observed high viability showed that the leaching products from the casted films are nontoxic. These studies encourage the application of these two polymers in bioelectronics.

3. Conclusion

In conclusion we have presented a systematic and comprehensive study of donor-acceptor polymers based on polydiketopyrrolopyrroles with increasing hydrophilicity for the application as mixed ion-electron conductors (MIEC). With an increasing content of ethylene glycol substitution, the MIEC properties improve drastically and, concomitantly, the performance in organic electrochemical transistors. Up to an ethylene glycol content of 13 wt.% no OECT-behavior is observable and beyond 40 wt.%, excellent OECT properties such as a very high volumetric capacitance in the range of 170 to 330 Fcm⁻³ and a μC^* product of 14 to 45 Fcm⁻¹V⁻¹s⁻¹ are obtained. These polymers do not require a crosslinking step or any other additives after the film-fabrication, to sustain prolonged immersion into water. Moreover, we could show a cyclability up to 1200 simulated measurement cycles. Finally, we have shown successful OECT operation under a cell-growth medium for the first time, demonstrating its potential for future in vitro and in vivo bioelectronics. This work is one of the few studies, where PDPPs were purposefully tailored, comprehensively studied from the dry to the wet and swollen state and successfully employed as materials for bioelectronic applications. Furthermore, the extract of the films after 24 h in contact with fibroblasts did not cause any toxicity and cells maintained their normal morphology as well as a high viability 94 – 99 %.

4. Experimental Section

Materials and Methods

Reactions sensitive toward humidity and oxygen were conducted under argon atmosphere in Schlenk apparatuses which were previously flame-dried under high-vacuum. Anhydrous solvents were purchased from Sigma Aldrich / Acros Organics in sealed bottles with molecular sieves. All other solvents, e.g. for workups or Soxhlet-extractions were freshly distilled in-house.

Dulbecco's Modified Eagles Medium (DMEM) was purchased from Sigma Aldrich. Reagents were used as received from commercial sources if not stated differently. Reactions under microwave-irradiation were carried out using a Biotage Initiator+ synthesis-microwave. NMR-spectra were recorded on a Bruker Avance spectrometer (300 MHz) at room temperature, using deuterated solvents, purchased from Deutero. The chemical shifts are reported relative to the residual solvent signal in the unit [ppm]. Mass spectra were recorded using a Finnigan MAT 8500 (Thermo Fischer Scientific) mass spectrometer (70 eV ionization energy) using the direct ionization probe (DIP-MS) method. Gas chromatography was conducted on an Agilent 7890 A GC-system with flame-ionization detection. UV/Vis spectra in the SEC measurements were recorded on a Jasco V-670 spectrophotometer in quartz cuvettes with an internal diameter of 10 mm and a Gamry Interface 1010T as the potentiostat. Thermogravimetric analysis was carried out using a Mettler Toledo TGA/SDTA 851, in a temperature range between 30 – 700 °C, with a heating rate of 10 Kmin⁻¹ under continuous nitrogen flow. Flash differential scanning calorimetry measurements were performed on a Mettler Toledo Flash DSC system, the temperature ranges and heating rates are given in the respective section below. Differential pulse polarography measurements were carried out using an electrochemical micro-cell kit from Ametek Scientific Instruments and a Gamry Interface 1010T as potentiostat.

OFET-Device Fabrication and Characterization

Substrates for organic field effect transistors with a bottom gate bottom contact (BGBC) geometry were purchased from Fraunhofer IPMS Dresden (OFET Gen. 4). Both, substrate and gate-electrode consisted of heavily n-doped silicon and 230 nm of thermally grown silicon oxide was the gate dielectric ($C = 1.501 \cdot 10^{-8} \text{ F}\cdot\text{cm}^{-2}$). Interdigitated electrodes were patterned from gold (30 nm) and used as source- and drain contacts, the channel-widths were varied between 5 μm and 20 μm . The substrates were thoroughly cleaned by sonication in isopropanol and acetone for 10 min each, followed by ozone plasma treatment (15 min / 50 °C). Subsequently, a self-assembled monolayer of hexamethyldisilazane (HMDS) was deposited by submerging the substrates in HMDS-vapor for 2 h. The substrates were thoroughly rinsed with isopropanol, dried in a nitrogen stream and the polymers were deposited by spin-coating from 5 mg mL⁻¹ solutions at 1000 – 5000 rpm under ambient conditions. Afterwards, the devices were transferred into a nitrogen-filled glovebox and the transistor characteristics were measured using the Agilent Technologies B1500A

Semiconductor Device Analyzer. The mobilities were extracted from the slope of the $I_D^{0.5}$ vs. V_G – plots in the saturation regime, using eq. 3 below.

$$I_D = \frac{W}{2L} \cdot \mu C \cdot (V_G - V_{Th})^2 \quad (\text{equation 3})$$

Where I_D : drain current, W : channel width, L : channel length, C : capacitance per unit area, μ : charge carrier mobility, V_G : gate-voltage and V_{Th} : threshold voltage. Annealing was conducted on a hot-plate under a nitrogen atmosphere, a minimum number of four devices were averaged per data point.

OECT-Device Fabrication and Characterization

Micro structured substrates for OECTs were developed together with, and purchased from Fraunhofer Institute for Electronic Nano Systems, Chemnitz, with an architecture consisting of a silicon oxide wafer, 10 nm chromium adhesion layer and 100 nm patterned gold electrodes and two parylene C layers with a thickness of 2 μm each. The channel-widths were varied between 5 μm and 15 μm . The polymer solutions were spin-coated with a concentration of 5 mg mL^{-1} at 1000 rpm, yielding film-thicknesses of around 50 nm. The film thicknesses were measured using a DEKTAK 150 stylus profilometer. The Ag/AgCl gate electrode was activated before the measurement by dipping into a diluted bleach solution (e.g. Domestos) for 15 min, followed by thorough rinsing with deionized water. A clean custom-made PDMS-holder was placed onto the substrate and its cavity was filled with the electrolyte solution, the gate electrode was placed in the electrolyte-droplet and the source- and drain electrodes were contacted. Transistor characteristics were measured using a Tektronix Keithley 2636B source meter and the Keithley KickStart Software. The transconductances g_m were obtained by numerical derivation of the drain current with respect to the gate voltage. The figure of merit (“ μC^* -product”) was extracted by plotting the maximum transconductance g_m vs. $WdL^{-1}(V_{Th} - V_g)$, and fitting the linear regime. According to eq. 1 below, the slope of the linear fit equals μC^* .

$$g_m = \frac{Wd}{L} \cdot \mu C^* \cdot (V_{Th} - V_G) \quad (\text{equation 1})$$

With g_m : transconductance, W : channel width, d : film thickness, L : channel length, μ : (OECT) charge carrier mobility, C^* : volumetric capacity, V_{Th} : threshold voltage, V_G : gate voltage. The threshold-voltage was determined by the x-axis intersect of the linear regime of the $|I_D|^{0.5}$ vs. V_G .

Electrochemical Quartz-Crystal Microbalance with Dissipation Monitoring

E-QCMD experiments were conducted on a QSense Explorer QCMD unit with an electrochemical cell (QE 401) using aq. 0.1 m NaCl solution as the electrolyte. For the measurement, first the gold sensors (QSX 338 Au, titanium adhesion layer) in air and in the electrolyte were measured. Thereafter, films of each polymer were prepared on the same previously measured quartz crystal sensor by spin coating from a 5 mg mL^{-1} solution from chloroform or 1,1,1,3,3,3-hexafluoroisopropanol solution in ambient conditions. The polymer-

deposited sensors were measured subsequently. The obtained data of the bare- and coated sensors in air and electrolyte were compared using the data stitching tool of the QSoft software package to exclude the influence of the density of the different media (air and electrolyte). By combining the data sets of the bare and the coated QCM-sensors, the shift in frequency and dissipation can directly be attributed to the shift caused by the polymer. For the E-QCMD experiments a Zahner Zennium potentiostat comprising a three-electrode setup with Ag/AgCl reference and platinum counter electrode was used and the polymer-coated sensor served as working electrode. For the stepped E-QCMD experiments, voltage pulses of 200 mV magnitude were applied to the working electrode from 0 to 800 mV for 5 minutes each, followed by 5 minutes of open circuit potential. In order to obtain the swelling from the frequency shifts, the Sauerbrey model using the 7th overtone of the oscillation could be applied, as the dissipation changes were negligible upon swelling.

Ultraviolet Photoelectron Spectroscopy

UPS measurements were carried out on a PHI 5000 VersaProbe III system fitted with a He discharge light source providing stable and continuous He I and He II lines, under ultrahigh vacuum (ca. 10^{-10} mbar). Polymer samples for UPS measurements were spin cast on clean ITO (15 ohm sq.^{-1}) substrates using dry chlorobenzene solutions (5 mg mL^{-1}) in a N_2 filled glovebox. The thickness of the spun films is ca. 30 nm, measured by using a dummy sample in a profilometer. The samples were directly transported to the UPS instrument by using a N_2 filled, sealed stainless steel transport vessel without exposing them to the ambient conditions.

Electrochemical Impedance Spectroscopy

EIS-measurements were carried out using a Metrohm Germany PGSTAT 204 analyzer module and a NOVA 2.1 software package for analysis. For the measurement, a butylene rubber gasket with a circular aperture of 1 cm diameter was placed on top of the OECT substrates and mechanically pressed onto the substrate with an UHMWPE microcell of 2 mL capacity. The cavity was filled with 1.5 mL aqueous 0.1 M NaCl solution and allowed to settle for 5 min. The underlying planar electrode was used as the working electrode and sense line of the potentiostat. An aqueous Ag/AgCl reference electrode and platinum wire counter electrode were dipped into the electrolyte solution, completing the three-electrode setup. See figure S10 for the sketch of the set up. Up to 0.8 V vs. Ag/AgCl_{aq.} the impedance was recorded in a frequency range of 1 kHz to 100 kHz in 30 discrete potential steps with an equilibration time of 5 s between each step. The system was excited with 1 mV_{RMS} and measured with a resolution of 10 frequency steps per decade. Parameters for fitting and extraction of the capacitance values are given in the supporting information.

Cell culture studies

M-MSV-BALB/3T3 fibroblasts (ECACC: 90030802) suggested by ISO Standard 10993-5 was used as cell line and obtained from Public Health England (UK). Cells were cultured per the manufacturer's specifications in Dulbecco's Modified Eagle's Medium - high glucose (DMEM)

supplemented with Fetal Bovine Serum Gold Plus (FBS, Serena USA), GlutaMAX, HEPES buffer and Gentamycin all from Sigma-Aldrich (USA). Trypsin/EDTA (0.05%), Trypan- Blue reagent 0.4%, and Dulbecco's Phosphate Buffered Saline (DPBS) were used all from Sigma-Aldrich (USA). Agarose NEEO ultra quality was purchased from Roth.

Cytotoxicity Assays

Cells were plated and grown to sub-confluency prior to initiating the assays. Cells cultured under normal conditions and without any contact with materials were used as a blank control (Blank). For all assays, high density polyethylene film (HDPE, Hatano Research Institute) was used as a negative, or noncytotoxic, control and ZDEC polyurethane (ZDEC, Hatano Research Institute) was used as a positive or cytotoxic control. Following ISO standard 10993-5, two different culturing methods were implemented to evaluate whether there is a cytotoxic response to polymers in terms of indirect contact (agar test), and extract tests. For the indirect contact test (agar test), after sub-confluency of cells, a layer of sterilized agarose gel (0.5 % in DMEM) containing all complete medium ingredient was casted on the top of cell monolayer and after one hour of gelation, the sterilized polymeric films were laid down on the gel facing the cells. The materials and cells were incubated at 37 °C and 5% CO₂ for 24 h after which the morphology of the cells was monitored using optical microscopy. For the extract test, similarly, cells were plated and grown to sub-confluency prior to initiating the assay. The materials (PDPP[T]2{TEG}-EDOT and PDPP[T]2[TEG]-3-MEET) as well as positive and negative controls were incubated at 37 °C and 5% CO₂ with the 500µl culture media for 24 h. After 24 h, the cell culture media was removed and replaced with the 500 µl of extract media. Cells were then incubated at 37 °C and 5% CO₂ for 24 h prior to cytotoxic evaluation. For extract test, cytotoxicity of the material was evaluated qualitatively using fluorescence microscopy and quantitatively through the CellTiter-Blue® Cell Viability Assay (Promega) and live dead assay (Thermo Fisher Scientific Inc). The detail of these assays is presented in supplementary information.

Statistics

The data were expressed as the mean ± standard deviation (SD) (3 replicates were conducted). One-way analysis of variance (ANOVA) were performed to analyze the differences between 2 and more than 2 experimental groups, respectively. A value of $p < 0.05$ was considered statistically significant.

References:

- [1] N. Thejo Kalyani, S.J. Dhoble, *Renewable and Sustainable Energy Reviews*, **16**, **2012**, 2696.
- [2] Tianyu Huang, Wei Jiang, Lian Duan, *J. Mater. Chem. C*, **2018**, **6**, 557.
- [3] Changyeon Lee, Seungjin Lee, Geon-U Kim, Wonho Lee, Bumjoon J. Kim, *Chem. Rev.* **2019**, **119**, 8028.
- [4] Mario Leclerc, Mathieu Mainville, *ACS Energy Lett.* **2020**, **5**, 1186.
- [5] Hang Yin, Cenqi Yan, Hanlin Hu, Johnny Ka Wai Ho, Xiaowei Zhan, Gang Li, Shu Kong So, *Materials Science & Engineering R*, **140**, **2020**, 100542.
- [6] Alexandra F. Paterson, Saumya Singh, Kealan J. Fallon, Thomas Hodsden, Yang Han, Bob C. Schroeder, Hugo Bronstein, Martin Heeney, Iain McCulloch, Thomas D. Anthopoulos, *Adv. Mater.* **2018**, **30**, 1801079.
- [7] Ioannis Petsagkourakis, Klas Tybrandt, Xavier Crispin, Isao Ohkubo, Norifusa Satoh, Takao Mori, *Sci. Technol. Adv. Mater.* **2018**, **19** (1), 836.
- [8] Mahima Goel, C. David Heinrich, Gert Krauss, Mukundan Thelakkat, *Macromol. Rapid Commun.* **2019**, **40**, 1800915.
- [9] Renee Kroon, Desalegn Alemu Mengistie, David Kiefer, Jonna Hynynen, Jason D. Ryan, Liyang Yu and Christian Müller, *Chem. Soc. Rev.*, **2016**, **45**, 6147.
- [10] Qian Zhang, Yimeng Sun, Wei Xu, Daoben Zhu, *Adv. Mater.* **2014**, **26**, 6829.
- [11] Jonathan Rivnay, Sahika Inal, Alberto Salleo, Róisín M. Owens, Magnus Berggren, George G. Malliaras, *Nat. Rev. Mater.* **2018**, **3**, 17086.
- [12] Sahika Inal, George G. Malliaras, Jonathan Rivnay, *Nat. Commun.* **2017**, **8**, 1767.
- [13] Sahika Inal, Jonathan Rivnay, Anna I. Hofmann, Ilke Uguz, Muhammad Mumtaz, Dimitrios Katsigiannopoulos, Cyril Brochon, Eric Cloutet, Georges Hadziioannou, George G. Malliaras, *J. Polym. Sci., Part B: Polym. Phys.* **2016**, **54**, 147.
- [14] Anna Hakansson, Shaobo Han, Suhao Wang, Jun Lu, Slawomir Braun, Mats Fahlman, Magnus Berggren, Xavier Crispin, Simone Fabiano, *J. Polym. Sci. Part B Polym. Phys.* **2017**, **55** (10), 814.
- [15] Daniele Mantione, Isabel del Agua, Wandert Schaafsma, Mohammed ElMahmoudy, Ilke Uguz, Ana Sanchez-Sanchez, Haritz Sardon, Begoña Castro, George G. Malliaras, David Mecerreyes, *ACS Appl. Mater. Interfaces* **2017**, **9**, 18254.
- [16] Sahika Inal, Jonathan Rivnay, Pierre Leleux, Marc Ferro, Marc Ramuz, Johannes C. Brendel, Martina M. Schmidt, Mukundan Thelakkat, George G. Malliaras, *Adv. Mater.* **2014**, **26**, 7450.
- [17] Philip Schmode, David Ohayon, Paul M. Reichstein, Achilleas Savva, Sahika Inal, Mukundan Thelakkat *Chem. Mater.* **2019**, **31**, 5286.
- [18] Alexander Giovannitti, Dan-Tiberiu Sbircea, Sahika Inal, Christian B. Nielsen, Enrico Bandiello, David A. Hanifi, Michele Sessolo, George G. Malliaras, Iain McCulloch, Jonathan Rivnay; *Proc Natl Acad Sci USA* **2016**, **113**(43), 12017.
- [19] Philip Schmode, Achilleas Savva, Robert Kahl, David Ohayon, Florian Meichsner, Oleksandr Dolynchuk, Thomas Thurn-Albrecht, Sahika Inal, Mukundan Thelakkat, *ACS Appl. Mater. Interfaces* **2020**, **12**, 11, 13029.
- [20] Yazhou Wang, Erica Zeglio, Hailiang Liao, Jinqiu Xu, Feng Liu, Zhengke Li, Iuliana Petruta Maria, Damia Mawad, Anna Herland, Iain McCulloch, Wan Yue, *Chem. Mater.* **2019**, **31**, 9797.
- [21] Alexander T. Lill, David X. Cao, Max Schrock, Joachim Vollbrecht, Jianfei Huang, Tung Nguyen-Dang, Viktor V. Brus, Brett Yurash, Dirk Leifert, Guillermo C. Bazan, Thuc-Quyen Nguyen, *Adv. Mater.* **2020**, **32**, 1908120.
- [22] Weiwei Li, Koen H. Hendriks, Martijn M. Wienk, René A. J. Janssen, *Acc. Chem. Res.* **2016**, **49**, 78.

- [23] Christian J. Mueller, Eliot Gann, Chetan R. Singh, Mukundan Thelakkat, Christopher R. McNeill, *Chem. Mater.* **2016**, 28, 7088.
- [24] Christian J. Mueller, Chetan R. Singh, Martina Fried, Sven Huettner, Mukundan Thelakkat, *Adv. Funct. Mater.* **2015**, 25, 2725.
- [25] Ting Lei, Ming Guan, Jia Liu, Hung-Cheng Lin, Raphael Pfattner, Leo Shaw, Allister F. McGuire, Tsung-Ching Huang, Leilai Shao, Kwang-Ting Cheng, Jeffrey B.-H. Tok, Zhenan Bao, *Proc Natl Acad Sci USA*, **2017**, 114 (20), 5107.
- [26] Weiyuan Du, David Ohayon, Craig Combe, Lorene Mottier, Iuliana P. Maria, Raja S. Ashraf, Hubert Fiumelli, Sahika Inal, Iain McCulloch, *Chem. Mater.* **2018**, 30, 17, 6164.
- [27] Brian Schmatz, Augustus W. Lang, John R. Reynolds, *Adv. Funct. Mater.* **2019**, 29, 1905266.
- [28] Alexander Giovannitti, Reem B. Rashid, Quentin Thiburce, Bryan D. Paulsen, Camila Cendra, Karl Thorley, Davide Moia, J. Tyler Mefford, David Hanifi, Du Weiyuan, Maximilian Moser, Alberto Salleo, Jenny Nelson, Iain McCulloch, Jonathan Rivnay, *Adv. Mater.* **2020**, 32, 1908047.
- [29] Maximilian Moser, Achilleas Savva, Karl Thorley, Bryan D. Paulsen, Tania Cecilia Hidalgo, David Ohayon, Hu Chen, Alexander Giovannitti, Adam Marks, Nicola Gasparini, Andrew Wadsworth, Jonathan Rivnay, Sahika Inal, Iain McCulloch, *Angew. Chem. Int. Ed.* 10.1002/anie.202014078
- [30] Xihu Wu, Qian Liu, Abhijith Surendran, Steven E. Bottle, Prashant Sonar, Wei Lin Leong, *Adv. Electron. Mater.* **2020**, 2000701.
- [31] Qian Liu, Kaito Kanahashi, Keiichiro Matsuki, Sergei Manzhos, Krishna Feron, Steven E. Bottle, Kazuhiro Tanaka, Tomonori Nanseki, Taishi Takenobu, Hisaaki Tanaka, Prashant Sonar, *Adv. Electron. Mater.* **2020**, 6, 1901414.
- [32] Christian J. Müller, Chetan R. Singh, Mukundan Thelakkat, *J Polym Sci Pol Phys.* **2016**, 54, 639.
- [33] Christian J. Mueller, Eliot Gann, Chetan R. Singh, Mukundan Thelakkat, and Christopher R. McNeill, *Chem. Mater.* **2016**, 28, 19, 7088.
- [34] Christian J. Mueller, Chetan R. Singh, Martina Fried, Sven Huettner, Mukundan Thelakkat, *Adv. Funct. Mater.* **2015**, 25, 2725.
- [35] Yu Zhu, Ingo Heim, Bernd Tieke, *Macromol. Chem. Phys.* **2006**, 207, 2206.
- [36] Ban Xuan Dong, Christian Nowak, Jonathan W. Onorato, Joseph Strzalka, Fernando A. Escobedo, Christine K. Luscombe, Paul F. Nealey, Shrayesh N. Patel, *Chem. Mater.* **2019**, 31, 4, 1418.
- [37] Xikang Zhao, Guobiao Xue, Ge Qu, Vani Singhania, Yan Zhao, Kamal Butrouna, Aristide Gumyusenge, Ying Diao, Kenneth R. Graham, Hanying Li, Jianguo Mei; *Macromolecules* **2017**, 50, 16, 6202.
- [38] Catherine Kanimozhi, Nir Yaarcobi-Gross, Kang Wie Chou, Aram Amassian, Thomas D. Anthopoulos, Satish Patil, *J. Am. Chem. Soc.* **2012**, 134, 40, 16532.
- [39] Si-Fen Yang, Zi-Tong Liu, Zheng-Xu Cai, Matthew J. Dyson, Natalie Stingelin, Wei Chan, Hua-Jun Ju, Guan-Xing Zhang, De-Qing Zhang, *Adv. Sci.*, **2017**, 4, 1700048.
- [40] Christian B. Nielsen, Alexander Giovannitti, Dan-Tiberiu Sbircea, Enrico Bandiello, Muhammad R. Niazi, David A. Hanifi, Michele Sessolo, Aram Amassian, George G. Malliaras, Jonathan Rivnay, Iain McCulloch, *J. Am. Chem. Soc.* **2016**, 138, 10252.
- [41] Alexander Giovannitti, Iuliana P. Maria, David Hanifi, Mary J. Donahue, Daniel Bryant, Katrina J. Barth, Beatrice E. Makdah, Achilleas Savva, Davide Moia, Matyáš Zetek, Piers R.F. Barnes, Obadiah G. Reid, Sahika Inal, Garry Rumbles, George G. Malliaras, Jenny Nelson, Jonathan Rivnay, Iain McCulloch, *Chem. Mater.* **2018**, 30, 9, 2945–2953.

Supporting Information

Supporting Information on synthetic details as well as detailed experimental data is available from the Wiley Online Library or from the author.

Acknowledgements

We kindly acknowledge financial support from the Deutsche Forschungsgemeinschaft (TH807/7-1) and Bavarian Ministry of State for Science and Arts (Solar Technologies Go Hybrid, SolTech). We thank the department of physical chemistry II, University of Bayreuth (Prof. Georg Papastavrou and Steffen Trippmacher) for support in E-QCMD measurements. We also thank Prof. Sahika Inal (KAUST) for support in designing OECT devices and the Fraunhofer ENAS (Chemnitz) for the joint development of OECT microelectrodes.

Supporting Information

Polydiketopyrrolopyrroles Carrying Ethylene Glycol Substituents as Efficient Mixed-Ion Conductors for Biocompatible Organic Electrochemical Transistors

Krauss, Gert; Meichsner, Florian; Hochgesang, Adrian; Mohanraj, John; Salehi, Sahar; Schmode, Philip; Thelakkat, Mukundan[§]*

*Applied Functional Polymers, Macromolecular Chemistry I, University of Bayreuth, 95440 Bayreuth, Germany.

[§]Bavarian Polymer Institute, University of Bayreuth, 95440 Bayreuth, Germany.

*Corresponding author: mukundan.thelakkat@uni-bayreuth.de

Table of Contents:

1. Monomer Synthesis and Characterization
 - 1.1. Diketopyrrolopyrrole-monomers
 - 1.2. EDOT-monomer
 - 1.3. 3-MEET monomer
2. Polymerizations
3. Polymer Characterization
 - 3.1. NMR-Data
 - 3.2. Gel-permeation chromatography
 - 3.3. Thermal properties (TGA, FlashDSC)
 - 3.4. Charge carrier mobility measurements in organic field effect transistors
 - 3.5. Ultraviolet Photoelectron Spectroscopy measurements
 - 3.6. Differential pulse polarography
 - 3.7. Spectroelectrochemical Absorption Measurements
 - 3.8. Electrochemical Impedance Spectroscopy
 - 3.9. Electrochemical Quartz-Crystal-Microbalance measurements
 - 3.10. Organic electrochemical transistors and cycling experiments
 - 3.11. OECT transient response time measurements
 - 3.12. In vitro cytotoxicity and cell viability test
4. References

1. Monomer Synthesis and Characterization

1.1. Diketopyrrolopyrrole monomers

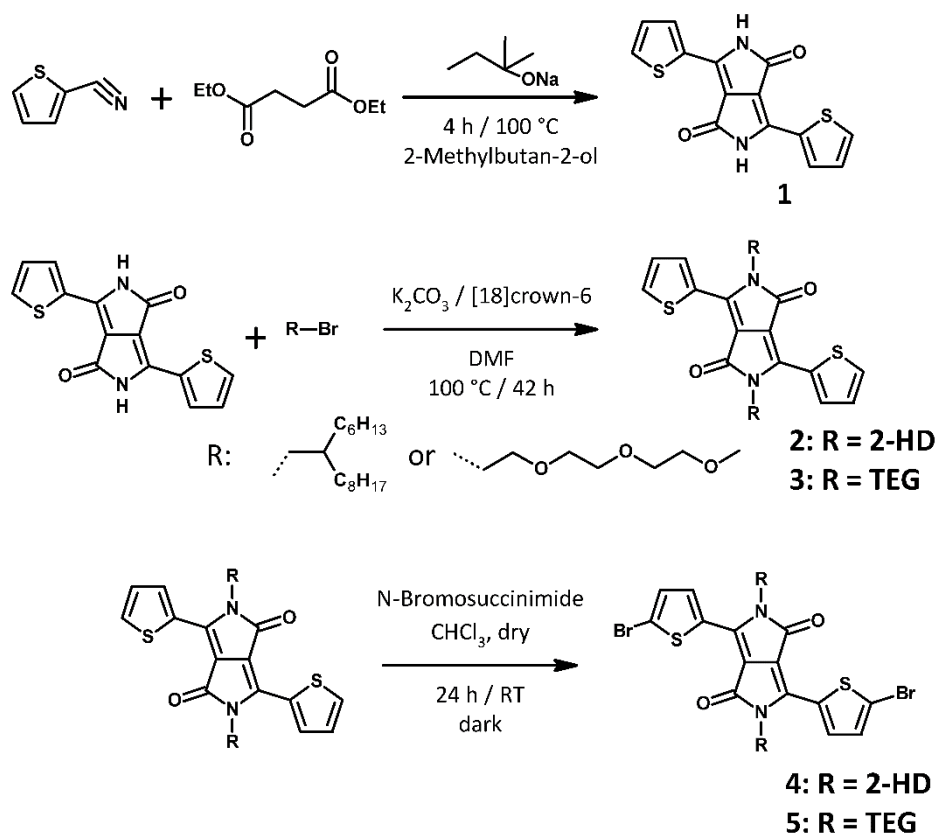


Figure S1 – Synthetic route toward the 2-hexyldodecyl- and triethylene glycol substituted diketopyrrolo-pyrrole monomers.

3,6-di(thiophen-2-yl)-2,5-dihydropyrrolo[3,4-c]pyrrole-1,4-dione (**1**):

In a three-necked 500 mL round-bottom flask sodium-2-methylbutan-2-olate (19 g / 172 mmol) was dissolved in dry 2-methylbutan-2-ol (70 mL) at 100 °C. Thiophene-2-carbonitrile (12.5 g / 115 mmol) was added in one part and diethyl succinate (10 g / 57 mmol) were added slowly (3 mL h⁻¹) using a syringe-pump and the resulting dark red mixture was stirred overnight at 100 °C. Thereafter, it was cooled to 65 °C and methanol (200 mL) was added carefully. Acetic acid (11 mL) were added to neutralize the mixture and precipitate the crude product which was filtered off, while still warm. The crude solid was washed with methanol and water, dried at 40 °C in vacuo and used as obtained. Yield: 8.8 g (29 mmol / 51 %) of a dark red solid. ¹H NMR (300 MHz, DMSO-*d*₆, δ): 10.39 (br. s., 2 H), 7.35 (dd, *J*=3.86, 1.22 Hz, 2 H), 7.10 (dd, *J*=4.90, 1.13 Hz, 2 H), 6.44 (dd, *J*=4.90, 3.77 Hz, 2 H). DIP-MS: 300 [M], 272, 244, 216, 188, 163, 135, 111.

3,6-di(thiophen-2-yl)-2,5-bis(2-hexyldodecyl)-pyrrolo[3,4-c]pyrrole-1,4-dione (**2**):

A 250 mL three-necked round bottom flask was charged with compound **1** (10 g / 33 mmol), potassium carbonate (18.4 g / 133 mmol) and 18-crown-6 (0.62 g / 2.3 mmol) and kept under

HV for some time and flushed with argon. Then, dry DMF (111 mL) was added and the mixture was heated to 130 °C and 2-hexyldecylbromide (25.4 g / 83 mmol) were added slowly and stirred 42 h at 100 °C. Thereafter, water (100 mL) were added, stirred for 30 min and extracted with chloroform. The combined organic layers were washed with water, dried over MgSO₄ and concentrated in vacuo. The raw material was purified via silica flash chromatography (hexanes : DCM = 1 : 1) and subsequent recrystallization from ethanol. Yield: 10.1 g (13 mmol / 40 %). ¹H NMR (300 MHz, CHLOROFORM-*d*, δ) 8.63 (d, *J*=4.14 Hz, 2 H), 7.22 (d, *J*=4.14 Hz, 2 H), 3.92 (d, *J*=7.72 Hz, 4 H), 1.78 - 1.97 (m, 2 H), 1.07 - 1.41 (m, 48 H), 0.77 - 0.93 (m, 12 H).

2,5-bis(2-(2-(2-methoxyethoxy)ethoxy)ethyl)-3,6-di(thiophen-2-yl)pyrrolo[3,4-*c*]pyrrole-1,4(2H,5H)-dione **3**:

A 1 L three-necked round bottom flask was charged with **1** (15 g / 50 mmol), potassium carbonate (20.7 g / 150 mmol) and 18-crown-6 (660 mg / 2.5 mmol) and kept under HV for some time before flushing with argon. Dry DMF (500 mL) were added under argon counter-flow and the mixture was heated to 125 °C for 45 min, then cooled to 0 °C. Dry 1-bromo-2-[2-(2-methoxyethoxy)ethoxy]ethane (28.3 g / 125 mmol) were added dropwise under argon counter-flow and the ice-bath was removed, stirred for 15 min at RT and 24 hat 130 °C. The solution was allowed to come to RT, poured into 500 mL water and stirred for 30 min, the mixture was extracted with chloroform and the combined organic layers were washed with water, dried over MgSO₄ and concentrated in vacuo. The crude product was dissolved in a small amount of chloroform, poured into 500 mL methanol and stored at -25 °C to encourage crystallization. Yield: 5.6 g (9 mmol / 19 %) of bright shiny red crystals. ¹H NMR (300 MHz, CHLOROFORM-*d*, δ): 8.75 (dd, *J*=3.96, 1.13 Hz, 2 H), 7.63 (dd, *J*=4.90, 1.13 Hz, 2 H), 7.23 - 7.28 (m, 2 H), 4.27 (t, *J*=6.31 Hz, 4 H), 3.78 (t, 4 H), 3.45 - 3.67 (m, 16 H), 3.34 (s, 6 H).

3,6-di(5-bromothiophen-2-yl)-2,5-bis(2-hexyldodecyl)-pyrrolo[3,4-*c*]pyrrole-1,4-dione (**4**) and 2,5-bis(2-(2-(2-methoxyethoxy)ethoxy)ethyl)-3,6-di(5-bromothiophen-2-yl)pyrrolo[3,4-*c*]pyrrole-1,4(2H,5H)-dione (**5**):

A Schlenk-flask was wrapped with aluminium foil and charged with the respective diketopyrrolopyrrole substrate (**2 or 3**) (1 eq.), kept under HV for 5 min and flushed with argon, before dry chloroform was added until a concentration of 50 mM was reached. The solution was cooled to 0 °C and N-bromosuccinimide (2.2 eq.) were added portion wise under argon counter flow. The ice bath was removed after 5 min and stirred overnight at RT. Afterwards, the mixture was poured in 300 mL methanol and stored at -25 °C for crystallization. The product was filtered and dried at 45 °C in vacuo.

Yield (**4**): 54 % of fine red shiny crystals. ¹H NMR (300 MHz, CHLOROFORM-*d*, δ): 8.61 (d, *J*=3.77 Hz, 2 H), 7.20 (d, *J*=4.14 Hz, 2 H), 3.91 (d, *J*=7.54 Hz, 4 H), 1.86 (br. s., 2 H), 1.07 - 1.42 (m, 51 H), 0.76 - 0.92 (m, 12 H). DIP-MS: 906 [M], 682, 458, 392.

Yield (**5**): 78 % of a red-purple powder. ^1H NMR (300 MHz, CHLOROFORM-*d*, δ): 8.49 (d, $J=4.14$ Hz, 2 H), 7.21 (d, $J=4.33$ Hz, 2 H), 4.17 (t, $J=5.93$ Hz, 4 H), 3.78 (t, 4 H), 3.46 - 3.67 (m, 16 H), 3.35 (s, 6 H). DIP-MS: 750 [M], 663, 648, 604, 502, 458.

1.2. EDOT-monomer

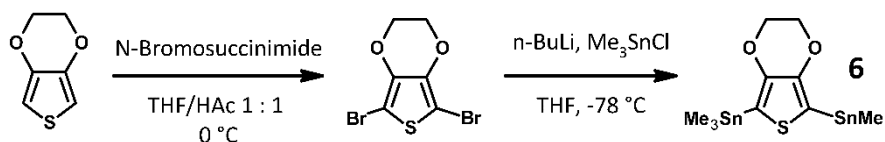


Figure S2 – Synthetic route of 2,5-bis(trimethylstannyl)-3,4-ethylenedioxythiophene. Bis-stannylated EDOT was synthesized following a procedure published by our group. [1]

Yield: 5.6 g (87 %). ^1H NMR (300 MHz, CHLOROFORM-*d*, δ): 4.15 (s, 4 H), 0.21 - 0.46 (m, 18 H).

1.3. 3-MEET-monomer

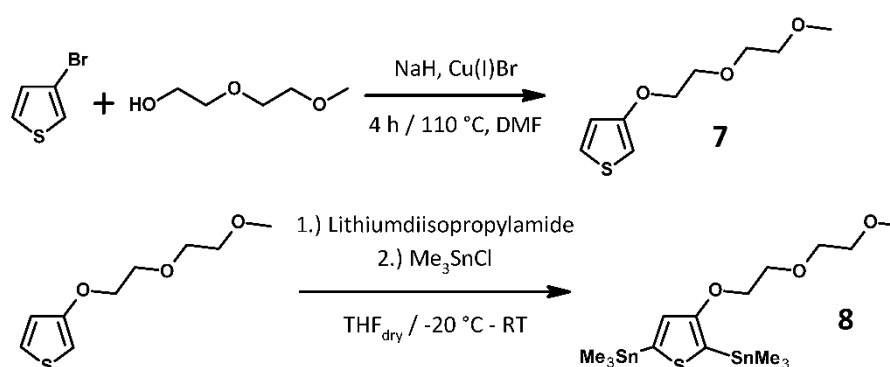


Figure S3 – Synthetic route toward 2,5-bis(trimethylstannyl) 3-[2-(2-methoxyethoxy)ethoxy]thiophene.

3-[2-(2-methoxyethoxy)ethoxy]thiophene “3-MEET” (**7**):

Compound (**7**) was synthesized following a procedure published by our group.^[2]

Yield: 17.8 g (88 mmol / 71 %) of a colorless oil. ^1H NMR (300 MHz, CHLOROFORM-*d*, δ): 7.16 (dd, $J=5.27, 3.20$ Hz, 1 H), 6.78 (dd, $J=5.27, 1.51$ Hz, 1 H), 6.25 (dd, $J=3.20, 1.51$ Hz, 1 H), 4.08 - 4.16 (m, 2 H), 3.80 - 3.88 (m, 2 H), 3.53 - 3.74 (m, 4 H), 3.39 (s, 3 H). GC showed 99 % purity.

2,5-bis(trimethylstannyl)-3-[2-(2-methoxyethoxy)ethoxy]thiophene (**8**):

A flame-dried 250 mL Schlenk-flask was charged with diisopropylamine (4.5 mL / 32 mmol) in dry tetrahydrofuran (144 mL) and cooled to 0 °C. *n*-butyl lithium was added dropwise and the solution was stirred 1 h at 0 °C and the ice-bath was replaced with a NaCl frigorific mixture to reach -20 °C. HV-dried compound (**7**) (3 g / 15 mmol) was added dropwise and the solution was allowed to react 15 min at -20 °C, 30 min at 0 °C and 1 h at RT before being cooled back to 0 °C. Trimethyltin chloride (6.2 g / 31 mmol) was added in some portions under argon counter-flow. The solution was stirred for 2 h at 0 °C and 2 h at RT. The reaction mixture was

washed with brine (containing 0.5 % triethylamine) and extracted with diethyl ether and tetrahydrofuran. The solution was concentrated in vacuo without drying over MgSO_4 , affording a brown oil. The crude oil was purified by vacuum distillation ($\vartheta_{\text{vap.}} = 125\text{-}128\text{ }^\circ\text{C}$, $p = 4 \cdot 10^{-3}$ mbar). Yield: 2.4 g (4.5 mmol / 30 %). GC showed 95 % purity. ^1H NMR (300 MHz, $\text{CHLOROFORM-}d$, δ): 7.03 (s, 1 H), 4.14 - 4.19 (m, 2 H), 3.76 - 3.82 (m, 2 H), 3.52 - 3.73 (m, 4 H), 3.40 (s, 3 H), 0.10 - 0.56 (m, 18 H). DIP-MS: 513 [M- CH_3], 409, 351, 319, 275, 165, 132, 59.

2. Polymerizations

All polymerizations were conducted following a general procedure for Stille cross-coupling polycondensation reported in the literature.^[1]

A 5 mL microwave-vial was charged with an equimolar amount of the respective brominated DPP- Br_2 -monomer and the stannylated thiophene- or EDOT(SnMe_3)₂ monomer (0.2 mmol each), tri(o-tolyl)phosphine (6.7 mg / 0.02 mmol) and chlorobenzene (4.8 ml) and the mixture was degassed by bubbling with argon for 15 min. Tris(dibenzylideneacetone)dipalladium(0) (5.3 mg / 0.01 mmol) was added under argon-counter flow and the vial was sealed. The headspace was flushed with argon and the polymerization mixture was stirred at 180 °C for 45 min. End-capping was performed by addition of 2-(tributylstannyl)thiophene (32 μL / 0.1 mmol), flushing the headspace with argon and heating for 5 min at 180 °C. Next, 2-bromothiophene (64 μL / 0.67 mmol) was added, the headspace was flushed once more and the mixture was heated to 180 °C for 15 min. The viscous solutions were dissolved with some mL of chlorobenzene and precipitated in an excess of methanol. Reaction by-products, catalyst, ligand and unreacted monomers were removed by Soxhlet-extraction with methanol, followed by a consecutive series of Soxhlet-extractions with acetone, hexane, dichloromethane, chloroform, chlorobenzene to isolate the polymer.

3. Polymer Characterization

3.1. ^1H -NMR

PDPP[T]₂{2-HD}-EDOT: (300 MHz, $\text{CHLOROFORM-}d$, δ) 8.22 - 9.57 (br., 2 H), 5.85 - 6.89 (br., 2 H), 3.71 - 5.11 (br., 4 H), 0.11 - 2.71 (br., 66 H).

PDPP[T]₂{TEG}-EDOT: insoluble in NMR solvents / not measured.

PDPP[T]₂{TEG}-3-MEET: (300 MHz, $\text{CHLOROFORM-}d$, δ) 8.59 - 9.13 (br., 2 H), 6.41 - 7.15 (br., 3 H), 2.84 - 5.09 (br., 41 H).

PDPP[T]₂{2-HD}-3-MEET: (300 MHz, $\text{CHLOROFORM-}d$, δ) 8.76 - 9.27 (br., 2 H), 6.67 - 7.22 (br., 2 H), 3.53 - 4.76 (br., 8 H), 3.28 - 3.51 (br., 3 H), 0.44 - 2.14 (br., 66 H).

3.2. Gel-permeation chromatography

GPC measurement was performed on an instrument having an SDV linear XL gel column (particle size = 5 μm) with separation range from 100 to 3 000 000 Da (PSS, Mainz, Germany)

together with a refractive index detector (1200 Series, Agilent Technologies). CHCl_3 (HPLC grade) was used as solvent (for dissolving polymer and as eluting solvent) with a flow rate of 0.5 mL/min at room temperature. As internal standard toluene (HPLC grade) was used. The calibration was done with narrowly distributed polystyrene (PS) homo-polymers (PSS calibration kit). An injection volume of 20 μL was used for the measurements. The sample was dissolved in CHCl_3 and filtered through a 0.22 μm PTFE filter before analysis. The Polymers PDPP[T]₂{2-HD}-EDOT, PDPP[T]₂{TEG}-3-MEET and PDPP[T]₂{2-HD}-3-MEET were measured using this setup. The polymer PDPP[T]₂{TEG}-EDOT was insoluble in Chloroform and therefore measured on an instrument having a PFG precolumn and two PSS-PFG gel columns (particle size = 7 μm) with porosity range from 100 to 300 Å (PSS, Mainz, Germany) together with a refractive index detector (Gynkotek). HFIP (HPLC grade) with potassium trifluoroacetate (4.8 g in 600 mL HFIP) was used as solvent (for dissolving polymer and as eluting solvent) with a flow rate of 0.5 mL/min. As internal standard toluene (HPLC grade) was used. The calibration was done with narrowly distributed poly(methyl methacrylate) (PMMA) homopolymers (PSS calibration kit). The sample was dissolved in HFIP with potassium trifluoroacetate and filtered through a 0.22 μm PTFE filter before analysis. An injection volume of 20 μL was used for the measurement and the GPC columns were maintained at room temperature. The molar masses reported are in reference to PMMA standards. The obtained values are given below.

PDPP[T]₂{2-HD}-EDOT: $M_n = 25 \text{ kg mol}^{-1}$, $\text{Đ} = 3.2$.

PDPP[T]₂{TEG}-EDOT: $M_n = 9 \text{ kg mol}^{-1}$, $\text{Đ} = 1.1$.

PDPP[T]₂{TEG}-3-MEET: $M_n = 22 \text{ kg mol}^{-1}$, $\text{Đ} = 2.5$.

PDPP[T]₂{2-HD}-3-MEET: $M_n = 14 \text{ kg mol}^{-1}$, $\text{Đ} = 2.9$.

3.3. Thermal properties (TGA and FlashDSC)

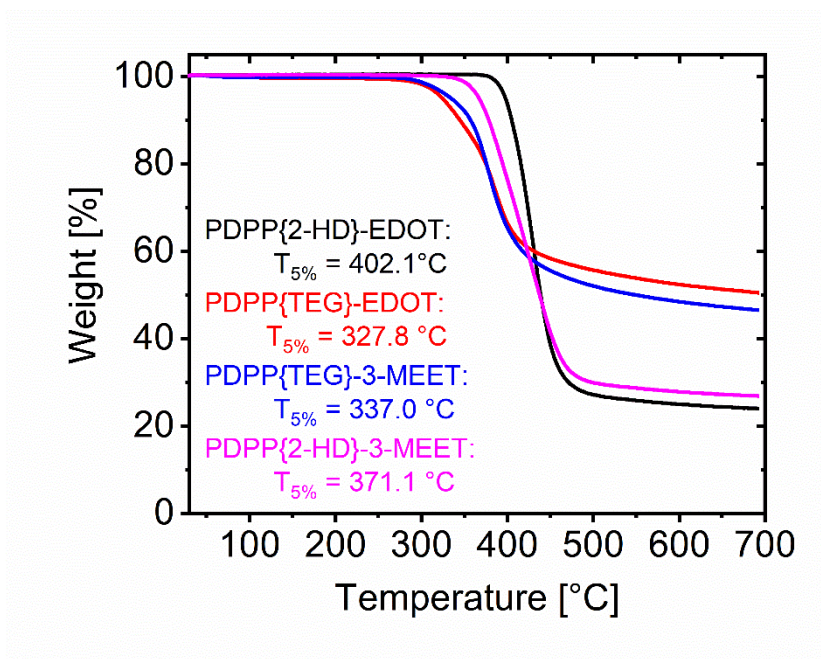


Figure S4 – Thermogravimetric analysis (TGA) measurement under nitrogen atmosphere, with a heating-rate of 10 K min⁻¹ within a temperature window between 30 °C and 700 °C.

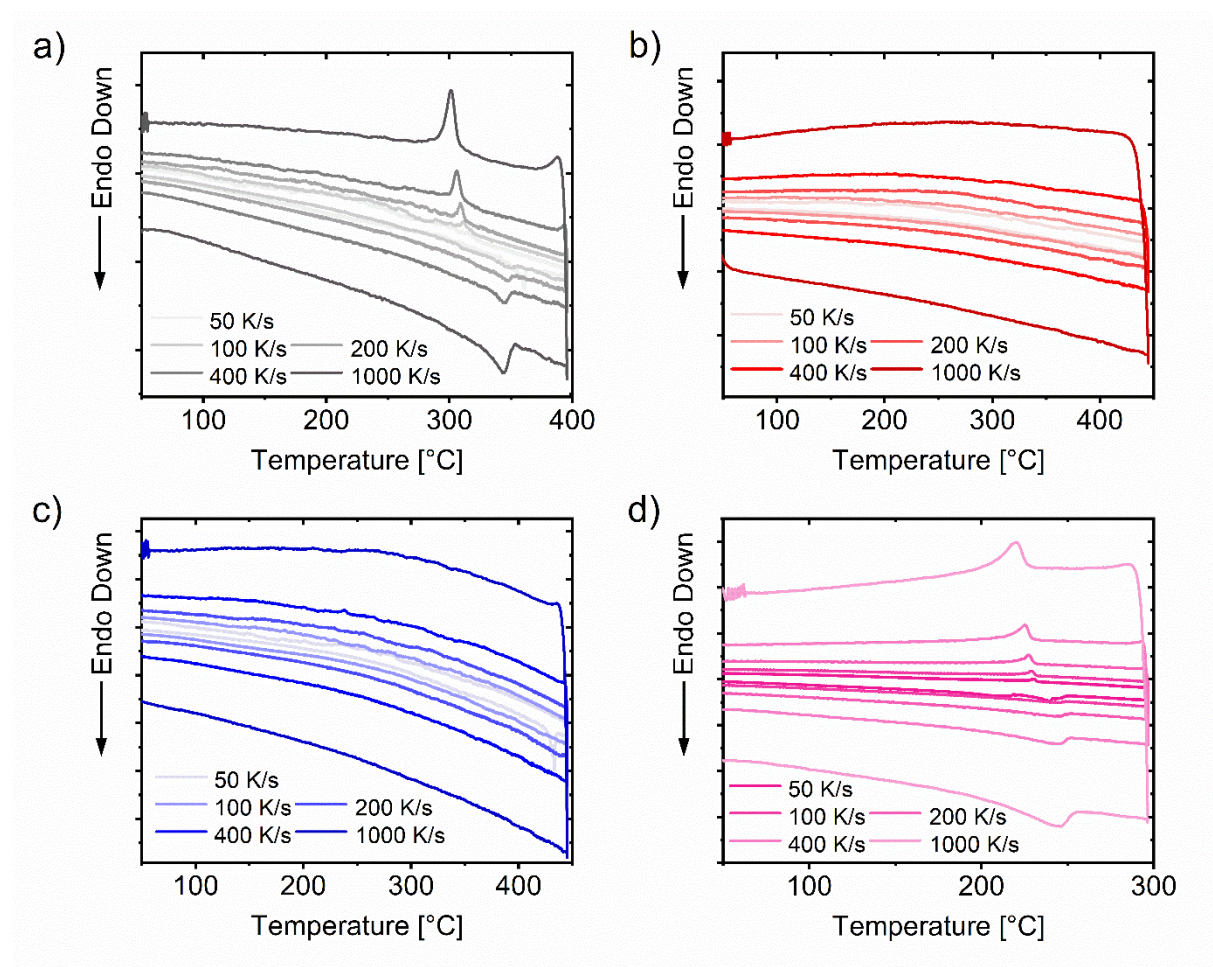


Figure S5 – Flash Differential Scanning Calorimetry (FlashDSC) measurements under nitrogen atmosphere with scanning rates between 50 Ks⁻¹ and 1000 Ks⁻¹. a) PDPP[T]₂{2-HD}-EDOT, b) PDPP[T]₂{TEG}-EDOT, c) PDPP[T]₂{TEG}-3-MEET, d) PDPP[T]₂{2-HD}-3-MEET.

3.4. Hole mobility measurement in organic field-effect transistors (OFETs)

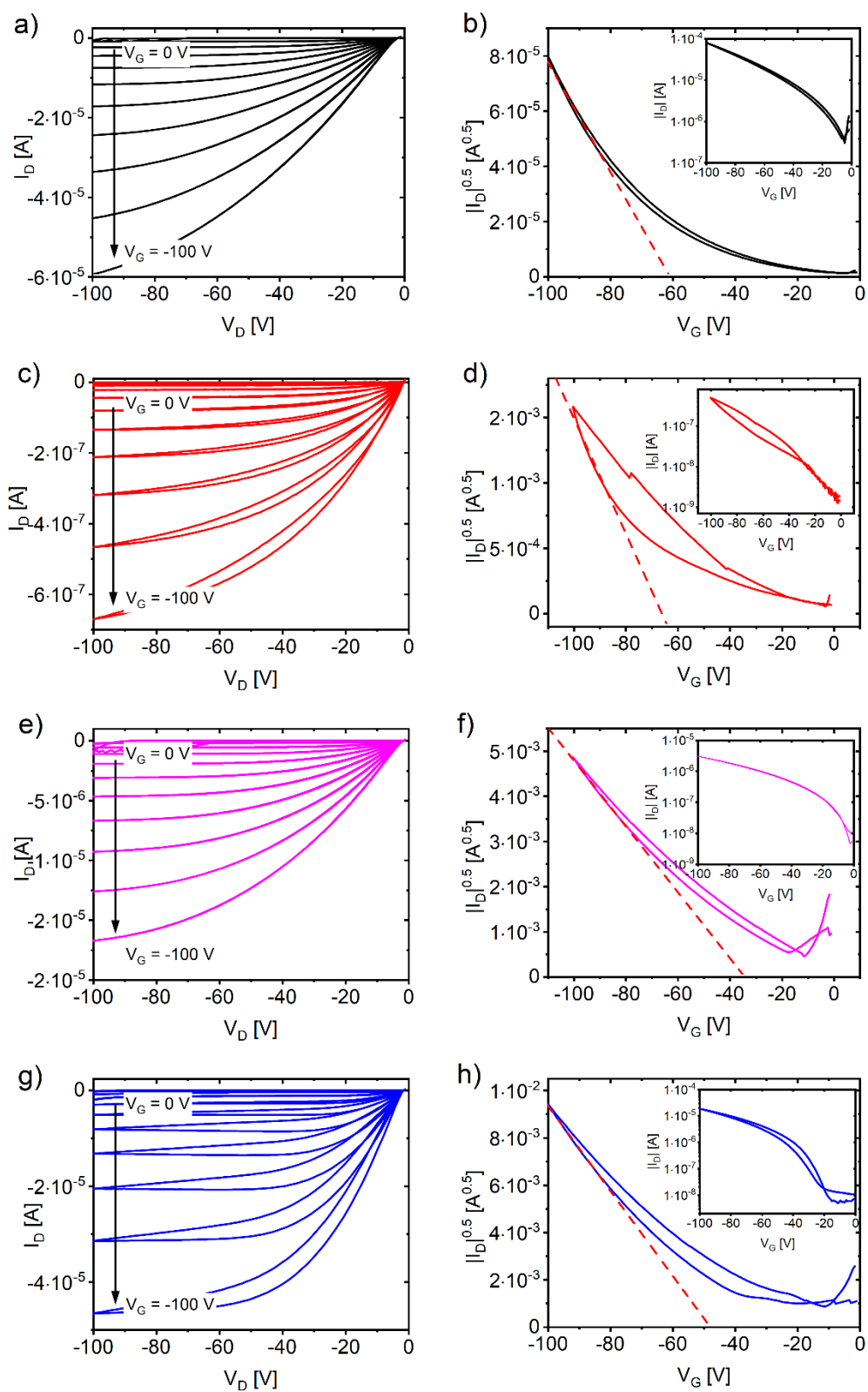


Figure S6 – OFET-output and transfer characteristics of the polymers a) and b) PDPP[T]₂{2-HD}-EDOT, c) and d) PDPP[T]₂{TEG}-EDOT, e) and f) PDPP[T]₂{TEG}3-MEET and g) and h) PDPP[T]₂{2-HD}-3-MEET.

The annealing conditions yielding the highest charge carrier mobilities are listed below:

PDPP[T]₂{2-HD}-EDOT: 20 min at 250 °C. PDPP[T]₂{TEG}-EDOT: 5 min 150 °C.

PDPP[T]₂{2-HD}-3-MEET: 5 min at 150 °C. PDPP[T]₂{TEG}-3-MEET: 20 min at 250 °C.

3.5 Ultraviolet Photoelectron Spectroscopy

All measurements reported in this study were carried out with the He I (21.22 eV, 40 W) line with -5V sample biasing and the corresponding photoemission with 90° take-off angle was collected at the multichannel analyzer. The Fermi level (E_F) and vacuum level (E_{vac}) were determined using a sputter cleaned gold foil. Ionization potential of the polymers is calculated as the energy difference between E_{vac} and the leading edge of the HOMO peaks. The resolution of the UPS measurements is ± 0.15 eV, calculated using the Fermi edge full-width-half-maximum of the gold spectrum and the presented work function and IP values are reproducible within ± 0.05 eV, consistent with the resolution limit.

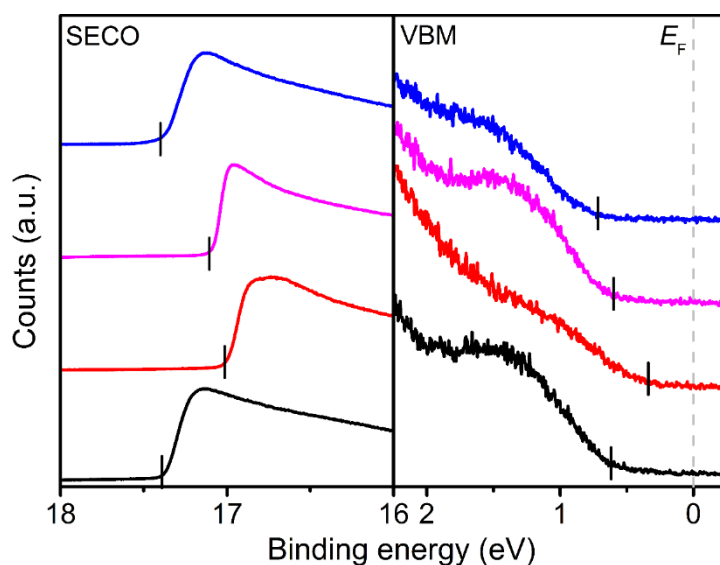


Figure S7 – Ultra-violet photoemission spectra showing the valence band maximum (right) and secondary electron cut-off (left) regions of PDPP[T]₂{2-HD}-EDOT (black), PDPP[T]₂{TEG}-EDOT (red), PDPP{2-HD}[T]₂-3-MEET (magenta) and PDPP[T]₂{TEG}-3-MEET (blue), scaled with respect to the Fermi level (vertical grey dashed line).

3.6. Differential pulse polarography

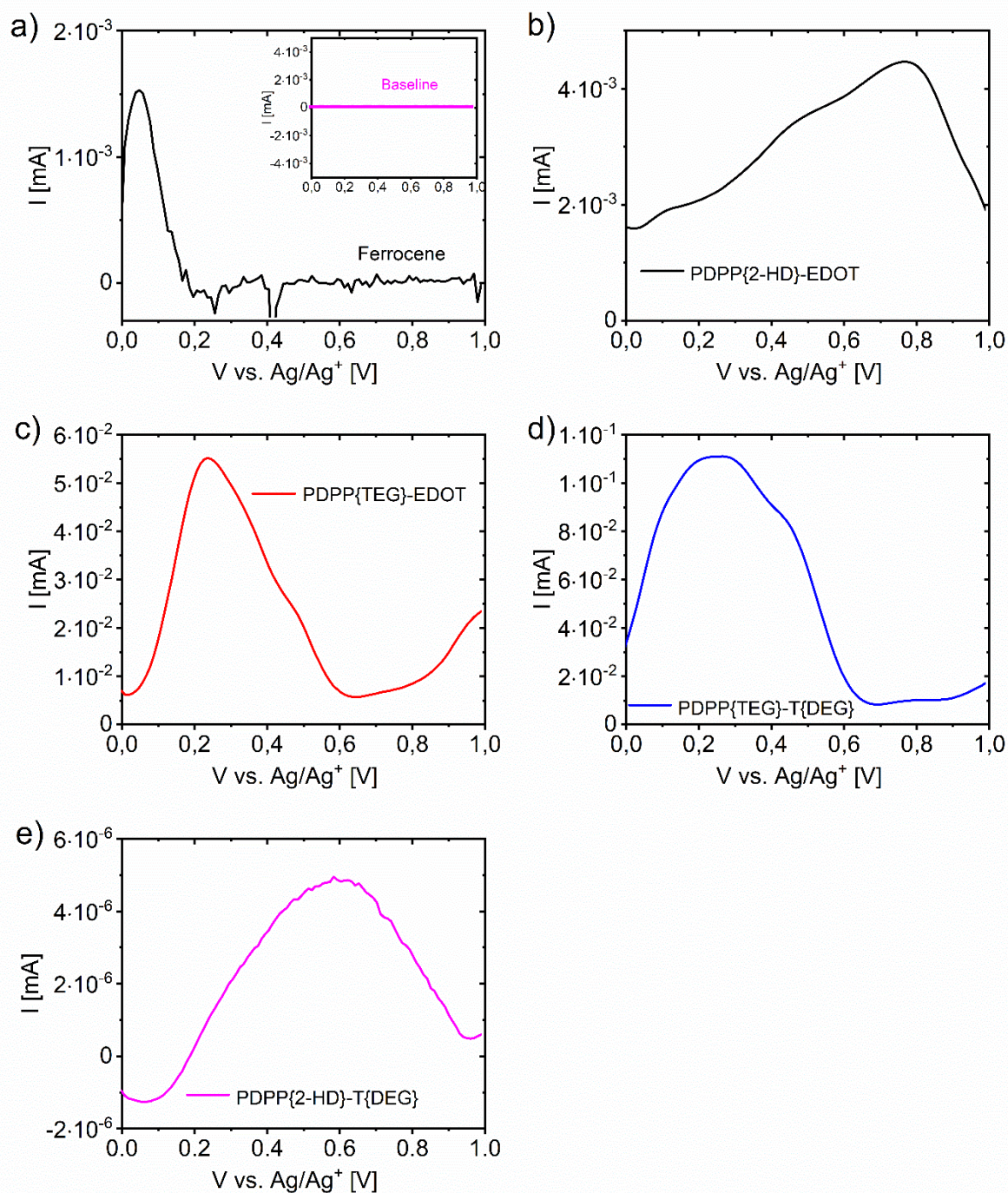


Figure S8 – Differential pulse polarography in thin films on platinum coated indium-tin-oxide (ITO) glass using a three-electrode setup in acetonitrile with 0.1 M tetrabutylammonium hexafluorophosphate as supporting electrolyte. a) ferrocene (Fc) as external reference, b) - e) differential pulse polarograms of the four polymers.

3.7 Spectroelectrochemical Absorption measurements:

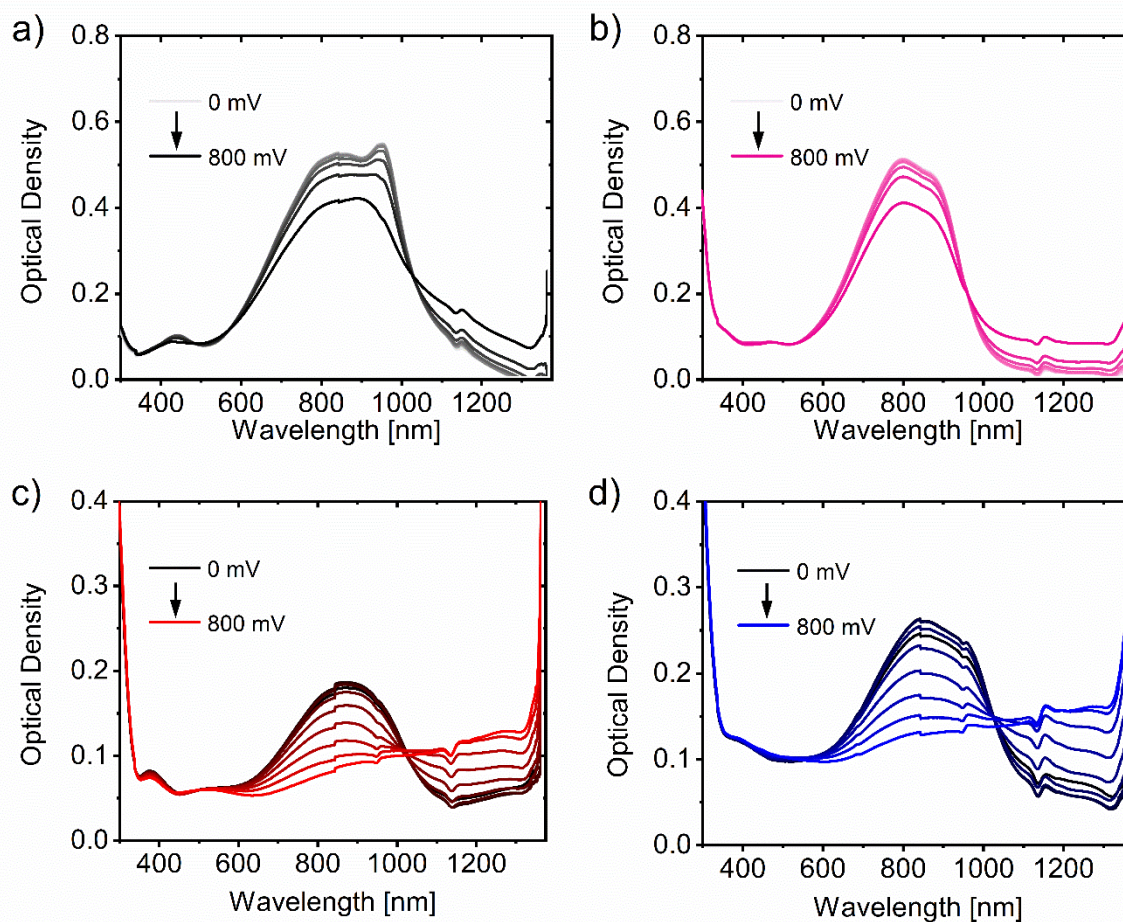


Figure S9 – Measured SEC-curves of the four polymers on ITO/glass substrates in 0.1 M aq. NaCl solution. a) PDPP[T]₂{2-HD}-EDOT, b) PDPP[T]₂{2-HD}-3-MEET, c) PDPP[T]₂{TEG}-EDOT, d) PDPP[T]₂{TEG}-3-MEET.

3.8. Electrochemical Impedance Spectroscopy

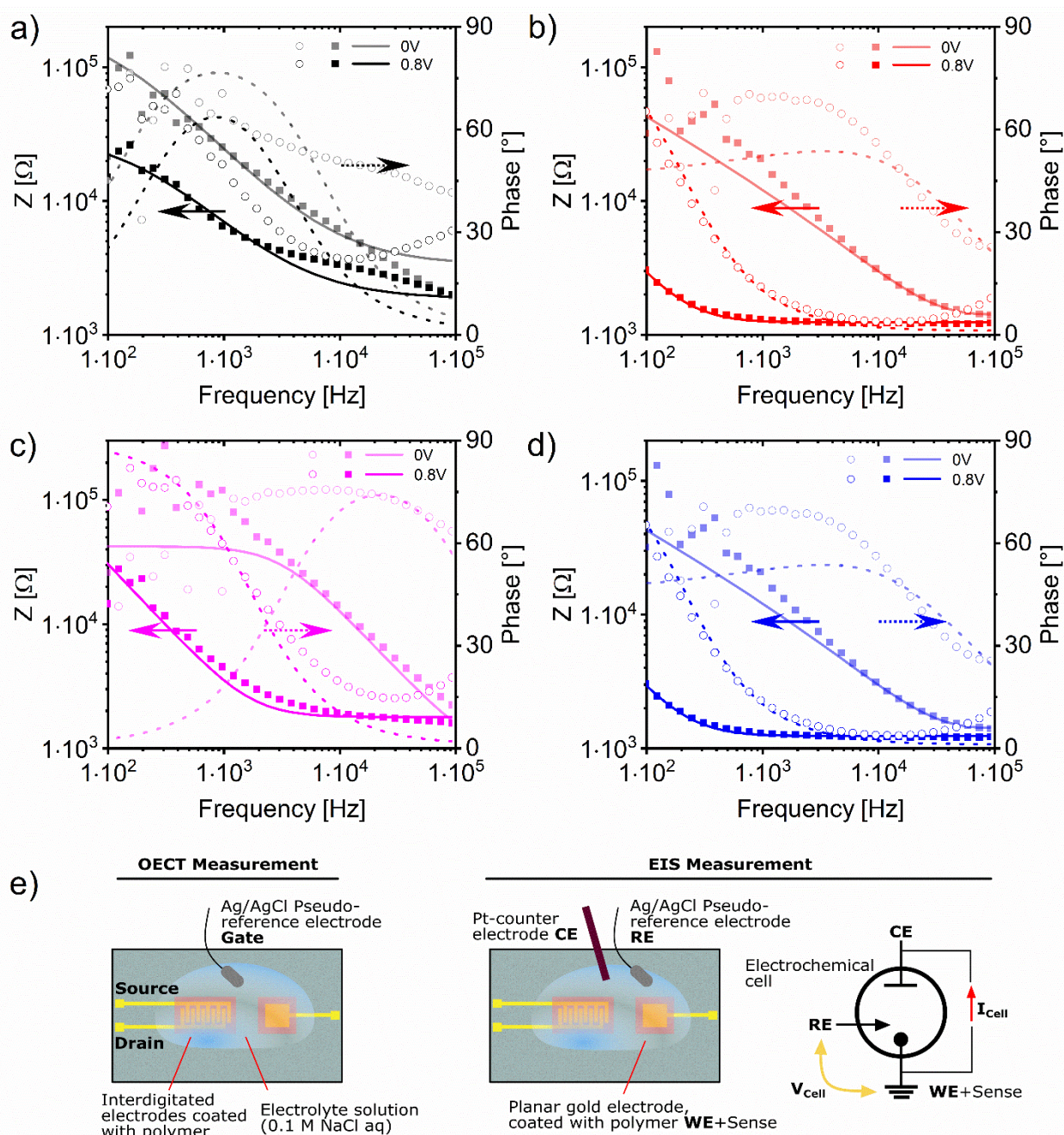


Figure S10 – Electrochemical impedance spectra (Bode-plots) of a) PDPP[T]₂{2-HD}-EDOT, b) PDPP[T]₂{TEG}-EDOT, c) PDPP[T]₂{2-HD}-3-MEET and d) PDPP[T]₂{TEG}-3-MEET, recorded at $V = 0$ V and at $V = 0.8$ V, where the maximum transconductance was attained. Electrolyte: 0.1 M NaCl_{aq}. e.) Schematic of the electrodes and substrate setup used for OECT as well as EIS measurements. Filled squares represent impedance data points, open circles represent phase data, lines represent the fits (continuous: impedance, broken: phase).

To extract the chemical capacitance C^* at each applied potential, an $R_s(R_pC_p)$ circuit was fitted to the absolute impedance $|Z|$ utilizing eq. 4:

$$Z_{R(RC)} = R_s + \frac{1}{i\omega C_p + \frac{1}{R_p}} \quad (\text{equation 4})$$

From which the phase angle can be calculated with eq. 5 and splitting $|Z|$ into its real Z' and imaginary part Z'' :

$$\varphi_{R(RC)} = \arctan\left(\frac{Z''}{Z'}\right) \quad (\text{equation 5})$$

Samples with significant diffusion were modelled by including a Warburg element W into the aforementioned equivalent circuit, yielding the known Randles circuit $R_S(C_P[R_P W])$. It should be noted, that the Warburg impedance has no effect on the parallel capacitance encountered at higher measurement frequencies. Combining the dry polymer film thickness d_{Pol} and exposed gate electrode area A_{Gate} ($2.5 \cdot 10^{-3} \text{ cm}^2$) yields the volumetric chemical capacitance C^* in Fcm^{-3} at the applied potential E :

$$C^*(E) = \frac{C_P(E)}{d_{Pol}A_{Gate}} \quad (\text{equation 6})$$

3.9 QCMD and E-QCMD Measurements

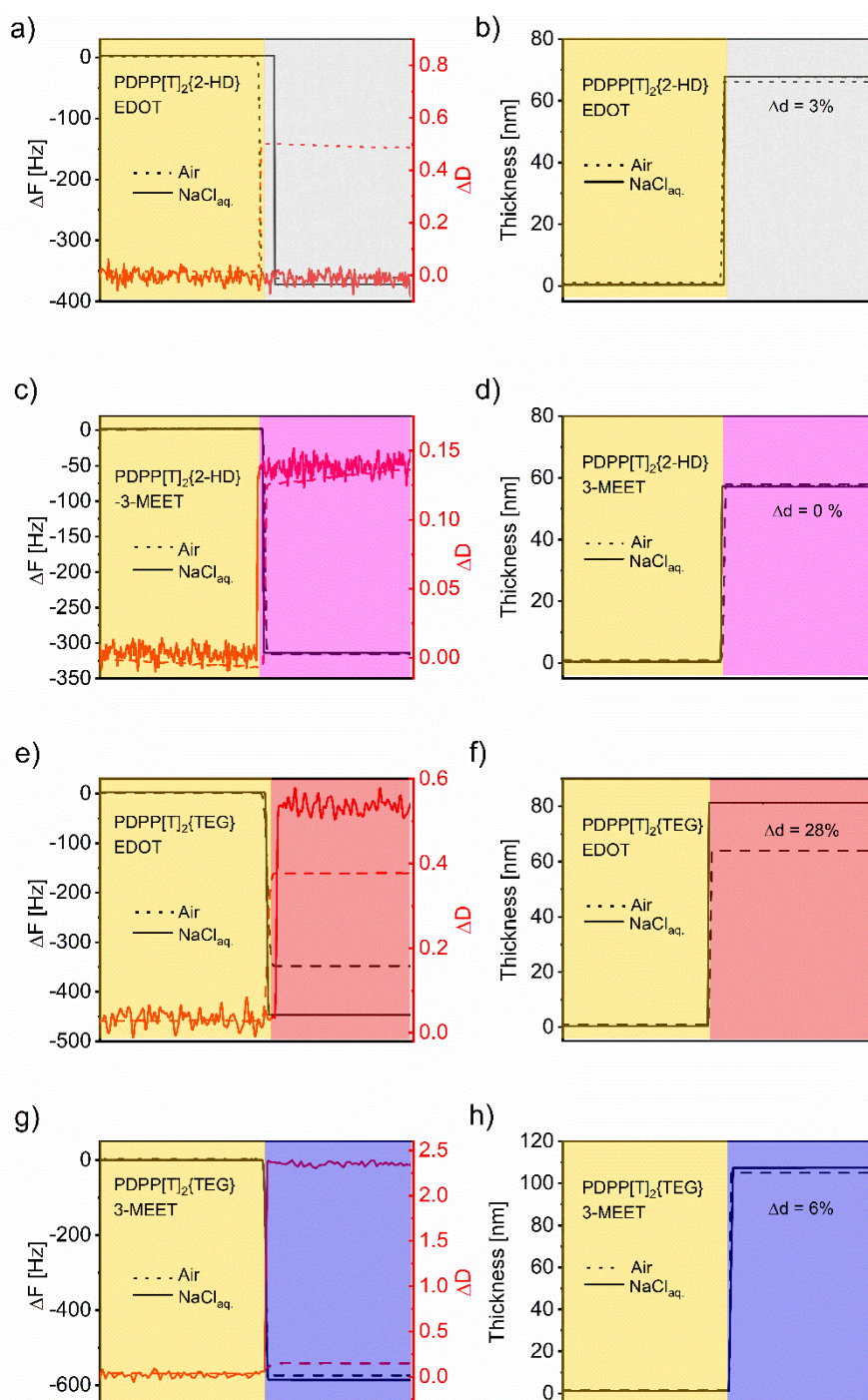


Figure S11 – QCMD measurements of the various polymers for determining passive swelling. Left column: shifts of the QCMD frequency (Δf) and changes in the dissipation (ΔD). Right column: Calculated thicknesses, based on the Sauerbrey-model using the seventh overtone.

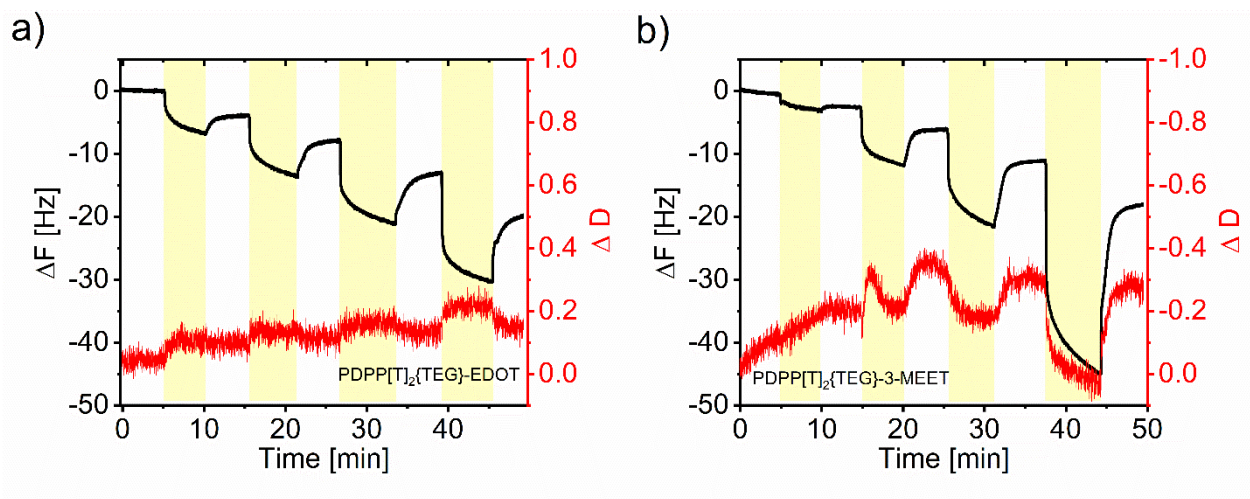


Figure S12 – Pulsed E-QCMD measurements of a) PDPP[T]2{TEG}-EDOT and b) PDPP[T]2{TEG}-3-MEET for calculating the active swelling. Frequency and dissipation shifts of the seventh overtone are shown.

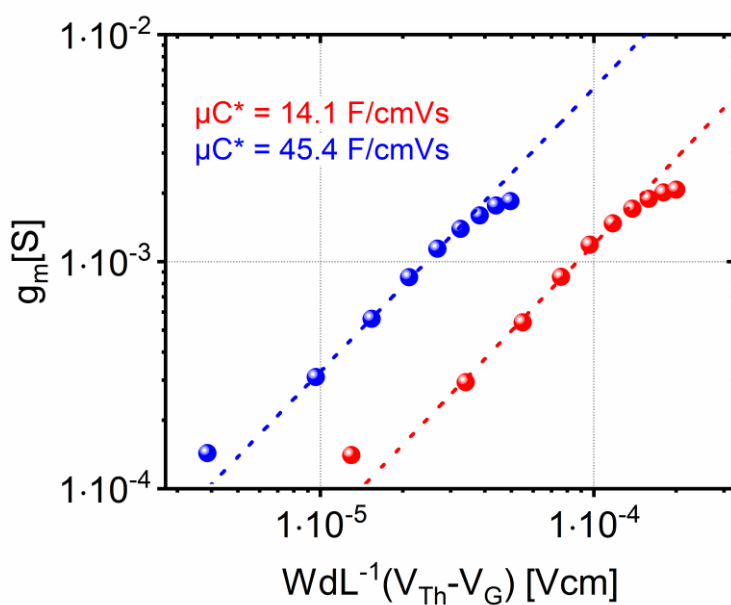


Figure S13 – Plot of the transconductance vs. the geometric device parameter for the extraction of the figure of merit as the slope of the linear regime in the linear plots, transformed to a double logarithmic scale for better visibility.

3.10. OECT - Cycling Experiments

The cycling experiments were conducted using the same setup as described in the experimental part (*Organic electrochemical transistors*). For each cycle, the respective drain- and gate voltage is applied for two seconds, followed by two seconds of unbiased gate- and drain contacts. The resulting drain current is monitored over the time. The three different drain- and gate voltages were chosen purposefully, using the threshold voltage and the output characteristics of the previously measured OECT devices. Because $V_{Th} \approx -0.35$ V, the smallest reasonable gating potential is $V_G = -0.5$ V. At this gate voltage the drain current saturates beyond a $V_D = -0.4$ V, therefore, we adjusted the cycling parameters to $V_G = -0.5$ V / $V_D = -0.4$ V for the smallest gate voltage. When increasing the gate voltage in 100 mV steps, the corresponding saturated regimes in the output curve result in the parameter couples of $V_G = -0.6$ V / $V_D = -0.5$ V and $V_G = -0.7$ V / $V_D = -0.6$ V.

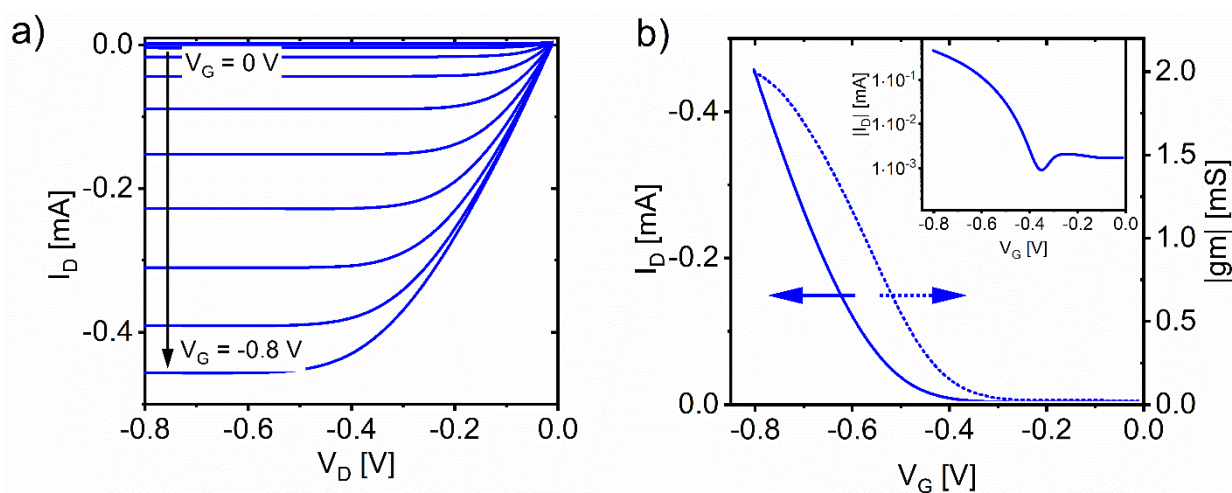


Figure S14 – OECT- output (a) and transfer curves with the corresponding transconductance-progressions b) PDPP[T]2{TEG}-3-MEET using DMEM as electrolyte.

3.11. OECT transient response time measurements

The transient response time measurements were conducted on the same OECT samples as the preceding measurements to ensure comparability. For the measurement, square-wave potentials of $V_D = -0.7$ V and $V_G = -0.8$ V were simultaneously applied to the device and the corresponding drain-current was measured. The response time τ_{90} is given as the time in ms, after which 90 % of the final drain current are reached. 1 M $\text{NaCl}_{aq.}$ was used as the electrolyte, channel lengths were 15 μm and the final values represent the average of three different pulse measurements on the same device.

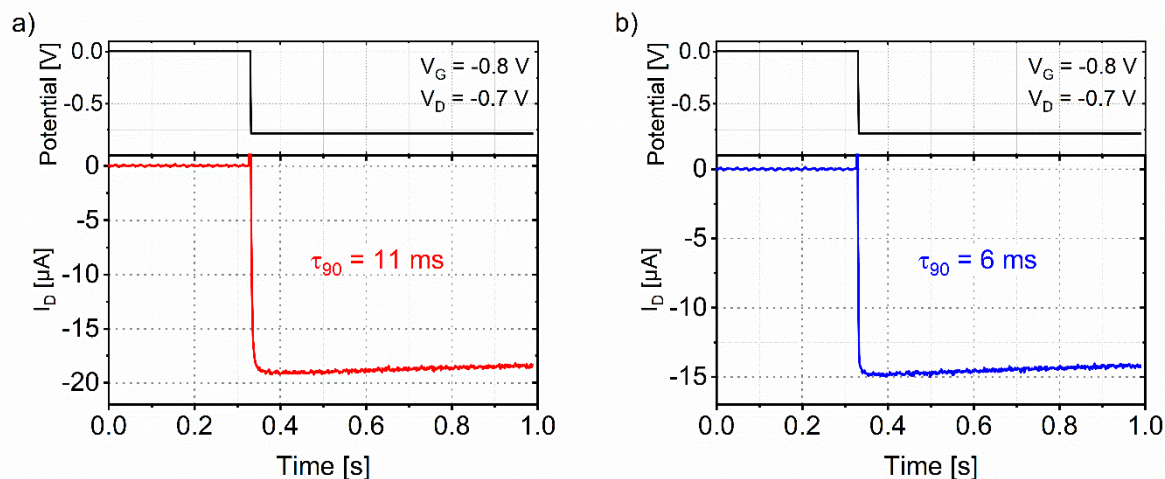


Figure S16 – Measurement of the transient response time of the two polymers a) PDPP[T]₂{TEG}-EDOT and b) PDPP[T]₂{TEG}-3-MEET.

3.12 In vitro cytotoxicity and cell viability test

CellTiter-Blue Assay

The CellTiter-Blue[®] Cell Viability Assay (Promega) was used to quantitatively evaluate cell metabolic activity according to the manufacturer's protocols. An initial solution of cell culture medium and CellTiter reagent in a ratio of 10% v/v was prepared, pipetted to each of the samples and incubated at 37°C for $\approx 2.5\text{ h}$. After incubation, $100\ \mu\text{l}$ of AB solution from each sample was pipetted on a 96-well plate and the fluorescence was recorded at $560/590\text{ nm}$ using a plate reader (Mithras LB 940, Germany). Obtained data were used to calculate the fluorescence absorbance using three replicated for each samples. Relative cell metabolic activity was normalized to the mean of the blank culture media. Samples were evaluated, and the mean cell metabolic activity and standard deviations are reported ($n = 3$).

Fluorescence Imaging

Live/dead Assay was also performed on cells after the CellTiter-Blue[®] Assay to qualitatively evaluate their viability. A live/dead solution was prepared with $4\ \mu\text{M}$ of calcein AM and $2\ \mu\text{M}$ of ethidium homodimer in PBS. After washing the CellTiter-Blue reagent with DPBS, live dead staining solution was added to cells following by 20 min incubation at room temperature in dark prior to imaging. Next, cells were imaged using the fluorescent microscope Leica DMI8 (Leica Microsystems, Germany) and minimum 5 pictures were obtained per sample and number of cells was calculated using the manual cell counter Plugin ImageJ. Finally, cell viability was determined by dividing the live cells to the total number of cells.

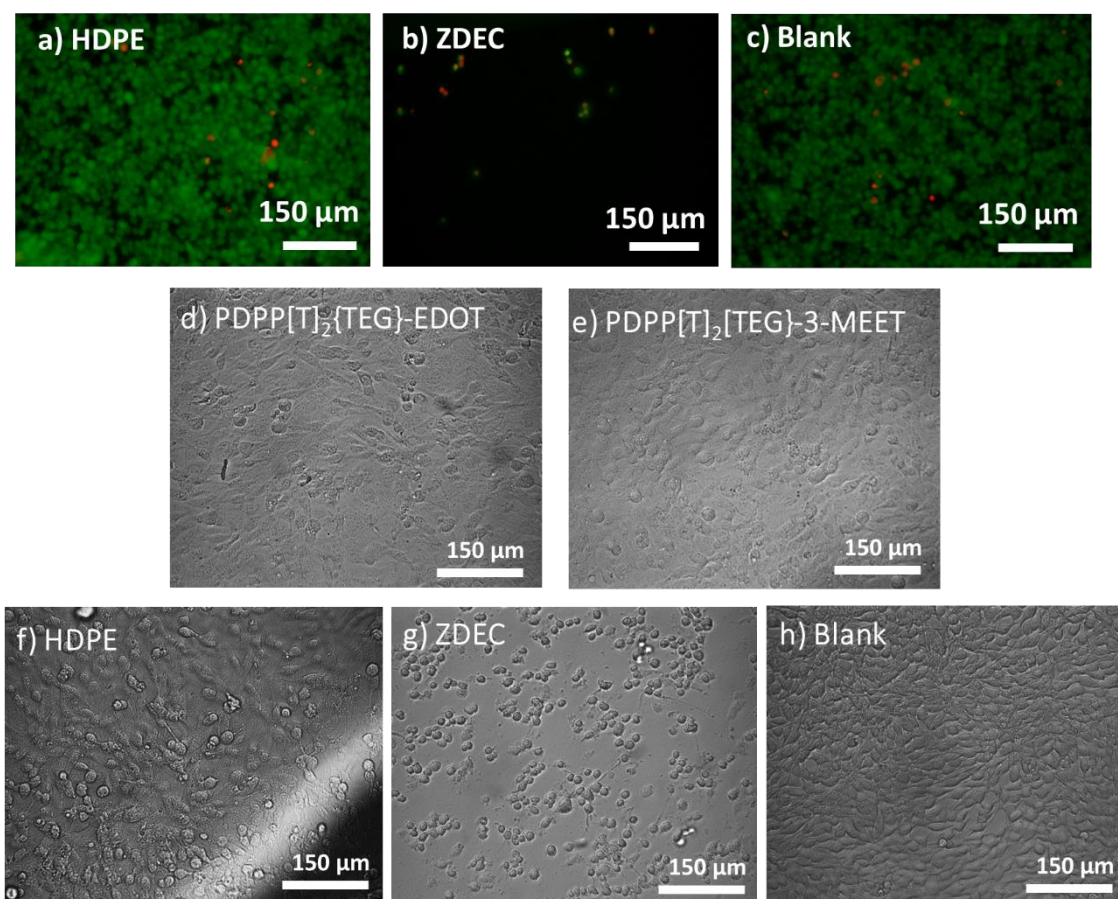


Figure S15 – Fibroblasts cells after 24 h in contact with extract of a) HDPE, b) ZDEC and c) Blank. Fluorescent images of cells taken after live/dead staining. Calcein AM (green) represents live cells, and ethidium homodimer (red) represents dead cells. Fibroblasts cells after 24 h in contact with agar layer and polymeric films as well as controls d) PDPP[T]₂{TEG}-EDOT e) PDPP[T]₂{TEG}-3-MEET f) HDPE, g) ZDEC and h) Blank. Normal morphology of fibroblasts was seen in contact with both polymers as well as negative control HDPE and Blank. Cells in contact with ZDEC are round shape and dead.

4. SI-References

[1] Christian J. Müller, Chetan R. Singh, Mukundan Thelakkat, *J Polym Sci Pol Phys*. 2016, 54, 639.

[2] Philip Schmode, Achilleas Savva, Robert Kahl, David Ohayon, Florian Meichsner, Oleksandr Dolynchuk, Thomas Thurn-Albrecht, Sahika Inal, Mukundan Thelakkat, *ACS Appl. Mater. Interfaces* 2020, 12, 11, 13029.

6. HOMO–HOMO Electron Transfer: An Elegant Strategy for p-Type Doping of Polymer Semiconductors toward Thermoelectric Applications

Published as “HOMO–HOMO Electron Transfer: An Elegant Strategy for p-Type Doping of Polymer Semiconductors toward Thermoelectric Applications” in *Advanced Materials* **2020**, 32, 2003596 by Mahima Goel, Marie Siegert, Gert Krauss, John Mohanraj, Adrian Hochgesang, David C. Heinrich, Martina Fried, Jens Pflaum and Mukundan Thelakkat*.

M. Goel, G. Krauss, J. Mohanraj, A. Hochgesang, D. C. Heinrich, M. Fried, M. Thelakkat
Applied Functional Polymers, Macromolecular Chemistry I, University of Bayreuth,
Universitätsstr. 30, Bayreuth, 95440, Germany
E-mail: mukundan.thelakkat@uni-bayreuth.de

M. Siegert, J. Pflaum
Experimental Physics VI
University of Würzburg, Am Hubland, Würzburg 97074, Germany

Prof. M. Thelakkat
Bavarian Polymer Institute (BPI), University of Bayreuth,
Universitätsstr. 30, Bayreuth, 95440, Germany

Keywords: Organic semiconductors, molecular doping, polymer thermoelectrics, ultraviolet photoelectron spectroscopy, Mott-Schottky.

Abstract

Unlike the conventional p-doping of organic semiconductors (OSCs) using acceptors, here an efficient doping concept for diketopyrrolopyrrole based polymer PDPP[T]₂-EDOT (OSC-1) is presented using an oxidized p-type semiconductor, Spiro-OMeTAD(TFSI)₂ (OSC-2), exploiting electron transfer from HOMO_{OSC-1} to HOMO_{OSC-2}. A shift of work function towards the HOMO_{OSC-1} upon doping was confirmed by ultraviolet photoelectron spectroscopy (UPS). Detailed X-ray photoelectron spectroscopy (XPS) and UV-vis-NIR absorption studies confirmed HOMO_{OSC-1} to HOMO_{OSC-2} electron transfer. We also confirmed the reduction products of Spiro-OMeTAD(TFSI)₂ to Spiro-OMeTAD(TFSI) and Spiro-OMeTAD and determined their relative amounts in doped samples. Mott-Schottky analysis showed two orders of magnitude increase in free charge carrier density and one order of magnitude increase in the charge carrier mobility. The conductivity increased considerably by four orders of magnitude to a maximum of 10 S/m for a very low doping ratio of 8 mol%. The doped polymer films exhibited high thermal and ambient stability resulting in a maximum power factor of 0.07 $\mu\text{W m}^{-1} \text{K}^{-2}$ at a Seebeck coefficient of 140 $\mu\text{V/K}$ for a very low doping ratio of 4 mol%. Also, the concept of HOMO_{OSC-1} to HOMO_{OSC-2} electron transfer is a highly efficient, stable and generic way to p-dope other conjugated polymers.

Doped semiconductor polymers are gaining huge interest as materials in future energy conversion applications such as low-power polymeric thermoelectrics (TEs), because they are light weight, flexible, printable and suitable for large area applications like wearable technologies.^[1, 2, 3, 4] The basic challenge in TE, however, lies in efficient doping of the organic semiconductors (OSCs), because OSCs have extremely low intrinsic charge carrier concentrations and hence very low electrical conductivities in the range of 10^{-6} to 10^{-12} S cm⁻¹. Molecular doping,^[5] commonly used to increase the electrical conductivities of OSCs, involves the addition of a redox active organic or inorganic molecule as dopant. These dopants are capable of accepting (for p-type doping) or donating electrons to OSCs (for n-type doping), thereby generating free holes or electrons in OSCs. For p-type doping, acceptor dopants such as I₂,^[6] FeCl₃,^[7] molybdenum tris(1,2-bis(trifluoromethyl)ethane-1,2-dithiolene) (Mo(tfd)₃),^[8] tetrafluorotetracyano-quinodimethane (F₄TCNQ) and its derivatives^[9, 10] have been extensively used. Although the precise mechanism of molecular doping in disordered semiconductors is still under discussion,^[5, 11, 12] it is widely accepted that molecular doping involves either an integer charge transfer (ICT) or a ground state charge transfer complex (CPX) formation, followed by a charge separation in each case. In the more common ICT mechanism for polymers, an integer number of electrons is transferred from the highest occupied molecular orbital of the OSC (HOMO_{osc}) to the lowest unoccupied molecular orbital of the dopant (LUMO_{dopant}) during p-type doping, generating a coulombically bound electron hole pair. Since the HOMO energy levels of most OSCs are commonly in the range of 4.5–5.5 eV,^[13] this process requires p-dopants with low lying LUMOs, which is challenging in terms of their synthesis and stability.^[14, 15] Moreover, as the dielectric constants of OSCs are low (often in the range of 3 to 4), the coulomb binding energy of the OSC cation and dopant anion pair is high, which lies in the range of 0.5–0.8 eV^[16] and needs to be overcome to generate free charge carriers. This leads to poor doping efficiencies in OSCs and large amounts of dopants up to 30–40 % percent are generally employed. However, theoretical results from Salzman et al.^[17] predict that the density of holes in the HOMO of the OSC reaches a maximum around 50 % dopant concentration, at which the percentage of ionized dopants decreases below 10 %, emphasizing the need to keep the dopant concentrations as low as possible. Moreover, doped systems obtained using acceptor dopants such as F₄TCNQ usually suffer from stability issues.

These general limitations of conventional redox doping led us to a new concept of doping by mixing two p-type semiconductors (OSC-1 and OSC-2): OSC-1 being a pristine (non-doped) semiconductor polymer and major component, and OSC-2 a chemically oxidized semiconductor (low mol. wt. molecule and minor component), which can function as a dopant for OSC-1. Here, the electrons can be transferred from the fully occupied HOMO_{OSC-1} of the polymer to the partly occupied HOMO_{OSC-2}. This partly filled HOMO is most probably a singly occupied molecular orbital (SOMO) as in radicals, but the term SOMO is here not specifically used due to the fact that the presence of unpaired electron is not proven. Thus, electron transfer features a HOMO_{OSC-1} to HOMO_{OSC-2} type transition rather than the conventional

HOMO_{osc} – LUMO_{dopant} type process, and therefore no dopants with extremely low LUMOs are required.

For this purpose, we selected the well-known hole conductor Spiro-OMeTAD(TFSI)₂, a chemically oxidized radical cation salt of pristine 2,2',7,7'-tetrakis(*N*, *N*-di-*p*-methoxyphenylamine)-9,9'-spirobifluorene (Spiro-OMeTAD) as OSC-2, which has a partly filled HOMO to serve as p-type dopant. It is to be noted that Spiro-OMeTAD(TFSI)₂ has been known as an additive to Spiro-OMeTAD from the earlier works of Cappel et al.^[18] and Nguyen et al.^[19] to improve its electrical conductivity when employed in hole transport layers in solar cells. In our approach, we expect that Spiro-OMeTAD(TFSI)₂ may get reduced to Spiro-OMeTAD(TFSI) or Spiro-OMeTAD upon doping the polymer, and the resulting doped system becomes a mixture of two or more hole conductors. Additionally, charge delocalization in conjugated polymer chains can be favorable for charge transport. Since, no new acceptor anions/or radical anions are formed as a result of doping in addition to the highly stable TFSI anion already present, a potential improvement in the thermal and air stability of doped films are also expected. All these factors may give added advantage to the overall electrical conductivity/charge transport of the system and a possibility of reaching the saturation conductivity at much lower concentrations of the dopant.

To check the validity of our doping strategy, we chose a diketopyrrolopyrrole based PDPP[T]₂-EDOT polymer^[20] (IP = -4.49eV), such that its HOMO lies above the HOMO of Spiro-OMeTAD(TFSI)₂ (IP = -5.33 eV). The main questions that we have addressed to answer in this communication are: a) Is electron transfer possible between a PDPP[T]₂-EDOT (OSC-1) and Spiro-OMeTAD(TFSI)₂ (OSC-2), resulting in higher electrical conductivity than Spiro-OMeTAD(TFSI)₂? b) What is the optimum Spiro-OMeTAD(TFSI)₂ concentration required to reach the saturation conductivity and can it be kept low compared to the conventional acceptor dopants such as F4TCNQ?, c) What is the consequence of such a HOMO-HOMO charge transfer on charge carrier concentration, carrier mobility, electrical conductivity, stability and thermoelectric properties of the doped polymer films? and d) Can Spiro-OMeTAD(TFSI)₂ be successfully used as a generic dopant for other classes of p-type polymers?

The chemical structures of the investigated diketopyrrolopyrrole based polymer PDPP[T]₂-EDOT (OSC-1), Spiro-OMeTAD(TFSI)₂ (OSC-2) and Spiro-OMeTAD are shown in **Figure 1a**. PDPP-[T]₂-EDOT (M_n = 19420 g.mol⁻¹; T_m = 334°C in flash DSC at 200K/s) and Spiro-OMeTAD(TFSI)₂ were synthesized using procedures known in the literature and described in the supporting information (SI).^[19, 20, 21,22] Spiro-OMeTAD(TFSI)₂ was characterized using X-ray photoelectron spectroscopy (XPS) and UV-vis spectroscopy. (See **Figures SI 1, SI 2**) for its atomic and chemical composition. Detailed XPS studies (**Figure SI 3 to SI 5**) showed that upon addition of ca. 1, 2 and 9 mol% of Spiro-OMeTAD(TFSI)₂ into PDPP[T]₂-EDOT, the maxima of the N1s and S2p peaks of the latter slightly shifted to a higher binding energy region of 400.3 eV (from 399.8 eV) and 164.4 eV (from 163.9 eV), respectively, indicating the oxidation of the

polymer backbone, i.e., an electron transfer from PDPP[T]₂-EDOT to Spiro-OMeTAD(TFSI)₂ (**Figure SI 5**).^[23, 24]

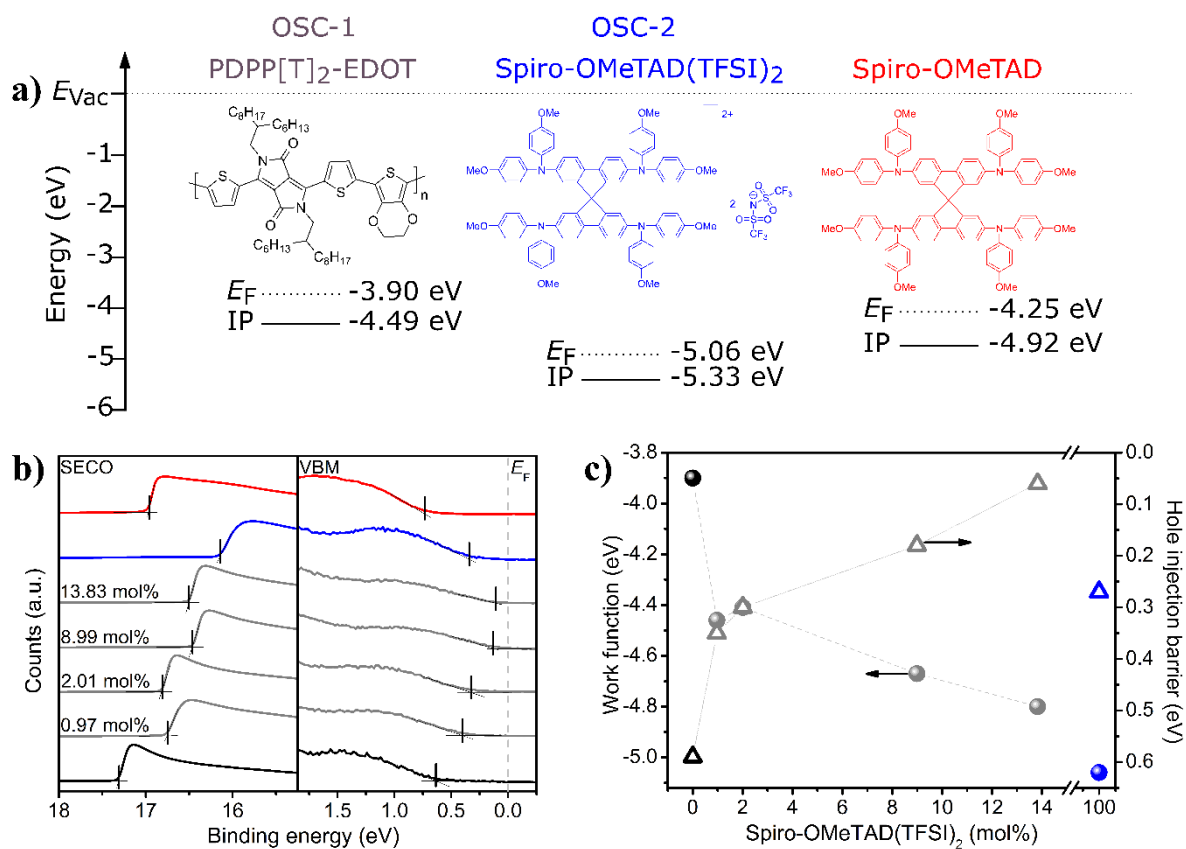


Figure 1 – a) Chemical structures of PDPP[T]₂-EDOT (OSC-1), Spiro-OMeTAD(TFSI)₂(OSC-2) and Spiro-OMeTAD, and schematic diagrams of the corresponding Fermi- and occupied frontier energy levels, measured by UPS; b) Photoemission spectra showing the secondary electron cut-off SECO (left) and valence band maximum VBM (right) regions of OSC-1 (black), doped samples (gray), OSC-2 (blue) and pristine Spiro-OMeTAD (red), scaled with respect to the Fermi energy level (E_F : vertical gray dashed line set at zero eV); c) Variation of the work function (black and gray spheres) and hole injection barriers HIB (triangles) of OSC-1 upon doping with OSC-2 as well as the values for OSC-2 (blue) derived from UPS measurements. The lines in 3d are guidelines for the eye.

While XPS studies give indications of the electron transfer interactions between PDPP[T]₂-EDOT and Spiro-OMeTAD(TFSI)₂, a quantitative assessment of p-doping on the electronic energy levels of the polymer was obtained using UPS. As derived from the valence band maximum and secondary electron cut-off (**Figure 1b**), the work function and ionization energy of the pristine polymer corresponds to 4.49 and 3.90 eV, whereas Spiro-OMeTAD(TFSI)₂ exhibits -5.33 and -5.06 eV, respectively. Details of the ionization energies, work functions (E_F) and the hole injection barriers (HIBs) for differently doped samples (0.97, 2.01, 8.99 and 13.83 mol%) are collected in **Table SI 1**. It can be seen that the E_F of the polymer is shifted from - 3.90 down to -4.77 eV, whereas the ionization energy is stabilized at ca. -4.8 eV. An initial change of 240 meV in the HIB at ca. 0.99 mol% of Spiro-OMeTAD(TFSI)₂ indicates a high trap density in the polymer matrix.^[17, 25] As shown in **Figure 1c**, further increasing the dopant ratio leads to a steady decrease of the HIB from 590 meV (in pristine) down to 60 meV (for 13.83 mol% dopant concentration), virtually merging the HOMO of the polymer with E_F . Such a shift of the HOMO towards E_F ascertains unambiguously p-doping the PDPP[T]₂-EDOT. Further, a

linear approximation of work function and HIB exhibits a slope of ca. $10 k_B T$ across the entire concentration range, a value higher than $k_B T$, commonly observed due to dopant induced disorder in the organic matrix (**Figure SI 6**).^[26] Similarly, a relative broadening of the occupied valence states, i.e., FWHM of the Gaussian peak from 1.11 eV for pristine PDPP[T]₂-EDOT to 1.54 eV for 13.83 mol% of Spiro-OMeTAD(TFSI)₂ doped system (**Figure SI 7**) confirmed the formation of new states due to the oxidation of the polymer matrix or reduction of the dopant, which contributes to the valence states. These observations clearly indicate the highly efficient p-doping capability of Spiro-OMeTAD(TFSI)₂ towards PDPP[T]₂-EDOT.

UV-vis-NIR absorption spectroscopy was used to characterize the absorption features of doping induced novel species and thus to quantify the doping process. The absorption spectra of pristine PDPP[T]₂-EDOT polymer, and doped samples are given in **Figure 2a** and the concentrations are tabulated in **Table SI 2**. Pristine PDPP[T]₂-EDOT exhibits main absorption peaks/shoulders at 440, 860 and 955 nm. As the doping progresses, a decrease in the intensities of the absorption bands of the neutral polymer and a concomitant increase in intensities of the new absorption features at about 1100 nm were observed, confirming charge transfer. Spectro-electrochemical (SEC) measurements (**Figure 2c**) were used to assign the new absorption band to polaronic (oxidized species) absorption at 1100 nm. The small differences in peak positions between SEC spectra and absorption of chemically doped samples (**Figure 2b and c**) arise from the different degrees of oxidation and polarity differences in the medium in both methods. See details of SEC plots under different conditions in **Figure SI 8**.

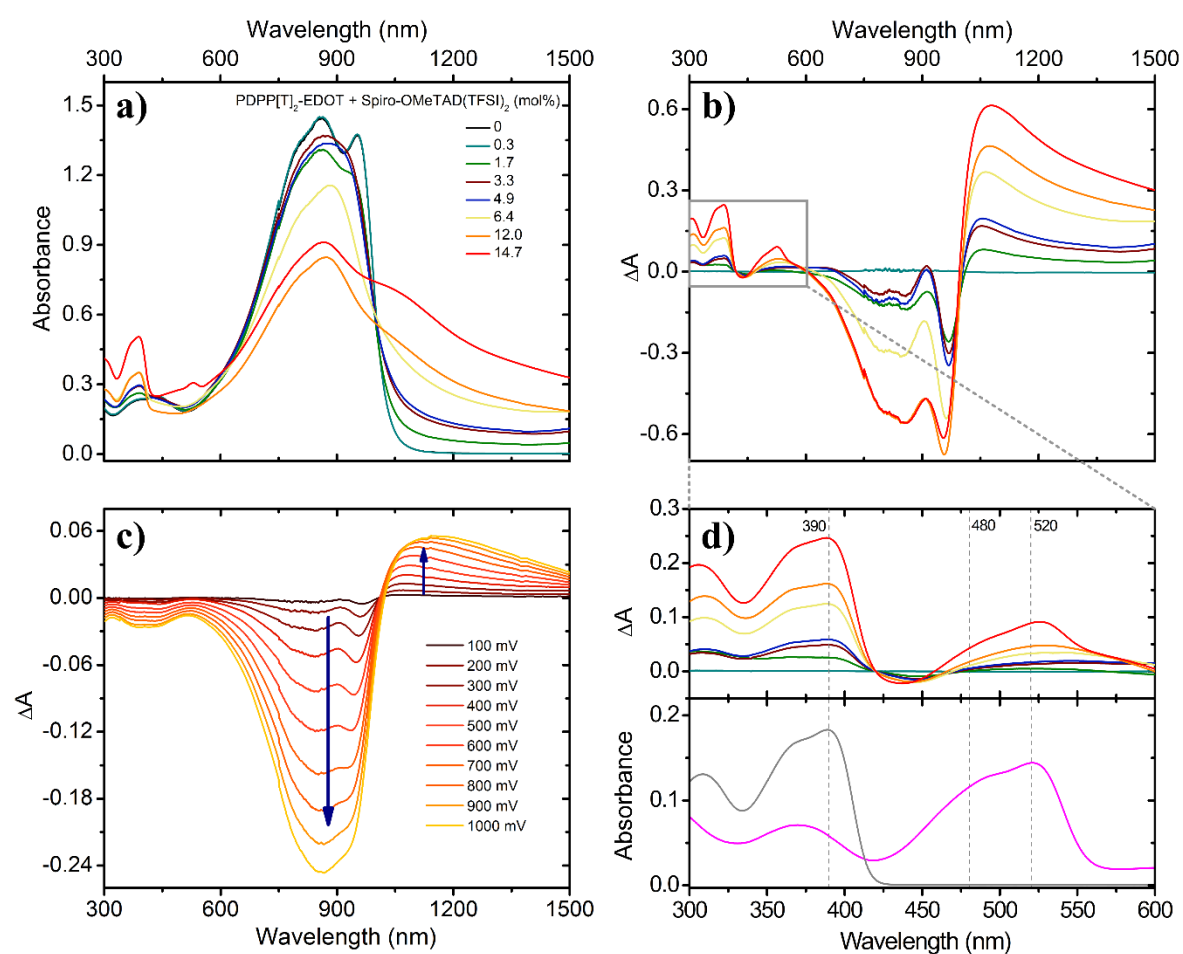


Figure 2 – (a) Absorption spectra of pristine and doped PDPP[T]₂-EDOT solutions at different concentrations of Spiro-OMeTAD(TFSI)₂. (b) Absolute changes in the absorption spectra obtained by subtracting the absorption spectrum of the neutral polymer from the absorption spectra of the doped polymer solutions. (c) Differential spectro-electrochemical UV-Vis-NIR plots of neat PDPP[T]₂-EDOT in solution (d) Expanded absorption spectra of 2b from the region 300 to 600nm along with the absorption of Spiro-OMeTAD(TFSI)₂ (shown in magenta), and Spiro-OMeTAD (shown in gray).

To fundamentally understand the reduction of the Spiro-OMeTAD(TFSI)₂ during the oxidation of PDPP[T]₂-EDOT, difference spectra (ΔA) (**Figure 2b**) were plotted by subtracting the absorption spectrum of the pristine polymer from the absorption spectra of the doped samples. The magnified part (300-600 nm) of this, shown in **Figure 2d** corresponds mainly to the various reduced dopant species since the change in absorption of oxidized polymer species in this range is negligible as shown in SEC studies. Comparing the ΔA spectra with the absorption spectra of Spiro-OMeTAD(TFSI)₂ and Spiro-OMeTAD, (**shown in Figure 2d**) gives a clear indication that pristine Spiro-OMeTAD is formed during doping. However, Fig. 2d alone cannot differentiate the formation of relative amounts of each species. In order to estimate the relative amounts of the Spiro-OMeTAD, Spiro-OMeTAD(TFSI), and the unreacted Spiro-OMeTAD(TFSI)₂ present in doped polymer solutions at different doping concentrations, we used reported molar extinction coefficients ^[19] of Spiro-OMeTAD at 390nm, Spiro-OMeTAD(TFSI) and Spiro-OMeTAD(TFSI)₂ at 390, 480 and 520 nm respectively. . The molar

concentrations of each species were then calculated using Beer-Lambert law. Details are shown in the **Figure SI 9** and **Table SI 3**. As can be seen in **Figure SI 9**, the slope of concentration plot for Spiro-OMeTAD(TFSI) is the highest, indicating a rapid increase in the concentration of Spiro-OMeTAD(TFSI) compared to the other two species. Additionally, the sum of the relative concentration of the reduced products (Spiro-OMeTAD(TFSI) and Spiro-OMeTAD) saturates around 70% (**Table SI 3**). This clearly confirms a HOMO_{OSC-1} to HOMO_{OSC-2} electron transfer from PDPP[T]₂-EDOT to Spiro-OMeTAD(TFSI)₂ and its reduction from +2 to +1 as well as to the pristine state. A similar doping pattern was also observed in the absorption spectra of solid thin films (**Figure SI 10**). The high ambient stability of the doped polymer solutions and films was confirmed by the persistence of the absorption spectra during five days under inert atmosphere and afterwards in air (**Figure SI 11**).

In order to evaluate the consequences of doping PDPP[T]₂-EDOT with Spiro-OMeTAD(TFSI)₂, the charge carrier density (N_D) was calculated from the Boltzmann corrected Mott-Schottky equation (equation 1) for capacitance-voltage measurements on metal-insulator-semiconductor (MIS) devices at RT (**Figure SI 12** and **Table SI 4**)^[27] using impedance spectroscopy (**Figure 3a** and **Table SI 5**, and **6** for details).

$$\frac{1}{C_{tot}^2} = \frac{2}{q\epsilon_0\epsilon_{OSC}A^2N_D} \left(V_{Fb} - V_{Bias} - \frac{k_B T}{q} \right) \quad \text{equation 1}$$

where C_{tot} is the total capacitance obtained from the impedance, q is the elementary charge, ϵ_0 and ϵ_{OSC} are the dielectric constants of the vacuum and the organic layer (~ 3), A the active area, V_{Fb} the flat band voltage, V_{Bias} the applied bias voltage, k_B the Boltzmann constant and T the junction temperature.

Also, the zero field mobility of majority charge carriers (μ_0) was calculated by extrapolating the obtained Poole-Frenkel type field dependency (Equation 2) in conjunction with negative differential susceptance measurements ($-\Delta B$) of metal-semiconductor (MS) devices (**Figure 3a** and **Table SI 7** for details).

$$\mu = \frac{4}{3} \frac{d^2}{\tau_t V_{Bias}} \quad \text{equation 2}$$

where τ_{tr} is the transit time obtained from ($-\Delta B$) measurements and d being the thickness of the organic layer.

The pristine polymer PDPP[T]₂-EDOT exhibits N_D of $9.80 \pm 3.09 \cdot 10^{19} \text{ cm}^{-3}$, which increases to a maximum of low cm^{-3} , when doped with 4.74 mol% of Spiro-OMeTAD(TFSI)₂. Similarly, μ_0 increased from $1.18 \pm 0.16 \cdot 10^{-3} \text{ cm}^2\text{V}^{-1}\text{s}^{-1}$ to $9.81 \pm 0.71 \cdot 10^{-3} \text{ cm}^2\text{V}^{-1}\text{s}^{-1}$, until it starts decreasing at higher concentrations of Spiro-OMeTAD(TFSI)₂. A general trend of increasing N_D and μ_0 was observed up to 5 mol% of Spiro-OMeTAD(TFSI)₂. A deterioration in the electronic transport properties (N_D and μ_0) above 5 mol% can be attributed to increased static disorder or precipitation of the active dopant.^[28] Although Arkhipov^[16] et al predicted that an initial decrease in the mobility could occur due to doping-induced coulombic disorder, we could not observe this behavior because the zero-field mobilities for 0 mol% and 2 mol% Spiro-OMeTAD(TFSI)₂ lie well within each other's error margin. Using Pasveer's theory, the DOS width of doped PDPP[T]₂-EDOT can be estimated as ca. 126 meV at 3.3 mol% of Spiro-

OMeTAD(TFSI)₂, which proves the high level of disorder in our investigated system. [29] Thus impedance studies confirm the increase in charge carrier density as well as the mobility.

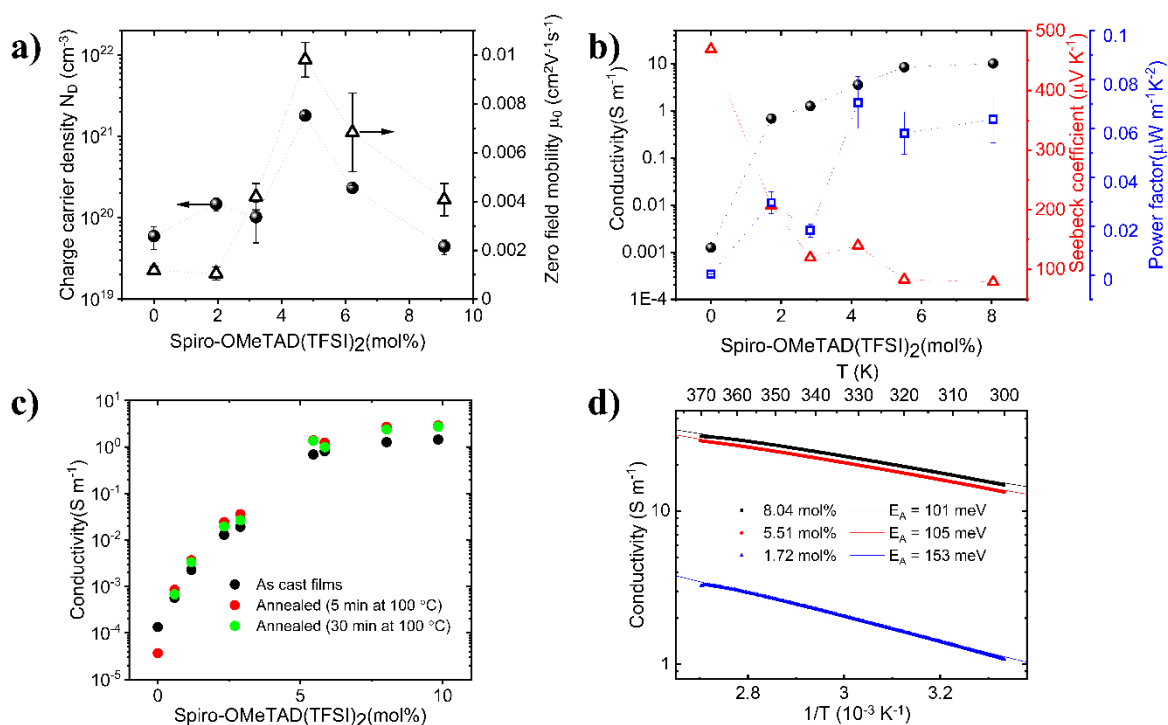


Figure 3 – a) Charge carrier density N_D (circles) and zero-field mobility μ_0 (triangles) of PDPP[T]₂-EDOT (OSC-1) doped with Spiro-OMeTAD(TFSI)₂ (OSC-2) (3b) Electrical conductivity (σ) (black), Seebeck coefficient (S) (red), and corresponding Power Factor ($PF = \sigma S^2$) (blue) as function of Spiro-OMeTAD(TFSI)₂ concentration at room temperature, (3c) Temperature stability of conductivity for doped samples: as-prepared films (black), annealed at 100 °C for 5 min (red) and annealed at 100 °C for 30 min (green) in glovebox and (3d) Temperature dependent conductivity measurements in the range of 300 to 370 K on samples with doping concentrations of 1.72 mol% (blue), 5.51 mol% (red) and 8.04 mol% (black). From Arrhenius fits, the activation energies of 153, 105 and 101 meV respectively were obtained.

Furthermore, electrical conductivity, Seebeck coefficient and resulting power factor ($PF = \sigma S^2$) of PDPP[T]₂-EDOT films with varying Spiro-OMeTAD(TFSI)₂ concentrations were measured as shown in Figure 3b and all values are collected in Table SI 8. The conductivities of the doped films increased by four orders of magnitude from $1.25 \cdot 10^{-3}$ S/m for the pristine PDPP[T]₂EDOT to a maximum of 10.21 S/m, with a saturation in conductivity attained around 5 mol% of Spiro-OMeTAD(TFSI)₂ in PDPP[T]₂EDOT films. It is to be noted that this saturation value is more than two orders of magnitude higher than the measured value for pure Spiro-OMeTAD(TFSI)₂ ($\sigma = 5.41 \cdot 10^{-2}$ S/m), indicating the additional contribution of doped conjugated polymers towards σ via delocalization of charges. A comparison with other literature reports on F4TCNQ doped polymers such as PDPP(6-DO)2TT ($\sigma_{max} = 6.4 \times 10^{-2}$ S/m at a molar doping ratio = 0.33) [30] or P3HT-PEO blends ($\sigma_{max} = 84.7$ S/m at a mol% = 20) [31] reflect that, with Spiro-OMeTAD(TFSI)₂ a saturation conductivity of 10.21 S/m could be reached using quite low amounts of dopant. As expected for a molecular doping process, the measured conductivity σ rises steeply upon trap-filling. Further introduction of the dopant leads to dopant saturation and eventually dopant reserve, causing σ to asymptotically approximate a steady value. [32] This behaviour was also verified by measuring conductivity through IV-curve tracing of planar,

interdigitated electrode structures. The high thermal and air stability of the doped conducting polymer films was confirmed by the excellent retention of electrical conductivity after annealing at 100°C as well as exposing the samples to air (**Figure 3c** and **Figure SI 13**). We assume that the absence of any acceptor radical anions as in the case of F4TCNQ doped systems contribute strongly towards the thermal and ambient stability. The Seebeck coefficients of the doped polymer films were measured (**Figure SI 14**) to estimate their power factor ($PF = \sigma S^2$). The Seebeck coefficients gradually decreased from 469 $\mu\text{V/K}$ for the pristine PDPP[T]₂EDOT film to 79 $\mu\text{V/K}$ as the amount of Spiro-OMeTAD(TFSI)₂ increased to 8.04 mol%. This reciprocal interdependence of σ and S agrees with theoretical descriptions of charge carrier transport in organic semiconductors based on an effective transport band model yielding equation 3^[33]

$$S = -\frac{k_B}{q} \int_{-\infty}^{\infty} \frac{(E-E_F)}{k_B T} \frac{\sigma(E)}{\sigma} dE \quad \text{equation 3}$$

Here, q refers to the elementary charge, E_F to the Fermi-energy and $\sigma(E)$ to the electrical conductivity for a given energy E within the transport band. However, depending on the respective density of states for a given polymer as well as on its energetic disorder, the Seebeck-coefficient does not necessarily scale inversely proportional to σ but rather as $S \sim \sigma^x$, with $0 < x < 1$. Fitting the experimental Seebeck data as a function of σ reveals the relation $S \sim \sigma^{-0.2}$ (**Figure SI 15**), which is in line with the previously reported empirical power law $S \sim \sigma^{-0.25}$ for doped polymeric semiconductors.^[34] In good agreement with this empirical model, the corresponding Power Factor PF is found to increase with $\sigma^{0.6}$.

As depicted in **Figure. 3b**, the power factor increases with higher doping concentrations from 0.0003 $\mu\text{W m}^{-1} \text{K}^{-2}$ for the undoped polymer to reach its maximum of about 0.07 $\mu\text{W m}^{-1} \text{K}^{-2}$ at an intermediate Spiro-OMeTAD(TFSI)₂ doping concentration of 4.19 mol%. The trade-off between the increase in conductivity and the decrease in Seebeck coefficient results in a net improvement of two orders of magnitude in PF as shown in figure. 3b Temperature dependent conductivity measurements (**Figure 3d**) revealed an increase in electrical conductivity with temperature. The charge carrier activation energy E_A has been extracted by fitting the data according to equation 4. As can be seen by the semi-logarithmic plot of $\sigma(1/T)$ in **Figure 3d**, for all samples the electrical conductivity shows an increase with temperature according to an Arrhenius-type behavior that can be described by:

$$\sigma(T) = \sigma_0 \exp\left(-\frac{E_A}{k_B T}\right) \quad \text{equation 4}$$

with σ_0 : saturation conductivity at high temperatures, E_A : thermal activation energy of charge carrier transport, T : absolute temperature and k_B : Boltzmann constant. The activation energies decrease towards higher doping concentrations from (153 ± 19) meV at 1.72 mol% of Spiro-OMeTAD(TFSI)₂ to (101 ± 8) meV at 8.04 mol%, due to the incremental filling of the Gaussian-distributed density of states (DOS) accompanied by an increase in contributing transport states.

We also tested if this concept of HOMO-HOMO electron transfer using Spiro-OMeTAD(TFSI)₂ can be extended to other common semiconductor polymers such as P3HT and a soluble PEDOT derivative (**Figure SI 16**), in order to widen the applicability and scope of this strategy. Our preliminary results show that this concept has general validity and the electrical conductivities of P3HT and PEDOT increased from $3.33 \cdot 10^{-4}$ S/m to $8.99 \cdot 10^{-1}$ S/m and from $9.12 \cdot 10^{-4}$ S/m to $1.28 \cdot 10^{-1}$ S/m, respectively, upon doping. Further detailed doping studies of P3HT and PEDOT using Spiro-OMeTAD(TFSI)₂ are currently under investigation.

In summary, we demonstrated a highly efficient p-doping strategy for the diketopyrrolopyrrole based PDPP[T]₂-EDOT polymer (OSC-1) by mixing with another p-type semiconductor Spiro-OMeTAD(TFSI)₂ (OSC-2), achieving a HOMO to HOMO electron transfer from OSC-1 to OSC-2. The doping was confirmed by the gradual shift of the E_F towards polymer HOMO upon adding Spiro-OMeTAD(TFSI)₂ using UPS analysis. The evidences for p-doping via electron transfer from HOMO_{OSC-1} to HOMO_{OSC-2} were corroborated using XPS, SEC and UV-vis-NIR studies. Mott-Schottky analysis of impedance measurements on MIS devices exhibited two orders of magnitude increase in free charge carrier density with a maximum N_D of $8.81 \pm 3.77 \cdot 10^{21}$ cm⁻³. Similarly, zero-field mobility (μ_0) of the pristine polymer increased from $1.18 \cdot 10^{-3}$ cm²V⁻¹s⁻¹ to $9.81 \cdot 10^{-3}$ cm²V⁻¹s⁻¹. The electrical conductivities of the doped films showed four orders of magnitude increase from $1.25 \cdot 10^{-3}$ S/m for the pristine PDPP[T]₂-EDOT to a maximum of 10.21 S/m. Both, the electrical conductivity and the Seebeck measurements confirmed the high stability of the doped polymer films upon thermal annealing as well as upon exposing the films to air. This is a major advantage of doping OSC-1 with OSC-2. Finally, a maximum power factor of 0.07 μ W/mK² was reached at a Seebeck coefficient value of 140 μ V/K for a doping ratio of 4.19 mol%. The general validity of this doping concept was demonstrated by employing Spiro-OMeTAD(TFSI)₂ as dopant for other classes of polymers such as PEDOT and P3HT. This innovative doping approach enables the use of a wide variety of doped hole conductors as dopants as well as blend components without the requirement of any additional acceptor molecules with low LUMO values.

Supporting Information

Supporting Information is available from the Wiley Online Library or from the author.

Acknowledgements

Bavarian State Ministry for Education, Science and the Arts (Project: SolTech) is acknowledged for financial support. Also the XPS/UPS facility (PHI 5000 VersaProbe III system) at Keylab Device Engineering in Bavarian Polymer Institute, University of Bayreuth is acknowledged. M.S. gratefully acknowledges financial support by the Deutsche Bundesstiftung Umwelt.

Conflict of Interest

The authors declare no conflict of interest.

Keywords

Organic semiconductors, molecular doping, polymer thermoelectrics, ultraviolet photoelectron spectroscopy, Mott-Schottky.

- [1] A. C. Arias, J. D. MacKenzie, I. McCulloch, J. Rivnay, A. Salleo, *Chem. Rev.* **2010**, *110*, 3.
- [2] H. M. Elmoughni, A. K. Menon, R. M. W. Wolfe, S. K. Yee. *Adv. Mater. Technol.* **2019**, *4*, 1800708.
- [3] B. Russ, A. Glaudell, J. J. Urban, M. L. Chabinyc, R. A. Segalman. *Nat. Rev. Mater.* **2016**, *1*, 16050.
- [4] M. Goel, M. Thelakkat. *Macromolecules* **2020**, *53*, 3632
- [5] I. E. Jacobs, A. J. Moulé. *Adv. Mater.* **2017**, *29*, 1703063.
- [6] C. J. Boyle, M. Upadhyaya, P. Wang, L. A. Renna, M. Lu-Díaz, S. P. Jeong, N. Hight-Huf, L. Korugic-Karasz, M. D. Barnes, Z. Aksamija, D. Venkataraman. *Nat. Commun.* **2019**, *10*, 2827.
- [7] Z. Liang, M. J. Boland, K. Butrouna, D. R. Strachanb, K. R. Graham. *J. Mater. Chem. A* **2017**, *5*, 15891.
- [8] Y. Qi, T. Sajoto, S. Barlow, E.-G. Kim, J. -L. Bre´das, S.R. Marder, Antoine Kahn. *J. Am. Chem. Soc.* **2009**, *131*, 12530.
- [9] D. Kiefer, R. Kroon, A. I. Hofmann, H. Sun, X. Liu, A. Giovannitti, D. Stegerer, A. Cano, J. Hynynen, L. Yu, Y. Zhang, D. Nai, T. F. Harrelson, M. Sommer, A. J. Moulé, M. Kemerink, S. R. Marder, I. McCulloch, M. Fahlman, S. Fabiano, C. Müller. *Nat. Mater.* **2019**, *18*, 149.
- [10] P. Pingel, D. Neher. *Phys. Rev. B* **2013**, *87*, 115209.
- [11] M. L. Tietze, J. Benduhn, P. Pahner, B. Nell, M. Schwarze, H. Kleemann, M. Krammer, K. Zojer, K. Vandewal, K. Leo. *Nat. Commun.* **2018**, *9*, 1182.
- [12] A. Mityashin, Y. Olivier, T. V. Regemorter, C. Rolin, S. Verlaak, N. G. Martinelli, D. Beljonne, J. Cornil, J. Genoe, P. Heremans. *Adv. Mater.* **2012**, *24*, 1535.
- [13] J. Chen, Y. Cao. *Acc. Chem. Res.* **2009**, *42*, 1709.
- [14] J. Saska, G. Gonel, Z. I. Bedolla-Valdez, S. D. Aronow, N. E. Shevchenko, A. S. Dudnik, A. J. Moulé, M. Mascal. *Chem. Mater.* **2019**, *31*, 1500.
- [15] V. A. Kolesov, C. F.-H., W.-F. Chou, N. Aizawa, F. A. Larrain, M. Wang, A. Perrotta, S. Choi, S. Graham, G. C. Bazan, T.-Q. Nguyen, S. R. Marder, B. Kippelen. *Nat. Mater.* **2017**, *16*, 474.
- [16] V. I. Arkhipov, P. Heremans, E. V. Emelianova, H. Bäessler, *Phys. Rev. B* **2005**, *71*, 045214.
- [17] I. Salzmann, G. Heimel, M. Oehzelt, S. Winkler, N. Koch. *Acc. Chem. Res.* **2016**, *49*, 370.
- [18] U. B. Cappel, T. Daeneke, U. Bach. *Nano Lett.* **2012**, *12*, 4925.
- [19] W. H. Nguyen, C. D. Bailie, E. L. Unger, M. D. McGehee. *J. Am. Chem. Soc.* **2014**, *136*, 10996.
- [20] C. J. Mueller, C. R. Singh, M. Thelakkat. *J. Polym. Sci, Part B: Polym. Phys.* **2016**, *54*, 639
- [21] C. J. Mueller, E. Gann, C. R. Singh, M. Thelakkat, C. R. McNeill. *Chem Mater.* **2016**, *28*, 7088.
- [22] B. Tan, S. R. Raga, A. S. R. Chesman, S. O. Fürer, F. Zheng, D. P. McMeekin, L. Jiang, W. Mao, X. Lin, X. Wen, J. Lu, Y.-B. Cheng, U. Bach, *Adv. Energy Mater.* **2019**, *9*, 1901519.
- [23] R. Schölin, M. H. Karlsson, S. K. Eriksson, H. Siegbahn, E. M. J. Johansson, H. Rensmo, *J. Phys. Chem. C* **2012**, *116*, 26300.
- [24] C. G. Wu, Y. R. Yeh, L. N. Chien, *Polymer* **2000**, *41*, 5839.
- [25] M. L. Tietze, L. Burtone, M. Riede, B. Lüssem, K. Leo, *Phys. Rev. B* **2012**, *86*, 035320.
- [26] S. Olthof, W. Tress, R. Meerheim, B. Lüssem, K. Leo, *J. Appl. Phys.* **2009**, *106*, 103711.
- [27] K. Gelderman, L. Lee, S. W. Donne. *J. Chem. Educ.* **2007**, *84*, 685.
- [28] M. Schwarze, C. Gaul, R. Scholz, F. Bussolotti, A. Hofacker, K. S. Schellhammer, B. Nell, B. D. Naab, Z. Bao, D. Spoltore, K. Vandewal, J. Widmer, S. Kera, N. Ueno, F. Ortman, K. Leo. *Nat. Mater.* **2019**, *18*, 242.
- [29] R. Coehoorn, W. F. Pasveer, P. A. Bobbert, M. A. J. Michels. *Phys. Rev. B* **2005**, *72*, 155206.
- [30] Y. Karpov, T. Erdmann, I. Raguzin, M. Al-Hussein, M. Binner, U. Lappan, M. Stamm, K. L.

Gerasimov, T. Beryozkina, V. Bakulev, D. V. Anokhin, D. A. Ivanov, F. Günther, S. Gemming, G. Seifert, B. Voit, R. D. Pietro, A. Kiriya. *Adv. Mater.* **2016**, *28*, 6003.

[31] D. Kiefer, L. Yu, E. Fransson, A. Gómez, D. Primetzhofer, A. Amassian, M. Campoy-Quiles, C. Müller. *Adv.Sci.* **2017**, *4*, 1600203.

[32] M. L. Tietze, P. Pahnner, K. Schmidt, K. Leo, B. Lüssem. *Adv. Funct. Mater.* **2015**, *25*, 2701.

[33] G. Kim, K. P. Pipe. *Physical Review B*, **2012**, *86*, 085208.

[34] A. M. Glauddell, J. E. Cochran, S. N. Patel, M. L. Chabinyc. *Adv. Energy Mater.* **2015**, *5*, 1401072.

Electronic Supplementary Information

HOMO – HOMO Electron Transfer: An Elegant Strategy for p-type Doping of Polymer Semiconductors towards Thermoelectric Applications

*Mahima Goel, Marie Siegert, Gert Krauss, John Mohanraj, Adrian Hochgesang, David C. Heinrich, Martina Fried, Jens Pflaum, Mukundan Thelakkat**

Experimental Section and Methods:

General: Electronic grade Spiro-OMeTAD (SHT-263 Solarpur®) was purchased from Merck KGaA, Germany. ¹H-NMR spectra were measured on a Bruker Avance Spectrometer 300 MHz (Bruker Corp., Billerica, MA, USA). Gas-Chromatography measurements were conducted on an Agilent 7890A GC-System with an Agilent 19091J-413 HP-5 (5 % Phenyl Methyl Siloxane, 30 m x 320 μm x 0.25 μm) column and FID-detector (Agilent Technologies GmbH, Oberhaching, Germany). Size exclusion chromatography was performed utilizing a Waters 515 HPLC pump and THF with 0.25 wt% tetrabutylammonium bromide (TBAB) as eluent at a flow rate of 0.5 mL/min. 100 μL of polymer solution (1-2 mg/mL) was injected with a 707 Waters auto-sampler into a column setup comprising a guard column (Agilent PLgel Guard MIXED-C, 5 × 0.75 cm, particle size 5 μm) and two separation columns (Agilent PLgel MIXED-C, 30 × 0.75 cm, particle size 5 μm). Polymer size distributions were monitored with a Waters 998 photodiode array detector at 254 nm and a Waters 414 refractive index detector. Narrow distributed polystyrene standards were used for calibration and 1,2-dichlorobenzene as an internal reference. Solvents for the use in polymerizations were extra dry solvents, used as purchased from Acros Organics (Acros Organics, Geel, Belgium). Solvents for Soxhlet-extractions were P.A. grade solvents, used without further purification.

Synthesis of PDPP-[T]₂-EDOT: Both, the synthesis of the diketopyrrolopyrrole-, and the 3,4-ethylenedioxythiophene co-monomers, as well as the polymerization were conducted following procedures reported by our group. ^[1, 2] **GPC:** $M_n = 19420 \text{ g} \cdot \text{mol}^{-1}$, $M_w = 39661 \text{ g} \cdot \text{mol}^{-1}$, $\bar{D} = 2.03$. **¹H-NMR:** ¹H NMR (300 MHz, CDCl₃) δ [ppm] = 9.25 - 8.62 (br. s, 2 H), 6.81 - 6.30 (br., 2 H), 5.35 - 4.49 (br., 4 H), 4.48 - 3.71 (m, 4 H), 2.13 - 0.55 (s, 48 H). $T_m = 334 \text{ }^\circ\text{C}$ in flash DSC at 200 K/s.

Synthesis of Spiro-OMeTAD(TFSI)₂: The dopant Spiro-OMeTAD(TFSI)₂ was synthesized by oxidizing N₂,N₂,N₂',N₂',N₇,N₇,N₇',N₇'-octakis(4-methoxyphenyl)-9,9'-spirobi[9H-fluorene]-2,2',7,7'-tetramine (Spiro-OMeTAD) with silver bis(trifluoromethanesulfonyl)imide. A flame dried Schlenk-flask was charged with 0.2 mmol of Spiro-OMeTAD and 0.44 mmol silver bis(trifluoromethanesulfonyl)imide in 25 mL of dry DCM. The violet mixture was stirred for 24 h at room temperature. Precipitated silver was removed by filtration, the filtrate was concentrated in vacuum to afford a dark violet solid. The solid was precipitated with (C₂H₅)₂O, from dry DCM three times and dried under high vacuum. The product was obtained in 84 %

yield (309 mg) as deep violet powder. $^1\text{H-NMR}$ and $^{13}\text{C-NMR}$: no signals. Spiro-OMeTAD(TFSI) $_2$ was characterized using X-ray photoelectron spectroscopy and UV-vis spectroscopy.

Characterization Methods:

XPS measurements: XPS spectra were measured with a PHI 5000 VersaProbe III system fitted with an Al K α excitation source ($h\nu = 1486.6$ eV) and a dual neutralizer (electron gun and Ar^+) at 10^{-10} mbar pressure. An X-ray source diameter of 100 mm was used to locally excite the samples; the corresponding photoemission with 45° take-off angle was collected at the multichannel analyzer. The survey and the detailed spectra were measured with pass energies of 224 eV and 69 eV, respectively. The standard deviation on the reported energy values is ± 0.1 eV. The reproducibility of the observed results was confirmed by performing at least three measurements at different places of the samples. The spectra were analyzed with a Multipak software pack, provided by the manufacturers. All emission signals were referenced to adventitious C1s peak at 284.8 eV. For quantitative analysis of the spectra, Shirley background correction was used. XPS spectra of spiro-OMeTAD(TFSI) $_2$ and pristine spiro-OMeTAD are compared in Figure SI 1. Both compounds show characteristic emission lines of carbon (C1s), oxygen (O1s) and nitrogen (N1s) elements; in addition, fluorine (F1s, 688.5 eV) and sulphur (S2p, 168.4 eV) lines are observed from spiro-OMeTAD(TFSI) $_2$ due to the presence of TFSI anion. Interestingly, the chemical oxidation of the spiro-OMeTAD to spiro-OMeTAD(TFSI) $_2$ doesn't seem to impart significant changes in the characteristic peak positions; however, full-width half maximum (FWHM) of the oxygen and nitrogen lines of spiro-OMeTAD(TFSI) $_2$ is comparatively larger than that of the same lines from pristine spiro-OMeTAD (Figure SI 2). It is to be noted that both oxygen and nitrogen are part of the TFSI anion in which both elements are at different chemical environment compared to the ones present in pristine spiro-OMeTAD. Thus, it is precarious to attribute the change in the FWHM to oxidized spiro-OMeTAD.

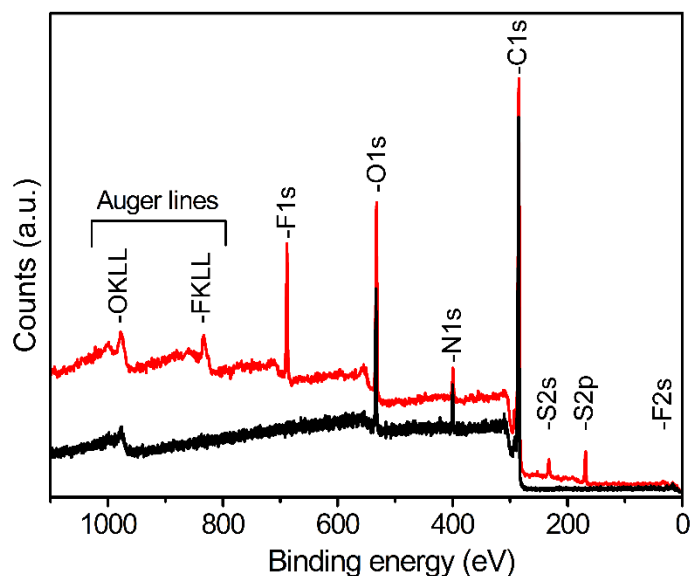


Figure SI 1. XPS survey spectra of pristine Spiro-OMeTAD (black) and Spiro-OMeTAD(TFSI)₂ (red) powders showing characteristic emission lines of carbon, oxygen, nitrogen elements; in addition, Spiro-OMeTAD(TFSI)₂ displays sulphur and fluorine peaks, originating from the TFSI anion.

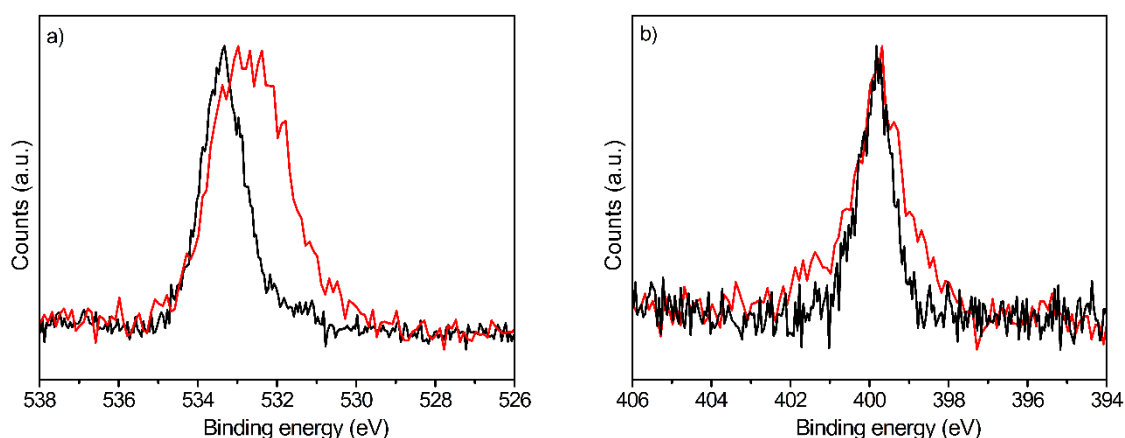


Figure SI 2. Detailed XPS spectra of pristine Spiro-OMeTAD (black) and Spiro-OMeTAD(TFSI)₂ (red) powders collected at the emission regions of a) oxygen (O1s) and b) nitrogen (N1s).

The atomic composition of the chemically oxidized Spiro-OMeTAD(TFSI)₂ is derived based on the quantitative analysis of the detailed spectra collected at nitrogen (N1s), fluorine (F1s) and sulphur (S2p) regions. Theoretically, the atomic ratio between nitrogen to sulphur (N/S) in Spiro-OMeTAD(TFSI) and Spiro-OMeTAD(TFSI)₂ is 2.5 and 1.5, respectively, whereas, the same between nitrogen to fluorine (N/F) is 0.83 and 0.5 in singly and doubly oxidized Spiro-OMeTAD. Based on the standard quantification method, the calculated N/S and N/F from the detailed spectra obtained from Spiro-OMeTAD(TFSI)₂ are 1.87 and 0.59 respectively. Its atomic composition as derived from the detailed spectra collected at nitrogen (N1s), fluorine (F1s) and sulphur (S2p) regions suggest about 60 to 70 % of Spiro-OMeTAD(TFSI)₂, indicating the possible presence of traces of Spiro-OMeTAD(TFSI) in the dopant, as it is practically challenging to quantitatively control the chemical oxidation of Spiro-OMeTAD and further purification processes.

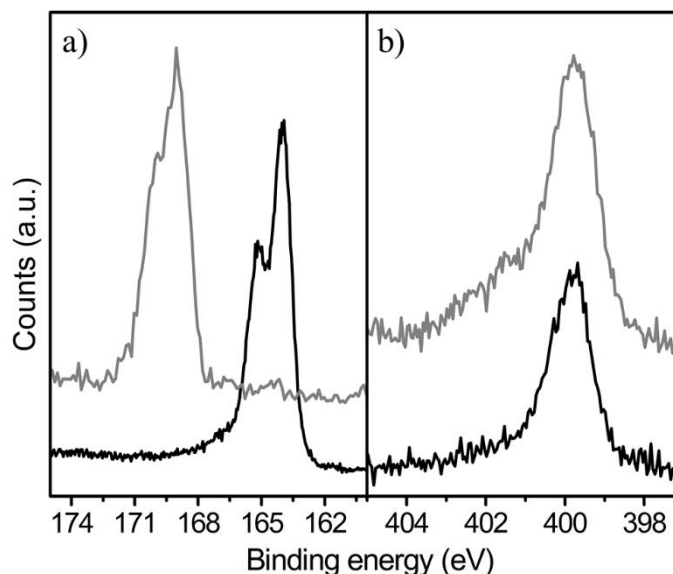


Figure SI 3. X-ray photoelectron spectra of PDPP-[T]₂-EDOT (black) and Spiro-OMeTAD(TFSI)₂ (grey) focused on a) S2p region and b) N1s region.

Both PDPP[T]₂-EDOT and Spiro-OMeTAD(TFSI)₂ contain mostly same elements (C, O, N and S) except Fluorine from TFSI anion; however, variation in the oxidation state of N and S in these compounds result in slight differences in their characteristic core peak features. The S2p doublet (S2p_{3/2} and S2p_{1/2}) from Spiro-OMeTAD(TFSI)₂ is observed at 169.03 eV, corresponding to the sulfonyl group, whereas a doublet with a maximum at 163.93 eV stems from thiophene unit in PDPP[T]₂-EDOT. In the case of nitrogen, the difference in N1s peak from Spiro-OMeTAD(TFSI)₂ and PDPP[T]₂-EDOT is subtle as there is no obvious binding energy shift of the peak maxima; however, nitrogen in Spiro-OMeTAD(TFSI)₂ is supposed to exist in two different oxidation states, i.e. neutral as well as +1, which results in a broad N1s peak with an extended tail in the high binding energy region. In fact, fitting this broad peak with Gaussian-Lorentzian function results in two peaks; a low binding energy peak with the maximum at 399.73 eV and full width half maximum (FWHM) of 1.3 eV, and a broad high binding energy peak with the maximum at 401.3 eV and FWHM of 2 eV (**Figure SI4a**).

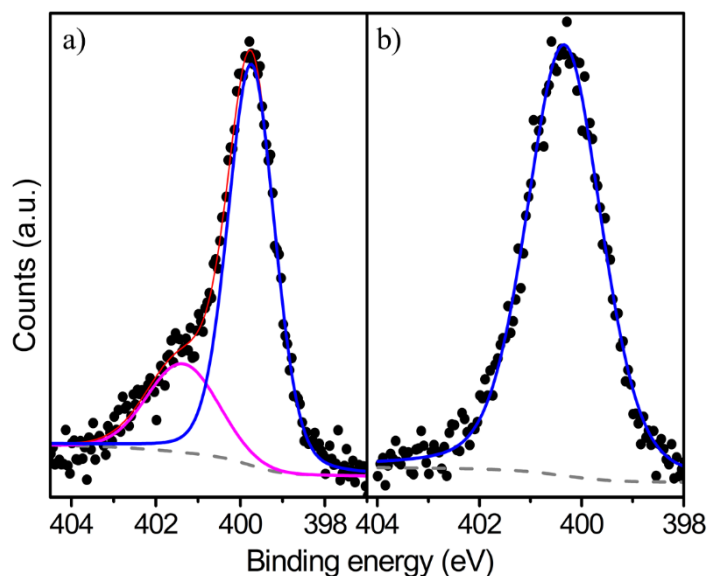


Figure SI 4. Deconvolved N1s spectra of a) Spiro-OMeTAD(TFSI)₂ and b) PDPP-[T]₂-EDOT using Gaussian functions. Color code: black dots-experimental curves; red line-composite spectrum; blue and magenta lines-fitted curves; grey dashed line-shirley background.

In contrast, N1s peak from PDPP[T]₂-EDOT is mostly a narrow single Gaussian peak, despite the presence of a weak, unresolvable tail with a poor signal to noise ratio, with the maximum at 399.8 eV and FWHM of 1.76 eV (Figure S4b, Supporting Information).

Mixing Spiro-OMeTAD(TFSI)₂ with Spiro-OMeTAD is reported to lead to disproportionation reaction ^[3] whereas the electronic interactions of Spiro-OMeTAD(TFSI)₂ with polymer semiconductors are not investigated till now. As evidenced in XPS, upon addition of ca. 1, 2 and 9 mol% of Spiro-OMeTAD(TFSI)₂ into PDPP[T]₂-EDOT, the maxima of N1s and S2p peaks of the latter slightly shifted to a higher binding energy region 400.3 eV and 164.4 eV, respectively, indicating the oxidation of polymer backbone, i.e., an electron transfer from PDPP[T]₂-EDOT to Spiro-OMeTAD(TFSI)₂. The S2p region also shows an additional weak band at the high binding energy region (ca. 169 eV) in the case of polymer-dopant mixtures, which originates from TFSI anion of the dopant. ^[4] Notably, N1s feature from the redox mixtures is a single Gaussian-Lorentzian peak with an increased FWHM of 1.8, 1.7 and 1.65 eV for 1, 2 and 9 mol%, respectively, compared to the pristine polymer (1.3 eV), indicating the presence of nitrogen in multiple chemical environment in different components.

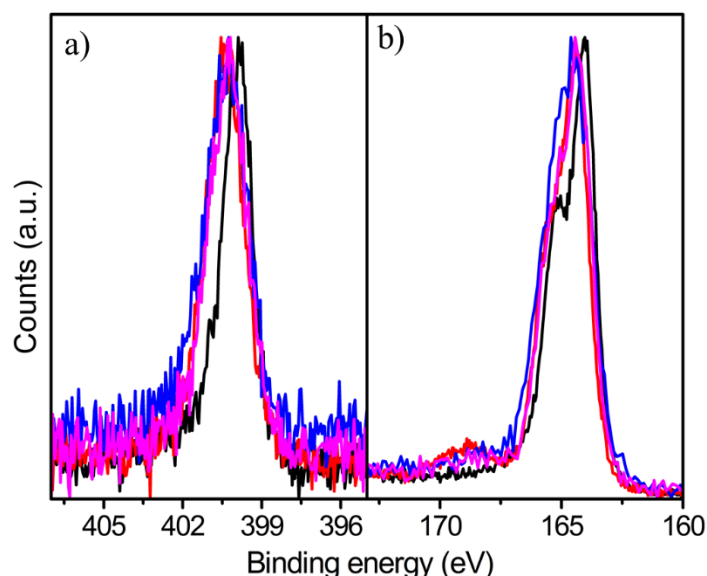


Figure SI 5. a) N1s and b) S2p normalized detailed spectra of polymer PDPP-[T]₂-EDOT (black) with 1 (red), 2 (blue) and 9 (magenta) mol% of Spiro-OMeTAD(TFSI)₂.

UPS measurements: pre-prepared ITO substrates were cut into rectangular pieces of 14 by 14 mm and cleaned by ultra-sonication in 2 vol% aqueous hellmanex-III solution, water, acetone, isopropanol and pre-treated with O₃/UV for 15 min at 50 °C. PDPP-[T]₂-EDOT (5.4 mg in 540 μL chlorobenzene) and Spiro-OMeTAD(TFSI)₂ (2.15 mg in a binary solvent mixture consisting of 90 μL chlorobenzene and 10 μL of CH₃CN) were mixed in appropriate amounts to obtain the molar ratios of Spiro-OMeTAD(TFSI)₂ as 0.97 mol%, 2.01 mol%, 8.99 mol% , 13.83 mol%. The pristine PDPP-[T]₂-EDOT film for UPS measurement was prepared by dissolving 2mg of polymer in 200 μL of chlorobenzene solution. All the solutions were stirred for 15 min at 50 °C and filtered through a hydrophobic 0.2 μm pore size PTFE membrane. Thin films (20-40nm) were spin coated at 2000 rpm for 90 s in argon filled glovebox with O₂ ≈ (< 1 ppm). UPS measurements were carried out on the same PHI 5000 with VersaProbe III system fitted with a He discharge light source providing stable and continuous He I and He II lines. The samples were directly transported to the UPS system by using a N₂ filled, sealed stainless steel transport vessel without exposing them to the ambient conditions. All measurements reported in this study were carried out with the He I (21.22 eV) line with -9V sample biasing and the corresponding photoemission with 90° take-off angle was collected at the multichannel analyzer. The Fermi level was calculated using a sputter cleaned gold foil. The standard deviation on the reported energy values is ± 0.2 eV, calculated using the Fermi edge full-width-half-maximum of the gold foil.

6 | HOMO–HOMO Electron Transfer: An Elegant Strategy for p-Type Doping of Polymer Semiconductors toward Thermoelectric Applications

Table SI 1: Calculated WF, IE and hole injection barrier of pristine and doped PDPP[T]₂-EDOT films using UPS measurements. The 100% sample denotes pure dopant Spiro-OMeTAD(TFSI)₂.

Sample		Workfunction ^a [eV]	Ionization Energy (IP) ^b [eV]	Hole injection barrier [eV]
mol%	[wt]			
0	0	-3.90	-4.49	0.59
0.97	2.10	-4.46	-4.81	0.35
2.01	4.12	-4.41	-4.71	0.30
8.99	16.57	-4.67	-4.79	0.12
13.83	24.38	-4.77	-4.83	0.06
100	100	-5.06	-5.33	0.27
Spiro-OMeTAD		-4.25	-4.92	0.67

^aWork function = 21.22 eV (He I) – Binding energy of secondary electron edge (w.r.t. E_F)

^bIonization energy = Work function + Hole injection barrier (DE between E_F and VBM onset).

It is important to note that the hole injection barrier HIB (energy gap between E_F and the onset of the valence band) in Spiro-OMeTAD(TFSI)₂ is 270 meV, which is lesser than that in spiro-OMeTAD (HIB= 670 meV).

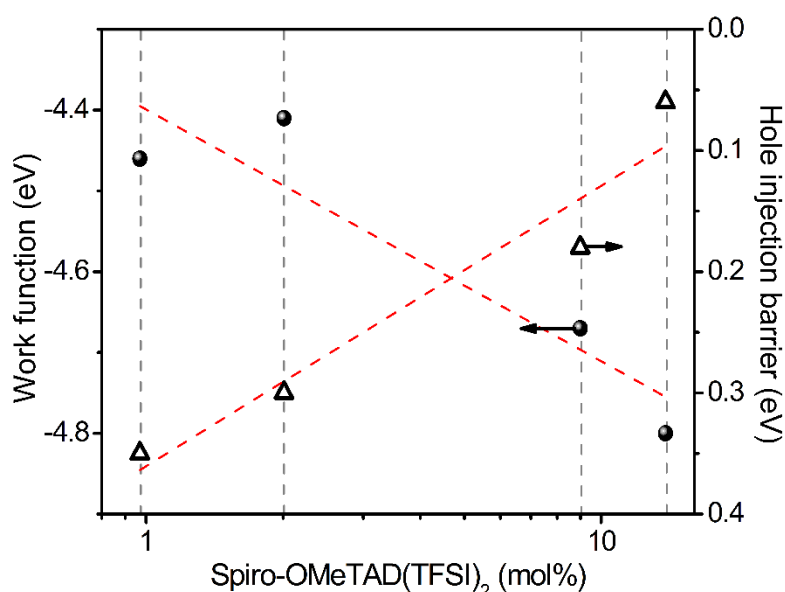


Figure SI 6. Change in work function (filled dots) and hole injection barrier values (empty triangles) of PDPP[T]₂-EDOT with increasing Spiro-OMeTAD(TFSI)₂ concentration, plotted in a semi-logarithmic scale and by using simple linear fit method slope values are obtained. A linear dependency of work function and HIB of the polymer matrix is observed with a slope of ca. $10 k_B T$, with increasing dopant concentration, and no saturation is observed up to 14 mol% of Spiro-OMeTAD(TFSI)₂. In p-doped organic systems, the slope is directly correlated to the width of occupied density of states (DOOS) and slope values higher than $k_B T$ are commonly observed due to dopant induced disorder in the organic matrix.

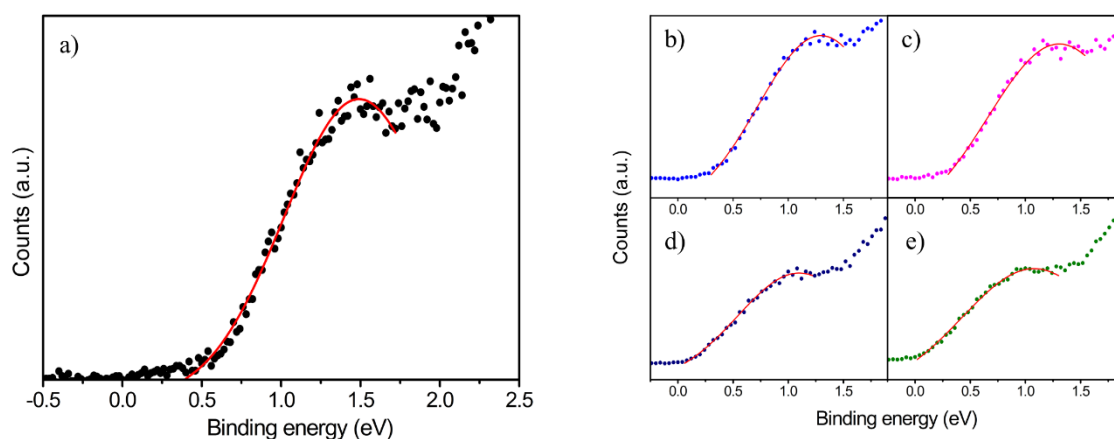


Figure SI 7. Valence band spectra of a) pristine PDPP[T]₂-EDOT and the same with b) 1 mol%, c) 2 mol%, d) 9 mol% and e) ca.14 mol% of Spiro-OMeTAD(TFSI)₂.

The FWHM of these valence states is obtained by fitting the same with a single Gaussian peak with an assumption that despite latter includes contributions from multiple states of the redox couple, all are collectively considered as one peak to compare within a series of systems studied under the same experimental conditions. The calculated FWHM are 1.11 eV, 1.34 eV, 1.52 eV, 1.32 eV and 1.54 eV for 0, 1, 2, 9 and ca. 14 mol% Spiro-OMeTAD(TFSI)₂ doped PDPP[T]₂-EDOT, respectively. This parameter is determined by fitting the band nearest to E_F with a single Gaussian peak with an assumption that despite latter includes contributions from multiple states of the redox couple, all are collectively considered as one peak to compare within a series of systems studied under the same experimental conditions. This relative broadening of the occupied valence states is observed due to two reasons: increasing disorder in the polymer matrix due to dopants or formation of new states due to the oxidation of the polymer matrix or reduction of the dopant, which contributes to the valence states.^[5] In case of increasing matrix disorder due to dopant induced coulombic interactions, Arkhipov et al.^[6] suggests that it could be beneficial for the formation of free charge carriers, i.e., increasing the doping efficiency, and facilitate charge carrier mobility.

UV-vis-NIR spectroscopy: UV–vis-NIR spectra were recorded on a Jasco V-670 spectrophotometer. For solution studies, PDPP-[T]₂-EDOT (0.25mg/mL) was dissolved in extra dry chlorobenzene and appropriate amounts of Spiro-OMeTAD(TFSI)₂ solution (5mg in a binary solvent mixture consisting of 500 μ l chlorobenzene and 200 μ l of chloroform) were added to obtain the desired mole ratios of Spiro-OMeTAD(TFSI)₂. The spectra were recorded in quartz cuvettes with an internal diameter of 1 mm. For thin solid films, PDPP-[T]₂-EDOT (18.16 mg in 900 μ L of CHCl₃) and Spiro-OMeTAD(TFSI)₂ (4 mg in a binary solvent mixture consisting of 180 μ l CHCl₃ and 20 μ l of CH₃CN) were appropriately mixed and spin-coated on precleaned quartz substrates.

Table SI 2. Molar concentrations of Spiro-OMeTAD(TFSI)₂ dopant and PDPP-[T]₂-EDOT in doped polymer solutions shown in the **Figure 2a**:

Spiro-OMeTAD(TFSI) ₂		PDPP-[T] ₂ -EDOT [M · 10 ⁻⁴]	Spiro-OMeTAD(TFSI) ₂ [M · 10 ⁻⁵]	PDPP-[T] ₂ -EDOT [mg]	Spiro-OMeTAD(TFSI) ₂ [mg]
[mol%]	[wt%]				
0.3	0.67	2.91	0.09	1.036	0.007
1.7	3.36	2.91	0.50	1.036	0.036
3.3	6.41	2.91	0.99	1.036	0.071
4.9	9.36	2.90	1.49	1.036	0.107
6.4	12.13	2.90	1.99	1.036	0.143
12.0	21.58	2.89	3.96	1.036	0.285
14.7	25.79	2.88	4.93	1.036	0.360

Spectroelectrochemistry: Spectro-electrochemical UV/vis measurements were performed using a Gamry Interface 1010 T potentiostat with a platinum gauze working electrode, a silver/silver nitrate reference electrode and a platinum wire as counter electrode and a Jasco V-670 spectrophotometer with quartz cuvettes with an optical path length of 1 mm.

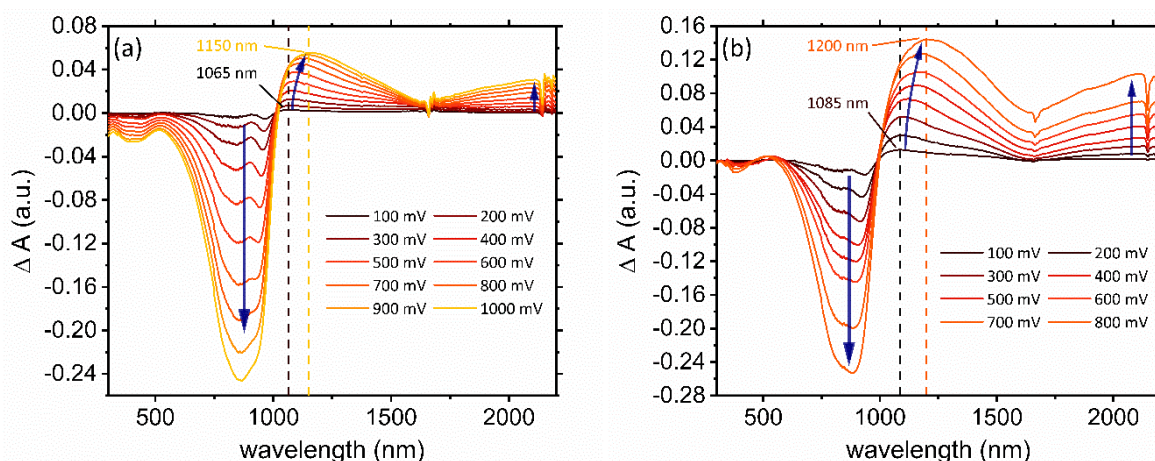


Figure SI 9. Differential spectro-electrochemical UV-Vis-NIR plot of PDPP[T]₂-EDOT at 0.2 mg · mL⁻¹ in chlorobenzene solution, (a) with 0.1 mM tetrabutylammonium hexafluorophosphate (TBA-PF₆) as the supporting electrolyte and (b) with 0.1 mM TBA-PF₆ + 10 mM LiTFSI as the supporting electrolyte. Latter is obtained by mixing 1 part of a 100 mM LiTFSI solution in acetonitrile to 9 parts of a 0.1 mM TBA-PF₆ solution in CB. By adding a 100-fold excess of TFSI⁻ anions, as compared to TBA ions, the influence of the counter ion present in chemical doping was probed. Upon electrochemical oxidation, the main absorption centred at 860 nm is progressively diminished, accompanied by the appearance of the polaronic absorption peak and sub-band gap absorptions toward the infrared region. In both cases, the polaron peak shifts with increased potential until it saturates. Without TFSI⁻ it saturates at 1150 nm, with excess of TFSI⁻ it saturates at 1200 nm. This shift of 50 nm corresponds to a small energy difference of 45 meV which is explained by an improved stabilization of the polaron in the presence of TFSI⁻ or a slightly increased polarity of the acetonitrile containing solution.

Determination of concentrations of reduced species of the dopant from UV-vis spectroscopy:

Individual molar concentrations of Spiro-OMeTAD(TFSI)₂, Spiro-OMeTAD(TFSI), and Spiro-OMeTAD in doped polymer solutions were calculated using reported molar extinction coefficients of pure systems at 390, 480 and 520 nm using Beer-Lambert law. The wavelengths were so selected in order to avoid overlap of absorption between pristine and oxidized species. At 480 and 520 nm the pristine Spiro-OMeTAD does not absorb, whereas the other two species absorb at these wavelengths. These were used to calculate the concentrations of Spiro-OMeTAD(TFSI)₂ and Spiro-OMeTAD

(TFSI) by solving following equations for each doped sample:

$$(A_{\text{total}})_{520} = (\epsilon_2)_{520}C_2l + (\epsilon_1)_{520}C_1l$$

$$(A_{\text{total}})_{480} = (\epsilon_2)_{480}C_2l + (\epsilon_1)_{480}C_1l$$

Here, $(A_{\text{total}})_{520}$ and $(A_{\text{total}})_{480}$ are the total absorbance's of the samples, $(\epsilon_2)_{520}$ and $(\epsilon_2)_{480}$ are the molar absorption coefficients of Spiro-OMeTAD(TFSI)₂ at 520 and 480 nm, $(\epsilon_1)_{520}$ and $(\epsilon_1)_{480}$ are the molar absorption coefficients of Spiro-OMeTAD(TFSI) at 520 and 480 nm, respectively. c_1 and c_2 refer to the concentrations of Spiro-OMeTAD(TFSI)₂ and Spiro-OMeTAD(TFSI). l is cell length, which is 0.1cm. After determining the concentrations of the two species, the third species (Spiro-OMeTAD) was determined by substituting the values of c_2 and c_1 in the following equation:

$$(A_{\text{total}})_{390} = (\epsilon_2)_{390}C_2l + (\epsilon_1)_{390}C_1l + (\epsilon_0)_{390}C_0l$$

Here, $(A_{\text{total}})_{390}$ is the total absorbance of the sample, $(\epsilon_2)_{390}$, $(\epsilon_1)_{390}$ and $(\epsilon_0)_{390}$ are the molar absorption coefficients of Spiro-OMeTAD(TFSI)₂, Spiro-OMeTAD(TFSI) and Spiro-OMeTAD at 390 nm, respectively. c_0 refers to the concentration of Spiro-OMeTAD. The same procedure was repeated for each sample with different mol% of dopant and the values of c_2 , c_1 and c_0 are summarized in the **Table SI 3** and **Figure SI 9**.

Table SI 3. Molar concentrations of Spiro-OMeTAD(TFSI)₂, Spiro-OMeTAD(TFSI) and Spiro-OMeTAD using molar extinction coefficients of pure systems at 390, 480 and 520 nm using Beer-lambert law. [7]

Feed in Dopant		Spiro-OMeTAD(TFSI) ₂	Spiro-OMeTAD(TFSI)	Spiro-OMeTAD	Spiro-OMeTAD(TFSI) ₂ Relative %	Spiro-OMeTAD(TFSI) Relative %	Spiro-OMeTAD Relative %
(mol%)	(wt%)						
0.3	0.67	6.75E-7	1.33E-6	9.09E-7	23.2	45.6	31.2
1.7	3.36	1.64E-5	2.67E-5	9.97E-6	30.9	50.3	18.8
3.3	6.41	3.38E-5	5.61E-5	2.17E-5	30.3	50.3	19.4
4.9	9.36	3.95E-5	6.61E-5	2.55E-5	30.1	50.4	19.4
6.4	12.13	8.01E-5	1.34E-4	5.09E-5	30.2	50.6	19.2
12.0	21.58	9.56E-5	1.62E-4	6.01E-5	30.1	50.9	18.9
14.7	25.79	1.39E-4	2.43E-4	9.51E-5	29.1	50.9	19.9

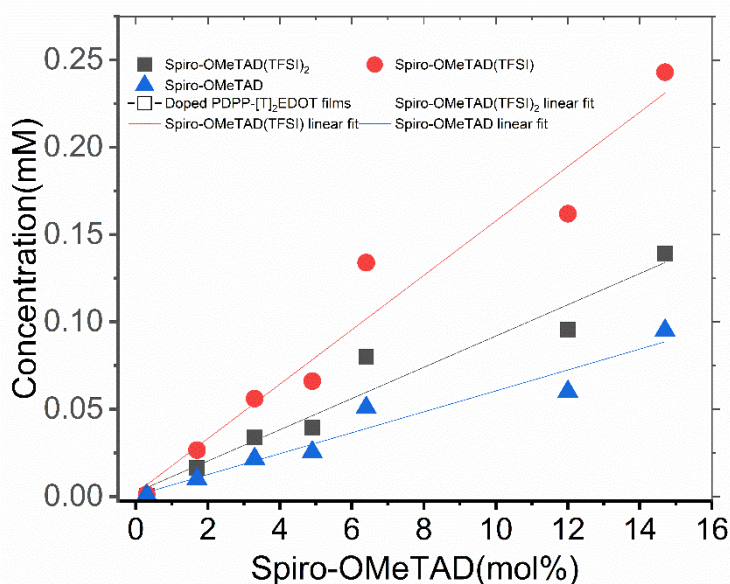


Figure SI 9. Individual molar concentrations of Spiro-OMeTAD(TFSI)₂ (black squares), Spiro-OMeTAD(TFSI) (red circles) and Spiro-OMeTAD (blue triangles) in doped polymer solutions plotted versus mol % of the feed-in dopant.

It is seen that as the amount of dopant progressively increased, a rapid increase in the concentration of Spiro-OMeTAD(TFSI) (slope = 0.01558 ± 0.00157) as compared to unreacted Spiro-OMeTAD(TFSI)₂ (slope = $0.00895 \pm 9.13543E-4$) or Spiro-OMeTAD (slope = $0.00599 \pm 6.50854E-4$) is observed. Similarly, comparing the relative percentages of each species in **Table SI 3**, it becomes clear that the relative percentage of Spiro-OMeTAD(TFSI) is the highest (45–51%) among the three at each doping concentration. This indicates the HOMO to HOMO electron transfer from polymer and reduction of Spiro-OMeTAD(TFSI)₂ to Spiro-

OMeTAD(TFSI). To determine the actual amount of Spiro-OMeTAD(TFSI)₂ in the used dopant, its absorption spectrum was measured and with Beer-Lambert law, the percentage of Spiro-OMeTAD(TFSI)₂, Spiro-OMeTAD(TFSI) and Spiro-OMeTAD were determined to be 61%, 29.32% and 9.68% , respectively. The values obtained for Spiro-OMeTAD(TFSI)₂ is close to the value obtained from XPS.

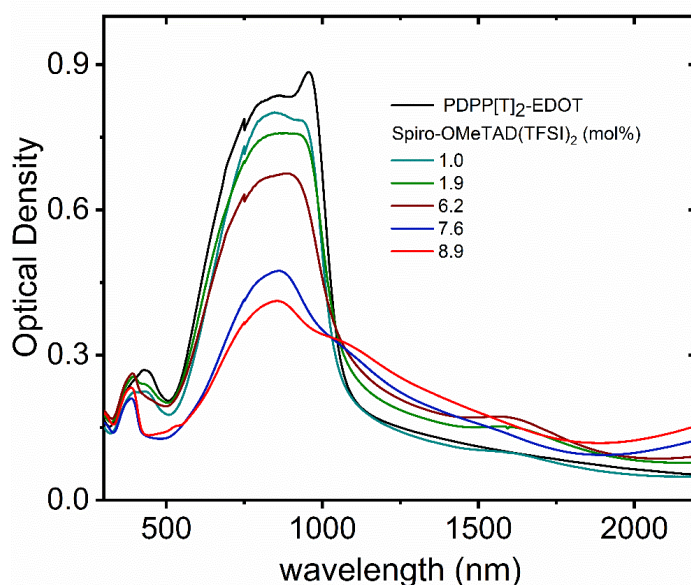


Figure SI 10. Absorption spectra of pristine and doped PDPP[T]₂-EDOT at different concentrations of Spiro-OMeTAD(TFSI)₂ in solid films.

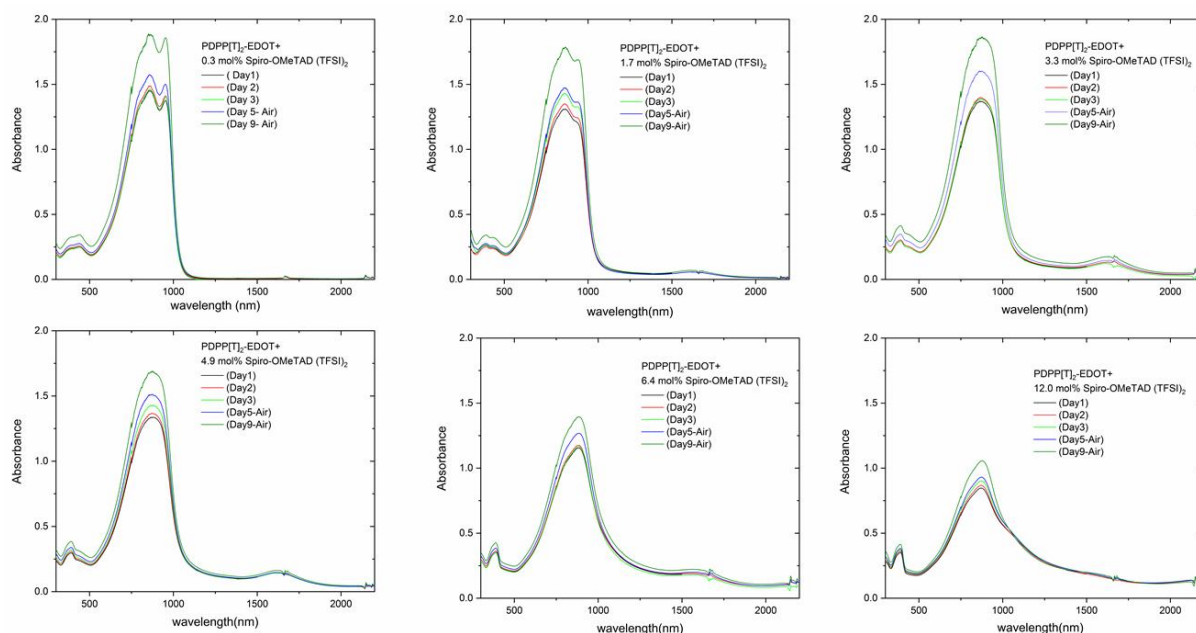


Figure SI 11. Time dependent absorption spectra of doped PDPP[T]₂-EDOT at different dopant concentrations. The samples were kept under argon atmosphere up to 5 days. On day 5, the samples were exposed to air. No appreciable change in the absorption spectra was found under argon, with slight increase in the absorption intensities on exposure to air.

Charge carrier mobility and charge carrier density measurements:

Sample preparation: All following steps were conducted under inert atmosphere (nitrogen) and in absence of H₂O (< 1 ppm) and O₂ (< 1 ppm). 18 mg of PDPP[T]₂-EDOT (22.5 μmol) were dissolved in 900 μl of CHCl₃ and stirred for 15 min at 50 °C. A dopant stock solution was prepared by dissolving 4 mg of spiro(TFSI)₂ (2.24 μmol) in a binary solvent mixture consisting of 45 μl CHCl₃ and 5 μl of CH₃μCN. The dopant stock solution was stirred for 15 min at 50 °C. To obtain the desired molar ratios of PDPP[T]₂-EDOT to spiro(TFSI)₂, the following amounts of dopant stock solution were added to 150 μl of the polymer solution: 100:0 (0 μl), 50:1 (1.5 μl), 30:1 (2.5 μl), 20:1 (3.75 μl), 15:1 (5 μl) and 10:1 (7.5 μl). The PDPP[T]₂-EDOT:Spiro-OMeTAD(TFSI)₂ solutions were stirred for 15 min at 50 °C and filtered (Hydrophobic PTFE membrane, 0.2 μm pore size).

Determination of μ₀ (−ΔB-method): A p-doped silicon wafer (Silchem 4508/90, 100 mm diameter, (100) orientation, boron doped, 42.5 Ω/cm) was cut into rectangular pieces of 5 by 4 cm and cleaned by ultra-sonication in 2 vol% aqueous hellmanex-III solution, water, acetone and isopropanol. The PDPP[T]₂-EDOT:Spiro-OMeTAD(TFSI)₂-solutions were spin-coated (1500 rpm, 90 sec, 20 μl) on the Si-substrate under inert atmosphere and used without further thermal annealing. Finally, five circular Au top electrodes (1 mm diameter) on top of the organic layer and five Au back-contacts were thermally evaporated using a shadow mask (*d*_{Au} = 75 nm). The impedance of the devices was measured with a two-electrode setup and increasing electrical field (1 MHz to 100 Hz, 16 points per frequency decade, 0-1 V_{Bias} in 10 voltage steps, 7 mV_{RMS}). The Au top electrode was grounded and connected to the sense-input, while a potential was applied to the back-contact. Devices under test were shielded from ambient light and external electrical fields. From the imaginary Z'' and real Z' impedance, the capacitance of the organic layer was extracted assuming an R(RC) equivalent circuit:

$$\hat{Z}(i\omega)_{R(RC)} = R_{Series} + \frac{1}{i\omega C_{Parallel} + \frac{1}{R_{Parallel}}} \quad (1.1)$$

which can be solved for *C*_{Parallel} to yield

$$C_{Parallel} = \frac{Im(Z)}{(-Im(Z)^2 + (Re(Z) - R_S)^2)\omega} \quad (1.2)$$

The geometric capacitance *C*_{Geo} of each device was determined in the high frequency region of the *C*(*f*)-plot. Together with the measured capacitance, the mobility was extracted from the negative differential susceptance −Δ*B* at different electrical fields. The negative differential susceptance −Δ*B* can be calculated

$$-\Delta B = -\omega(C(\omega) - C_{geo}) \quad (1.3)$$

The global maximum *f*_{max} of the −Δ*B*(*f*)-plot was extracted and used to calculate the transit time τ_{tr}

$$\tau_{tr} = 0.72f_{max}^{-1} \quad (1.4)$$

Local maxima above the transit frequency without physical meaning were discarded. The mobility can then be extracted as

$$\mu = \frac{4}{3} \frac{d^2}{\tau_t V_{Bias}} \quad (1.5)$$

with d being the thickness of the organic layer.

The zero-field mobility μ_0 was calculated by extrapolating the obtained Poole-Frenkel type field dependency. The results were averaged over at least four working devices.

Determination of N_D (Mott Schottky measurements):

TEC-7 (XOP glass, 1" x 1" x 2.2 mm, 6 – 8 Ω /square, ~500 nm FTO on glass) substrates were etched with dilute HCl/Zn-dust. After obtaining the etched electrode pattern, the substrates were brushed manually with sodium dodecyl sulfate and deionized water, followed by ultrasonication in 2 vol% aqueous hellmanex-III solution, water, acetone and isopropanol. The substrates were blown dry with nitrogen and pre-treated with O_3 /UV for 15 min at 50 °C. 170 nm of Al_2O_3 were deposited on the FTO-electrodes using ALD ($H_2O/Al(CH_3)_3$, 15 ms pulse duration, 150 °C, 5 s purge time, 2000 cycles), while leaving areas insulator-free for contacting the device during measurements. The substrates were immersed in a solution of *n*-octadecyltrichlorosilane (ODTS) in toluene (10 mmol/l) for 45 min at 60 °C in air to cap surface oxide groups. After SAM-formation, the substrates were rinsed with hexane, followed by ultra-sonication in acetone and isopropanol to remove excess ODTS and blown dry with nitrogen. The PDPP[T]₂-EDOT: Spiro-OMeTAD(TFSI)₂-solutions were coated onto the substrates using doctor blading (70 °C, 120 μ m blade height, 16.5 mm/s blade speed) under inert atmosphere and used without further thermal annealing. To enhance the wettability, $CHCl_3$ was doctor bladed onto the substrates prior to PDPP[T]₂-EDOT: Spiro-OMeTAD(TFSI)₂-coating and dried completely. Finally, Au electrodes were thermally evaporated using a shadow mask ($d_{Au} = 70$ nm).

The impedance of the devices was measured with a two-electrode setup and increasing electrical field (200 kHz to 5 Hz, 6 points per frequency decade, -2-4 V_{Bias} in 60 voltage steps, 7 mV_{RMS}). The Au top electrode was grounded and connected to the sense-input, while a potential was applied to the FTO-contact. Devices under test were shielded from ambient light, external electrical fields and kept under inert atmosphere. From the impedance Z , the capacitance of the organic layer was extracted for a fixed frequency assuming an (RC) equivalent circuit:

$$C_{tot} = \frac{Im(Z)}{\omega|Z|^2} \quad (1.6)$$

It should be noted, that the total capacitance C_{tot} is composed of the constant insulator capacitance $C_{Insulator}$ and variable depletion layer capacitance $C_{Depletion}$ in series^[1]:

$$C_{tot} = \frac{C_{Insulator}C_{Depletion}}{C_{Insulator} + C_{Depletion}} \quad (1.7)$$

Where $C_{Insulator}$ can be calculated for a given thickness $d_{Insulator}$, area A and dielectric constant $\epsilon_{Insulator}$ relative to the vacuum permittivity ϵ_0 :

$$C_{Insulator} = \frac{\epsilon_{Insulator}\epsilon_0A}{d_{Insulator}} \quad (1.8)$$

If the device exhibits significant series resistance R_s , eq. (1.2) may be used. $\frac{1}{C_{tot}^2}$ was plotted against the applied bias voltage V_{Bias} . Using the Mott-Schottky equation (1.9),

$$\frac{1}{C_{tot}^2} = \frac{2}{q\epsilon_0\epsilon_{OSC}A^2N_D} \left(V_{Fb} - V_{Bias} - \frac{k_B T}{q} \right) \quad (1.9)$$

the doping density N_D was extracted as the slope of a linear fit in the depletion regime, whereas the extrapolated x-intercept gave the flat band voltage V_{Fb} . Here, A is the active area, ϵ_{OSC} the dielectric constant of the organic layer (Approximated with $\epsilon_{OSC} = 3$), q the elementary charge, k_B the Boltzmann constant and T the junction temperature. The measurement was repeated for at least 2 different frequencies to prove the independence of N_D and V_{Fb} from f . The results were averaged over at least four working devices. Care was taken to ensure the organic layer was sufficiently thick to obey the depletion approximation in all devices.

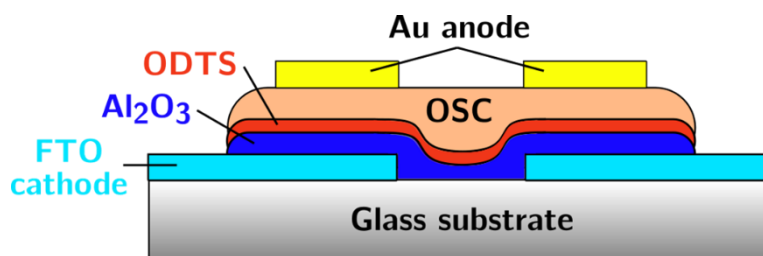


Figure SI 12. Schematic cross section of metal-insulator-semiconductor (MIS) devices used for extracting the charge carrier density N_D by measuring the device capacitance C at different applied potentials and applying the Mott-Schottky theory.

6 | HOMO–HOMO Electron Transfer: An Elegant Strategy for p-Type Doping of Polymer Semiconductors toward Thermoelectric Applications

Table SI 4: Organic layer thickness of MS and MIS-diodes.

		MS	MIS
Spiro-OMeTAD(TFSI) ₂		Thickness ^a	Thickness
[mol%]	[wt%]	[nm]	[nm]
0 (pristine polymer)		378 ± 17	303
1.95	3.92	342 ± 19	235
3.30	6.63	306 ± 9	242
4.74	9.52	380 ± 20	277
6.22	12.49	296 ± 30	465
9.10	18.28	274 ± 24	505

Determined by Dektak surface profilometry. a: Thickness averaged over five line scans per device.

Table SI 5: Charge carrier densities of MIS-diodes (Values averaged over four devices).

Device		60 Hz	44 Hz
Spiro-OMeTAD(TFSI) ₂		Charge carrier density N_D	Charge carrier density N_D
[mol%]	[wt%]	[cm ⁻³]	[cm ⁻³]
0 (pristine polymer)		5.96e19 ± 1.86e19	9.80e19 ± 3.09e19
1.95	3.92	1.48e20 ± 2.65e19	4.13e20 ± 2.04e19
3.30	6.63	1.02e20 ± 5.27e19	3.13e20 ± 2.08e20
4.74	9.52	1.81e21 ± 2.81e19	8.81e21 ± 3.77e20
6.22	12.49	2.33e20 ± 1.52e19	4.59e20 ± 4.85e19
9.10	18.28	4.45e19 ± 9.40e18	5.76e19 ± 1.80e19

Table SI 6: Flat band voltages of MIS-diodes.

Device		60 Hz	44 Hz
Spiro-OMeTAD(TFSI) ₂		Flatband voltage V_{Fb}	Flatband voltage V_{Fb}
[mol%]	[wt%]	[V]	[V]
0 (pristine polymer)		2.41 ± 0.54	2.17 ± 0.59
1.95	3.92	1.91 ± 0.18	1.70 ± 0.20
3.30	6.63	1.88 ± 0.24	1.65 ± 0.27
4.74	9.52	1.58 ± 0.02	1.76 ± 0.13

6.22	12.49	3.57 ± 0.44	4.98 ± 0.90
9.10	18.28	1.72 ± 0.1	2.06 ± 1.10

Values averaged over four devices.

Table SI 7. Zero-field mobilities μ_0 of MS-diodes.

Device		Zero-field mobility μ_0
Spiro-OMeTAD(TFSI) ₂		[cm ² V ⁻¹ s ⁻¹]
(mol%)	[wt%]	
Pristine		$1.18 \cdot 10^{-3} \pm 0.16 \cdot 10^{-3}$
2	4.02	$1.05 \cdot 10^{-3} \pm 0.27 \cdot 10^{-3}$
3.30	6.63	$4.20 \cdot 10^{-3} \pm 0.54 \cdot 10^{-3}$
5	10.04	$9.81 \cdot 10^{-3} \pm 0.71 \cdot 10^{-3}$
7.5	15.06	$6.83 \cdot 10^{-3} \pm 1.61 \cdot 10^{-3}$
10	20.09	$4.08 \cdot 10^{-3} \pm 0.66 \cdot 10^{-3}$

Values averaged over four devices. Extracted from impedance data via negative differential susceptance.

Note: 1. Above 5 mol%, the measured lateral conductivity differs significantly from N_D and μ_0 measured in vertical MIS respectively MS devices. At this molar concentration, the solubility limit of Spiro-OMeTAD(TFSI)₂ in PDPP[T]₂-EDOT is reached in the thin vertical OSC layers used (ca. 50 - 100 nm).

2. It should be emphasized that the loss in charge carrier mobility and density above 5 mol% represents the limits of thin film homogeneity in this particular system and renders the Mott Schottky equation as not applicable.

Stability of doped samples on annealing and exposure to ambient conditions: OFET Gen 4 substrates were purchased from Fraunhofer IPMS. These substrates, where the source and drain electrodes were a 30 nm thick gold layer on a 10 nm ITO adhesion layer were used as interdigitated electrodes. The substrates were cleaned with acetone and subsequently with isopropanol in an ultrasonic bath for 5 minutes each and pre-treated with O₃/UV for 15 min at 50 °C. PDPP-[T]₂-EDOT (19.98 mg in 1.2 mL) and spiro(TFSI)₂ (5.99 mg in 300 μL) were dissolved in chloroform and stirred for 15 min at 50 °C. Appropriate amounts of dopant were added to obtain the desired molar ratios of spiro(TFSI)₂ in PDPP[T]₂-EDOT. The doped polymer solutions were stirred for 15 min at 50 °C and filtered through a Hydrophobic PTFE membrane, 0.2 μm pore size. Thin films were spin coated (1500 rpm for 90 s) on precleaned substrates for conductivity measurements. All steps of sample preparation were performed in argon filled glovebox with O₂ ≈ (< 1 ppm). Each substrate (chip) consists of four groups with four identical interdigitated electrodes, with a channel length of 2.5, 5, 10 and 20 μm respectively and a constant channel width of 1cm. For calculating conductivity, a voltage (V) was applied

between the the electrodes and the current I was measured as a function of the voltage. An increase in the potential V led to a linear increase in the current I . From the linear fit of the I - V plots, the slope was used to calculate the conductivity using the following equation:

$$\sigma = \frac{\text{slope} \cdot l}{w \cdot h}$$

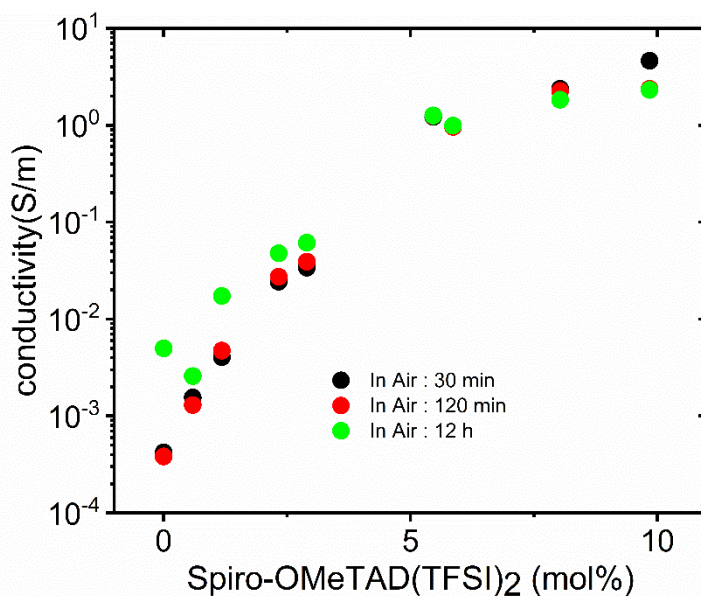


Figure SI 13. Conductivity of doped PDPP[T]₂-EDOT at different Spiro-OMeTAD(TFSI)₂ dopant concentrations measured by IV-curve tracing of planar, interdigitated electrode structures after exposing the films to air.

Thermoelectric measurements:

Sample preparation: Quartz substrates (13 mm x 13 mm x 1 mm) were cut and cleaned with 2 vol% aqueous hellmanex-III solution, water, acetone and isopropanol and pre-treated with O₃/UV for 15 min at 50 °C. PDPP-[T]₂-EDOT (18.44 mg in 0.9 mL chloroform) and Spiro-OMeTAD(TFSI)₂ (8 mg in a binary solvent mixture consisting of 180 μL CHCl₃ and 20 μL of CH₃CN 180 μL chloroform and 20 μL) were dissolved in chloroform and stirred for 15 min at 50 °C. Appropriate amounts of dopant were added to obtain the desired molar ratios of Spiro-OMeTAD(TFSI)₂ in PDPP[T]₂-EDOT. The doped polymer solutions were stirred for 15 min at 50 °C and filtered through a Hydrophobic PTFE membrane, 0.2 μm pore size. The PDPP[T]₂-EDOT:Spiro-OMeTAD(TFSI)₂-solutions were coated using doctor blading (70 °C, 120 μm blade height, 16.5 mm/s blade speed) in argon filled glovebox with O₂ ≈ (< 1 ppm). and used without further thermal annealing. Gold contact structures of 100 nm thickness were prepared via thermal evaporation onto the squared samples of 13 mm length under high vacuum (HV) at a base pressure of 10⁻⁶ mbar.

Conductivity Measurements: Temperature dependent resistance measurements were performed by adjusting the desired temperature via the halogen lamp in the copper base, feedback-looped to an Eurotherm 91E controller. The current temperature is determined by

a PT100 element mounted on top of one of the heater blocks to minimize thermal delay effects. The resistance was measured using a four-point probe technique. An incrementing current I is fed through the sample by a Keithley 236 source unit via the outer two electrical contacts, while simultaneously measuring the resulting voltage drop V at the inner contact pair with an Agilent 34420 nanovoltmeter. From the slope of the resulting I-V curve the resistance R can be extracted, and hence, the conductivity σ can be calculated:

$$\sigma = \frac{1}{R} \frac{b}{Ld} \quad (1.10)$$

Where $b = 1$ mm is the distance between the voltage contact, $L = 6.25$ mm their length and d the thickness of the polymer layer.

Seebeck Coefficient and temperature dependent conductivity: The Seebeck as well as the temperature dependent conductivity measurements were performed in HV to minimize heat dissipation. The setup consists of a copper base with a built-in halogen lamp to change the overall temperature of the sample holder. On top of the base two copper blocks (heater 1 and 2) are mounted which can be individually heated by means of embedded Kapton heater foils. A thermal insulation underneath the heater foils ensures a stable temperature gradient across the sample. The temperature gradient is monitored independently by means of a differential copper-constantan-copper thermocouple (type T) fixed onto a separate reference substrate. The sample as well as the reference substrate are glued on top of the heater blocks using silver paint to guarantee good thermal connection. A temperature gradient is established across the sample by applying a voltage to the heater foil of the first block. When the desired temperature difference of around 1.5 K is reached, the voltage is applied to the second block until the temperature gradient vanishes and eventually is inverted to -1.5 K. Then, the first block is heated again to reach an effective temperature gradient of 0 K. During this process the voltage of the thermocouple and the Seebeck voltage are simultaneously recorded using an Agilent 34420 nanovoltmeter.

Measurement Accuracy for thermoelectric measurements: The uncertainties of the activation energy are estimated by the discrepancy between the temperature dependent conductivity data taken while heating versus cooling the sample. The accuracy of the electrical conductivity values is primarily limited by the uncertainty of the film thickness of the samples. To determine the thickness, a Dektak profilometer with an accuracy of ± 10 nm is used, from which we can estimate an error of ± 5 % for our conductivity data. The uncertainty of the Seebeck measurements arises mainly from the fact, that the measurements are performed using two independent heaters, resulting in a $U_{\text{Seebeck}}(\Delta T)$ curve separated in three parts (I)–(III) as shown in Figure SI 7. These parts are fitted separately and, thereafter, their slopes are averaged. Thus, the accuracy of the measurement is determined by the symmetry of the thermo-voltage hysteresis and can be estimated from the least symmetric data set to be ± 5 %. With this, the relative uncertainty of the corresponding Power Factor can be estimated to be less than ± 15 %.

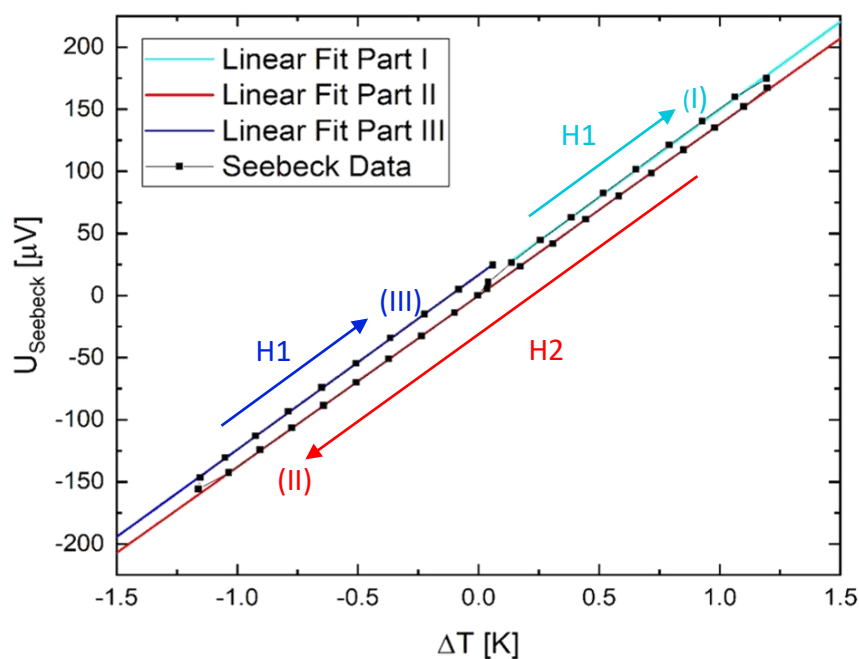


Figure SI 14 Exemplary data set of a Seebeck measurement. To generate a temperature gradient ΔT across the sample, a voltage is applied to the first heater H1. The temperature gradient built-up is subsequently inverted by applying the voltage to the second heater (H2). Finally, heating H1 again, the temperature difference between the blocks decreases. The hysteresis of the curve can be attributed to a delay in the thermal response of the sample holder. The three parts of the data are fitted separately and the Seebeck coefficient is determined by averaging their slopes.

Table SI 8: Thermoelectric Parameters of PDPP[T]₂-EDOT thin films as a function of Spiro-OMeTAD(TFSI)₂ doping concentration.

Spiro-OMeTAD(TFSI) ₂		film thickness (nm)	σ (S/m)	S ($\mu\text{V}/\text{K}$)	PF (σS^2) ($\mu\text{W}/\text{m}/\text{K}^2$)
(mol%)	(wt%)				
1.72	3.76	797	0.691	207	0.0296
2.83	6.11	553	1.267	120	0.0182
4.19	8.90	526	3.58	140	0.0706
5.51	11.50	812	8.47	83	0.0581
8.04	16.34	617	10.21	79	0.0637
PDPP[T] ₂ -EDOT		632	0.00125	469	2.75e-4

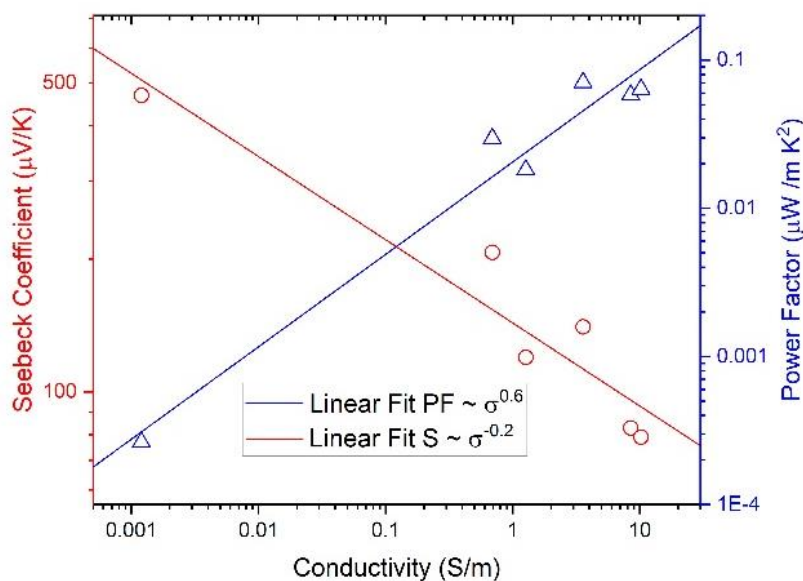


Figure SI 15. Seebeck coefficient S (red) and Power Factor PF (blue) as a function of the electrical conductivity σ . S is found to decrease with $\sigma^{-0.2}$, while PF increases with $\sigma^{0.6}$.

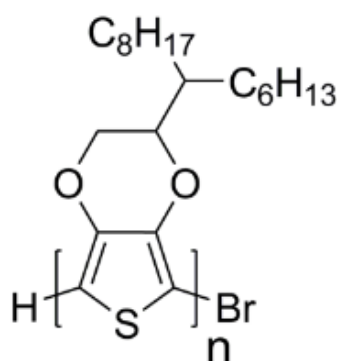


Figure SI 16. Chemical structure of PEDOT C_6C_8 .

References:

- [1] C. J. Mueller, E. Gann, C. R. Singh, M. Thelakkat, C. R. McNeill. *Chem Mater.* **2016**, *28*, 7088.
- [2] C. J. Mueller, C. R. Singh, M. Thelakkat. *J. Polym. Sci. Part B Polym. Phys.* 2016, *54*, 639.
- [3] B. Tan, S. R. Raga, A. S. R. Chesman, S. O. Fürer, F. Zheng, D. P. McMeekin, L. Jiang, W. Mao, X. Lin, X. Wen, J. Lu, Y.-B. Cheng, U. Bach, *Adv. Energy Mater.* 2019, *9*, 1901519.
- [4] M. L. Tietze, L. Burtone, M. Riede, B. Lüssem, K. Leo, *Phys. Rev. B* 2012, *86*, 035320.
- [5] S. Winkler, P. Amsalem, J. Frisch, M. Oehzelt, G. Heimel, N. Koch, *Mater. Horiz.* 2015, *2*, 427.
- [6] V. I. Arkhipov, P. Heremans, E. V. Emelianova, H. Bässler, *Phys. Rev. B* 2005, *71*, 045214.
- [7] W. H. Nguyen, C. D. Bailie, E. L. Unger, M. D. McGehee. *J. Am. Chem. Soc.* 2014, *136*, 10996.

7. Highly Efficient Doping of Conjugated Polymers using Multielectron Acceptor Salts

Published as “Highly Efficient Doping of Conjugated Polymers using Multielectron Acceptor Salts” in *Macromolecular Rapid Communications* **2021**, 42, 2100443 by Gert Krauss, Adrian Hochgesang, John Mohanraj and Mukundan Thelakkat*.

G. Krauss, A. Hochgesang, J. Mohanraj, M. Thelakkat
Applied Functional Polymers, Macromolecular Chemistry I, University of Bayreuth,
Universitätsstr. 30, Bayreuth, 95440, Germany
E-mail: mukundan.thelakkat@uni-bayreuth.de

Prof. M. Thelakkat
Bavarian Polymer Institute (BPI), University of Bayreuth,
Universitätsstr. 30, Bayreuth, 95440, Germany

Keywords: doping, electron transfer, polymers, radical ions, semiconductors.

Abstract

Chemical doping is a vital tool for tuning electronic properties of conjugated polymers. Most single electron acceptors necessitate high doping concentrations to achieve good electrical conductivities. However high molar doping ratios hamper doping efficiency. Here a new concept of using multielectron acceptor (MEA) salts as dopants for conjugated polymers is presented. Two novel MEA salts are synthesized and their doping efficiency towards two polymers differing in their dielectric properties are compared with two single electron acceptors such as NOPF6 and magic blue. Cutting-edge methods such as UPS/XPS, Impedance spectroscopy, XPS mapping and DOS analysis in addition to UV-VIS-NIR absorption, spectroelectrochemistry and Raman spectroscopy methods are used to characterize the doped systems. The tetracation salt improves the conductivity by two orders of magnitude and quadruples the charge carrier concentration compared to single electron acceptors for the same molar ratio. The differences in charge carrier density and activation energy on doping are delineated. Further, a strong dependency of the carrier release on the polymer polarity is observed. High carrier densities at reduced dopant loadings and improved doping efficacies using MEA dopants offer a highly efficient doping strategy for conjugated polymers.

1. Introduction

In recent years, doped conjugated polymers have emerged into different areas of applications and the scientific interest in this field of research is unbroken. A variety of modern devices require doped conjugated polymers as their active materials, for example in high-mobility OFETs^[1-3], as novel thermoelectric materials^[4] or in organic photovoltaics.^[5,6] Inherently insulating conjugated polymers primarily require doping in order to achieve high electrical conductivity. During molecular doping, the conjugated polymer transfers electrons to the dopant (p-type doping leading to oxidized radical cation states) or back (n-type doping resulting in radical anion states). These redox processes introduce one preferred majority carrier type e.g., holes in the case of p-doping and causes the shift of the Fermi level towards either valence band (p-doping) or conduction band (n-doping).^[7] Depending on the electronic structure and sterical demands of the host:dopant system, hybridization of the frontier orbitals with a concomitant formation of charge transfer complexes or redox reactions can be observed. The simplest doping mechanism is described by the integer charge transfer, where an integer number of electrons is transferred between the host and dopant. During p-type doping, the redox process occurs in which electrons are transferred from HOMO (highest occupied molecular orbital) of the conjugated polymer to empty (lowest unoccupied molecular orbital, LUMO) or partially filled (singly occupied molecular orbital, SOMO) states of the dopant.^[8] The most common p-type dopants are tetracyanoquinodimethane (F₄TCNQ)^[9-11] or its derivative, hexafluorotetracyanonaphthoquinodimethane (F₆TCNNQ).^[12] Other dopants are conventional oxidizing agents like iron(III)chloride (FeCl₃), nitrosonium tetrafluoroborate (NOBF₄) or nitrosonium hexafluorophosphate (NOPF₆)^[4,13,14] which are usually capable of accepting one electron per dopant molecule. This circumstance necessitates the employment of high dopant loadings in the range of 20 mol% or more in order to achieve appreciable electrical conductivities, which suffice the intended application.^[11,15] By doping, the charge carrier concentration is increased and ideally the conductivity and charge carrier mobility are enhanced concurrently,^[16] predominantly in the low-doping regime (< 1 mol%) due to filling of deep-lying trap states.^[17] On the other hand, it is accepted that excessive amounts of dopants have detrimental effects on the polymer microstructure and film morphology, leading to decreased charge transport properties.^[18-20] Lying dormant, the acceptor anions or the ionized dopant molecules act as Coulombic traps, i.e., charge carriers are temporarily bound by these trap states and contribute significantly less to the overall current.^[21] This problem is amplified by a rapidly decreasing doping efficiency with increasing doping ratio, meaning that less and less dopants participate in the desired redox reaction.^[8,22] As a consequence, the introduced molar dopant amounts need to be kept as low as possible to fully exploit the potential of both, high doping efficiency as well as good charge transport in the doped conjugated polymer. In this context, it is known that radical cation salts of hole transport materials (HTM) such as spiro-MeOTAD²⁺(TFSI)₂ or MeOTPD⁺(TFSI)⁻ can be used as additives to the pristine spiro-MeOTAD to redistribute the charges and thus to improve the electrical conductivity of such hole transport layers.^[23-25] Inspired by this fact, we have earlier

demonstrated the proof of principle of a highly thermally stable doping strategy for conjugated polymers where spiro-MeOTAD²⁺(TFSI)₂ was employed for HOMO-HOMO electron transfer with a conjugated polymer.^[26] In a similar fashion, Hofmann et al. showed that a singly oxidized triarylammonium radical cation salt, tris(4-bromophenyl) ammonium hexachloroantimonate, (Magic Blue) is capable of p-doping a variety of conjugated polymers.^[27] In most of these reported cases, only one electron is accepted by such a radical cation dopant molecule and therefore to achieve high conductivity high molar dopant ratio is required. Since spiro-MeOTAD can be theoretically oxidized to a tetracation salt and MeOTPD to its dication salt, here we ask a fundamental question on the efficacy of such multivalent radical cation salts as multielectron acceptors (MEAs). Our motivation is based on the idea that theoretically the tetracation salt of spiro-MeOTAD should exhibit the highest degree of doping for the same molar dopant ratio, if it can take up four electrons from the conjugated polymer. This can then fulfill the requirement of desired low doping levels, as explained earlier, if we can make use of multication salts. To study this, we chemically synthesized fully oxidized novel radical cation salts, spiro-MeOTAD⁴⁺(PF₆⁻)₄ and MeOTPD²⁺(PF₆⁻)₂ and addressed the feasibility and efficacy of using such multication salts (which are themselves HTMs) as MEA dopants for two different polydiketopyrrolopyrroles (PDPPs) differing in their polarity and dielectric constants. To quantify the results, we compare the properties of the doped systems with those doped with the well-known mono radical cation salts, magic blue as well as NOPF₆. We study in details how the doping efficiency and the electronic properties of the doped polymers change. The three triphenylamine radical cation salts having oxidation states 1, 2 and 4 used here are: tris(4-bromophenyl)ammonium hexachloroantimonate ("Magic Blue", D2), *N,N,N',N'*-tetrakis(4-methoxyphenyl)benzidine hexafluorophosphate ("MeOTPD²⁺(PF₆⁻)₂", D3) and 2,2',7,7'-tetrakis[*N*-(4-methoxyphenyl)amino]-9,9'-spirobifluorene hexafluorophosphate (spiro-MeOTAD⁴⁺(PF₆⁻)₄ D4). Here the dication salt D3 and tetracation salt D4 are expected to have very similar electronic energies and absorption features, thus enabling a fair comparison of doping efficiency just based on their capacity to accept two or four electrons respectively. Two DPP based polymers with varying hydrophilicity, but similar electronic properties were selected as host materials to study the changes in electrical conductivity, charge carrier mobility and charge carrier density imparted by the different dopants in environments of different polarity. We address the following scientific questions in this work:

- 1) Can the tetracation dopant D4 (spiro-MeOTAD⁴⁺(PF₆⁻)₄) generate four times the charge carrier density compared to single electron acceptors, NOPF₆ or Magic Blue?
- 2) What are the consequences on electrical conductivity, charge carrier mobility and activation energy on using triphenylamine radical cation salts, which are themselves HTMs, as p-dopants compared with the conventional redox-dopant NOPF₆? and
- 3) How does the polarity of the host polymer affect the doping process?

Here, the compatibility of dopant and host as a key requirement for efficient doping is studied using X-ray photoelectron spectroscopy (XPS) mapping. The electronic properties and energy levels of the dopants and polymers are assessed by ultraviolet-photoelectron spectroscopy (UPS). The doping process is monitored using optical absorption spectroscopy as well as UPS. The electrical conductivity and thermal activation energy thereof are measured to study the impact of different dopants on macroscopic charge transport properties, depending on the polymer polarity and polarizability. To study the differences in charge carrier density in the doped polymers using mono-, di- and tetracation salt dopants as compared to single electron oxidants and to determine the resulting doping efficiency, impedance spectroscopy experiments were performed. We also elucidated how HTM-dopants such as D3 and D4 differ on their influence on the charge carrier density, charge carrier mobility, activation energy for charge transport and density of states of doped polymers compared to a non-HTM dopant such as NOPF₆. Altogether, we present a comprehensive and comparative study of a series of triarylamine cation salt dopants with increasing oxidation state from 1 to 4 in two different DPP-polymers, thus highlighting the benefits and drawbacks, if any, of multiple oxidized triarylamine based HTM-dopants. Thereby, the electrical conductivity gained by doping with 5 mol % of a tetracation dopant spiro-MeOTAD⁴⁺(PF₆⁻)₄ is 255 times higher than that obtained with an equal molar amount of NOPF₆. Thus, we introduce an elegant concept for highly efficient doping of conjugated polymers using multi-electron acceptors at unprecedented low dopant molar ratios, opening up innovative and novel p-doping strategies.

2. Results and Discussion

The chemical structures of all the dopants and conjugated polymers investigated in this work are displayed in **Figure 1a**. We studied two polydiketopyrrolopyrroles (PDPPs) with an identical backbone structure consisting of a thiophene-flanked DPP-core (DPP[T]₂) and 3-(2-(2-methoxyethoxy)ethoxy)thiophene (3-MEET) as comonomer. The presence of 3-MEET as comonomer helps to maintain a low ionization potential in the range of 4.6 eV.^[28] These are donor-acceptor polymers capable of undergoing p-doping.^[29,30] The DPP[T]₂ core is either equipped with hydrophilic triethylene glycol {TEG} substituents in the polymer PDPP[T]₂{TEG}₂-3-MEET denoted as P1, or hydrophobic 2-hexyldecyl {2-HD} chains in the polymer PDPP[T]₂{2-HD}₂-3-MEET, denoted as P2. Both polymers exhibit sufficient solubility in common organic solvents. Further, the replacement of the 2-HD substituents with TEG chains leads to an increase of the fraction of ethylene glycol from 13 to 52 wt.%. Due to this, a difference in miscibility between the dopant salts and polymer can be expected and the dissociation of generated charge-transfer state may be facilitated by the higher dielectric constant due to ethylene glycol groups. This may influence both charge carrier mobilities and electrical conductivities.^[11,31,32] The three HTM-dopants are based on the common basic structural motif triphenylamine and have different oxidation states. The singly oxidized Magic Blue (D2) carrying hexachloroantimonate as counter ion was purchased. The new dication

salts, *N,N,N',N'*-tetrakis(4-methoxyphenyl)benzidine hexafluorophosphate (D3, MeOTPD²⁺(PF₆⁻)₂) and the tetracation salt, 2,2',7,7'-tetrakis[*N,N*-di(4-methoxyphenyl)amino]-9,9'-spirobifluorene hexafluorophosphate (D4, spiro-MeOTAD⁴⁺(PF₆⁻)₄) were chemically synthesized by reacting the pristine molecules, MeOTPD and spiro-MeOTAD with carefully dried nitrosonium hexafluorophosphate in large molar excesses required for complete oxidation under extreme dry conditions under argon (see SI). Ultraviolet photoelectron spectroscopy (UPS) was conducted on thin film samples of P1, P2 and D2 to D4 on ITO to assess the HOMO energy levels and work functions (**Figure S1**). From the energy diagram in Figure 1b it is apparent, that both polymers exhibit very similar ionization potentials of 4.6 - 4.7 eV, in accordance with the fact that the polymer backbones are identical, which dictate the HOMO energy levels. All three triarylamine dopants, D2 to D4 are thermodynamically capable of oxidizing the polymers, as their partially occupied HOMOs (5.7, 5.3 and 5.3 eV respectively) lie well below those of the polymers. From the measured SOMO levels, the most exothermic electron transfer from polymer to dopant can be expected for D2, followed by D3 and D4. We postulate that the doping-mechanism of the HTM-dopants occurs via integer charge transfer, as hybridization and the formation of charge-transfer complexes is unlikely in these sterically demanding dopants and non-planar polymers.^[33,34] First we confirmed the uniform distribution of the dopants in our doped polymer thin films using an XPS mapping technique for 5 mol% D2, D3 and D4 (highest molar ratio) over an area of 0.56 mm². By selecting binding energies which are exclusive to either the polymer (Thiophene sulfur 2p_{3/2}) or dopant (Antimony 3d_{3/2} or Fluorine 1s), we could demonstrate a uniform distribution of D2 to D4 in both polymers with a lateral resolution of 10 μm (Figure 1d-e). High miscibility in both alkyl- and TEG side chain substituted polymers results in astonishing compatibility of our HTM dopants with semiconducting PDPP polymers. This also excludes inhomogeneities, which may otherwise will have to be considered in the electrical characterisations and interpretations of the resulting thin films.

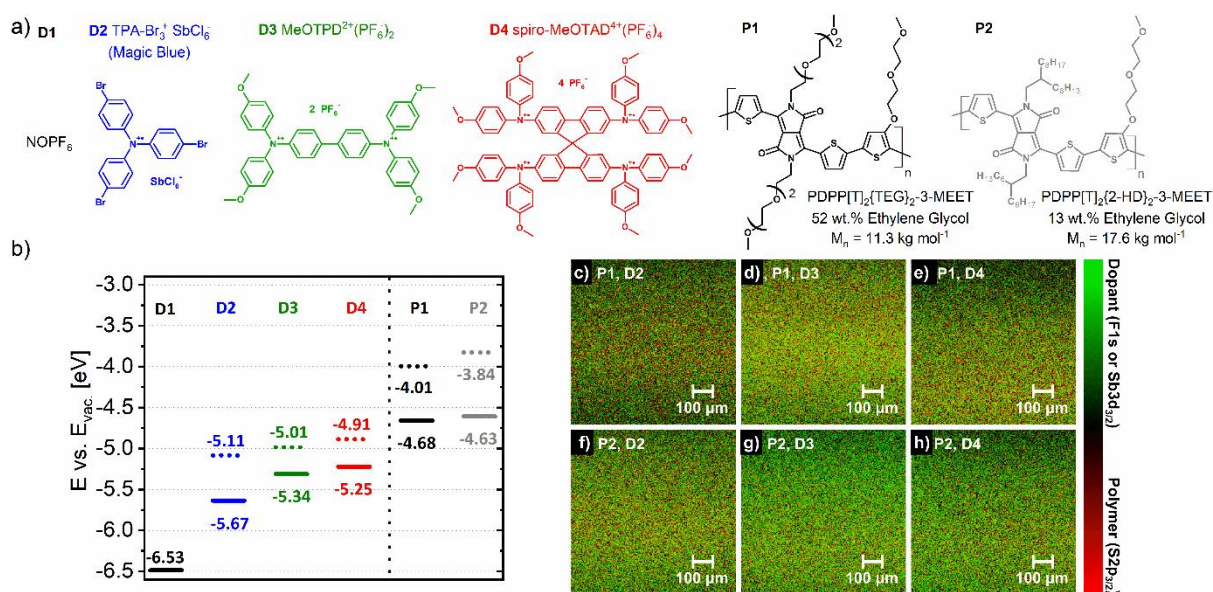


Figure 1. a) Structures of the studied dopants D1 (NOPF₆, black), D2 (Magic Blue, blue), D3 (MeOTPD²⁺(PF₆)₂, green), D4 (spiro-MeOTAD⁴⁺(PF₆)₄, red) and the polymers P1 (PDPP[T]₂{TEG}₂-3-MEET, black) and P2 (PDPP[T]₂{2-HD}₂-3-MEET, grey). b) Ionization potentials (solid lines) and work function (dotted lines) of D2-D4, P1 and P2 w.r.t. vacuum level as obtained from UPS experiments. D1 value taken from reference.^[35] c) - h) XPS elemental maps of P1 and P2 doped with 5 mol% D2, D3 and D4 over an area of 750 μm by 750 μm featuring a lateral resolution of 10 μm. Colors represent the peak intensity of the mapped elements at a particular binding energy, which are exclusive to either polymer or dopant. P1 and P2 are attributed to their thiophene sulfur 2p_{3/2} (165 eV, red) signal, D2 to the antimony 3d_{3/2} (539 eV, green) signal, D3 and D4 to the fluorine 1s signal (688 eV, green).

2.1. Dopant Characterization

The triarylamine based cation salts D2-D4 were thoroughly characterized using additional spectroscopic methods such as UV/Vis/NIR and Raman spectroscopy as given in Figures S2, and S3 respectively. All the triarylamine dopants, D2-D4 feature an absorption at ca. 700 nm due to localized HOMO-LUMO transitions of the triphenylamine moiety (Figure S2).^[35] The close similarity of electronic levels of D3 and D4 are reflected both in the HOMO energy values (both ca. 5.3 eV) as well as in the maximum absorption in the near-infrared region at ca. 900 nm, which arises due to optically induced hole transfer from the triarylamine unit to the linking bridge leading to this strong and broad absorption. This peak is obviously not visible in Magic Blue for the lack of any bridging units between the Ar₃N units.^[35] It is to be noted that D3 shows similar absorption signatures as a reported dication obtained from MeOTPD by oxidation using a silver salt of perfluorinated alkoxyaluminates.^[36] A small shoulder visible in the absorption spectrum of D2 at 630 nm is explained by symmetry breaking of the tris(4-bromophenyl)amine radical cation, which is not present in D3 and D4 due to their twisted arrangement of the phenyl groups around the nitrogen centers.^[36,37] In the Raman spectra of thin films (Figure S3) typical aromatic hydrocarbon stretching vibrations are present; most notably, the C-H out-of-plane wagging from mono substituted benzene (908 cm⁻¹, Δ), C-H in

plane bending from benzene rings (1175 cm^{-1} ,*) and C-N stretching (1320 cm^{-1} , +) are observable. C-C stretching bands are susceptible to quinoid to benzoid transitions of the mesomeric structures. This explains the higher intensity of the more stabilized quinoid vibration in the biphenyl bridged cations, MeOTPD²⁺(PF₆)₂ and spiro-MeOTAD⁴⁺(PF₆)₄ (1564 cm^{-1}) as compared to the energetically more favored benzoid structure in the less stabilized Magic Blue (1606 cm^{-1}).^[36,38] The redox behaviour and energy levels of our dopants and their pristine states are further studied by measuring the frontier orbitals using cyclic voltammetry (CV), as well as differential pulse polarography (DPP) by sequentially oxidizing the pristine molecules (**Figure S4**) All the values are summarized in Table 1 below, together with the UPS values.

Table 1: HOMO energy E_{HOMO} values of neutral tris(4-bromophenyl)amine (TPA-Br₃), MeOTPD and spiro-MeOTAD obtained by cyclic voltammetry (CV) half wave potential and differential pulse polarography (DPP) peak potential. Oxidation states of the corresponding peaks are given as (+x) in brackets. Ionization potential IP and workfunction WF were obtained by ultraviolet-photoelectron spectroscopy on D2, D3 and D4.

Compound	CV	DPP	UPS		
	E_{HOMO} (+x) [eV]	(a) Compound	IP ^(b) [eV]	WF ^(b) [eV]	
TPA-Br ₃	-5.69(+I)	-5.81(+I)	D2	-5.67	-5.11
MeOTPD	-5.50(+I)	-5.51(+I)	D3	-5.34	-5.01
	-5.77(+II)	-5.76(+II)			
	-5.38(+I)	-5.39(+I)			
spiro-MeOTAD	-5.53(+II)	-5.54(+II)	D4	-5.25	-4.91
	-5.75(+IV)	-5.75(+IV)			

^{a)} Measured in dry dichloromethane (sample concentration 10^{-3} - 10^{-5} m) using, supporting electrolyte: 0.1 m TBAPF₆, reference electrode: Ag/AgNO₃, counter electrode: Platinum disc, and working electrode: Platinum disc at a scan rate: 100 mV s^{-1} , at RT and ambient pressure. For DPP measurements, a pulse size of 20-50 mV with 100 ms pulse duration was chosen. The half wave potentials $E^{1/2}$ vs. Ag/AgNO₃ were referenced to the vacuum level by $E^{\text{HOMO}}(\text{Compound}) = [-e\{E^{1/2}(\text{Compound vs. ref. Ag/AgNO}_3) - (E^{1/2}(\text{Fc/Fc}^+ \text{ vs. Ag/AgNO}_3))\}] + E^{\text{HOMO}}(\text{Fc/Fc}^+ \text{ vs. } E_{\text{vac}}, \text{ solvent corrected})$. The ferrocene reference half-wave potential $E^{1/2}(\text{Fc/Fc}^+ \text{ vs. Ag/AgNO}_3)$ was determined to be +0.10 V in DCM at a scan rate of 100 mV s^{-1} , $E_{\text{HOMO}}(\text{Fc/Fc}^+ \text{ vs. } E_{\text{vac}}, \text{ solvent corrected})$ was taken as -5.16 eV.^[40] For complete dataset, see Table S1. ^{b)} UPS was measured on 20 nm thin films of D2, D3 and D4 on ITO.

To avoid radical cross-coupling of the dopants, high scan rate was chosen for CV, which results in large peak-to-peak separation energies ΔE_{p} (Table S1). All the pristine molecules show fully reversible redox cycles; the number of redox peaks depending on the number of nitrogen centres (Figure S4). Obviously, TPA-Br₃ shows a single reversible oxidation, whereas MeOTPD exhibit two (mono- and dication) and spiro-MeOTAD three (mono-, di- and tetracation) oxidation steps in both CV and DPP measurements. The monooxidation step of MeOTPD to

MeOTPD¹⁺ and the dioxidation step of spiro-MeOTAD¹⁺ to spiro-MeOTAD²⁺ are almost degenerate in energy (-5.50 and -5.53 eV, respectively in CV). This indicates that most probably, spiro-MeOTAD²⁺ resembles the monocation, MeOTPD¹⁺ electronically. Therefore, it can be deduced that spiro-MeOTAD²⁺ consists of two decoupled MeOTPD¹⁺ radical cations anchored at one common spiro carbon center, rather than a doubly charged MeOTPD²⁺ moiety linked to another neutral half. The chemical structures of all four possible spiro-MeOTAD oxidation states are compiled in **Figure S5**. Moreover, both spiro-MeOTAD¹⁺ and MeOTPD¹⁺ possess sufficient low ionization potentials or E_{HOMO} of -5.38 and -5.50 eV, making exothermal multielectron electron transfer from P1 or P2 (IP = 4.6-4.7 eV) feasible to reach the zero oxidation states of both D3 and D4. The peak current obtained from the DPP experiment is directly related to the amount of electrons transferred and the concentration of the redox species, which is constant in our experiment.^[39] When comparing the differential pulse polarogram peak current of spiro-MeOTAD²⁺ and spiro-MeOTAD⁴⁺ signal, a two electron oxidation process from dication to tetracation can be inferred (Figure S4b). This implies an intrinsically unstable triply charged spiro-MeOTAD³⁺, consistent with an earlier report by Zhang et al.^[40]. Quantitative X-ray photoelectron spectroscopy analysis was employed to obtain the atomic composition (N/P) of D3 and D4 powder samples (See Table S2). By comparing the theoretical nitrogen to phosphorous atomic ratios (N/P = 1 for both tetracation, D4 and dication D3) to experimentally determined nitrogen 1s and phosphorous 2p signal integral ratios (1.2 and 1.4 respectively), average contents of at least 60 % for D3 and 80% for D4 can be assessed from XPS. Considering all the supporting data from CV, DPP, UPS and XPS, it can be very well concluded that the di- and tetracation organic salts D3 and D4 were successfully synthesized, where both the dopants are capable of exothermal multielectron transfer from the polymers P1 and P2.

2.2. Monitoring of the doping process

As a first step to study the charge transfer between dopants and polymers, we performed UV/Vis/NIR absorption spectroscopy experiments, as it is a simple, yet powerful technique to probe changes in electronic states due to doping of polymers. Prior to chemical doping, the changes in spectral features of polymers P1 and P2 on electrochemical oxidation were determined by spectroelectrochemical (SEC) measurements in solution to identify the polaron features. For this, both polymers were biased from zero to +800 mV oxidation potential in 200 mV steps and absorption spectra are measured (**Figure 2a**). The ground-state absorptions for both P1 and P2 are located at 820 nm and upon electrochemical oxidation, the ground state absorption is bleached and new polaronic features appear at ca. 1200 nm in the near-infrared region. The detailed absorption spectra for P1 and P2 for all the dopant concentrations ranging from 0.1 to 5 mol% for D1-D4 are given in the supporting information (**Figure S6**). Figure 2b shows the absorption spectra of chemically doped P1 and P2 for the four different dopants D1-D4 at a typical 2 mol% dopant concentration in 0.01 mg mL⁻¹ polymer solution. For both polymers, the MEAs, D3 and D4 show pronounced doping effects compared to the

monovalent dopants D1 and D2. For all dopant concentrations, the TEG substituted polymer P1 exhibit the highest polaron absorption intensities in the increasing order from D2, over D3 to D4. Similarly, in the 2-hexyldecyl substituted polymer P2, a lower and less gradually expressed polaron absorption is observed with both D1 and D2. To delineate the changes in the absorption spectra, difference spectra were plotted in Figure 2c. Difference spectra are obtained by subtracting the spectrum of the pristine polymer from each spectrum of the doped polymers, thus emphasizing spectral changes upon doping. The upper plot in Figure 2c shows the difference spectra of the TEG substituted polymer P1 at a typical dopant concentration of 2 mol% for all four dopants. It shows a clear trend with increasing polaron intensity from D1 over D2 to D3 and D4. In the lower part, the difference plots for the alkyl substituted polymer P2 are shown. As before, only low doping can be achieved using D1, and the intensity of the polaron absorption increases with the oxidation state of the dopants. A notable difference for P2 is that D1 and D2 yield similar and low polaron intensities, as compared to D3 and D4. For dopant molar ratios up to 2 mol% (Figure 2c), there is no other considerable difference between P1 and P2 in terms of polaron intensity. However, for the dopant D4, a higher absolute polaron absorption was measured in the case of the hydrophilic polymer P1 as compared to the hydrophobic derivative P2 at 5 mol% doping ratio (Figure 2d). This can be attributed probably due to better miscibility of D4 in the former at higher concentrations. Similar behavior was previously observed by Kroon et al., who doped ethylene glycol substituted polythiophenes using F₄TCNQ and found an improved solubility and conductivity by the introduction of polar side chains.^[11] This can be explained as follows: For a successful molecular doping, the polar dopants must access the conjugated polymer backbone whereby the glycol substitution assists this mixing and therefore, a more steady and uniform doping process is attained with the more hydrophilic polymer P1.

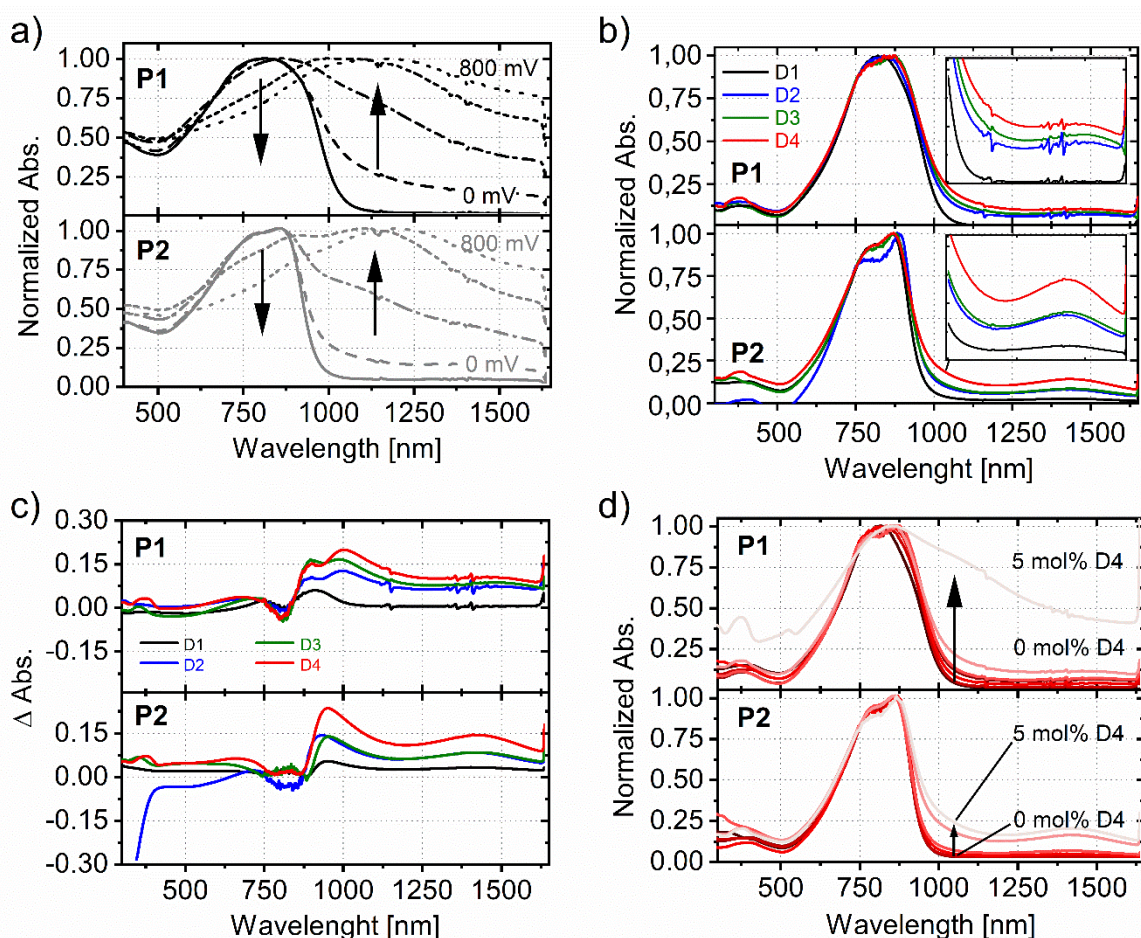


Figure 2. (a) Spectroelectrochemical spectra of the polymers P1 and P2 in DCM obtained by biasing from 0 mV to +800 mV. A dedoping step of -100 mV was applied prior to measurement to ensure pristine polymer samples. (b) Comparison of the optical absorption spectra of the doped P1 and P2 for four different dopants. D1-D4 at 2 mol% dopant loading in 0.01 mg mL^{-1} polymer solution. (c) Comparative difference spectra of both polymers with 2 mol% dopant loading, obtained by subtracting the pristine polymer absorption from the oxidized polymer absorption b). (d) Change in absorption for P1 on doping with 0 to 5 mol% D4 in DCM. Spectra (b) – (d) obtained under inert and anhydrous conditions.

Concomitant with polymer doping, the formation of reduced dopant species can be expected and consequently their original absorption changes. The pristine precursors (non-oxidized forms) of D2-D4 absorb only below 400 nm. To identify the optical signatures of intermediate reduction products of D3 and D4, i.e., $\text{MeOTPD}^+(\text{PF}_6^-)$ monocation and spiro- $\text{MeOTAD}^{2+}(\text{PF}_6^-)_2$ dication salts, these were prepared by titration of their respective neutral precursors MeOTPD or spiro-MeOTAD using the necessary equivalents of oxidizing agents. Spectra of these salts can be found in Figure S2b. Both exhibit pronounced NIR absorption at ca. 1500 nm with almost no absorption at 900 nm (typical absorption for the dopant D3 and D4, Figure S2a). Since the polaron absorption of P1 and P2 overlaps with the absorption of the reduced dopant intermediates at about 1500 nm, it is very difficult to elucidate the contribution of the reduced species towards near infrared absorption. It is to be noted that the contribution of the reduced species at low molar dopant regime is negligibly small. However, the increase in absorption

below 400 nm can be attributed to the neutral triarylamine species of the dopants, even though the molar amount of the dopant used is very small. Nevertheless, it is valid to focus on the polaron absorptions for the first estimate of the doping process. It is clearly demonstrated, that D4 introduces a much higher polaron concentration than all other dopants for the whole dopant concentration up to 5 mol% in both polymers P1 and P2 studied here, regardless of the polarity of the polymer.

2.3. Impact on the electrical conductivity and activation energies

The above discussed absorption studies have proven the highly efficient doping of polymers by the multication salts in general and the highly pronounced nature of doping using D4. The coulombically bound polaron-counter ion pair can now release electrons upon thermal activation, thus increasing the bulk conductivity. **Figure 3a** shows the electrical conductivity values of the doped systems measured in thin films in the range of zero to 5 mol% dopants for both the hydrophilic polymer P1 and the hydrophobic polymer P2. Interestingly, an increase in electrical conductivity over one to two orders of magnitude develops within 1 mol% of doping for any dopant for both P1 and P2. Below 1 mol% dopant concentrations, no big differences among the doping capabilities of D1-D4 are discernible. This initial strong increase of the conductivity at low doping concentrations is well-known in the literature and characteristic for filling of energetically deep lying states in highly disordered systems.^[41] On increasing dopant concentration, substantial differences for the four different dopants, as well as for the two polymers are evident. For example, above 1 mol%, the conductivity of doped P1 increases drastically for D3 and D4, whereas it levels off for D1 and D2, with the highest conductivity reached for the samples doped with D4 throughout the whole dopant concentration range. The final value for P1 doped with D3 reaches $1.9 \cdot 10^{-2} \text{ S cm}^{-1}$ and with D4 0.2 S cm^{-1} is obtained at 5 mol% dopant. In comparison, D1 and D2 increase the bulk conductivity of P1 to a mere $9.13 \cdot 10^{-4} \text{ S cm}^{-1}$, and $1.12 \cdot 10^{-3} \text{ S cm}^{-1}$ respectively (Table S4, S5). Thus the tetracation salt D4 causes two orders and D3 results in one order of magnitude higher conductivity compared to monocation salts D1 and D2 at 5 mol% doping. In the hydrophobic polymer P2 also a strong increase in electrical conductivity is observed at lower dopant loadings, which however increases slower than in the hydrophilic polymer. This can be attributed to the lack of glycol-substitution leading to a decreased accessibility of the polar dopants to the polymer backbones and, therefore, to a lower efficiency of polaron formation in P2. In P2, D1 and D2 have an identically lower doping effect as compared to D3 and D4. Here, the final conductivity values at 5 mol% reach $1.8 \cdot 10^{-4}$ and $2.3 \cdot 10^{-4} \text{ S cm}^{-1}$ for D1 and D2, respectively, and $2.6 \cdot 10^{-3}$ and $1.7 \cdot 10^{-3} \text{ S cm}^{-1}$ for D3 and D4, respectively. Thus a distinctive difference between the low efficient monocation salts (D1, D2) and highly efficient multication salts (D3 and D4) can be observed with respect to the achieved conductivity values. Further, an increased polarity of the conjugated polymer in P1 facilitates the doping process.

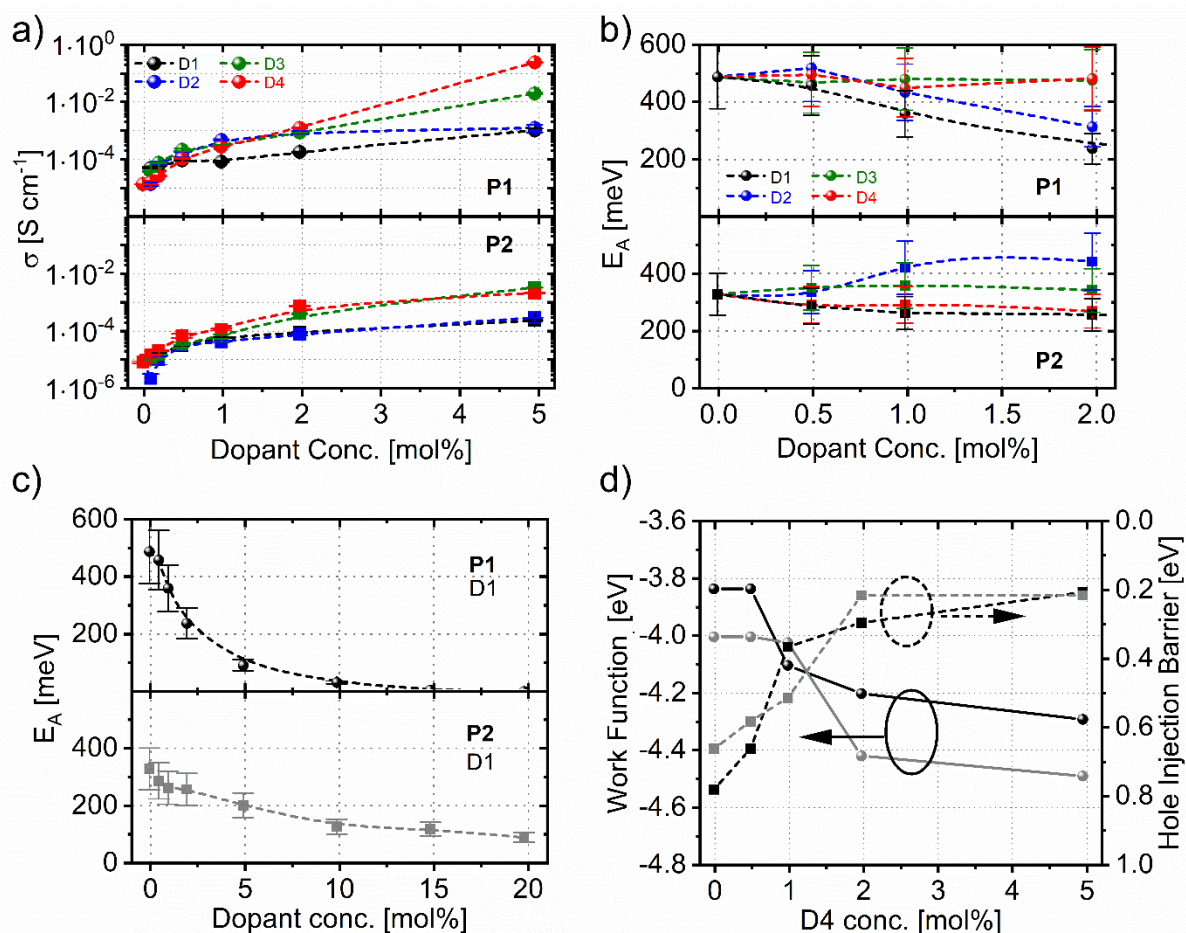


Figure 3. (a) Electrical conductivity measurement (b) Evolution of the activation energies. (c) E_A -progression of NOPF₆-doped films up to 20 mol% showing the drop of activation energy, which accompanies shift of the Fermi energy towards the transport level. (d) Variation of work function (left y-axis, solid lines) and hole-injection barrier (right y-axis, dashed lines) of P1 (black) and P2 (grey) as a function of molar doping ratio from 0 to 5 mol% D4.

To gain an understanding of the charge transport mechanism, the thermal activation energies of the conductivity in doped polymers were determined. The activation energies E_A were calculated from Arrhenius plots by measuring the temperature dependent conductivity $\sigma(T)$ for a range between room temperature and 100 °C. From the Arrhenius-plots (**Figure S7**), the activation energy values E_A were extracted using the Arrhenius equation $\sigma(T) = \sigma_0 e^{-E_A/(k_B T)}$, where k_B is the Boltzmann constant. The activation energy obtained by this consists of two processes: a contribution for the charge transfer salt dissociation and the contribution of the thermally activated hopping, as described earlier by Schwarze et al.^[42] The activation for charge transfer dissociation, schematically shown in Equation 2 below, is typically at least one order of magnitude greater than the activation for hopping.^[42,43] Interestingly, we found drastic differences in E_A both, among the dopants, as well as between the two polymers. Figure 3b shows the activation energies of both doped polymers using different dopants for a dopant molar ratio up to 2 mol%. In the first glance, there is a distinct difference in behaviour between NOPF₆ (D1) and the triarylamine cation salts (D2-D4). In the hydrophilic polymer P1, a steadily decreasing activation energy is obtained for D1 starting

from 0 to 5 mol% (Figure 3b). This steady decline is very distinctive for an increased charge carrier density in organic semiconductors. By filling low lying, exponentially distributed trap states and shifting the Fermi level closer to the transport energy E_{Tr} , the hole injection barrier and the thermal activation energy for charge transport is lowered.^[17] E_t delimits mobile from trapped charges, with only states higher in energy contributing to charge transport.^[44] The hydrophobic polymer P2 exhibits a comparable behavior, although the decrease of the activation energy upon doping with D1 proceeds much slower than for P1 (Figure 3b). This is also observable in the doping regime beyond 2 mol% (Table S4) and it is explained with the inferior compatibility of the NOPF₆ salt with the hydrophobic polymer. In order to fully understand the steady decrease in E_A , for D1, we measured additionally the E_A for dopant concentrations up to 20 mol% of D1 for both P1 and P2. Figure 3c clearly shows, that E_A asymptotically approaches zero for 20 mol% D1.

The activation energy upon doping P2 with the oxidized triarylamine cations (D3-D4), which are HTM-dopants, remains, as in the polar polymer, almost constant. A slightly increasing activation energy is however found for D2 in polymer P2, which indicates an obstructed charge transport. On the contrary, in the case of the multication HTM-dopants D3 and D4, the activation energy for charge transport remains unchanged upon the introduction of dopants. In the context of hopping transport, this indicates a relatively unchanged distance between Fermi- and transport level. UPS experiments on the polymers P1 and P2 doped with D4 (Figure 3d) confirm the downshift of E_F towards the respective HOMO, with a distinct pinning at 200 meV above the valence band maximum for both polymers. Since the transport levels E_{Tr} in a Gaussian density of states (DOS) remains fairly independent of the charge carrier concentration, the downshift of the Fermi level E_F seems to be compensated by the additional broadening of the DOS by doping.^[45] To determine the impact of the (partially or fully) reduced HTM-dopant compared to a non-HTM dopant on the HOMO density of states (DOS) and their distribution in polymers, ultraviolet photoelectron spectroscopy was carried out on 20 nm thin films of undoped P1 and P2 and their doped samples with NOPF₆ (non-HTM dopant) and spiro-MeOTAD⁴⁺(PF₆⁻)₄ (HTM-dopant). After measurement of the valence band maximum (VBM), the onset was fitted with a modified exponential Gaussian distribution to account for localized/tail states arising due to ionized dopants (Equation S10). The broadening of the DOS was quantified by fitting Equation S10 to the VBM. (**Figure 4a**, numerical results summarized in Table S8). A comparison of the standard deviation of the gaussian distribution of DOS (σ_{GDOS}) confirms that D1 ($\sigma_{GDOS} = 120$ meV) causes less change in the variance of the Gaussian part of the fit function than D4 ($\sigma_{GDOS} = 198$ meV) in P1. A similar broadening of DOS is observed in using an HTM-dopant like D4 in P2. Additionally, the most pronounced disorder, and exponential tailing of the pristine polymers was measured for the the polar TEG-substituted P1, which is consistent with the experimental observations made by Borsenberger and Bässler, that static dipole moments increase the energetic disorder in organic semiconducting systems.^[46] Together with the increased energetic disorder found via UPS experiments and the high number of dipoles (i.e. static disorder) added in the form of multiply charged small

molecules, the constant activation energy for P1 and P2 using HTM-dopants can be attributed to a highly disordered system. However, at doping concentrations of 2 mol% and above, the use of multivalent dopants D3 and D4 result in doped polymers having conductivities orders of magnitude higher than D1 and D2. This advantage, however, comes along with the disadvantage, that a significant amount of static disorder is introduced by the highly charged HTM materials, causing no considerable decrease in activation energies for charge transport on increasing doping content.

Additionally, the difference in behaviour of P1 and P2 towards the dopants can be explained as follows. As the ionization potential difference between P1 and P2 is almost negligible (ca. 0.05 eV), we do not expect the IP to cause any difference in the degree of ionization after doping by a significant amount. In addition, both polymers support an exothermic electron transfer to all dopants. Especially at higher doping ratios (i.e. 5 mol%), tail states should not impact the doping efficiency, as the Fermi level has well crossed all intra-gap and tail states at this point (Figure 3d). This leaves the polarity/side-chains as the only major difference in both polymers, as the possible cause for the difference in doping efficiency and ultimately the observed conductivity trend.

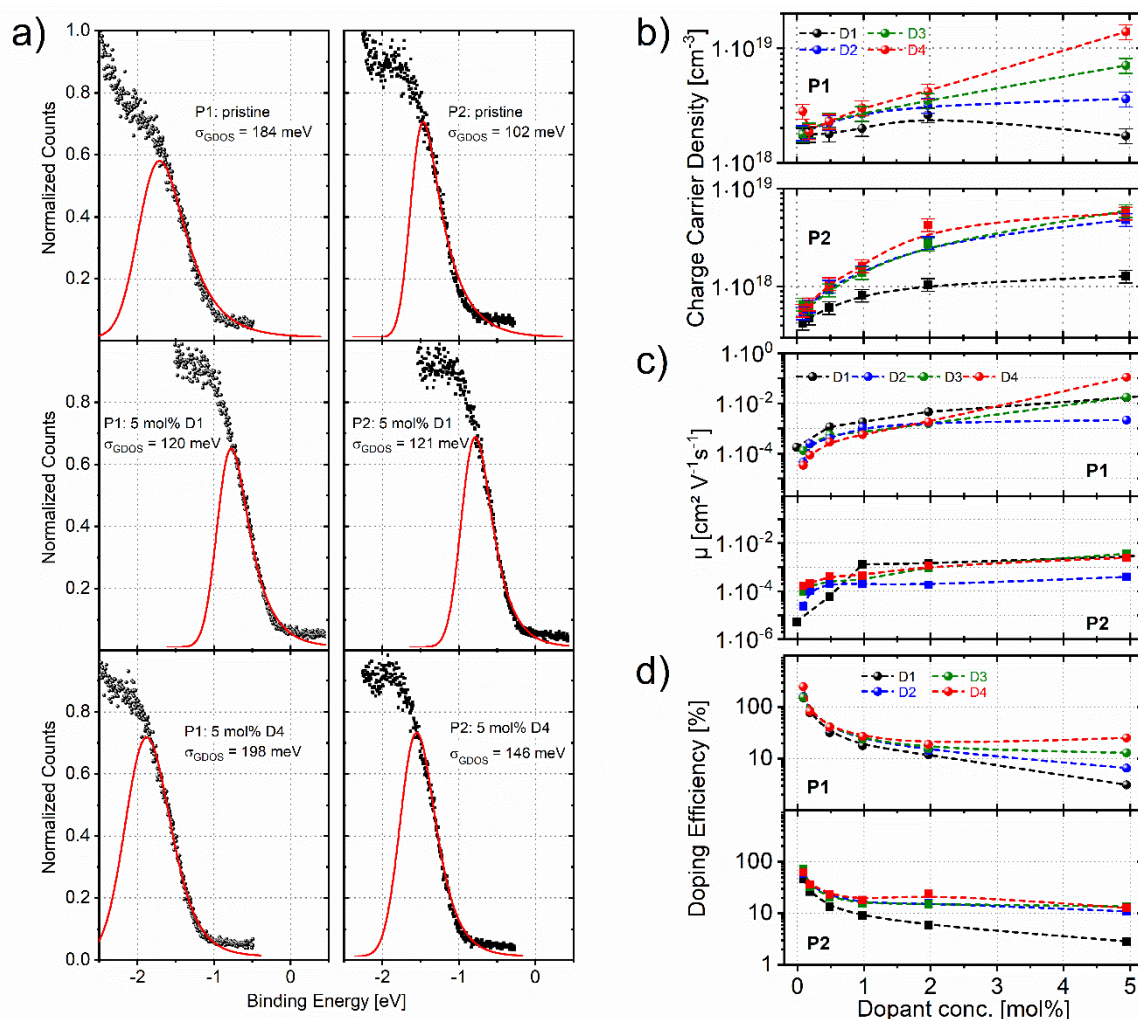


Figure 4. (a) Valence band maxima of P1 and P2 doped with 0 mol% (top), 5 mol% D1 (center) and 5 mol% D4 (bottom) obtained from UPS and fitted with an exponentially modified Gaussian distribution (See SI for detailed calculation). p-doping with D4 induces a higher variance of the Gaussian distribution as compared to doped polymers. (b) Charge carrier density obtained from a calibration curve (See SI for detailed information). (c) Calculated charge carrier mobility μ of P1 and P2 doped with D1-D4, determined from Equation 1 using the measured charge carrier concentration and conductivity. Holes were assumed as the majority carrier type in the p-doped systems, neglecting electron contribution. (d) Doping efficiency of the polymers P1 and P2, upon doping with the different dopants D1-D4. The doping efficiencies of D3 and D4 are normalized to 100 % (denoting the uptake of two and four electrons respectively).

2.4. Charge carrier density

The number of introduced charge carriers N_D is an important figure of merit in unipolar (p- or n-type) doped systems and is directly linked to the elementary charge e , the hole mobility μ_h and conductivity σ via *equation 1*:

$$\sigma = e N_D \mu_h \quad (\text{equation 1})$$

In doped systems, N_D is conveniently accessible via capacitance-voltage (Mott-Schottky) experiments on metal-insulator-semiconductor devices.^[26] In metal-insulator-semiconductor devices, holes are either accumulated or depleted at the semiconductor-insulator interface upon applying an electrical bias at the metal contact. Spatial width and capacitance of this depletion- or space-charge layer is, inter alia, very sensitive to the amount of ionized donors N_D present in the bulk. Using impedance spectroscopy, the change in depletion layer capacitance and consequently N_D of the doped system can be monitored (See SI for detailed information). Therefore, we have measured the charge carrier densities (N_D) of polymer films doped with D1 from 0 to 20 mol% and correlated the resulting values with the respective polaron absorption intensities from optical absorption spectroscopy measurements. Since N_D correlates perfectly linear with the polaron peak integral obtained from UV/vis studies, a calibration curve can be obtained to deduce N_D , once the polaron intensity is measured (**Figure S8, S9**). Based on this calibration curve, the charge carrier densities for both polymer films doped with the other three dopants D2 - D4 were read out from the polaron absorption values. Details regarding the method are elaborated in the respective section of the supporting information. For both polymers, for the whole range of dopant concentration, the doped samples using triarylamine dopants D2 - D4 exhibit considerably higher N_D values compared to the NOPF₆. The charge carrier densities in the doped hydrophilic polymer P1 scale with the oxidation state of the HTM-dopants; D4 doping exhibiting almost 3-5 times the value of D2 doping. Figure 4b shows this clear trend for P1 above 2 mol% dopant. At the highest concentration of 5 mol%, the anticipated scaling of the charge carrier density with the oxidation state is perfectly expressed: the mono-valent dopant D2 creates a carrier density of $3.5 \cdot 10^{18} \text{ cm}^{-3}$ which doubles to $6.9 \cdot 10^{18} \text{ cm}^{-3}$ for D3 (dication) and quadruples for the four-fold oxidized D4, reaching a carrier density of $13.8 \cdot 10^{18} \text{ cm}^{-3}$. This correlation could not be observed in the doped hydrophobic polymer P2; indeed, the charge carrier density of D4 doped P2 films rises more strongly below 2 mol% dopant concentration, as compared to all the other dopants. Beyond 2 mol% in P2 however, the charge carrier densities generated by all three HTM-dopants D2-D4 merge and saturate reaching $5 \cdot 10^{18} \text{ cm}^{-3}$ at 5 mol%. This is still almost 5 times the value obtained for NOPF₆-doped P2. Thus, the HTM-dopants induce drastically higher carrier densities than D1, which affords a saturated value of only $1.2 \cdot 10^{18} \text{ cm}^{-3}$ at 5 mol%. The fact that for both, the polar polymer P1, and the non-polar polymer P2, the redox dopant D1 performs worse than any of the HTM-dopants D2-D4 for the whole range of dopant concentrations up to 5 mol%, indicates the increased efficacy of doping conjugated

polymers using triarylamine-cation based salts in general. Moreover, the higher the oxidation state of the dopant, the more efficient is the doping process.

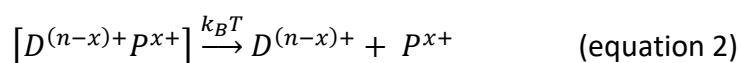
2.5. Charge carrier mobility

The widely studied p-type dopants such as F₄TCNQ, and the fluorinated Fullerene C₆₀F₃₆ are being reduced upon doping to form their anions such as F₄TCNQ⁻, and C₆₀F₃₆⁻, or charge transfer salts thereof.^[7] Typically, these reduced species do not contribute to the charge transport, or may even hamper it, ultimately resulting in reduced charge carrier mobilities. Our dopants D2-D4, consisting of oxidized triarylamine hole conductors, are able to transport charges in their pristine as well as partially oxidized states. The lower oxidized states (which are de facto the reduced dopant species after doping the polymer) are extensively used as charge transport layers for e.g. solar cells.^[47] We therefore examined if the use of cation salts of hole conductors as dopants can have additional contributions towards charge transport within the host:dopant mixture, as compared to NOPF₆, which has no HTM component at all. For this, first the zero-field charge carrier mobilities μ_0 of the pristine dopant precursors TPA-Br₃, MeOTPD and spiro-MeOTAD were determined by impedance spectroscopy by fitting a Poole-Frenkel field-dependency (Figure S10a). For this, negative differential susceptance measurements on hole-only FTO/semiconductor/Au devices were carried out. Holes are injected at one electrode if a sufficient electrical field F across the device is applied. By measuring the capacitive response of the biased device at different frequencies, an average carrier transit time for a given organic layer thickness and electrical field can be deduced. This ultimately yields μ_0 of the organic semiconductor after extrapolating $\mu(F)$ against zero electrical field. Details of calculation are published elsewhere and explained in supporting information.^[26] It was found, that all the pristine compounds possess similar values of μ_0 (MeOTPD: $2.6 \cdot 10^{-3} \text{ cm}^2\text{V}^{-1}\text{s}^{-1}$, followed by spiro-MeOTPD: $2.0 \cdot 10^{-3} \text{ cm}^2\text{V}^{-1}\text{s}^{-1}$ and TPA-Br₃: $1.3 \cdot 10^{-3} \text{ cm}^2\text{V}^{-1}\text{s}^{-1}$). Röhr et al reported a similar value of $3.2 \cdot 10^{-3} \text{ cm}^2\text{V}^{-1}\text{s}^{-1}$ for spiro-MeOTAD from space-charge limited current measurements (SCLC).^[48] The impact of the HTM-dopants on charge carrier mobility of the doped polymer P1 and P2 was estimated by extracting the charge carrier mobility from the known parameters such as charge carrier density and conductivity using equation (1). The results for both polymers doped with D1-D4 (0-5 mol%) are summarized in Figure 4c. Both, the polar P1 and the alkyl-substituted P2 improve in charge carrier mobility upon doping, regardless of the used dopant. This leads to the conclusion, that the presence of charged HTM dopants or their reduced products does not introduce trap states deeper in energy than already present in the disordered polymer semiconductor.^[49] This is substantiated by the measured activation energy, which remains virtually constant upon doping with D3 or D4 (Figure 3b). The more polar P1 shows signs of filling energetically low-lying tail states below the gaussian HOMO DOS (“trap-filling”), as evidenced by lowered activation energy in the case of D1 and D2. Trap-filling substantially increases the charge carrier mobility at low doping ratios, consistent with the mobility data shown in Figure 4c).^[17,22] The strong initial increase in μ_h tends to flatten more for the alkyl-substituted

polymer P2 and is in agreement with the initial steep drop of the hole-injection barrier and the Fermi-level pinning at > 2 mol% of D4 as seen in UPS experiments for both polymers (Figure 3d). When comparing the mobilities of the both doped polymers using the HTM dopants and NOPF₆, it appears that none of them affect the charge carrier mobility adversely and no considerable advantage is observed for the former, even though doping as such improves the charge carrier mobility.

2.6 Doping efficiency

Besides fundamental electronic properties such as conductivity, charge carrier mobility and charge carrier density, the doping efficiency (η_{Dop}) allows for comparison of our HTM-dopants vs. NOPF₆. η_{Dop} is defined as the ratio of the number of free holes N_{D} (obtained by Mott-Schottky measurements) and the total number of dopant molecules N_{A} per unit volume. A higher η_{Dop} implies a more efficient dissociation of the bound charge transfer state formed by [Dopant^{(n-x)+}Polymer^{x+}] into free majority charge carriers as given in *equation 2*, where D and P stand for dopant and the polymer respectively.



One important point to note here is, that the first step in the integer charge transfer doping reaction, i.e. the formation of the so called charge-transfer state is temperature independent.^[50] This implies, that nearly all dopants introduced into the system form ionized CT states, which are coulombically bound semiconductor-dopant pairs. In a second step, via thermal activation, free charge carriers responsible for the conductivity increase can be generated from the CT states. The ratio between the total amount of dopant molecules in the bulk vs. free charge carriers can be understood as the doping efficiency. As evident from Figure 4d, the polar polymer P1 displays an exponential decrease in η_{Dop} at the lowest doping ratios, to below 25 % ionization efficiency at 1 mol% dopant concentration. The pronounced loss in carrier generation efficiency with an increasing amounts of dopant molecules is known in the literature for organic semiconductors. It can be explained by a free hole capture process by ionized dopant molecules, which become statistically more likely, the more dopant is present in the system.^[22] Accumulation of unreacted dopant was detected in the absorption spectra for the highest doping concentration of 5 mol% D4 at 380 nm in Figure 2d. Consistent with our electrical conductivity and UV/Vis/NIR absorption studies, the more hydrophobic polymer P2 overall hinders the charge transfer salt dissociation, resulting in lower doping efficiency. This can be traced back to a decreased accessibility of the polymer backbone for dopant molecules and molecular miscibility. Ethylene glycol polar side chains are known to improve the dopant miscibility and doping efficacy for donor-acceptor copolymers.^[51–53] Further, a large relative permittivity ϵ_r introduced by the TEG sidechains ($\epsilon_r(\text{P1}) = 5.41$) helps to overcome Coulomb interaction of the charge-transfer salt compared to the alkyl-substituted P2 with $\epsilon_r(\text{P2}) = 4.74$ (Figure S10b, see SI for detailed calculation of dielectric constants). In both polymers, D4 offers the highest ratio of dissociated to total dopant molecules, closely followed by D3. To conclude,

multivalent oxidized HTM dopants offer an advantage in carrier generation efficiency from their charge transfer salts compared to Magic Blue and NOPF₆, which especially manifests itself at high dopant concentrations of > 2 mol%.

3. Conclusion

We synthesized novel and stable HTM-dopants, dication (MeOTPD²⁺(PF₆⁻)₂, D3) and tetracation (spiro-MeOTAD⁴⁺(PF₆⁻)₄, D4) salts and comparatively studied their use as p-dopants or MEAs for two conjugated polymers belonging to the class of polydiketopyrrolopyrroles (PDPPs) differing in their polarity and dielectric constants. Their superiority over conventional one-electron oxidants such as NOPF₆ (D1) and Magic Blue (D2) for p-doping was clearly proven. We observed a four-fold amount of positively charged polarons in both polymers when using the tetra cationic salt D4, resulting in a higher electrical conductivity and charge carrier density as compared to equivalent molar amounts of mono and divalent dopants. Unlike NOPF₆ (D1), a higher amount of energetic disorder is introduced in the density of states of doped polymer by MeOTPD²⁺(PF₆⁻)₂ and spiro-MeOTAD⁴⁺(PF₆⁻)₄, resulting in higher activation energies for charge transport. No negative effects on the charge carrier mobility were observed due to the presence of these dopants or their reduced species. Finally, the doping efficiency of D4 remains the highest among all the dopants for the whole range of dopant concentration from zero to 5 mol%. Thus, a highly efficient method of generating charge carriers in conjugated polymers is demonstrated using multiply charged salts of triarylamine derivatives to help decrease the dopant loading necessary for achieving strongly improved electronic properties, thereby overcoming issues associated with excess use of dopants. Synergistic effects between multivalent HTM dopants and hydrophilic polymers further boost the doping efficiencies. Our findings pave the way for a new and highly efficient route of doping conjugated polymers using MEA cation salts.

Supporting Information

Supporting Information is available from the Wiley Online Library or from the author.

Acknowledgements

We kindly acknowledge financial support from the Deutsche Forschungsgemeinschaft (SPP TH807/8-1) and Bavarian Ministry of State for Science and Arts (Solar Technologies Go Hybrid, SolTech). We acknowledge Dr. Holger Schmalz for providing the Raman data and the instrument facility, the confocal WITec alpha 300 RA+ imaging system equipped with a UHTS 300 spectrometer. The XPS/UPS facility (PHI 5000 VersaProbe III system) at the Keylab Device Engineering in Bavarian Polymer Institute, University of Bayreuth is also acknowledged. Gert Krauss and Adrian Hochgesang contributed equally to this work.

The authors declare no conflict of interest.

Received: July 23, 2021

Revised: September 23, 2021

Published online: October 22, 2021

References

- [1] B. H. Lee, G. C. Bazan, A. J. Heeger, *Adv. Mater.* **2016**, *28*, 57–62.
- [2] Y. Hu, Z. D. Rengert, C. McDowell, M. J. Ford, M. Wang, A. Karki, A. T. Lill, G. C. Bazan, T.-Q. Nguyen, *ACS Nano* **2018**, *12*, 3938–3946.
- [3] Y. Kim, S. Chung, K. Cho, D. Harkin, W.-T. Hwang, D. Yoo, J.-K. Kim, W. Lee, Y. Song, H. Ahn, Y. Hong, H. Sirringhaus, K. Kang, T. Lee, *Adv. Mater.* **2019**, *31*, 1806697.
- [4] I. H. Jung, C. T. Hong, U.-H. Lee, Y. H. Kang, K.-S. Jang, S. Y. Cho, *Scientific Reports* **2017**, *7*, 44704.
- [5] H. Yan, J. G. Manion, M. Yuan, F. P. García de Arquer, G. R. McKeown, S. Beaupré, M. Leclerc, E. H. Sargent, D. S. Seferos, *Adv. Mater.* **2016**, *28*, 6491–6496.
- [6] Y. Zhang, H. Zhou, J. Seifert, L. Ying, A. Mikhailovsky, A. J. Heeger, G. C. Bazan, T.-Q. Nguyen, *Advanced Materials* **2013**, *25*, 7038–7044.
- [7] H. Hase, I. Salzmann, in *Handbook of Organic Materials for Electronic and Photonic Devices (Second Edition)* (Ed.: O. Ostroverkhova), Woodhead Publishing, **2019**, pp. 349–383.
- [8] I. Salzmann, G. Heimel, M. Oehzelt, S. Winkler, N. Koch, *Acc. Chem. Res.* **2016**, *49*, 370–378.
- [9] J. Hynynen, D. Kiefer, L. Yu, R. Kroon, R. Munir, A. Amassian, M. Kemerink, C. Müller, *Macromolecules* **2017**, *50*, 8140–8148.
- [10] B. Lüssem, M. Riede, K. Leo, *Physica Status Solidi A* **2013**, *210*, 9–43.
- [11] R. Kroon, D. Kiefer, D. Stegerer, L. Yu, M. Sommer, C. Müller, *Advanced Materials* **2017**, *29*, 1700930.
- [12] Y. Karpov, T. Erdmann, M. Stamm, U. Lappan, O. Guskova, M. Malanin, I. Raguzin, T. Beryozkina, V. Bakulev, F. Günther, S. Gemming, G. Seifert, M. Hamsch, S. Mannsfeld, B. Voit, A. Kiriya, *Macromolecules* **2017**, *50*, 914–926.

- [13] H. Li, E. Plunkett, Z. Cai, B. Qiu, T. Wei, H. Chen, S. M. Thon, D. H. Reich, L. Chen, H. E. Katz, *Advanced Electronic Materials* **2019**, *5*, 1800618.
- [14] Y. Xuan, X. Liu, S. Desbief, P. Leclère, M. Fahlman, R. Lazzaroni, M. Berggren, J. Cornil, D. Emin, X. Crispin, *Phys. Rev. B* **2010**, *82*, 115454.
- [15] D. Kiefer, R. Kroon, A. I. Hofmann, H. Sun, X. Liu, A. Giovannitti, D. Stegerer, A. Cano, J. Hynynen, L. Yu, Y. Zhang, D. Nai, T. F. Harrelson, M. Sommer, A. J. Moulé, M. Kemerink, S. R. Marder, I. McCulloch, M. Fahlman, S. Fabiano, C. Müller, *Nature Mater* **2019**, *18*, 149–155.
- [16] G. Chauhan, R. Srivastava, A. Kumar, O. Rana, P. C. Srivastava, M. N. Kamalasanan, *Organic Electronics* **2012**, *13*, 394–398.
- [17] S. Olthof, S. Mehraeen, S. K. Mohapatra, S. Barlow, V. Coropceanu, J.-L. Brédas, S. R. Marder, A. Kahn, *Phys. Rev. Lett.* **2012**, *109*, 176601.
- [18] I. E. Jacobs, E. W. Aasen, J. L. Oliveira, T. N. Fonseca, J. D. Roehling, J. Li, G. Zhang, M. P. Augustine, M. Mascall, A. J. Moulé, *J. Mater. Chem. C* **2016**, *4*, 3454–3466.
- [19] F. Deschler, D. Riedel, A. Deák, B. Ecker, E. von Hauff, E. Da Como, *Synthetic Metals* **2015**, *199*, 381–387.
- [20] J. Euvrard, A. Revaux, P.-A. Bayle, M. Bardet, D. Vuillaume, A. Kahn, *Organic Electronics* **2018**, *53*, 135–140.
- [21] V. I. Arkhipov, E. V. Emelianova, P. Heremans, H. Bässler, *Phys. Rev. B* **2005**, *72*, 235202.
- [22] M. L. Tietze, L. Burtone, M. Riede, B. Lüssem, K. Leo, *Phys. Rev. B* **2012**, *86*, 035320.
- [23] B. Tan, S. R. Raga, A. S. R. Chesman, S. O. Furer, F. Zheng, D. P. McMeekin, L. Jiang, W. Mao, X. Lin, X. Wen, J. Lu, Y.-B. Cheng, U. Bach, *Advanced Energy Materials* **2019**, *9*, 1901519.
- [24] W. H. Nguyen, C. D. Bailie, E. L. Unger, M. D. McGehee, *J. Am. Chem. Soc.* **2014**, *136*, 10996–11001.
- [25] W. Zhang, F. Zhang, B. Xu, Y. Li, L. Wang, B. Zhang, Y. Guo, J. M. Gardner, L. Sun, L. Kloo, *ACS Appl. Mater. Interfaces* **2020**, *12*, 33751–33758.
- [26] M. Goel, M. Siegert, G. Krauss, J. Mohanraj, A. Hochgesang, D. C. Heinrich, M. Fried, J. Pflaum, M. Thelakkat, *Adv. Mater.* **2020**, *32*, 2003596.
- [27] A. I. Hofmann, R. Kroon, S. Zokaei, E. Järsvall, C. Malacrida, S. Ludwigs, T. Biskup, C. Müller, *Adv. Electron. Mater.* **2020**, *6*, 2000249.
- [28] P. Schmode, A. Savva, R. Kahl, D. Ohayon, F. Meichsner, O. Dolynchuk, T. Thurn-Albrecht, S. Inal, M. Thelakkat, *ACS Appl. Mater. Interfaces* **2020**, *12*, 13029–13039.
- [29] G. Krauss, F. Meichsner, A. Hochgesang, J. Mohanraj, S. Salehi, P. Schmode, M. Thelakkat, *Adv. Funct. Mater.* **2021**, 2010048.
- [30] C. J. Mueller, E. Gann, C. R. Singh, M. Thelakkat, C. R. McNeill, *Chem. Mater.* **2016**, *28*, 7088–7097.
- [31] B. Meng, J. Liu, L. Wang, *Polym. Chem.* **2020**, *11*, 1261–1270.
- [32] B. Meng, H. Song, X. Chen, Z. Xie, J. Liu, L. Wang, *Macromolecules* **2015**, *48*, 4357–4363.
- [33] H. Méndez, G. Heimel, A. Opitz, K. Sauer, P. Barkowski, M. Oehzelt, J. Soeda, T. Okamoto, J. Takeya, J.-B. Arlin, J.-Y. Balandier, Y. Geerts, N. Koch, I. Salzmänn, *Angewandte Chemie International Edition* **2013**, *52*, 7751–7755.
- [34] I. Salzmänn, G. Heimel, S. Duhm, M. Oehzelt, P. Pingel, B. M. George, A. Schnegg, K. Lips, R.-P. Blum, A. Vollmer, N. Koch, *Phys. Rev. Lett.* **2012**, *108*, 035502.
- [35] C. Lambert, G. Nöll, *J. Am. Chem. Soc.* **1999**, *121*, 8434–8442.
- [36] Y. Su, X. Wang, X. Zheng, Z. Zhang, Y. Song, Y. Sui, Y. Li, X. Wang, *Angew. Chem. Int. Ed.* **2014**, *53*, 2857–2861.
- [37] S. Amthor, B. Noller, C. Lambert, *Chemical Physics* **2005**, *316*, 141–152.
- [38] C. Kvarnström, A. Petr, P. Damlin, T. Lindfors, A. Ivaska, L. Dunsch, *J Solid State Electrochem* **2002**, *6*, 505–512.

- [39] D. J. Myers, J. Osteryoung, *Anal. Chem.* **1973**, *45*, 267–271.
- [40] W. Zhang, L. Wang, Y. Guo, B. Zhang, V. Leandri, B. Xu, Z. Li, J. M. Gardner, L. Sun, L. Kloo, *Chem. Commun.* **2020**, *56*, 1589–1592.
- [41] A. Fediai, F. Symalla, P. Friederich, W. Wenzel, *Nat Commun* **2019**, *10*, 4547.
- [42] M. Schwarze, C. Gaul, R. Scholz, F. Bussolotti, A. Hofacker, K. S. Schellhammer, B. Nell, B. D. Naab, Z. Bao, D. Spoltore, K. Vandewal, J. Widmer, S. Kera, N. Ueno, F. Ortmann, K. Leo, *Nature Mater* **2019**, *18*, 242–248.
- [43] H. Matsui, D. Kumaki, E. Takahashi, K. Takimiya, S. Tokito, T. Hasegawa, *Phys. Rev. B* **2012**, *85*, 035308.
- [44] J. O. Oelerich, F. Jansson, A. V. Nenashev, F. Gebhard, S. D. Baranovskii, *J. Phys.: Condens. Matter* **2014**, *26*, 255801.
- [45] B. Hartenstein, H. Bässler, *Journal of Non-Crystalline Solids* **1995**, *190*, 112–116.
- [46] P. M. Borsenberger, H. Bässler, *J. Chem. Phys.* **1991**, *95*, 5327–5331.
- [47] Z. Hawash, L. K. Ono, Y. Qi, *Adv. Mater. Interfaces* **2018**, *5*, 1700623.
- [48] J. A. Röhr, X. Shi, S. A. Haque, T. Kirchartz, J. Nelson, *Phys. Rev. Applied* **2018**, *9*, 044017.
- [49] S.-J. Yoo, J.-H. Lee, J.-H. Lee, J.-J. Kim, *Appl. Phys. Lett.* **2013**, *102*, 183301.
- [50] M. L. Tietze, J. Benduhn, P. Pahnner, B. Nell, M. Schwarze, H. Kleemann, M. Krammer, K. Zojer, K. Vandewal, K. Leo, *Nat. Commun.* **2018**, *9*, 1182.
- [51] D. Kiefer, A. Giovannitti, H. Sun, T. Biskup, A. Hofmann, M. Koopmans, C. Cendra, S. Weber, L. J. Anton Koster, E. Olsson, J. Rivnay, S. Fabiano, I. McCulloch, C. Müller, *ACS Energy Lett.* **2018**, *3*, 278–285.
- [52] J. Liu, L. Qiu, R. Alessandri, X. Qiu, G. Portale, J. Dong, W. Talsma, G. Ye, A. A. Sengrjan, P. C. T. Souza, M. A. Loi, R. C. Chiechi, S. J. Marrink, J. C. Hummelen, L. J. A. Koster, *Adv. Mater.* **2018**, *30*, 1704630.
- [53] J. Liu, G. Ye, H. G. O. Potgieser, M. Koopmans, S. Sami, M. I. Nugraha, D. R. Villalva, H. Sun, J. Dong, X. Yang, X. Qiu, C. Yao, G. Portale, S. Fabiano, T. D. Anthopoulos, D. Baran, R. W. A. Havenith, R. C. Chiechi, L. J. A. Koster, *Advanced Materials* **2021**, *33*, 2006694.

Supporting Information

Highly Efficient Doping of Conjugated Polymers using Multielectron Acceptor Salts

Krauss, Gert; Hochgesang, Adrian; Mohanraj, John; Thelakkat, Mukundan[†]*

Table of Contents

1. General methods
2. Monomer- and Polymer Synthesis
3. Dopant Synthesis
4. Supporting Measurement Data
5. References

Experimental Procedures

1. General methods

All the materials were thoroughly dried under high vacuum prior to their use. The reactions sensitive to humidity and/or oxygen were conducted in flame-dried Schlenk type apparatuses under argon atmosphere and the doping experiments were performed in a nitrogen-filled glovebox. Anhydrous solvents were purchased from Sigma Aldrich / Acros Organics in sealed bottles and were used as received. Other solvents for chemical reactions, Soxhlet extractions etc. were freshly distilled in-house and reagents for syntheses were used as received from commercial sources if not stated otherwise. *N,N,N',N'*-Tetrakis(4-methoxyphenyl)benzidine (abbr. 4-MeO-TPD) was obtained from TCI Chemicals, Japan. *N2,N2,N2',N2',N7,N7,N7',N7'*-octakis(4-methoxyphenyl)-9,9'-spirobi[fluorene]-2,2',7,7'-tetraamine (abbreviated as "Spiro-MeOTAD") was supplied by Sigma-Aldrich, Germany and used as received. 4-MeOTPD was dried under vacuum at RT for 1 h prior to use. Nitrosonium hexafluorophosphate was obtained from ThermoFischer, Germany and purified according to the synthetic procedure described below. Anhydrous dichloromethane and acetonitrile were supplied from ThermoFischer, Germany and used as received. Doped polymer solutions were fabricated by mixing of definite amounts of the respective polymer and dopant in dichloromethane; doped polymer films were similarly obtained by spin casting the respective polymer-dopant solution for 60 s at 1500 rpm. No further annealing was conducted. The polymerization reactions were conducted under microwave irradiation using a Biotage Initiator+ synthesis microwave machine. Solution NMR-spectra were recorded on a Bruker Avance spectrometer (300 MHz) at RT with deuterated solvents from Deutero GmbH and the chemical shifts are reported with respect to the residual solvent signal in units of [ppm]. Gel permeation chromatography (GPC)

measurements were performed on an instrument having an SDV linear XL gel column (particle size = 5 μm) with separation range from 100 to 3 000 000 Da (PSS, Mainz, Germany) together with a refractive index detector (1200 Series, Agilent Technologies). CHCl_3 (HPLC grade) was used as solvent (for dissolving polymer and as eluting solvent) with a flow rate of 0.5 mL/min at room temperature. As internal standard toluene (HPLC grade) was used. The calibration was done with narrowly distributed polystyrene (PS) homo-polymers (PSS calibration kit). An injection volume of 20 μL was used for the measurements. The sample was dissolved in CHCl_3 and filtered through a 0.22 μm PTFE filter before analysis. Optical absorption spectroscopy measurements were recorded using a Jasco V-670 spectrophotometer with a custom-built nitrogen flooded measurement chamber. Quartz-cuvettes of an internal diameter of 1 cm were employed and for spectroelectrochemical absorption measurements, a Gamry Interface 1010T was used as the potentiostat in a conventional three-electrode setup (Pt-mesh WE, Pt-wire CE, Ag/AgCl RE). Ultraviolet photoelectron spectroscopy was performed on a PHI 5000 VersaProbe III machine equipped with a helium discharge radiation source providing stable and continuous He I and II lines, under ultrahigh vacuum (10^{-10} mbar). Samples for UPS measurements were obtained by spin-coating on clean ITO ($15 \Omega \text{sq}^{-1}$), affording ca. 30 nm thick films (measured by using a dummy sample in a profilometer). The samples were transferred from the glovebox to the instrument in a nitrogen filled and sealed stainless steel transport vessel.

2. Monomer- and Polymer Synthesis

The synthetic pathway toward the polymers was described by us earlier. (Krauss et al., *Adv. Funct. Mater.* **2021**, 2010048). The obtained polymers exhibited the following basic properties.

¹H NMR:

PDPP[T]₂{TEG}₂-3-MEET: (300 MHz, CDCl₃): d = 8.59 - 9.13 (br., 2 H), d = 6.41 - 7.15 (br., 3 H), d = 2.84 - 5.09 (br., 41 H).

PDPP[T]₂{2-HD}₂-3-MEET: (300 MHz, CDCl₃): d = 8.76 - 9.27 (br., 2 H), d = 6.67 - 7.22 (br., 2 H), d = 3.53 - 4.76 (br., 8 H), d = 3.28 - 3.51 (br., 3 H), d = 0.44 - 2.14 (br., 66 H).

GPC:

PDPP[T]₂{TEG}₂-3-MEET: M_n = 11 kg mol⁻¹, Đ = 2.5, X_N = 14.

PDPP[T]₂{2-HD}₂-3-MEET: M_n = 14 kg mol⁻¹, Đ = 2.9, X_N = 18.

3. Dopant synthesis

***N*²,*N*²,*N*^{2'},*N*^{2'},*N*⁷,*N*⁷,*N*^{7'},*N*^{7'}-octakis(4-methoxyphenyl)-9,9'-spirobi[fluorene]-2,2',7,7'-tetraamine^{IV}, hexafluorophosphate salt (1:4)**

Commercially available nitrosonium hexafluorophosphate was dried under vacuum for 3 d in a desiccator loaded with phosphorus pentoxide. A 250 mL flame-dried Schlenk flask was flushed with Ar and charged with 45 mL of anhydrous and degassed benzene. The solvent was cooled to 0 °C and dry nitrosonium hexafluorophosphate (2 g, 11.4 mmol) was added in small portions using air-free techniques to remove nitronium hexafluorophosphate. The mixture was stirred for 1 h at 0°C. The solvent was removed and the purified nitrosonium hexafluorophosphate was dried under vacuum at RT and stored under inert conditions. Spiro-MeOTAD (107.6 mg, 87.8 μmol) was loaded into a flame-dried Schlenk flask flushed with Argon and dissolved in anhydrous dichloromethane (20 mL) cooled to 0°C under strong stirring for 10 min. Nitrosonium hexafluorophosphate (103.8 mg, 593 μmol, 6 eq.) was loaded into a Schlenk flask flushed with Argon and dissolved in anhydrous acetonitrile (10 mL) and stirred at RT for 5 min. The nitrosonium hexafluorophosphate solution was added drop-wise to the ice-cold Spiro-MeOTAD solution using air-free techniques. Upon addition, the solution turned dark red with a gradual color change to royal blue. After complete addition, the mixture was allowed to heat up to RT and stirred for 20 min. The solution was precipitated in ice-cold, anhydrous hexane (500 mL), dried at RT in vacuum and stored under nitrogen. Yield: 127.9 mg (70.8 μmol / 81 %) of a dark-green powder.

***N,N,N',N'*-Tetrakis(4-methoxyphenyl)benzidine^{II}, hexafluorophosphate salt (1:2)**

4-MeO-TPD (115.4 mg, 190 μmol) was loaded into a flame-dried Schlenk flask, flushed with Ar and dissolved in anhydrous dichloromethane (20 mL) cooled to 0°C under strong stirring for 10 min. Nitrosonium hexafluorophosphate (86.2 mg, 493 μmol, 2.6 eq.) was loaded into a Schlenk flask flushed with Ar and dissolved in anhydrous acetonitrile (10 mL) and stirred at RT for 5 min. The nitrosonium hexafluorophosphate solution was added drop-wise to the ice-cold 4-MeO-TPD solution using air-free techniques. Upon addition, the solution turned dark red with a gradual color change to dark blue. After complete addition, the mixture was allowed to heat up to RT and stirred for 20 min. The solution was precipitated in ice-cold, anhydrous hexane (500 mL), dried at RT in vacuum and stored under nitrogen. Yield: 114mg (127 μmol / 67 %) of a fine, dark-green powder.

4. Supporting Measurement Data

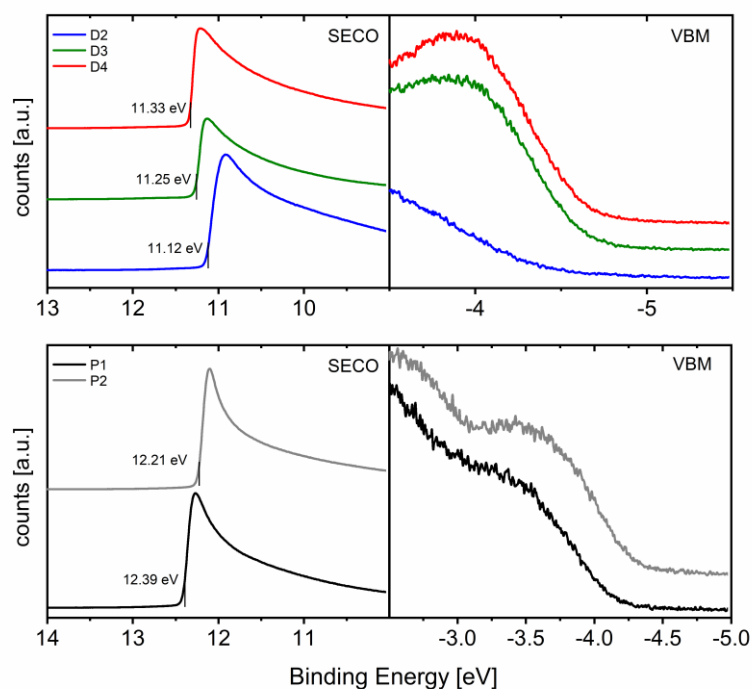


Figure S1. Ultraviolet photoelectron spectra showing the SECO (secondary electron cut-off, left) and VBM (valence band maximum, right) of D2 (blue), D3 (green), D4 (red), P1 (black) and P2 (grey), prepared as 20 nm thin films on ITO. Scaled w.r.t. Fermi Level (0 eV).

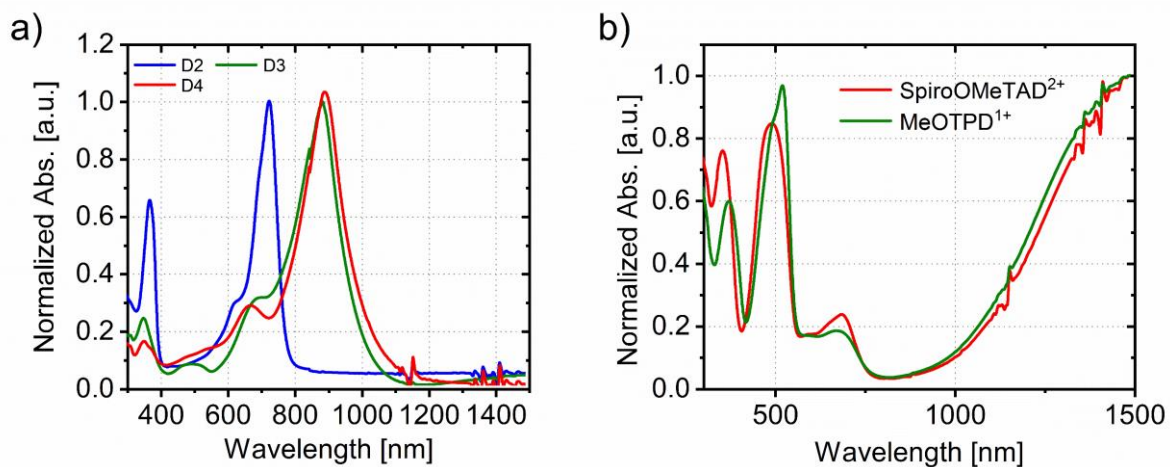


Figure S2. UV/vis/NIR spectra of the pure HTM-dopants in acetonitrile solution (a), and the intermediately oxidized HTM-dopants (b).

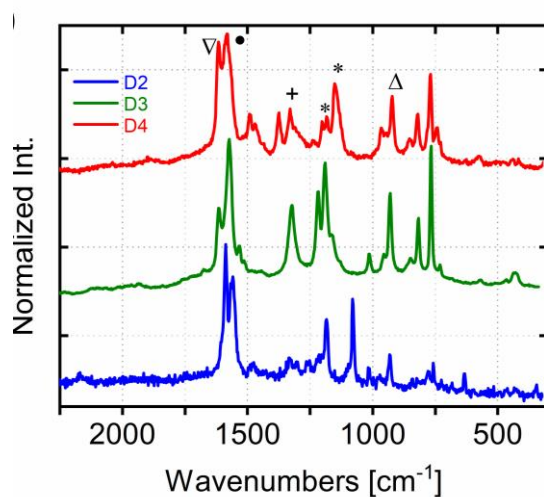


Figure S3. Raman spectra of the pure dopants D2, D3 and D4 measured on thin films on glass.

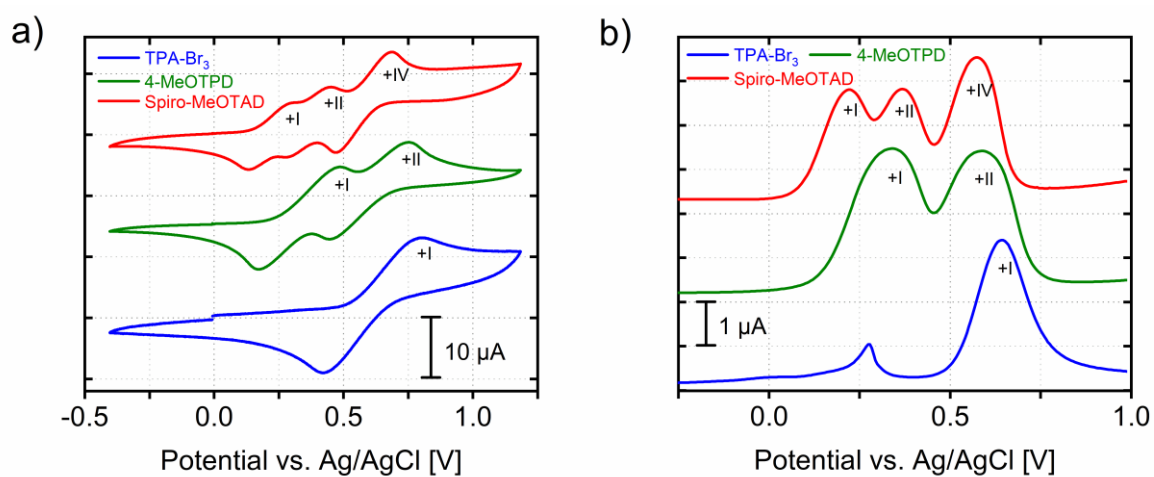


Figure S4. (a) Cyclic voltammograms and (b) differential pulse polarography (DPP) measured in dichloromethane solution using 0.1 M TBAPF₆ as the supporting electrolyte. A small redox current in the DPP measurement of Magic Blue at 260 mV vs. Ag/Ag⁺ indicates possible coupled by-products.

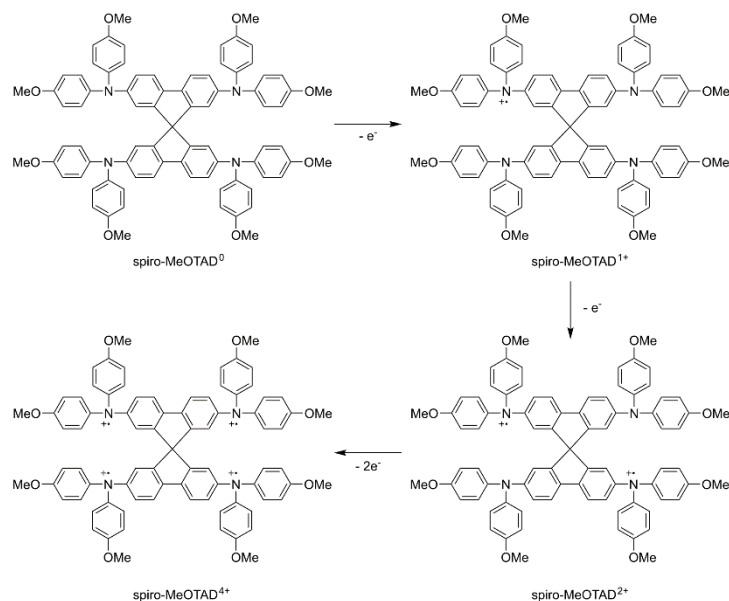


Figure S5. All the possible chemical structures of stepwise oxidation (removal of electrons) of spiro-MeOTAD.

Table S1. Cyclic voltammetry (CV) half wave $E_{1/2}$ potential (average of cathodic and anodic peaks) measured against Ag/AgNO_3 in DCM and peak-to-peak potential difference ΔE_p and differential pulse polarography (DPP) peak potential E_p for neutral tris(4-bromophenyl)amine (TPA- Br_3), 4-MeOTPD and spiro-MeOTAD. Oxidation states of the corresponding peaks are given as (+x) in brackets. Measured in anhydrous dichloromethane with 0.1 M TBAPF₆.

Compound	CV		DPP
	$E_{1/2}$ (+x) [mV]	ΔE_p [mV]	E_p [mV]
TPA- Br_3	628 (+I)	368(+I)	650 (+I)
4-MeO-TPD	339 (+I)	314(+I)	345 (+I)
	611 (+II)	302(+II)	595 (+II)
Spiro-MeOTAD	223 (+I)	162(+I)	230 (+I)
	374 (+II)	168(+II)	375 (+II)
	590 (+IV)	216(+IV)	585 (+IV)

X-Ray Photoelectron Spectroscopy

XPS measurements were carried out with a PHI 5000 VersaProbe III system fitted with an Al K α excitation source ($h\nu = 1486.6$ eV) and a dual neutralizer (electron gun and Ar^+) at 10^{-10} mbar. An X-ray source diameter of 100 mm was used to locally excite the samples; the corresponding photoemission with 45° take-off angle was collected at a multichannel analyzer. The survey and detailed spectra were measured with pass energies of 224 eV and 26/55 eV, respectively. The standard deviation on the reported energy values is ± 0.1 eV. The reproducibility of the observed results was confirmed by performing at least three

measurements at different places of the samples. The spectra were analyzed with a Multipak software pack provided by the manufacturers. All emission signals were referenced to adventitious C1s peak at 284.8 eV. For atomic composition determination, the samples were transported to the instrument using a N₂-filled transport vessel to avoid air/O₂ contamination. For quantitative measurements, at least two areas of ca. 400 x 400 mm² were selected in each samples using secondary ion X-ray imaging technique (SXI) to ensure spatial average composition of the dopants. The final reported atomic composition values are the average of 2 measurements. For quantitative analysis, the background of all spectra was corrected using the Shirley function.

For XPS mapping experiments, a homogeneous sample area of 750 μm by 750 μm was selected with the help of SXI imaging. The photoelectrons of the selected area were collected using parallel acquisition mode of the detector with a resolution of 256 by 256 pixel. A pass energy of 55 eV, 4 frames per element and 20 ms time per step were chosen to increase the sensitivity. P1 and P2 were mapped according to their thiophene sulfur 2p_{3/2} peak at 161.5 eV, D2 according to the antimony Sb3d_{5/2} peak at 539 eV, D3 and D4 to the fluorine 1s signal (688 eV). Prior to acquisition, the selected area was subjected to 30 sec Ar sputtering (2 by 2 mm, 2 kV, Zalar rotation) to remove surface residues. Finally, the colour coded images were overlaid to produce the mapped two-dimensional image.

Table S2. Comparison of the atomic composition of D3 and D4 between theoretical and XPS determined values.

Elements	Theoretical composition (ratio of atoms)		XPS determined
	Spiro-MeOTAD ²⁺ (PF ₆ ⁻) ₂	Spiro-MeOTAD ⁴⁺ (PF ₆ ⁻) ₄	
N	4	4	55.2 %
P	2	4	44.8 %
N/P	2	1	1.2
P	2	4	14.3 %
F	12	24	85.7 %
P/F	0.17	0.17	0.17
	MeOTPD ⁺ (PF ₆ ⁻)	MeOTPD ²⁺ (PF ₆ ⁻) ₂	
N	2	2	58.8 %
P	1	2	41.2 %
N/P	2	1	1.4
P	1	2	16.2 %
F	6	12	83.8 %
P/F	0.17	0.17	0.19

XPS determined values: atomic composition values are determined from ca. 400 x 400 mm² area scan with 55 eV pass energy and 100 mm X-ray source size. The values are the average from 2 measurements.

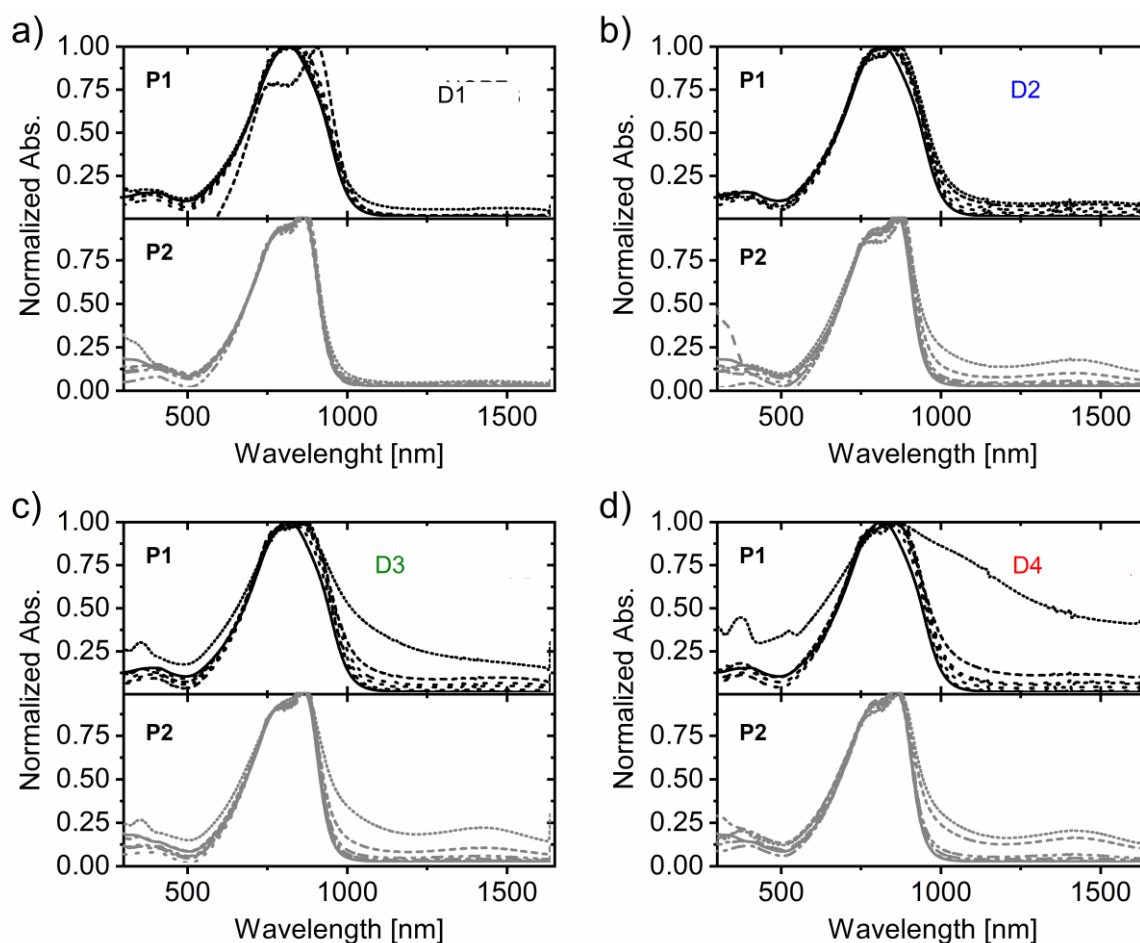


Figure S6. Solution (dichloromethane) UV/Vis/NIR progression of the two polymers P1 and P2 doped with D1 (a), D2 (b), D3 (c) and D4 (d) with the molar doping ratios of pristine (solid), 0.1 (dashed), 0.2 (dotted), 0.5 (dotted), 1 (dotted), 2 (dotted) and 5 mol% (dotted) in ascending order.

Electrical Conductivity

Electrical conductivities were measured using 30 nm thick interdigitated gold electrodes, patterned on thermally grown silicon oxide with a channel width of 2.5 μm and a channel length of 1 cm. The substrates were cleaned by sonication in isopropanol and acetone for 10 min each, followed by activation of the surface in an ozone plasma for 15 min at 50 $^{\circ}\text{C}$. Polymer and doped polymer films were deposited by spin-coating from 5 mg mL^{-1} solutions (dichloromethane) at 1500 rpm in a nitrogen filled glovebox. I-V characteristics were measured using an Agilent Technologies B1500A Semiconductor Device Analyzer. The electrical conductivities were extracted from the linear fit of the I-V curve in the Ohmic region according to the equation S1 below:

$$\sigma = \frac{a \cdot L}{W \cdot d} \quad \text{equation S1}$$

Where σ : electrical conductivity, a : slope of the linear fit, L : channel length, W : channel width, d : film thickness. The film thicknesses were measured after the conductivity measurements, using a profilometer. The activation energies for the charge transport were extracted from

temperature dependent electrical conductivity measurements. The sample preparation was done analogue to room-temperature electrical conductivity measurements. For the measurement, the devices were placed on a Linkam Scientific temperature control stage in a nitrogen filled glovebox and heated from RT to 100 °C in 5 K steps. The heating-rate between each step was adjusted to 5 K min⁻¹ and each temperature was kept constant for 30 s for equilibration before measuring the I-V characteristics. The activation energies were obtained from fitting the Arrhenius plot ($\ln \sigma$ vs. T^{-1}) with a linear curve and the Arrhenius equation yielded the activation energies.

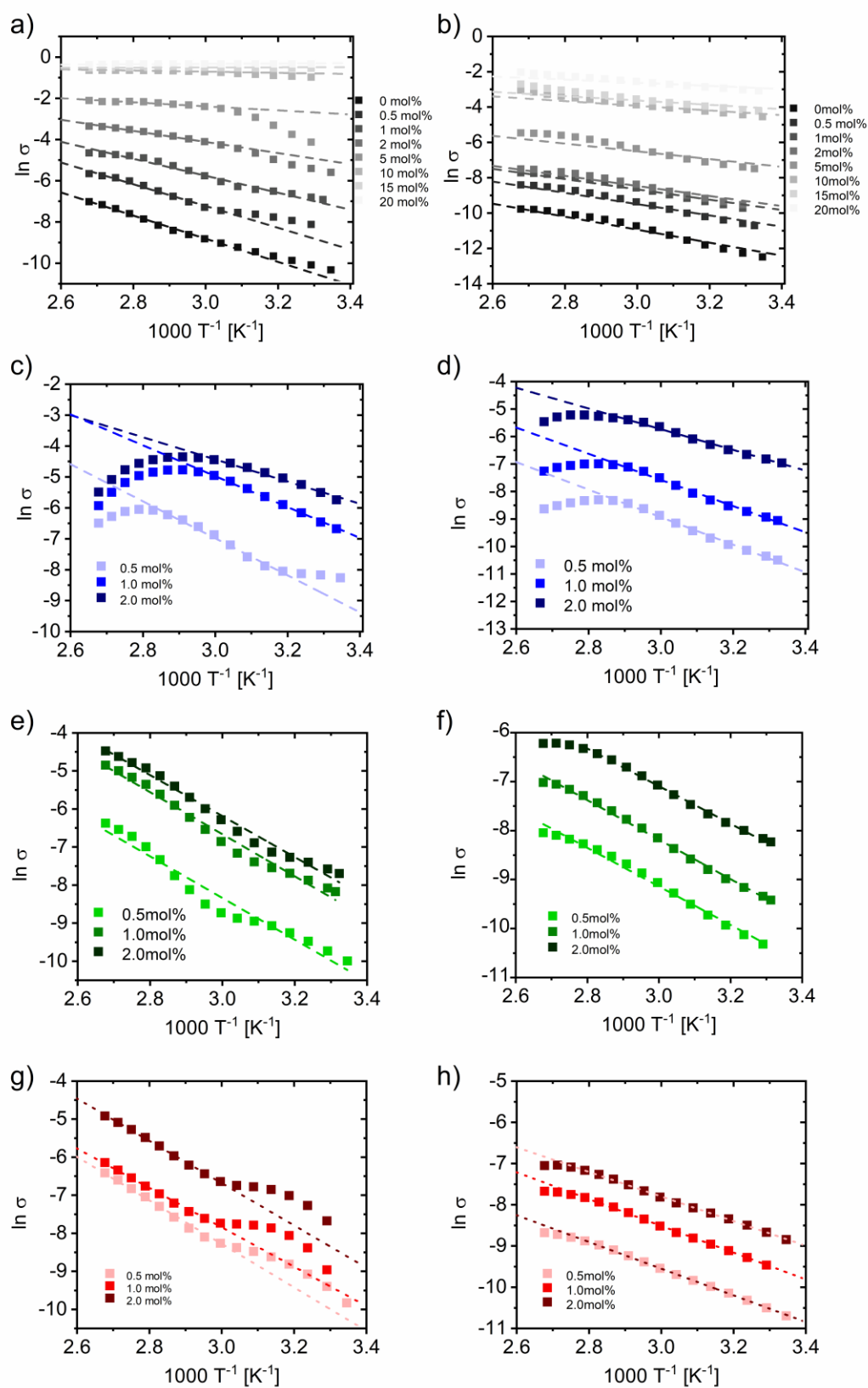


Figure S7. Arrhenius-plots of the polymer P1 (left side column) and P2 (right side column) for D1 (a, b), D2 (c, d), D3 (e, f) and D4 (g, h).

Table S4. Conductivity σ , thermal activation energy of conductivity E_A , charge carrier density N_D , doping efficiency η_{Dop} and hole mobility μ_h of P1 and P2 doped with D1 (NOPF₆).

System		σ [S cm ⁻¹]	E_A [meV]	N_D [cm ⁻³]	η_{Dop} [%]	μ_h [cm ² V ⁻¹ s ⁻¹]
P1 : D1 PDPP[T] ₂ {TEG} ₂ -3- MEET : NOPF ₆	0 mol%	$1.16 \cdot 10^{-5}$	484.9	$1.1 \cdot 10^{18}$	-	0.0081
	0.1 mol%	$4.4 \cdot 10^{-5}$	-	$1.7 \cdot 10^{18}$	148	-
	0.2 mol%	$5.05 \cdot 10^{-5}$	-	$1.7 \cdot 10^{18}$	75	-
	0.5 mol%	$8.04 \cdot 10^{-5}$	455.6	$1.7 \cdot 10^{18}$	30	0.00107
	1 mol%	$7.36 \cdot 10^{-5}$	355.6	$1.9 \cdot 10^{18}$	17	0.00168
	2 mol%	$1.6 \cdot 10^{-4}$	232.5	$2.5 \cdot 10^{18}$	11	0.00429
	5 mol%	$9.13 \cdot 10^{-4}$	84.8	$1.6 \cdot 10^{18}$	3	0.01579
	10 mol%	-	24.3	-	-	-
	15 mol%	-	0	-	-	-
	20 mol%	-	0	-	-	-
P2 : D1 PDPP[T] ₂ {2-HD} ₂ -3- MEET : NOPF ₆	0 mol%	$6.15 \cdot 10^{-6}$	317.5	$3.7 \cdot 10^{18}$	-	0.0019
	0.1 mol%	$1.04 \cdot 10^{-5}$	-	$3.9 \cdot 10^{17}$	41	-
	0.2 mol%	$1.26 \cdot 10^{-5}$	-	$4.4 \cdot 10^{17}$	23	-
	0.5 mol%	$2.38 \cdot 10^{-5}$	275.6	$5.6 \cdot 10^{17}$	12	$4.7 \cdot 10^{-5}$
	1 mol%	$4.54 \cdot 10^{-5}$	251.4	$7.6 \cdot 10^{17}$	8	0.00104
	2 mol%	$6.9 \cdot 10^{-5}$	245.8	$9.8 \cdot 10^{17}$	5	0.00116
	5 mol%	$1.78 \cdot 10^{-4}$	188.9	$1.2 \cdot 10^{18}$	2	0.00217
	10 mol%	-	114.3	-	-	-
	15 mol%	-	105.5	-	-	-
	20 mol%	-	76.5	-	-	-

Table S5. Conductivity σ , thermal activation energy of conductivity E_A , charge carrier density N_D , doping efficiency η_{Dop} and hole mobility μ_h of P1 and P2 doped with D2 (Magic Blue).

System		σ [S cm ⁻¹]	E_A [meV]	N_D [cm ⁻³]	η_{Dop} [%]	μ_h [cm ² V ⁻¹ s ⁻¹]
P1 : D2 PDPP[T] ₂ {TEG} ₂ -3- MEET : Magic Blue	0 mol%	$1.16 \cdot 10^{-5}$	484.9	$1.1 \cdot 10^{18}$	-	0.0081
	0.1 mol%	$1.16 \cdot 10^{-5}$	-	$1.8 \cdot 10^{18}$	156	$4.1 \cdot 10^{-5}$
	0.2 mol%	$6.67 \cdot 10^{-5}$	-	$1.9 \cdot 10^{18}$	82	0.00022
	0.5 mol%	$1.3 \cdot 10^{-4}$	516.9	$2.2 \cdot 10^{18}$	38	0.00037
	1 mol%	$4.24 \cdot 10^{-4}$	431.1	$2.6 \cdot 10^{18}$	23	0.00101
	2 mol%	$8.01 \cdot 10^{-4}$	309.5	$3.1 \cdot 10^{18}$	14	0.00161
	5 mol%	0.00112	-	$3.5 \cdot 10^{18}$	6	0.00198
P2 : D2 PDPP[T] ₂ {2-HD} ₂ -3- MEET : Magic Blue	0 mol%	$6.15 \cdot 10^{-6}$	317.5	$3.7 \cdot 10^{18}$	-	0.0019
	0.1 mol%	$1.45 \cdot 10^{-6}$	-	$5.0 \cdot 10^{17}$	53	$1.8 \cdot 10^{-5}$
	0.2 mol%	$7.5 \cdot 10^{-6}$	-	$5.9 \cdot 10^{17}$	31	$7.9 \cdot 10^{-5}$
	0.5 mol%	$2.49 \cdot 10^{-5}$	325.1	$9.4 \cdot 10^{17}$	20	0.00016
	1 mol%	$3.19 \cdot 10^{-5}$	410.8	$1.3 \cdot 10^{18}$	14	0.00015
	2 mol%	$6.03 \cdot 10^{-5}$	432.9	$2.6 \cdot 10^{18}$	14	0.00014
	5 mol%	$2.27 \cdot 10^{-4}$	-	$4.6 \cdot 10^{18}$	9	0.00031

Table S6. Conductivity σ , thermal activation energy of conductivity E_A , charge carrier density N_D , doping efficiency η_{Dop} and hole mobility μ_h of P1 and P2 doped with D3 (MeOTDP(PF₆)₂).

System		σ [S cm ⁻¹]	E_A [meV]	N_D [cm ⁻³]	η_{Dop} [%]	μ_h [cm ² V ⁻¹ s ⁻¹]
P1 : D3 PDPP[T] ₂ {TEG} ₂ -3- MEET : MeOTDP(PF ₆) ₂	0 mol%	$1.16 \cdot 10^{-5}$	484.9	$1.1 \cdot 10^{18}$	-	0.0081
	0.1 mol%	$3.29 \cdot 10^{-5}$	-	$1.7 \cdot 10^{18}$	152	0.00012
	0.2 mol%	$6.53 \cdot 10^{-5}$	-	$1.9 \cdot 10^{18}$	82	0.00022
	0.5 mol%	$1.9 \cdot 10^{-4}$	465.1	$2.3 \cdot 10^{18}$	40	0.00052
	1 mol%	$2.65 \cdot 10^{-4}$	477.2	$2.6 \cdot 10^{18}$	23	0.00063
	2 mol%	$7.76 \cdot 10^{-4}$	472.9	$3.4 \cdot 10^{18}$	15	0.00142
	5 mol%	0.0185	-	$6.9 \cdot 10^{18}$	12	0.01653
P2 : D3 PDPP[T] ₂ {2-HD} ₂ -3- MEET : MeOTDP(PF ₆) ₂	0 mol%	$6.15 \cdot 10^{-6}$	317.5	$3.7 \cdot 10^{18}$	-	0.0019
	0.1 mol%	$7.38 \cdot 10^{-6}$	-	$6.1 \cdot 10^{17}$	64	$7.5 \cdot 10^{-5}$
	0.2 mol%	$1.13 \cdot 10^{-5}$	-	$5.6 \cdot 10^{17}$	29	0.00012
	0.5 mol%	$2.7 \cdot 10^{-5}$	339.6	$8.6 \cdot 10^{17}$	18	0.001019
	1 mol%	$5 \cdot 10^{-5}$	347.8	$1.3 \cdot 10^{18}$	14	0.00024
	2 mol%	$3.12 \cdot 10^{-4}$	331.2	$2.6 \cdot 10^{18}$	13	0.00076
	5 mol%	0.00259	-	$5.7 \cdot 10^{18}$	12	0.00286

Table S7. Conductivity σ , thermal activation energy of conductivity E_A , charge carrier density N_D , doping efficiency η_{Dop} and hole mobility μ_h of P1 and P2 doped with D4 (SpiroMeOTAD(PF₆)₄).

System		σ [S cm ⁻¹]	E_A [meV]	N_D [cm ⁻³]	η_{Dop} [%]	μ_h [cm ² V ⁻¹ s ⁻¹]
P1 : D4 PDPP[T] ₂ {TEG} ₂ -3- MEET : Spiro(PF ₆) ₄	0 mol%	$1.16 \cdot 10^{-5}$	484.9	$1.1 \cdot 10^{18}$	-	0.0081
	0.1 mol%	$1.32 \cdot 10^{-5}$	-	$2.7 \cdot 10^{18}$	241	$2.9 \cdot 10^{-5}$
	0.2 mol%	$2.24 \cdot 10^{-5}$	-	$1.8 \cdot 10^{18}$	79	$7.7 \cdot 10^{-5}$
	0.5 mol%	$9.24 \cdot 10^{-5}$	493.8	$2.2 \cdot 10^{18}$	39	0.00026
	1 mol%	$2.44 \cdot 10^{-4}$	446.9	$2.9 \cdot 10^{18}$	26	0.00052
	2 mol%	0.00112	479.7	$4.1 \cdot 10^{18}$	18	0.0017
	5 mol%	0.233	-	$1.4 \cdot 10^{19}$	24	0.10506
P2 : D4 PDPP[T] ₂ {2-HD} ₂ -3- MEET : Spiro(PF ₆) ₄	0 mol%	$6.15 \cdot 10^{-6}$	317.5	$3.7 \cdot 10^{18}$	-	0.0019
	0.1 mol%	$1.11 \cdot 10^{-5}$	-	$5.3 \cdot 10^{17}$	56	0.00013
	0.2 mol%	$1.58 \cdot 10^{-5}$	-	$6.2 \cdot 10^{17}$	32	0.00016
	0.5 mol%	$5.26 \cdot 10^{-5}$	279.7	$9.9 \cdot 10^{17}$	21	0.00033
	1 mol%	$8.7 \cdot 10^{-5}$	280.4	$1.5 \cdot 10^{18}$	16	0.00036
	2 mol%	$5.88 \cdot 10^{-4}$	257.8	$4.0 \cdot 10^{18}$	21	0.00091
	5 mol%	0.00167	-	$5.4 \cdot 10^{18}$	11	0.00195

Impedance Spectroscopy

Solid State Mott Schottky Analysis

TEC-7 (XOP glass, 1" x 1" x 2.2 mm, 6 – 8 Ω /square, ~500 nm FTO on glass) substrates were etched with dilute HCl/Zn-dust. After obtaining the etched electrode pattern, the substrates were brushed manually with sodium dodecyl sulfate and deionized water, followed by ultrasonication in 2 vol% aqueous hellmanex-III solution, water, acetone and isopropanol. The substrates were blown dry with nitrogen and pre-treated with O₃/UV for 15 min at 50 °C. 100 nm of Al₂O₃ were deposited on the FTO-electrodes using ALD (H₂O/Al(CH₃)₃, 15 ms pulse duration, 150 °C, 5 s purge time, 1111 cycles), while leaving areas insulator-free for contacting the device during measurements. The aluminium oxide layer was passivated by spin coating 100 nm of BCB (10 vol% Cyclotene 3022-35 in toluene, 70 μ L, 50 sec, 3 krpm) on top and soft curing for 10 sec at 250 °C in air, followed by a hard bake at 250 °C for 1 h under Argon. The polymer:dopant-solutions were doctor bladed onto the substrates from DCM solutions (5 mg/mL, 40 μ L, manual speed control, 60 μ m blade height.) under inert atmosphere and used without further thermal annealing. To enhance the wettability, DCM was doctor bladed onto the substrates prior to polymer:dopant-coating and dried completely. Finally, Au electrodes were thermally evaporated using a shadow mask ($d_{Au} = 70$ nm). The impedance of the devices was measured with a two-electrode setup and varying electrical field (10 kHz to 10 Hz, 8 points per frequency decade, -1.5 to 1.5 V_{Bias} in 48 voltage steps, 7 mV_{RMS}) using a Metrohm Autolab PGSTAT204 equipped with an FRA32M module. The NOVA 2.1.4 Software package provided by Metrohm, Germany was used to process the impedance data. The Au top electrode was connected to the counter and reference electrode, the FTO contact to the working and sense electrode of the potentiostat. Devices under test were shielded from ambient light, external electrical fields and kept under inert atmosphere. From the imaginary Z'' and real Z' impedance, the capacitance of the organic layer was extracted assuming an R_s(RC) equivalent circuit:

$$\hat{Z}(i\omega)_{R(RC)} = R_{Series} + \frac{1}{i\omega C_{Parallel} + \frac{1}{R_{Parallel}}} \quad (S2)$$

which can be solved for $C_{Parallel}$ to yield

$$C_{Parallel} = \frac{Im(Z)}{(-Im(Z)^2 + (Re(Z) - R_s)^2)\omega} \quad (S3)$$

The density of free charge carriers N_D was the extracted by plotting C^{-2} vs the Boltzmann corrected applied bias voltage V_{Bias} and fitting (S5) to the linear depletion regime

$$C_{Parallel}^{-2} = \frac{2}{\epsilon_{OSC}\epsilon_0 A^2 q N_D} \left(V_{Bias} - \frac{k_B T}{q} \right) \quad (S4)$$

where ϵ_{OSC} and ϵ_0 are the dielectric constants of the organic semiconductor layer (Approximated with 3) and the vacuum permittivity, respectively. A^2 is the area of the organic layer in cm^2 , q the elementary charge and k_B the Boltzmann constant in eV K^{-1} .

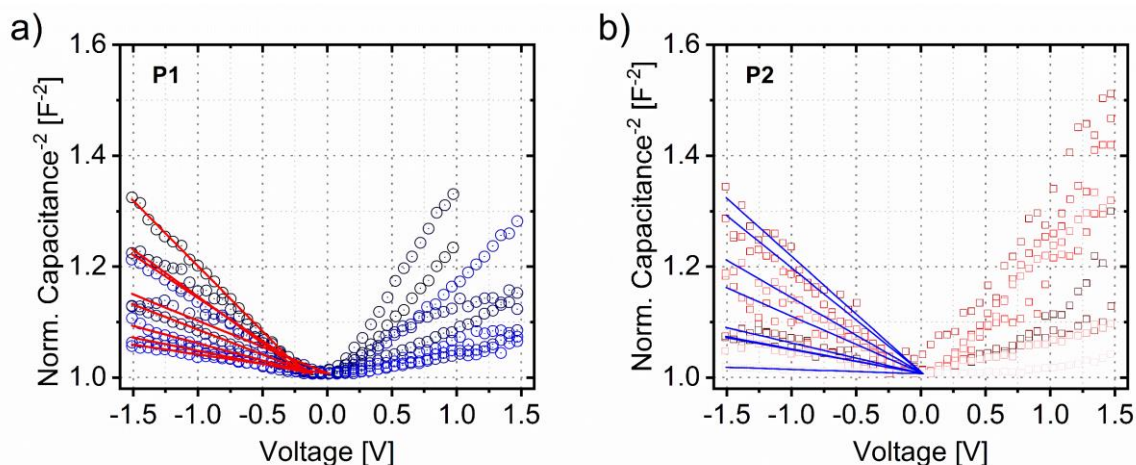


Figure S8. $1/C^2$ vs. applied bias voltage of metal-insulator-semiconductor (MIS) device structures of P1, resp. P2 doped with D1. The stack is comprised of FTO/ Al_2O_3 (100 nm)/x-linked BCB (100 nm)/Polymer:Dopant (500 nm)/Au. A negative voltage applied to the Au top electrode results in the formation of a depletion zone at the insulator/semiconductor interface, where Equation S4 is applied to calculate the charge carrier density N_D from the slope (Mott-Schottky measurement).

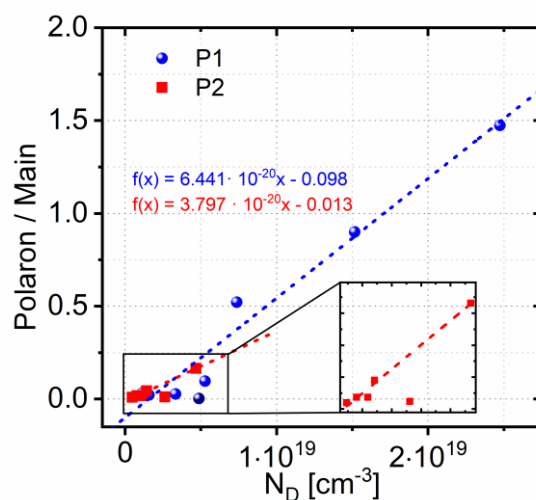


Figure S9. Linear correlations between measured charge carrier density N_D and measured absorption integral of polaron peak obtained by UV/Vis/NIR spectroscopy of solutions in DCM of P1 (blue) and P2 (red) doped with 0 to 20 mol% D1. N_D was obtained from Mott-Schottky measurements on metal-semiconductor-insulator devices (Figure S8). The obtained linear relationship was used to determine the charge carrier densities of P1 and P2 doped with D2, D3 and D4 from their respective polaron absorption integrals in solution, while keeping the concentrations of all species involved constant.

Impedance Spectroscopy

Negative differential susceptance measurements

TEC-7 (XOP glass, 1" x 1" x 2.2 mm, 6 – 8 Ω /square, ~500 nm FTO on glass) substrates were etched with dilute HCl/Zn-dust. After obtaining the etched electrode pattern, the substrates were brushed manually with sodium dodecyl sulfate and deionized water, followed by ultrasonication in 2 vol% aqueous Hellmanex-III solution, water, acetone and isopropanol. The substrates were blown dry with nitrogen and pre-treated with O₃/UV for 15 min at 50 °C. The organic semiconductor films were doctor bladed onto the substrates from DCM solutions (5 mg/mL, 40 μ L, manual speed control, 60 μ m blade height.) under inert atmosphere and used without further thermal annealing. To enhance the wettability, DCM was doctor bladed onto the substrates prior to coating and dried completely. To avoid edge effects, a part of the conductive electrodes was masked with Kapton tape, which was removed after the OSC deposition. 100 nm of Au was thermally evaporated on top of the OSC layer using a shadow mask to complete the device stack. The impedance of the devices was measured with a two-electrode setup and increasing electrical field (1 MHz to 100 Hz, 25 points per frequency decade, 0-2 V_{Bias} in 15 voltage steps, 10 mV_{RMS}) using a Metrohm Autolab PGSTAT204 equipped with an FRA32M module. The NOVA 2.1.4 Software package provided by Metrohm, Germany was used to process the impedance data. The ITO back contact was connected to the working electrode (WE) and sense (S), while the Au top electrode was connected to the counter electrode (CE) and reference electrode (RE). Devices under test were shielded from ambient light and external electrical fields. From the imaginary Z'' and real Z' impedance, the capacitance of the organic layer was extracted assuming an $R_S(RC)$ equivalent circuit:

$$\hat{Z}(i\omega)_{R(RC)} = R_{Series} + \frac{1}{i\omega C_{Parallel} + \frac{1}{R_{Parallel}}} \quad (S5)$$

which can be solved for $C_{Parallel}$ to yield

$$C_{Parallel} = \frac{Im(Z)}{(-Im(Z))^2 + (Re(Z) - R_S)^2} \omega \quad (S6)$$

The geometric capacitance C_{Geo} of each device was determined in the high frequency region of the $C(f)$ -plot. Together with the measured capacitance, the mobility was extracted from the negative differential susceptance $-\Delta B$ at different electrical fields. The negative differential susceptance $-\Delta B$ can be calculated

$$-\Delta B = -\omega(C(\omega) - C_{geo}) \quad (S7)$$

The global maximum f_{max} of the $-\Delta B(f)$ -plot was extracted and used to calculate the transit time τ_{tr}

$$\tau_{tr} = 0.56f_{max}^{-1} \quad (S8)$$

Local maxima above the transit frequency without physical meaning were discarded. The mobility can then be extracted as

$$\mu = \frac{4}{3} \frac{d^2}{\tau_t V_{Bias}} \quad (S9)$$

with d being the thickness of the organic layer. The zero-field mobility μ_0 was calculated by extrapolating the obtained Poole-Frenkel type field dependency.

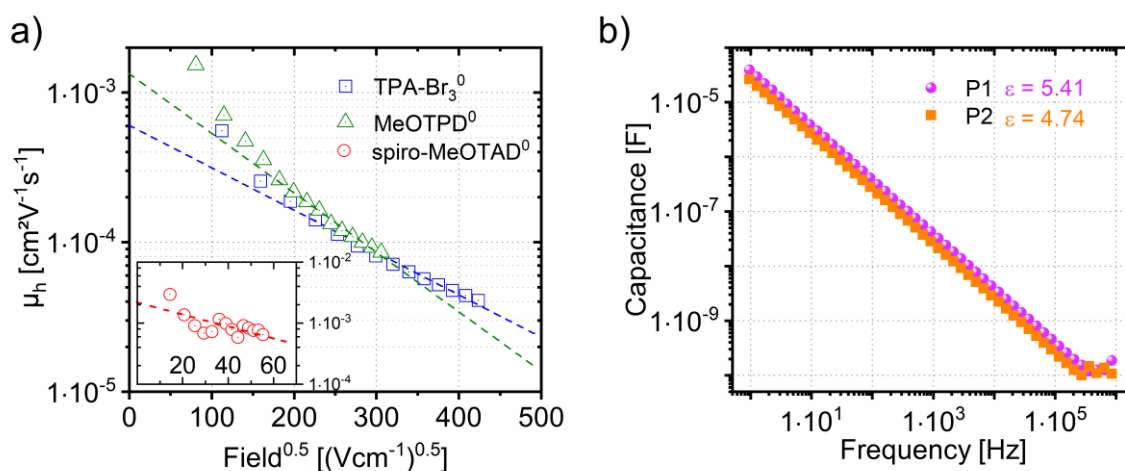


Figure S10. (a) Hole mobility μ_h of the pristine dopant molecules spiro-MeOTAD (red circles), MeOTPD (green triangles) and tris(4-bromo)phenylamine (TPA-Br₃, blue squares), measured by negative differential susceptance measurements on FTO/OSC/Au devices. The applied bias voltage was varied from 0 to 2 V with the working electrode connected to the Au top electrode, while the FTO contact was connected to the counter electrode in a two-electrode setup. The impedance was measured from 1 MHz to 10 Hz with 25 frequency steps per decade and 7 mV_{RMS} amplitude of the AC signal superimposed on the DC bias. By plotting the square root of the applied electrical field vs. the natural logarithm of the measured mobility, the zero field-mobility μ_0 can be extracted from the y-intercept of a linear fit, if the mobility obeys a Poole-Frenkel type field dependency. (b) Frequency dependent capacitance of a metal-insulator-semiconductor (MIS) stack, comprised of FTO/Al₂O₃ (100 nm)/x-linked BCB (100 nm)/Polymer:Dopant (500 nm)/Au measured at -1.5 V Bias at complete depletion. The constant high frequency capacitance C_{min} above 200 kHz was used to calculate the dielectric constant of the polymer using Equation S15.

Ultraviolet Photoelectron Spectroscopy

UPS measurements were carried out with a PHI 5000 VersaProbe III system fitted with a He discharge light source providing stable and continuous He I and He II lines. For measurement, all samples were spin cast on clean ITO (15 ohm/sq.) substrates to produce ca. 20 nm thick films using dry solvents in a N₂ filled glovebox. The thickness of the samples was measured by using dummy samples in a profilometer. The samples were directly transported to the UPS system by using a N₂ filled, sealed stainless steel transport vessel without exposing them to the ambient conditions. All measurements reported in this study were carried out with the He

I (21.22 eV) line with -5V sample biasing and the corresponding photoemission with 90° take-off angle was collected at the multichannel analyzer. The reproducibility of the signal position was confirmed by repeating the measurement at least in 2 spots from the same sample. The reference Fermi level was determined using a sputter cleaned gold foil. The standard deviation on the reported energy values is ± 0.15 eV, calculated using the full-width-half-maximum of the gold foil's Fermi edge. To determine the impact of the (partially or fully) reduced dopant on the HOMO density of states and their distribution, ultraviolet photoelectron spectroscopy was carried out on 20 nm thin films of PDPP[T]₂{TEG}₂-3-MEET and PDPP[T]₂{2-HD}-MEET, both undoped as well as doped samples with either NOPF₆ or spiro-MeOTAD⁴⁺(PF₆)₄. After measurement of the valence band maximum (VBM), the onset was fitted with an exponentially modified Gaussian distribution to account for localized/tail states arising due to ionized dopants (Equation S10).

$$g(E, h, \mu, \sigma_{GDOS}, \tau) \quad (S10)$$

$$= \frac{h\sigma_{GDOS}}{\tau} \sqrt{\frac{\pi}{2}} \exp\left(0.5 \left(\frac{\sigma_{GDOS}}{\tau}\right)^2 - \frac{E - \mu}{\tau}\right) \operatorname{erfc}\left(\frac{1}{\sqrt{2}} \left(\frac{\sigma_{GDOS}}{\tau} - \frac{E - \mu}{\tau}\right)\right)$$

where E is the energy w.r.t. vacuum level, h the peak height of the gaussian distribution, μ the center of the distribution, σ_{GDOS} the standard deviation of the gaussian distribution and τ the decay energy of the exponential tail. The parameters obtained by least squares fitting are summarized in Table S8 below.

Table S8. Values obtained by fitting Equation S10 to the VBM of P1 and P2 doped with 0 mol% and 5 mol% D4. $R^2 > 0.98$ for all fits.

Sample	h [1]	μ [eV]	σ_{GDOS} [meV]	τ [1]
P1, pristine	21.2	1.61	184	0.337
P1, 5 mol% D1	33.9	0.86	120	0.250
P1, 5 mol% D4	19.9	0.95	198	0.231
P2, pristine	18.0	1.31	102	0.294
P2, 5 mol% D1	33.1	0.82	121	0.218
P2, 5 mol% D4	17.3	0.86	146	0.215

Dielectric constants of semiconducting polymers

FTO/Al₂O₃ (100 nm)/BCB (100 nm)/OSC/Au devices were prepared for measurement of the dielectric constant. The impedance of the devices was measured with a two-electrode setup and varying electrical field (1 Hz to 1 MHz, 8 points per frequency decade, -5 to 5 V_{Bias} in 11 voltage steps, 1 V_{RMS}) using a Metrohm Autolab PGSTAT204 equipped with an FRA32M module. The NOVA 2.1.4 Software package provided by Metrohm, Germany was used to process the impedance data. The Au top electrode was connected to the counter and reference electrode, the FTO contact to the working and sense electrode of the potentiostat. Devices under test were shielded from ambient light, external electrical fields and kept under inert atmosphere. From the imaginary Z'' and real Z' impedance, the capacitance of the organic layer was extracted assuming an (RC) equivalent circuit [1]:

$$C(\omega) = C'(\omega) - iC''(\omega) \quad (S11)$$

where C'(ω) is the real part of the capacitance and C''(ω) the imaginary part:

$$C'(\omega) = \frac{-Im(Z)}{\omega|Z(\omega)|^2} \quad (S12)$$

$$C''(\omega) = \frac{Re(Z)}{\omega|Z(\omega)|^2} \quad (S13)$$

To avoid influences of the space charge conduction, the real capacitance was extracted in the high frequency depletion regime of the MIS device. To achieve this condition, a negative bias was applied to the gold electrode, resulting in the formation of a hole depletion zone at the insulator/semiconductor interface. Since the organic semiconductor was measured in its pristine, i.e. intrinsic state, the depletion layer width can extend throughout the whole film thickness. The minimal, constant real capacitance C_{min} was then extracted from the saturated region at high frequencies (depletion region). Response from a possible inversion charge can be ruled out by the high measurement frequency not allowing enough minority carriers to form at the insulator/semiconductor interface. Since the film stack consists of two capacitors, C_{OSC} and C_{Insulator} in series, C_{OSC} can then be extracted from C_{min}:

$$C_{OSC} = \frac{C_{min}C_{Insulator}}{C_{Insulator} - C_{min}} \quad (S14)$$

In our devices, C_{Insulator} itself consists of two separate stacks, therefore 1/C_{Insulator} = 1/C_{Al2O3}+1/C_{BCB}. Using the vacuum permittivity ε₀, the active area A_{OSC} and organic layer thickness d_{OSC} of the MIS device, one can extract the dielectric constant of the organic semiconductor ε_{OSC}:

$$\epsilon_{OSC} = \frac{C_{OSC}d_{OSC}}{\epsilon_0A_{OSC}} \quad (S15)$$

5. References

[1] C. Wang *et al.*, *Macromolecules* **2018**, 51, 9368-9381.

8. Annex: Principles of Structural Design of Conjugated Polymers Showing Excellent Charge Transport toward Thermoelectrics and Bioelectronics Applications

Published as “Principles of Structural Design of Conjugated Polymers Showing Excellent Charge Transport toward Thermoelectrics and Bioelectronics Applications” in *Macromolecular Rapid Communications* **2019**, 1800915 by Mahima Goel, C. David Heinrich, Gert Krauss and Mukundan Thelakkat.

*Dr. M. Goel, Dr. C. D. Heinrich, G. Krauss, Prof. M. Thelakkat
Applied Functional Polymers, Macromolecular Chemistry I, University of Bayreuth,
Universitätsstr. 30, Bayreuth, 95440, Germany
E-mail: mukundan.thelakkat@uni-bayreuth.de*

*Prof. M. Thelakkat
Bavarian Polymer Institute (BPI), University of Bayreuth,
Universitätsstr. 30, Bayreuth, 95440, Germany*

Keywords: second-generation conjugated polymers, thermoelectric, bioelectronics, charge carrier mobility

Abstract

Conjugated polymers, especially their second generation with a donor-acceptor alternating structure, have promising properties. These are suitable for two emerging fields: thermoelectrics and bioelectronics if appropriate structural designs are implemented. This review aims to give a perspective for the potentials and challenges of novel conjugated polymers in such applications. Especially, the aspects of synthetic design and the consequences of modifications of the chemical structure on the charge transport in selected second-generation conjugated polymers are reviewed. By understanding the effects of structural motifs on the overall material properties, polymers can be specifically tailored for the respective application. The basics of charge transport measurements are briefly summarized as the charge transport plays an important role for thermoelectrics as well as for bioelectronics. In particular, the correlation between the reported charge carrier mobility values and the structural design of the polymers are reviewed. Examples of the application of second-generation conducting polymers in thermoelectrics and bioelectronics are shown to demonstrate the current state of research. Finally, the prospect of a purposeful design of new materials for these two emerging fields is discussed.

1. Introduction: Conjugated Polymers and Conducting Polymers

Conjugated polymers have been known since the discovery of trans-polyacetylene (PAC) in 1976.^[1] After that many others were synthesized and studied. Initially, the most popular ones being polyaniline,^[2,3] poly(p-phenylene vinylene)^[4] and polypyrrole^[3] (see **Figure 1**). Most of the initial work was carried out in doped conjugated polymers with an aim to prepare highly conducting polymers. Undoped PAC exhibits hole mobilities in the range of $\mu_h \approx 1 \text{ cm}^2 \text{ V}^{-1} \text{ s}^{-1}$.^[5] When PAC is doped with potassium vapor conductivities as high as $\sigma \approx 10^4 \text{ S cm}^{-1}$ could be observed, demonstrating the potential of conductive polymers.^[6] Unfortunately, PAC suffers from poor solubility and low stability towards oxidation, preventing wide-spread application. Polyanilines (PANI) became popular because of their very simple synthesis via oxidative polymerization.^[7] Upon doping with protic acids like hydrochloric acid, conductivities of up to 5 S cm^{-1} were reached.^[8] More recently a further increase up to $\sigma > 500 \text{ S cm}^{-1}$ has been reported.^[9] Polypyrroles (PPy) can be obtained by a simple oxidative polymerization of pyrrole, either electrochemically or e.g. using ferric chloride.^[10,11] Polypyrroles offer high intrinsic electrical conductivities, which can be further improved up to the range of 2000 S cm^{-1} .^[12] In short, these early materials, even though they exhibit intriguing properties like very high electrical conductivities upon doping, all suffer from problems like poor solubility or a lack of stability in the doped state. A breakthrough in conducting polymers came with the stabilization of doped poly(3,4-ethylenedioxythiophene) (PEDOT) using poly(styrene sulfonate) (PSS). Acid-doped composites of PEDOT with PSS or *p*-toluene sulfonic acid (Tos) are well-studied and used in virtually every application where a conductive polymer is required.^[13] This is on the one hand due to their desirable properties, i.e. electrical conductivities up to 6000 S cm^{-1} and a good processability in the form of dispersions.^[14–16] On the other hand, manifold processing methods are possible including industrially relevant technologies for large-scale production like roll-to-roll processing, spin- or dip coating or inkjet printing.^[17–20] With the discovery of electroluminescence in pristine conjugated polymers, the interest in developing new conjugated polymers with a particular emission color arose.^[21] Many substituted derivatives of poly(p-phenylene vinylene) have been studied as the emissive layer (green to yellow) in OLEDs.^[22] The activity in the field of conjugated polymers expanded with the discovery of photoinduced charge transfer. Bringing such a polymer into contact with an electron acceptor such as fullerene paved the way for polymer solar cells, generally termed as organic photovoltaics (OPV).^[23,24] For OPV, poly(3-alkylthiophenes) (P3ATs) constitutes the most studied conjugated polymers of the first generation, because of their versatility regarding the structural design and desirable electrical and optical properties. Hole mobilities up to $\mu_h \approx 0.1 \text{ cm}^2 \text{ V}^{-1} \text{ s}^{-1}$ in organic field-effect transistors (OFETs) have been observed for poly(3-hexylthiophene) (P3HT).^[25–27] For the best performing materials, it is important to control both the molecular weight and the regioregularity of P3HT,^[28,29] which leads to well-defined polymers when synthesized via Kumada Catalyst Transfer Polymerization (KCTP).^[30–32] P3HT has been studied extensively and we refer interested readers to other comprehensive reports about many aspects of this polymer.^[33] The selenium-analogue of P3HT, poly(3-

hexylselenophene) P3HS shows similar properties as P3HT.^[34,35] Regioregular P3HS which can be obtained by the same synthetic approach as P3HT, exhibits a slightly smaller band gap than its sulfur analogue.^[36] In addition to the first generation of homopolymers of conjugated moieties (see Figure 1), a second generation of conjugated polymers, the so-called low band gap polymers evolved, mainly with the intention of tuning the absorption wavelength range for an efficient application in OPV. A lower band gap is achieved by the orbital overlap of an electron-rich (Donor D) and an electron-deficient (Acceptor A) moiety resulting in D-A polymers. The donor-acceptor (D-A) concept for band gap reduction was proposed by Havit et al. in 1992 and later well established for many structural motifs by Roncali, Leclerc, Andersson, Facchetti and others.^[37–42] In addition to the possibility to extend the absorption into the red and near-red spectral region, many of these conjugated polymers exhibit excellent hole or electron mobilities making them suitable candidates for novel challenging applications as discussed below. In this review, we will deal with specific aspects of synthetic design and the consequences of structural modifications for charge transport in some selected second-generation conjugated polymers. The potentials and challenges of conjugated polymers, both in pristine and doped states, allowing them to be suitable for two novel applications namely thermoelectrics and bioelectronics are reviewed with the aim to give the perspectives for such applications using novel conjugated polymers. This review mainly focuses on the underlying logic of synthetic principles and does not consider the evaluation or comparison of all conjugated polymers that were reported for applications such as solar cells or organic electronics. For these many reviews are available.^[43,44] This review also does not deal with the structure formation of such polymers in solutions or thin films, for which the readers are recommended to available reviews.^[33,45] Since the charge carrier transport and the stability of doped states play an important role in thermoelectrics and bioelectronics, we review the basics of charge transport measurements and correlate the structural design with the reported charge carrier mobilities and the stability of the doped state in the following.

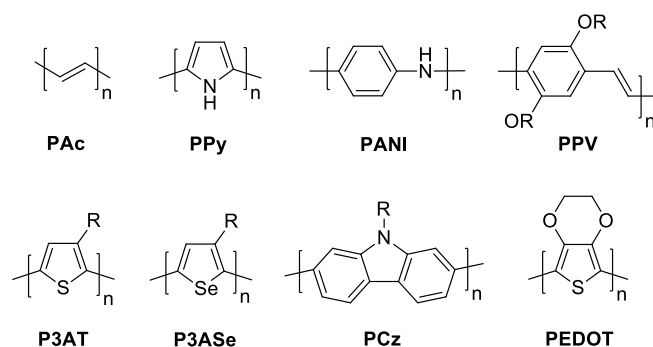


Figure 1. Examples for first generation conjugated polymers: trans-Polyacetylene (PAc), polypyrrole (PPy), polyaniline (PANI), poly-(p-phenylene vinylene) (PPV), poly(3-alkylthiophene) (P3AT), poly(3-alkylselenophene) (P3Ase), polycarbazole (PCz), poly(3,4-ethylenedioxythiophene) (PEDOT), R = alkyl.

2. Charge Carrier Transport in Organic Semiconductor Polymers

The charge carrier mobility μ of a semiconductor is a key parameter which is often used to compare the material properties of organic semiconductors. Especially, for challenging applications in thermoelectrics and bioelectronics, excellent unipolar charge carrier transport is required. The mobility of positive (holes) or negative (electrons) charges through a polymeric organic semiconductor does not only depend on the material's chemical composition but also strongly on the order/disorder of the material. In contrast to inorganic semiconductors the transport is not band-like, but can be described as disorder-controlled or hopping transport. This leads to a dependence of the charge carrier mobility on the electric field, temperature and also the charge carrier density which varies greatly depending on the method used to extract the mobility.^[46] Additionally, the semiconducting polymer is usually incorporated as a thin film in electronic devices. Therefore, the morphology in the confinement of a thin film greatly influences the measured charge carrier mobility, which depends strongly on the orientation of the crystallites within the film and at the interfaces to the electrodes. This is caused by the large anisotropy of the charge carrier mobility which can be observed in crystalline conjugated polymers. The highest mobility can generally be expected for a charge transport along the polymer backbone, followed by the one along the direction of the π - π stacked polymer chains. The charge transport along the third axis, usually across insulating sidechains, will be the most unfavorable leading to low charge carrier mobilities.^[47] Conjugated polymers are usually semi-crystalline and not fully amorphous and fully crystalline. The charge carrier mobility that can be observed in such a semi-crystalline material will be highly dependent on the transport between the crystalline regions. In a truly amorphous material charge carrier transport is limited to a thermally activated hopping process which has been reported to be limited to relative low values of about $0.08 \text{ cm}^2 \text{ V}^{-1} \text{ s}^{-1}$.^[48] Additionally, the complex nature of charge transport in conjugated polymers is highlighted by the fact that many novel polymers with exhibit high charge carrier mobilities are materials with high disorder.^[49] Additionally, a molecular weight dependence of the charge carrier mobility has been observed in conjugated polymers. This dependence was extensively studied for P3HT because a series of this polymer with defined molecular weight and narrow distribution can be synthesized. It could be shown that not only the FET mobility but also the mobility measured by other techniques such as SCLC or CELIV follows this trend.^[28,29,50] For P3HT the charge carrier mobility increases to a maximum at a certain molecular weight and saturates or decreases slightly when the molecular weight is increased further. It could be shown that this maximum seems to be the point at which chain folding within the polymer crystals occurs. The long period of the polymer crystal is highly correlated with charge carrier mobility as it linearly increases with the molecular weight up to the point at which chain folding occurs and it slightly decreases.^[29] Additionally, the concept of "tie molecules" has been proposed, i.e. the occurrence of polymer chains of sufficient length which tie crystalline regions together and facilitate charge transport through the amorphous regions.^[49,50] Similar trends have not been studied in detail for second generation polymers

mainly because a controlled polymerization of this class with well-defined molecular weights and low polydispersity is very difficult. There are several different methods to extract the charge carrier mobility in organic semiconductors which can give values that differ by several orders of magnitude depending on the charge carrier density in the device and the direction in which the transport is probed. The transport along the film normal e.g. can be measured by the so called space-charge limited current (SCLC) method in single carrier (i.e. hole-/electron-only) devices, in a diode setup (see **Figure 2 a**).^[51,52] The semiconductor films in these devices are several hundred nanometers thick and the extracted mobility values are a good measure for a true bulk mobility of the materials. The space-charge limited current is described by the Mott-Gurney equation:^[53]

$$J_{sc} = \frac{9}{8} \epsilon_0 \epsilon_r \mu \frac{V^2}{L^3} \quad (1)$$

A typical current-voltage plot for a diode showing the ohmic, SCLC and true trap-free SCLC regimes are depicted in Figure 2 a).

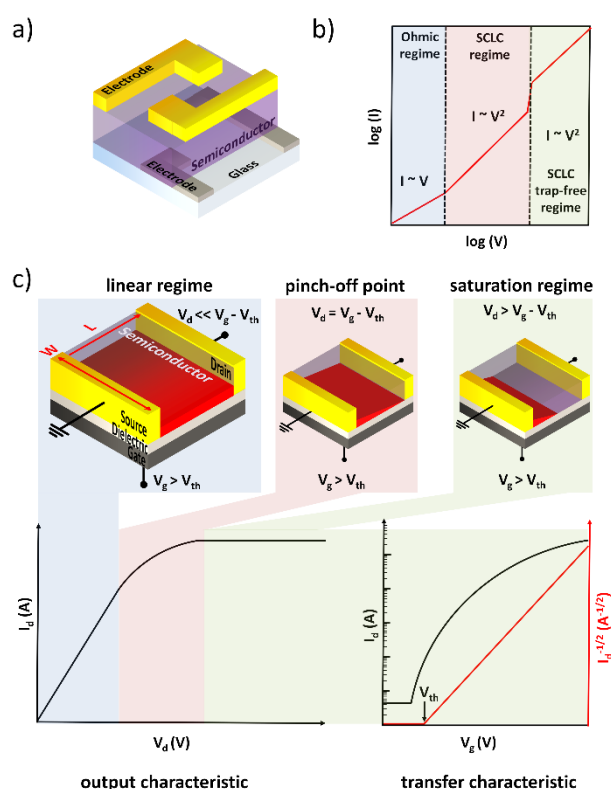


Figure 2. a) Sketch of two simplified SCLC devices on a substrate. b) Theoretical I-V curve illustrating the different regimes of an SCLC measurement. c) Scheme of an organic field-effect transistor (OFET) in bottom-contact, bottom-gate configuration (right). W is the channel width and L is the channel length. The operation of an OFET is schematically illustrated at a gate voltage V_G above the threshold voltage V_{Th} : For low potentials at the drain electrode, a linear increase of the drain current I_{DS} with the drain voltage V_{DS} is observed (linear regime). At the pinch-off point the start of the saturation regime can be observed. For even higher voltages V_{DS} , the accumulation layer is depleted and the drain current saturates (saturation regime). This V_d sweep is called output characteristic. The transfer characteristic, i.e. the V_g sweep, of an OFET is shown in the saturation regime (black) with the corresponding square root drain current $\sqrt{I_{DS}}$ (red).

In this method, correct mobility values μ can only be obtained when the current is truly space charge limited, i.e., the current is proportional to V^2 as well as L^{-3} . For this, the choice of the electrodes as well as an accurate determination of the film thickness is crucial. It is not trivial to build devices which exhibit SCLC behavior (see Figure 2 b). The mobility values obtained by the SCLC-method are also generally lower than the ones obtained from OFET, due to the lower charge carrier density in this device setup.^[54] Also SCLC probes the bulk mobility whereas the charge transport in OFETs occurs only in the channel close to the dielectric. Therefore, a favorable alignment at the interface can lead to a high OFET mobility values in materials with anisotropic charge transport. Due to these reasons the charge carrier mobility values are much more frequently extracted from OFETs. On the other hand, field-effect transistors are widely utilized to characterize semiconducting polymers and the obtained mobility values are used as a benchmark for novel materials. A brief introduction to the working principles of OFETs is given in the following. For a more detailed description of the operation of OFETs we want to refer to a number of excellent reviews and tutorials.^[46,55,56] In an organic field-effect transistor an electrical current is measured between two electrodes (source and drain) while a third

electrode – the gate – separated from the organic semiconductor by a dielectric is used to switch the device between the ON- and the OFF-state. Such a device can be realized in different geometries, e.g., as BGBC (bottom-gate, bottom-contact) device (Figure 2 c), which can have an influence on the obtained mobility values,^[57] but the working principle is always the same: The dielectric is polarized when a potential is applied at the gate electrode and a layer of positive/negative charges accumulates at the interface between the dielectric and the semiconductor. This layer of accumulated charges acts as the transport channel for charges between the source and the drain electrode. In a real device a certain voltage threshold V_{Th} must be overcome to fill the traps at the interface and create the channel. As the charge transport is limited to a channel close to the dielectric with a thickness of only a few nanometers, the charge carrier mobility extracted from an OFET depends highly on the morphology of the semiconductor at the interface to the dielectric layer. Usually, two different transistor characteristics can be discerned: the output- and the transfer-characteristic (Figure 2 c). For the output characteristic, the source-drain current I_{DS} is measured as a function of the source-drain voltage V_{DS} at a constant gate potential V_G . For small voltages ($V_{DS} < |V_G - V_{Th}|$), an increase of the drain potential V_{DS} leads to a linear increase of the current I_{DS} (linear regime). The increase of the electric field between source and drain changes the shape of the channel until it is pinched off at the drain electrode for $V_{DS} = |V_G - V_{Th}|$ (pinch-off point). For $V_{DS} > |V_G - V_{Th}|$, a greater V_{DS} does not further increase the current I_{DS} (saturation regime). The sweep of the gate voltage V_G at a constant V_{DS} – either in the linear regime or in the saturation region – is the transfer characteristic. Within the gradual channel approximation, the charge carrier mobility can be calculated from the transfer characteristics:^[58]

$$\mu_{lin} = \frac{L}{WC_i V_D} \frac{\partial I_{DS}}{\partial V_G} \quad (2) \quad \text{and} \quad \mu_{sat} = \frac{2L}{WC_i} \left(\frac{\partial \sqrt{I_{DS}}}{\partial V_G} \right)^2 \quad (3)$$

As L (channel length), W (channel width), C_i (capacitance of the dielectric) and V_D are all known and constant, the mobility μ can be calculated from the modulation of the current with a changing gate potential. These equations are only valid for the ideal case of a linear relationship of I_{DS} on V_g (linear regime) or $\sqrt{I_{DS}}$ on V_g (saturation regime) because the gradual channel approximation is only a model based upon various assumptions, e.g., electric field at the gate must be much greater than the field between the source- and drain-electrodes.^[58] In OFETs – especially for high mobility materials – non-ideal FET behavior is commonly observed. Problems with contact resistances in transistors, which lead to “kinks” in the transfer characteristics are a leading factor in the overestimation of the charge carrier mobility of many polymers.^[59] This problem has attracted increased attention in recent years.^[58–60] Paterson et al. reviewed the published mobility values in the field, giving a comprehensive comparison of the highest mobilities in different polymer classes. They found that out of all publications with claimed mobilities greater than $1 \text{ cm}^2 \text{ V}^{-1} \text{ s}^{-1}$, more than half seemed to deviate from the ideal FET model in one way or the other.^[60] In order to get more reliable and meaningful mobility values Choi et al. proposed a guideline for their accurate determination.^[58] The first focus

should always be the optimization of the devices until ideal characteristics are observed. The authors stress that, in case this is not possible, it is important to address the non-ideal behavior and introduce a way to calculate the reliability of the claimed mobility values. We want the readers of this review to keep this in mind when high mobility values are cited in the following sections. As this reviews focus is mainly on structural design aspects, we believe it is beyond the scope of this work to critically assess each of the claimed values. In addition to pristine systems, the doped semiconductors play a crucial role in terms of charge transport in thermoelectrics and bioelectronics. The implications of doping for charge transport is a topic in itself and therefore we draw the attention of the readers to two basic reviews in this field.^[61,62] Very recently, Leo et al. also addressed the fundamental question of carrier release by the dissociation of charge transfer complexes despite a Coulomb binding energy of several 100 eV.^[63]

3. Second-Generation Conjugated Polymers

3.1. Design Rules and Synthetic Strategies for p-Type Materials

Hole transport or p-type polymers can be obtained when electron-rich moieties with an inherent donor-ability are either coupled with other donor units, or with electron-deficient acceptor units. Depending on the ionization potential value of the polymer, it is susceptible for oxidation by air if its oxidation potential lies below the reduction potential of oxygen. The oxidized species however are relatively stable compared to the reduced species of the n-type counterparts.

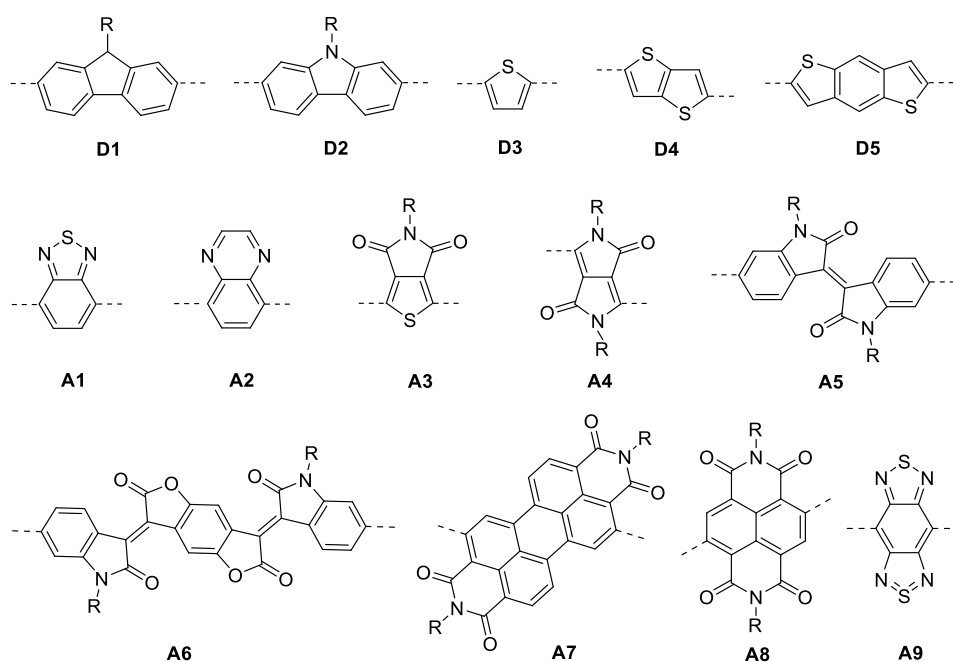


Figure 3. Common structural motifs for donor (D) and acceptor (A) units, which can be combined to obtain the second-generation conjugated polymers. R denotes any solubilizing group. **D1**: fluorene, **D2**: carbazole, **D3**: thiophene, **D4**: thieno[3,2-b]thiophene (thienothiophene “TT”), **D5**: benzo[1,2-b:4,5-b']bisthiophene (“BDT”) and **A1**: 2,1,3-benzothiadiazole, **A2**: quinoxaline, **A3**: 5-alkyl-4H-thieno[3,4-c]pyrrole-4,6-dione (“TPD”), **A4**: 2,5-dialkyl-pyrrolo[3,4-c]pyrrole-1,4-dione (“DPP”), **A5**: (3E)-1-alkyl-3-(1-alkyl-2-oxo-1,2-dihydro-3H-indol-3-ylidene)-1,3-dihydro-2H-indol-2-one (isoindigo “il”), **A6**: (3E,7E)-3,7-Bis(2-oxoindolin-3-ylidene)benzo-[1,2-b:4,5-b']difuran-2,6(3H,7H)-di-one (IBDF or BDOPV), **A7**: perylene-3,4,9,10-tetracarboxylic diimide (PDI), **A8**: naphthalene-1,4,5,8-tetracarboxylic diimide (NDI), **A9**: bisbenzothiadiazole (BBTz).

Exemplary building blocks are shown in **Figure 3**. Most of these building blocks have groups such as carbonyls, amides, imides or thiadiazoles which are generally bulky and provide significant steric hindrance, leading to a twisted backbone and, consequently, to a low charge carrier mobility. Therefore, the regular alteration of donor-acceptor (D-A) units, where acceptor units are copolymerized with suitable donor comonomers or flanking units is a widely used molecular design principle in a majority of second-generation conjugated polymers. For example, Macedo et al. have copolymerized fluorene **D1** with dithiophene, resulting in a moderate hole transport in the range of $\mu_h \approx 10^{-5} \text{ cm}^2 \text{ V}^{-1} \text{ s}^{-1}$.^[64] When carbazole **D2** was flanked with thiophene **D3** and copolymerized with benzimidazole, Song et al. already obtained a p-type material with a $\mu_h \approx 2 \cdot 10^{-3} \text{ cm}^2 \text{ V}^{-1} \text{ s}^{-1}$.^[65] When carbazole was copolymerized with 3-hexylthiophene **D3**, the mobility increased further by one order of magnitude to $\mu_h \approx 4 \cdot 10^{-2} \text{ cm}^2 \text{ V}^{-1} \text{ s}^{-1}$.^[66] For the planar donor-motif thienothiophene **D4** copolymerized with the acceptor unit thienopyrrolodione **A3**, Kim et al. have measured a hole mobility of $\mu_h = 2 \cdot 10^{-3} \text{ cm}^2 \text{ V}^{-1} \text{ s}^{-1}$ and when the same donor unit **D4** is combined with a small vinyl-spacer, the mobility increased further to $\mu_h = 3 \cdot 10^{-2} \text{ cm}^2 \text{ V}^{-1} \text{ s}^{-1}$.^[67,68] The electron-deficient units benzothiadiazole **A1** in combination with cyclopentadithiophene also imparts hole-transporting properties, however, only values in the range of $\mu_h \approx 10^{-4} \text{ cm}^2 \text{ V}^{-1} \text{ s}^{-1}$ are obtained.^[69] This value is in the same order of magnitude as the performance of isoindigo-

derivatives (**A5**) copolymerized with thiophene (**D3**) or thienothiophene (**D4**).^[70] Diketopyrrolopyrrole units (**A4**) are a widely in copolymers. In combination with benzodithiophene (**D5**) high mobility values of about $\mu_h \approx 2 \cdot 10^{-1} \text{ cm}^2 \text{ V}^{-1} \text{ s}^{-1}$ were observed by Yuan et al. and even outperformed by a thiophene-flanked DPP, copolymerized with a selenophene-derivative which showed a record-high hole-transport mobility of $\mu_h \approx 12 \text{ cm}^2 \text{ V}^{-1} \text{ s}^{-1}$.^[71,72] In the following, we highlight specific examples of D-A polymers and explain the underlying synthetic strategy for backbone planarization in a generalized way. The chemical structures of the discussed polymers **P1** to **P21** are shown in **Figure 5** and **Figure 6**, their reported charge carrier mobilities and the ionization potentials (IP) are listed in **Table 1**.

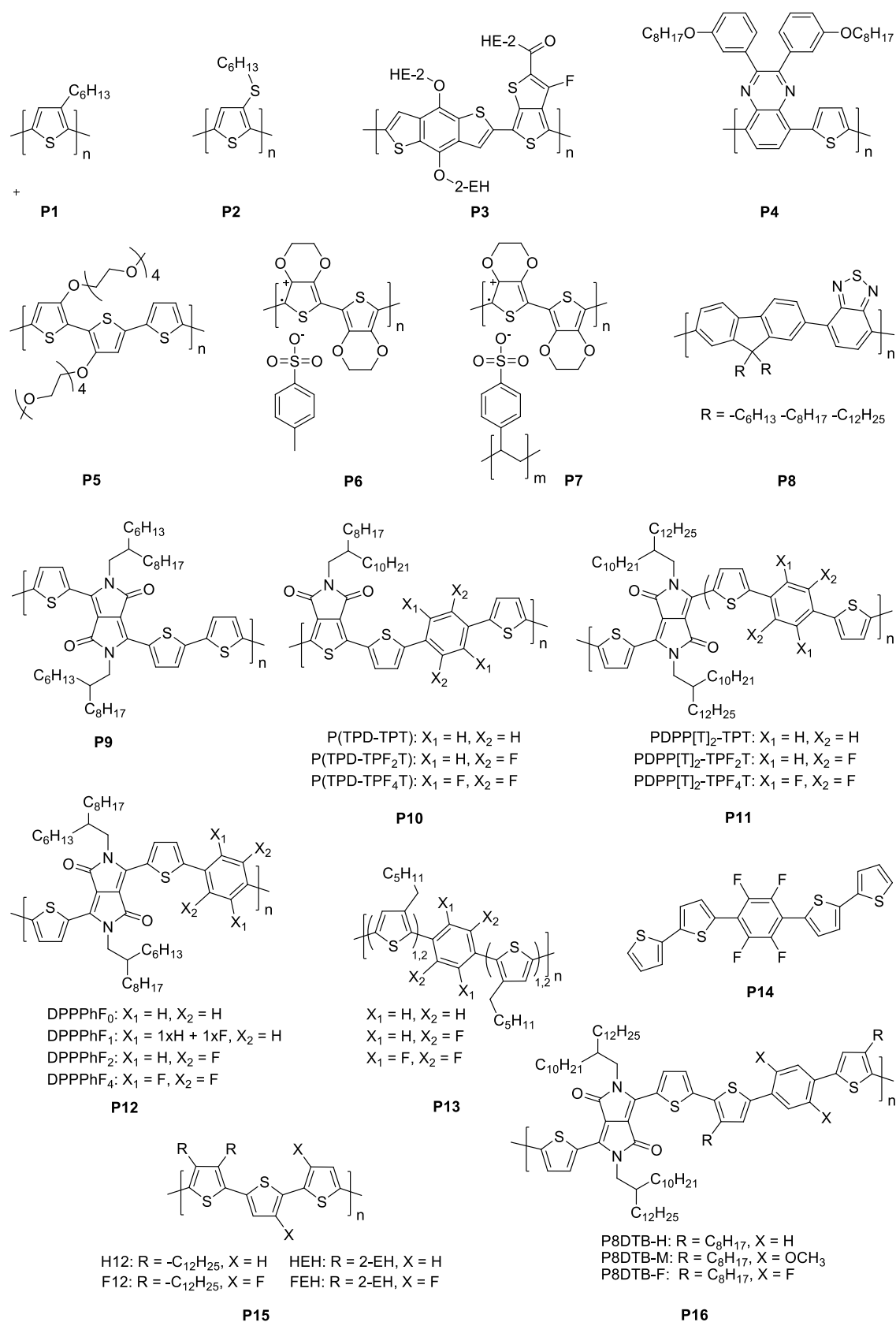


Figure 5. Chemical structures of p-type polymers P1–P16.

8 | Annex: Principles of Structural Design of Conjugated Polymers Showing Excellent Charge Transport toward Thermoelectrics and Bioelectronics Applications

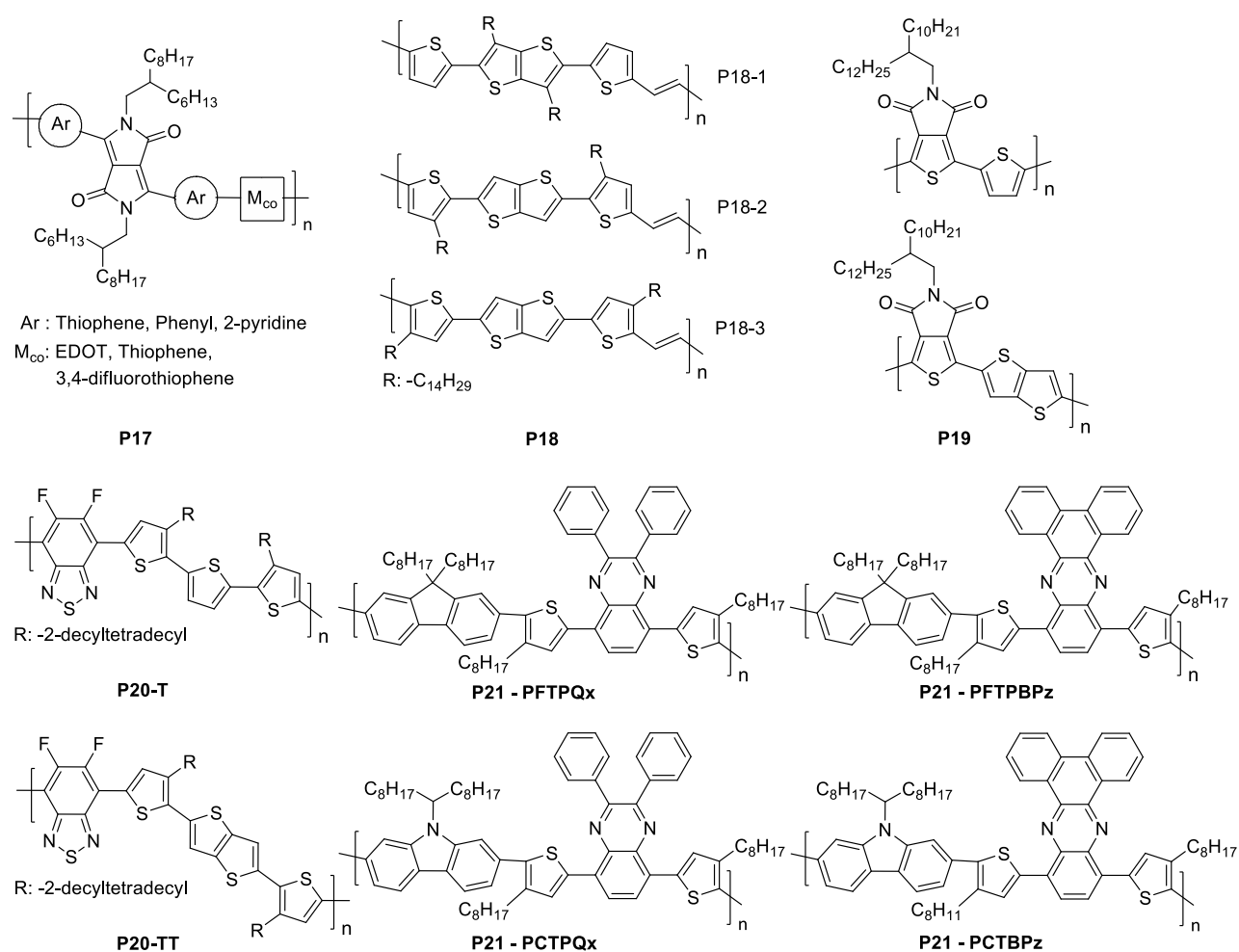


Figure 6. Chemical structures of the p-type polymers **P17–P21**.

Table 1. p-Type polymers with hole-/electron-mobilities and ionization potentials E_{IP}.

#	Abbreviation	μ_h [cm ² V ⁻¹ s ⁻¹] ^{a)}	μ_e [cm ² V ⁻¹ s ⁻¹] ^{a)}	E _{IP} [eV] ^{b)}	Ref.
P1	P3HT	10 ⁻³ – 10 ⁻¹	-	-5.2	[25,32,169,224]
P2	P3HTT	-	-	-5.05	[169]
P3	PTB7	5.8·10 ⁻⁴ c)	-	-5.03	[170,225]
P4	TQ1	9.5·10 ⁻⁵ c)	-	-5.16	[170,226]
P5	p(g ₄ 2T-T)	-	-	-4.4	[163]
P6	PEDOT:Tos	2.2	-	-	[158,161]
P7	PEDOT:PSS	1.1·10 ⁻³ c)	-	-	[15,227,228]
P8	F6BT	-	-	-5.86 -5.87 -5.93	[171]
P9	PDPP3T	1.5	-	-5.30 / -4.74 ^{d)}	[172,229]
P10	P(TPD-TPT)	0.4·10 ⁻⁴ 1.1·10 ⁻⁴	1.1·10 ⁻⁴	-5.46 -5.75 -6.03	[80]
	P(TPD-TPF ₂ T)	-	3.4·10 ⁻⁴		
	P(TPD-TPF ₄ T)	-	3.7·10 ⁻⁴		
P11	PDPP[T] ₂ -TPT	-	-	-5.69	[81]
	PDPP[T] ₂ -TPF ₂ T	-	-	-5.72	
	PDPP[T] ₂ -TPF ₄ T	-	-	-5.89	
	-	-	-	-	

8 | Annex: Principles of Structural Design of Conjugated Polymers Showing Excellent Charge Transport toward Thermoelectrics and Bioelectronics Applications

P12	DPPPhF ₀	0.3	0.2	-5.37	[79]
	DPPPhF ₁	0.2	0.2	-5.45	
	DPPPhF ₂	3·10 ⁻²	9·10 ⁻²	-5.57	
	DPPPhF ₄	0.2	2.0	-5.65	
P13		10 ⁻⁷ - 10 ⁻³	-	-5.6 - -6.0	[83]
P14	T-T-PhF ₄ -T-T	-	-	-	[84]
P15	PDAT-H12	-	-	-5.28	[85]
	PDAT-HEH	-	-	-5.27	
	PDAT-F12	-	-	-5.40	
	PDAT-FEH	-	-	-5.42	
P16	P8DTB-H	0.2	-	-5.11	[86]
	P8DTB-M	0.1	-	-5.03	
	P8DTB-F	1.2	-	-5.20	
P17	PDPP[T] ₂ -TF ₂	0.2 / 3.6·10 ^{-6 c)}	0.2 / 2.4·10 ^{-8 c)}	-5.91	[75,82]
	PDPP[T] ₂ -T			-5.75	
	PDPP[T] ₂ -EDOT	0.5 / 3.0·10 ^{-6 c)}	- / 2.1·10 ^{-8 c)}	-	
	PDPP[Py] ₂ -TF ₂	1.5·10 ^{-4 c)}	6.1·10 ^{-7 c)}	-5.97	
	PDPP[Py] ₂ -T	6·10 ^{-4 / 2.8·10^{-5 c)}}	- / 3.0·10 ^{-3 c)}	-6.11	
	PDPP[Py] ₂ -EDOT			-	
	PDPP[Ph] ₂ -TF ₂	- / 1.3·10 ^{-5 c)}	0.1 / 8.9·10 ^{-4 c)}	-	
	PDPP[Ph] ₂ -T			-6.04	
	PDPP[Ph] ₂ -EDOT	6.8·10 ^{-6 c)} 2.6·10 ^{-5 c)}	1.7·10 ^{-5 c)}	-	
		1·10 ^{-4 / 2.2·10^{-5 c)}}	2.7·10 ^{-5 c)}		
P18	P(BTTT)-1	0.1	-	-5.11	[88]
	P(BTTT)-2	0.3	-	-5.08	
	P(BTTT)-3	2.8	-	-4.97	
P19	PTPDT _{low}	MW 1.5·10 ⁻³	1.3·10 ⁻³	-6.08	[89]
	PTPDT _{high}	MW 1.5·10 ⁻²	2.3·10 ⁻²	-5.93	
	PTPDTT	0.1	0.2	-5.95	
P20	FBT-DTH _{DT} -1T	-	-	-5.46	[90]
	FBT-DTH _{DT} -TT	-	-	-5.47	
	FBT-DTh _{DT} -TT _{high}	MW -	-	-5.45	
P21	PFTPQx	5.8·10 ^{-5 c)}	-	-5.28	[91]
	PFTPBPz	3.0·10 ^{-4 c)}	-	-5.29	
	PCTPQx	7.3·10 ^{-5 c)}	-	-5.25	
	PCTBPz	4.1·10 ^{-4 c)}	-	-5.24	

a) Obtained from OFET-measurements if not stated differently. b) Measured via cyclic voltammetry if not stated differently. c) Measured via the SCLC method. d) HOMO measured by UPS.

3.1.1. Non-Covalent Interactions

In P3HT, obtained from mono-alkylated monomers like 3-hexylthiophene, the regioregularity is the key for a well-defined microstructure and, thus, highly ordered materials. Well-ordered materials are beneficial for efficient charge transport. However, in polymers consisting of the aforementioned D-A structural motifs, the microstructure is not dictated by the sidechains, but rather by the design of the building blocks themselves. These structural motifs have in common that they either consist of fused aromatic units or ones that are capable of participating in different non-covalent interactions. Both, ring-fusion and non-covalent interactions lead to planarization, i.e. a decrease in the torsional angle between two adjacent aromatic units. This leads to an increased orbital overlap, facilitating conjugation and charge transport, which is crucial for efficient materials. There are two main types of non-covalent interactions in conjugated polymers, which contribute to the rigidification of the polymer chain. First, the classical hydrogen-bond type, which predominantly consists of H \cdots F, H \cdots O, H \cdots S interactions. Secondly, the heteroatom interactions cannot be neglected, especially when there are no hydrogen-bond type interactions possible.^[73] In a theoretical work, Jackson et al. have assessed the role of different interactions between heteroatoms and predicted that hydrogen bonds between O \cdots H and N \cdots H cause conformational lock-in of the torsional angle, whereas F \cdots H and F \cdots S bonds are much weaker than expected and do not determine the structure.^[74] While S \cdots O and S \cdots N interactions are also present they are not influential and N \cdots F-, N \cdots O- and O \cdots F-interactions are not even bonding at all. We will show that these rules are not irrevocable, for example, some of the weaker interactions can still dictate the structure, if no competing interactions are present. In a comprehensive study of Conboy et al. mainly systems where no hydrogen-bonding was possible were studied to assess the role of heteroatom interactions.^[73] The predictions of Jackson et al. were corroborated in part, i.e. that attractive interactions between S \cdots N and S \cdots O are both relevant and comparably strong.^[74] Additionally, it was shown that the S \cdots S homoatom interaction is repulsive, leading to a severely twisted backbone. The oft-forgotten influence of an extended π -conjugation as such was mentioned and it was explained that the conjugation itself can help to improve planarity. Disrupting the π -conjugation may be energetically more expensive than relaxing weakly attractive or even repulsing heteroatom-distances. The importance of selecting groups and substituents in a way to minimize the dihedral angles is explained in **Figure 4** by considering differently substituted DPPs as a specific example.

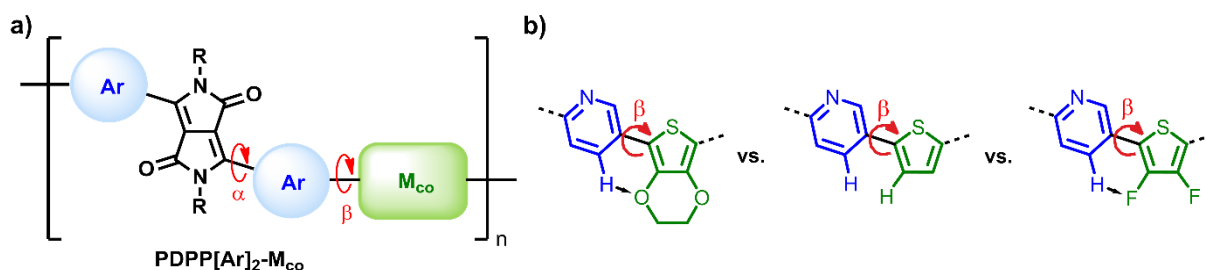


Figure 4. Schematic of torsional angles shown with the example of a DPP copolymer. a) Exemplary repeating unit where the aromatic unit Ar = T (thienyl), Ph (phenyl), Py (pyridyl) etc..., α being the dihedral (torsional) angle between the DPP core and the flanking Ar unit, and β the dihedral angle between the flanking unit and the comonomer M_{co}. b) Influence of non-covalent interactions on the dihedral angle β for Ar = Py and different comonomers M_{co}.

In the case of PDPPs, there are two options for the modification of the backbone in order to increase the planarity. The flanking aryl units Ar adjacent to the diketopyrrolo[3,4-c]pyrrole core can be altered (**P17**) in order to modify both of the dihedral angles α and β (see Figure 4 a).^[75] Generally, PDPPs employing phenyl flanking units show only modest charge carrier mobilities in OFET devices and poor power conversion (PCEs) efficiencies in organic photovoltaics (OPVs) when blended with fullerene acceptors.^[76,77] This poor performance is mostly ascribed to the large dihedral angle between the bicyclic DPP core and the phenyl groups as flanking aromatic units.^[78] In contrast, most of the thienyl-flanked PDPPs exhibit high charge carrier mobilities as well as high PCEs in OPV devices. On the one hand, the coplanar structure is more favorable due to H \cdots O interactions between the thiophene-proton at the keto-oxygen. On the other hand, the orbital overlap that profits from a push-pull-effect of the DPP core and the thiophene flanking units, which lowers the optical gap of the material, is very effective. In the case of pyridyl-substituted DPP, the proton in the ortho-position is missing, which drastically reduces the steric demand and, hence, allows for a much more planar system. For these polymers (**P17**), it was found that the crystallinity depends on the flanking units and increases from phenyl- over pyridyl- to thiophene-units.^[75] A versatile way of fixing the dihedral angle β between the diaryl-DPP and the comonomer is the exploitation of the aforementioned diffusive interactions. For example, the modification of the comonomer M_{co} (see Figure 4 b) either with oxygen or fluorine substituents can be utilized. The substitution of aromatic hydrogen atoms in the comonomer with fluorine gives rise to CH-F coordination sites and electron-deficient comonomers. This fluorination approach has been demonstrated by Park et al. in DPP polymers using perfluorinated phenyl-comonomers in order to improve the electron transport.^[79] Copolymers of DPP[T]₂ with non-fluorinated to perfluorinated phenylene, i.e. DPP[T]₂-PhF_{0,1,2,4} **P12** were also studied in the same report. It was shown that fluorination successively increases the coherence length along the backbone from 40 Å (non-fluorinated) to 61 Å (perfluorinated) which indicates a higher lattice order and crystallite size.^[79] In addition, the calculation of the torsional angles between the DPP[T]₂ and the phenylene units showed a decrease from $\Theta = 18^\circ$ in (DPP[T]₂PhF₀) to $\Theta = 9^\circ$ in

(DPP[T]₂PhF₄) and the electron mobility of DPP[T]₂PhF₄ ($2.0 \text{ cm}^2 \text{ V}^{-1} \text{ s}^{-1}$) was four times higher, as compared to that of DPP[T]₂PhF₀ ($\mu_e < 0.5 \text{ cm}^2 \text{ V}^{-1} \text{ s}^{-1}$). The fluorination concept was also explored in our group by using difluorothiophene or multi-fluorinated dithienyl benzenes as comonomer in combination with DPP or TPD.^[75,80–82] For example, Weller et al. studied the influence of increasing fluorination in copolymers of thieno[3,4-c]pyrrole-4,6-dione (TPD) with 2,2'-(1,4-phenylene)dithiophene (TPT) **P10** with the intention of generating an exclusive n-type material.^[80] Interestingly, the microstructure did not change drastically from no fluorine over TPF₂T (difluorinated) to TPF₄T (perfluorinated), only a tighter alkyl stacking and a slightly increased crystallinity could be observed. Still, the electron-mobility improved three-fold from $1.1 \cdot 10^{-4} \text{ cm}^2 \text{ V}^{-1} \text{ s}^{-1}$ to $3.7 \cdot 10^{-4} \text{ cm}^2 \text{ V}^{-1} \text{ s}^{-1}$. In similar copolymers of 3,6-di(thiophen-2-yl)pyrrolo[3,4-c]pyrrole-1,4-dione (DPP[T]₂) and TPT with different degrees of fluorination **P11**, it was found that moderate fluorination (TPF₂T) increases the crystallinity but perfluorination (TPF₄T) leads to phase separation in blends with PC₇₁BM.^[81] In the case of TPT oligomers and copolymers **P13**, the same circumstances have been found by Crouch et al., who observed an increased planarization and a tighter packing upon fluorination of the phenylene unit, resulting in lower torsional angles, improved structural order and improved hole mobilities.^[83] By fluorinating the central phenylene unit in oligothiophenes, Crouch et al. induced rigidification and a high coplanarity with a measured torsional angle between the thiophene- and the phenyl units below 2° in case of 5-[4-(2,2'-bithienyl-5-yl)-perfluorophenyl]-2,2'-bithienyl (T-T-PhF₄-T-T) **P14**.^[84] This is ascribed to strong S...F and H...F interactions, which will be discussed in more detail below. In simple polythiophenes, Jo et al. exploited partially fluorinated poly(3,4-dialkylterthiophenes) (PDATs) **P15** and computed the torsional angles between the individual thiophene units, concluding that fluorination fully planarizes the backbone from $\Theta = 17^\circ$ (non-fluorinated) to $\Theta = 0^\circ$ (fluorinated).^[85] Experimentally, the interchain distance was measured to decrease by about 20 % and the reduced π - π stacking distance lead to a two-fold increase of the hole mobility. By exploiting S...O and S...F interactions, Kim et al. achieved conformational control in DPP-TPT copolymers **P16** after incorporating either bulky methoxy-, hydrogen- or fluorine groups in the TPT unit.^[86] Thereby, the orientation with respect to the substrate was tuned between face-on (methoxy), mixed (hydrogen) and edge-on (fluorine), as probed by GIWAXS. Moreover, upon fluorination, the dihedral angles between phenyl- and thiophene units were drastically decreased from $\Theta = 21.3^\circ$ for methoxy-substituted phenylene to $\Theta = 12.7^\circ$ and $\Theta = 0.6^\circ$ for the hydrogen- and fluorine-substituted derivatives, respectively. Upon methoxy-substitution, the mobility decreased to a half ($0.2 \text{ cm}^2 \text{ V}^{-1} \text{ s}^{-1}$) of the initial value ($0.1 \text{ cm}^2 \text{ V}^{-1} \text{ s}^{-1}$) after fluorination, however, a six times higher hole mobility ($1.2 \text{ cm}^2 \text{ V}^{-1} \text{ s}^{-1}$) was measured. In DPP copolymers, the control of the conformation as well as the influence of the torsional angles on the charge carrier mobility were investigated.^[78] When comparing phenyl- with thiophene-flanked DPPs, it was observed that the large rotational freedom between DPP-core and phenyl flanking units lead to a large torsional angle. In comparison, the tighter solid-state structure and lower amount of torsional defects in the thiophene-flanked derivative increased the charge carrier

mobilities by one order of magnitude. Mueller et al. also conducted a thorough study on how both, the diffusive interactions and the choice of flanking units in DPP copolymers dictate the mode of orientation (face-on or edge-on), the degree of alignment and, importantly, the nature of charge transport (n-type, p-type or ambipolar).^[82] To conclude, in the case of PDPPs, flanking units have a more pronounced influence on charge transport than fluorination, because they induce more planarity and interchain packing. Aside from DPP and TPD-based polymers, which are known to exhibit very high charge carrier mobilities, Chen et al. also showed the importance of a highly planarized backbone in fluorene-based polymers.^[87] They introduced additional thiophene units in a copolymer of fluorene and benzothiadiazole. By this they obtained polymers with an enhanced planarization along the backbone, a more extended π -conjugation and by up to one order of magnitude higher ambipolar mobilities.

3.1.2. Planarization by Fused Aromatic Building Blocks

Another approach to increase the planarity is by introducing annulated rings as monomeric subunits. Thus, the inherent rigidity and planarity of the fused aromatic building blocks can be imparted on the polymer. By varying the position of the solubilizing sidechains in three isomeric thiophene-thienothiophene-thiophene copolymers **P18**, the dependency of the hole mobility on the torsional angles within the backbone was shown.^[88] As the torsional angle decreased from $\Theta \approx 31^\circ$ to $\Theta \approx 4^\circ$, the hole mobility improved by about one order of magnitude, from $0.1 \text{ cm}^2 \text{ V}^{-1} \text{ s}^{-1}$ to $2.8 \text{ cm}^2 \text{ V}^{-1} \text{ s}^{-1}$. Weller et al. observed the same trend for TPD-copolymers **P19** when thiophene was compared to thienothiophene TT (**D4**).^[89] Upon substituting the thiophene unit with the fused TT, the crystallinity and the π - π coherence length increased and, thus, the charge carrier mobilities increased by two orders of magnitude for both, hole- and electron-transport. Another impressive example for the utility of TT to improve the charge transport was given by Cai et al., who comparatively introduced thiophene and TT as comonomers in difluoro-benzothiadiazole-based low band gap polymers **P20**.^[90] By that, the hole mobility increased by two orders of magnitude from $3 \cdot 10^{-3} \text{ cm}^2 \text{ V}^{-1} \text{ s}^{-1}$ to $0.4 \text{ cm}^2 \text{ V}^{-1} \text{ s}^{-1}$. Beyond DPP- and thienothiophene-based systems, the enhancement of coplanarity was also realized via the introduction of bridged quinoxaline- or phenazine substituents in fluorene- or carbazole based copolymers **P21**.^[91] As expected, the bridged comonomer introduces planarity along the backbone, and furthermore lowered the steric demands, due to the suppressed twisting of the phenyl-rings. Thus, the π - π stacking distances was lowered by 0.2 \AA , resulting in a one order of magnitude higher hole mobility, as determined by SCLC-measurements. In summary, a careful selection and combination of building blocks by taking into account the possibilities of locking the planarity, using non-covalent interactions and additional planarization effects from fused aromatic building blocks serve as an elegant synthetic strategy for conjugated materials.

3.2. Design Rules and Intrinsic Air-Stability Issues in n-Type Materials

One of the major challenges in the field of organic electronics is the development of highly conducting and environmentally stable n-type organic semiconductors. They have always lagged far behind their highly efficient and robust p-type organic counterparts. In most of the electronic and optoelectronic applications, the semiconductor polymer must be very robust towards redox reactions, since the reversibility of the electrochemical reactions (oxidation of p-type and reduction of n-type) is a prerequisite in such applications. The fundamental reason for low electronic currents and operational instability of n-type materials lies in the fact that after electrons are added to n-type polymers by electrical injection, photogeneration or chemical doping, the reduced molecules, radical anions or charge carriers can be trapped or oxidized by oxygen and water. De Leeuw et al. were among the first to address the critical issue of the low electron current and environmental instability of doped n-type conducting polymers back in 1997.^[92] In this early study, they identified oxygen and water as the main atmospheric oxidants responsible for n-channel degradation. The electrochemical instability of n-type polymers was related to the standard reduction potential (E°) of water, which is -0.658 V versus a calomel standard reference electrode (SCE) at pH 7 with an overpotential of 0 V. Assuming that water is the main oxidant, the standard reduction potentials of n-type polymers should be more positive than -0.658 V, in order to be stable against oxidation from water. This potential can be translated to an electron affinity value of approximately -4 eV, implying that molecules with lowest unoccupied molecular orbitals (LUMOs) above -4 eV are expected to be unstable towards oxidation by water. Under these circumstances the water molecules act as electron traps, thus reducing the electron current that flows through the channel. The correlation of the n-channel stability of many acceptor molecules with their electrochemical characteristics was the subject of many works. It was found that n-type molecules such as pristine C_{60} , [6,6]-phenyl- C_{61} -butyric acid methyl ester and [6,6]-phenyl- C_{71} -butyric acid methyl ester, with LUMOs > -4 eV, were highly sensitive to air.^[93] On the contrary, n-type materials such as [6,6]-phenyl- C_{85} -butyric acid methyl ester,^[94] perfluorinated copper phthalocyanine,^[95] and naphthalenetetracarboxylic diimide derivatives^[96–100] with LUMOs deeper than -4 eV, exhibited a high n-channel stability in transistors. Anthopoulos et al. clearly demonstrated that a soluble dithiolene derivative, (diphenylethylenedithiolato) (1,3-dithiol-2-thione-4,5-dithiolato) nickel [Ni(dpdt)(dmit)], with a HOMO/LUMO of -4.43 eV/ -5.28 eV, respectively, showed no noticeable degradation on either electron or hole mobility in air.^[93] From these studies, it could be concluded that one must aim for organic molecules with electron affinities lower than -4 eV for a resistance against oxygen, water or a combination of these atmospheric oxidants. In 2012, Nicolai et al. investigated the precise nature of the oxidants responsible for this n-channel degradation.^[101] They investigated the electron transport in nine well-known semiconducting polymers covering a wide range of electron affinities, for example, poly(9,9-dioctylfluorene-alt-benzothiadiazole) (F8BT) with a LUMO level of -3.3 eV, poly[2,6-(4,4-bis-(2-ethylhexyl)-4H-cyclopenta[2,1-b;3,4-b]-dithiophene)-alt-4,7-(2,1,3-benzothiadiazole)] (PCPDTBT) with a LUMO level of -3.6 eV and poly[2-methoxy-5-

(3',7'-dimethyloctyloxy)-p-phenylene vinylene] (OC₁C₁₀-PPV), with a LUMO level of -2.8 eV. They found that the electron transport in most semiconducting polymers is limited by traps, known as trap-limited conduction. The electron-trap distribution was found to be identical for all polymers, $3 \cdot 10^{23}$ traps per m³, centered at an energy of -3.6 eV. These results pointed to a common origin for electron traps other than intrinsic defects like kinks in the polymer backbone, impurities remaining from the synthesis or contamination from the environment, but were related to hydrated oxygen complexes. They also suggested that in organic semiconductors with LUMOs deeper than -3.8 eV, such as [6,6]-phenyl C₆₁-butyric acid methyl ester (PCBM) and poly[*N,N'*-bis(2-octyldodecyl)-naphthalene-1,4,5,8-bis(dicarboximide)-2,6-diyl]-alt-5,5'-(2,2'-bithiophene)] (P(NDI2OD-T2)), the transport is trap-free, space-charge-limited, and characterized by a quadratic current-voltage dependence. These results, in addition to a large number of electrochemical studies suggest that n-type materials become increasingly stable against ambient atmosphere, when their LUMOs are deeper than -4 eV. Thus, air stable, high mobility n-type semiconducting polymers are highly electron-deficient materials with LUMO values < -4 eV. They are more readily reduced or n-doped and the corresponding radical anions are less prone to oxidation from atmospheric water and oxygen, as compared to materials with higher LUMO values.^[101] The following section discusses some general design principles that have been used to synthesize stable n-type semiconducting polymers and the outcomes on reduction potential, electron mobility and ambient stability of resulting polymers. This section on n-type polymers is divided into the following parts: The first part (3.2.1.) focusses on the selection of π -conjugated acceptor building blocks for polymers. The second part (3.2.2.) deals with some selected n-type polymers based on the donor-acceptor (D-A) strategy, where acceptor monomers are copolymerized with donor comonomers or flanking units to obtain (D-A) n-type polymers and copolymers from two acceptor units (A-A). It is worth mentioning that most of the best performing n-type polymers known so far are based on the same D-A design strategy which is used for p-type polymers. However, an all-acceptor approach combining two acceptor moieties (A-A) has recently gained a lot of interest since acceptor-acceptor (A-A) polymers exhibit more unipolar n-type transport. Such n-type polymers are obtained by the copolymerization of the same or different acceptor comonomers. This upcoming class of polymers is also discussed in detail in this review. In the last subsection (3.2.3), the potential of synthetic design rules of general validity such as core substitution with electronegative atoms and the use of fluorinated sidechains to improve the charge carrier mobilities and air stability are highlighted. Fluorination, which is becoming an important strategy to improve the device performance of n-type materials is discussed in light of several recent reports. As in the case of p-type polymers, only selected examples are shown to discuss the synthetic strategies for highly efficient material classes and no comprehensive description of all published polymers is given.

3.2.1. Selection of Acceptor monomers, Comonomers and Flanking Unit

The development of high performance n-type polymers requires highly electron-deficient building blocks or monomers with good solubility that can be readily polymerized to obtain high molecular weight polymers. The chemical structures of some widely used electron-deficient fused aromatic rings or motifs which are suitable for synthesizing n-type monomers are shown in Figure 3. The structural moiety, (3E,7E)-3,7-bis(2-oxoindolin-3-ylidene)benzo[1,2-b:4,5-b']difuran-2,6(3H,7H)-dione (**IBDF**) **A6**, which is widely known as benzodifurandione-based oligo(p-phenylene vinylene) (**BDOPV**) due to its structural similarity to oligo(p-phenylene vinylene), has four electron-withdrawing carbonyl groups and a low LUMO level of -4.24 eV. This motif is among the most electron-deficient building blocks known. The four carbonyl groups of **A6** form four intramolecular hydrogen bonds with the neighboring phenyl protons, which lead to a locked aromatic plane, a reduced torsional angle and an increased intrachain and interchain charge transport (see 3.1.).^[102–104] Historically, rylene diimide derivatives, mainly perylene diimide (**PDI**) **A7** and naphthalene diimide (**NDI**) **A8** have been an important class of n-type semiconductors.^[105] These moieties consist of two sets of π -accepting imide groups extending the conjugation length of the aromatic backbone, which makes them highly suitable for electron transport. In addition to their relatively high electron affinities ranging from -3.8 eV to -4.0 eV, easy synthesis, highly tunable electronic structures and excellent photochemical- and thermal stabilities make them very important building blocks for n-type polymers.^[106] In the context of acceptor monomers, 2,1,3-benzothiadiazole (**BTz**) **A1** also offers many attractive features, such as low LUMO levels of about -3.7 eV and two nitrogen atoms that help intramolecular hydrogen-bonding which leads to an increased planarization. This increased planarity has been shown to contribute to enhanced π -stacking and high charge carrier mobilities. Additionally, the possibility to introduce substituents at the 5 and/or 6 positions makes it possible to introduce solubilizing sidechains.^[107,108] Another acceptor, benzobisthiadiazole (**BBTz**) **A9**, is known for strong interchain interactions, needed for good electron transport.^[109] Isoindigo (**il**) **A5**, introduced by Stalder et al.,^[110] was first used in D-A conjugated p-type molecules and polymers (see 3.1.) and is now being explored for n-type applications.^[111] Diketopyrrolopyrrole (**DPP**)^[75,82] and thieno[3,4-c]pyrrole-4,6-dione (**TPD**)^[80] are also widely used electron-deficient cores for n-type applications. As the **DPP** moiety's strongly electron-withdrawing and polar nature enhances the tendency of **DPP**-based polymers to crystallize, they are known for their record high charge carrier mobilities.^[112,113] While all these acceptor units have different chemical structures, one common feature is their low LUMO levels in the range of -3.7 to -4.3 eV. The majority of high performance n-type polymers contain these acceptor motifs in the conjugated backbone either as repeating units or as part of it. Benzene and thiophene based donor comonomers such as bithiophene **D3** or thienothiophene **D4** are commonly used with acceptor counterparts, however, these electron-rich units increase the energy of both the LUMO and HOMO levels, which often results in increased ambipolar charge transport characteristics.

3.2.2. Synthetic Principles for by D-A and A-A n-Type Copolymers

Some interesting examples of high mobility n-type polymers based mainly on the D-A approach are shown in **Figure 7** to elucidate the basic principles of the D-A strategy for obtaining n-type polymers. The charge carrier mobility and electron affinity (E_{EA}) values are summarized in **Table 2**.

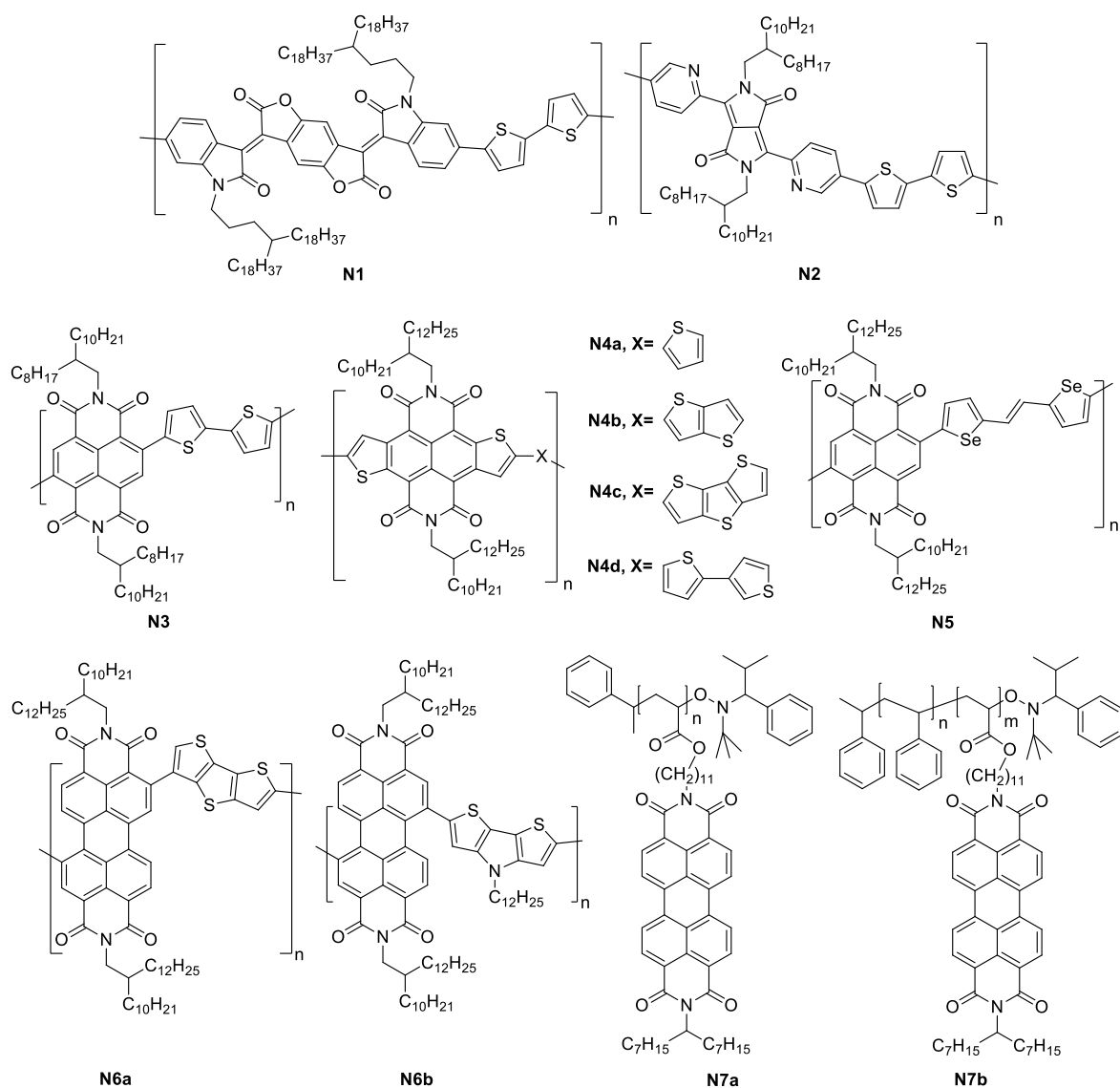


Figure 7. Examples of n-type donor-acceptor semiconducting polymers BDOPV-2T **N1**, PDBPyBT **N2**, P(NDIOD-2T) **N3**, PNNTI-T **N4a**, PNNTI-TT **N4b**, PNNTI-DTT **N4c**, PNNTI-BT **N4d**, PNNTI-SVS **N5**, P(PDI-DTT) **N6a**, P(PDI-DTP) **N6b**, PPerAc **N7a** and PS- block- PPerAc **N7b**.

Table 2. Selected n-Type polymers, and their hole-/electron-mobilities μ_h/μ_e and electron affinities values E_{EA} .

#	Abbreviation	μ_e [$\text{cm}^2 \text{V}^{-1} \text{s}^{-1}$] ^{a)}	μ_h [$\text{cm}^2 \text{V}^{-1} \text{s}^{-1}$] ^{a)}	E_{EA} [eV] ^{b)}	Ref.
N1	BDOPV-2T	1.8	0.2	-4.15	[104]
N2	PDBPyBT	6.3	2.2	-4.33	[114]
N3	P(NDI2OD-T2)	0.9	-	-3.91	[117]
N4a	PNDTI-T	$3.7 \cdot 10^{-2}$	$6.4 \cdot 10^{-3}$	-4.0	[118]
N4b	PNDTI-TT	0.3	$4.6 \cdot 10^{-2}$	-4.1	[118]
N4c	PNDTI-DTT	$2.1 \cdot 10^{-3}$	$3.0 \cdot 10^{-4}$	-4.0	[118]
N4d	PNDTI-BT	0.3	0.1	-4.1	[118]
N5	PNDI-SVS	2.4	-	-3.98	[120]
N6a	-	$1.2 \cdot 10^{-2}$	-	-3.9	[121,122]
N6b	-	$1.2 \cdot 10^{-3}$	-	-3.9	[122]
N7a	PPerAcr	$1.2 \cdot 10^{-3}$	-	-	[123]
N7b	PS- block- PPerAcr	$1.2 \cdot 10^{-3}$	-	-	[123]
N8	BBL	0.1	-	-4.4	[124]
N9	PNDI-0Th	$6 \cdot 10^{-4}$	-	-3.76	[125]
N10	P(il)	$3.7 \cdot 10^{-7}$	-	-3.84	[110]
N11	P(il-BTD)	-	-	-3.90	[110]
N12	PDTzTI	1.6	-	-3.77	[126]
N13	P(DPP5DH-4Tz)	$7 \cdot 10^{-2}$	-	-4.1 / -5.71 ^{d)}	[127]
N14a	BDPPV	1.1	-	-4.10	[129]
N14b	FBDPPV1	1.7	-	-4.26	[129]
N14c	FBDPPV2	0.8	-	-4.30	[129]
N14d	CIBDPPV	-	-	-4.30	[41]
N15a	F ₄ BDPPV-2T	14.9	-	-4.32	[131]
N15b	F ₄ BDPPV-2Se	6.1	-	-4.34	[131]
N16a	P(NDI2OD-T2Cl2)	$3 \cdot 10^{-2}$	-	-4.03	[132]
N16b	P(NDI2HD-T2Cl2)	$2 \cdot 10^{-2}$	-	-4.04	[132]
N17a	NDI-T-1FP-T	0.4	$8 \cdot 10^{-2}$	-3.73	[133]
N17b	NDI-T-2FP-T	0.2	$5 \cdot 10^{-2}$	-3.72	[133]
N17c	NDI-T-4FP-T	0.2	-	-3.77	[133]
N18a	PNFD-TE1	3.2	$6.4 \cdot 10^{-3}$	-4.00	[134]
N18b	PNFD-TE2	0.3	$1.7 \cdot 10^{-2}$	-4.00	[134]
N19	PDPP(Py) ₂ -TF ₂	$0.1 / 4.3 \cdot 10^{-3}$ ^{c)}	-	-3.81	[75]
N20	P(TPD-TPF ₄ T)	$3.7 \cdot 10^{-4}$	-	-3.90	[80]
N21a	PNDIFT2	3.9	-	-4.01	[139]
N21b	PNDIFTVT	3.8	-	-3.99	[139]

^{a)} Obtained from OFET-measurements if not stated differently. ^{b)} Measured *via* cyclic voltammetry if not stated differently. ^{c)} Measured *via* the SCLC method. ^{d)} measured by UPS

Lie et al. synthesized BDOPV-2T **N1** consisting of a BDOPV unit as acceptor with a long branched 4-octadecyldocosyl group as sidechain, and a centrosymmetric 2,2'-bithiophene as the donor unit.^[104] The polymer **N1** has a low-lying LUMO level of about -4.15 eV and good n-type transport characteristics with an electron mobility of up to 1.7 $\text{cm}^2 \text{V}^{-1} \text{s}^{-1}$ in OFETs. However, for devices fabricated under ambient conditions, the polymer showed ambipolar characteristics with a hole mobility of 0.5 $\text{cm}^2 \text{V}^{-1} \text{s}^{-1}$ and an electron mobility 1.5 $\text{cm}^2 \text{V}^{-1} \text{s}^{-1}$. Sun et al. studied the copolymer PDBPyBT **N2** consisting of a DPP core flanked with two 2-pyridinyl substituents and a new electron accepting building block, 3,6-di(pyridin-2-yl)pyrrolo[3,4-c]pyrrole-1,4(2*H*, 5*H*)-dione (DBPy).^[114] They suggested that six-membered aromatic rings such as pyridine, which are more electron-deficient than five-membered rings help to further lower the LUMO energy levels. Also, the positioning of the less sterically demanding nitrogen at the ortho position of pyridine increases the co-planarity. **N2** has a LUMO level of about -4.33 eV and exhibits a strong tendency to form highly crystalline and oriented thin films with a short π - π stacking distance of 0.36 nm. In OFETs an ambipolar charge-transport with a record electron-mobility value of 6.3 $\text{cm}^2 \text{V}^{-1} \text{s}^{-1}$ and a hole-mobility value 2.8 $\text{cm}^2 \text{V}^{-1} \text{s}^{-1}$ was observed for **N2**. Another widely studied n-type polymer poly{[N,N'-bis(2-octyl-dodecyl)-1,4,5,8-naphthalenedicarboximide-2,6-diyl]-alt-5,5'-(2,2'-bithiophene)} **N3** also known as P(NDI2ODT2) or ND2200 **N3** is based on NDI as electron-deficient core and bithiophene as the donor comonomer. The first to report **N3** were Guo and Watson in 2008^[115] but it has been extensively studied since then in the group of Facchetti in the context of developing high performance n-type polymeric materials for organic electronics.^[116,117] With a LUMO level of about -3.91 eV, an easy electron injection is facilitated and the fabrication of air-stable OFETs is possible. Electron mobilities of up to 0.9 $\text{cm}^2 \text{V}^{-1} \text{s}^{-1}$ and excellent ambient stability were demonstrated for this polymer.^[116,117] Due to the remarkable success of **N3**, a lot of synthetic effort was done to improve the electron mobility of this polymer, e.g. by sidechain engineering of the donor unit or by replacing thiophene units with other electron-rich systems.

Naphtho[2,3-b:6,7-b']dithiophene-4,5,9,10-diimide (NDTI) is an NDI analogue and a promising building block for n-type, p-type, and ambipolar organic semiconductors.^[118] The combination of the electron-rich NDTI with an electron-deficient diimide leads to a narrower energy gap. When thiophene **D3** or fused aromatic moieties such as thienothiophene (TT) **D4** or dithienothiophenes (DTT) were introduced as comonomers in NDTI-based materials (**N4a-d**), it was observed that **D4** offers superior thin film alignment and the electron as well as the hole mobilities were increased dramatically.^[118] However, it must be noted that other than the crystallinity, the orientation changed from face-on to edge-on upon the introduction of **D4**. This also improves the charge transport in OFETs and the highest electron mobility (0.3 $\text{cm}^2 \text{V}^{-1} \text{s}^{-1}$) was observed for the NDTI copolymer with a TT unit and edge-on orientation. NDI polymers have been reviewed in detail by many others, most recently by Quinn et al. who comprehensively covered the reports on structure-property optimization.^[119] From the point

of high electron mobilities, a particularly interesting example is the NDI and selenophene-vinylene-selenophene (SVS) based conjugated polymer PNDI-SVS **N5**. This polymer has a LUMO energy level of -3.98 eV, which is lower than for **N3**. This is attributed to the change in the donor moiety from bithiophene to SVS. In OFETs a maximum electron mobility of $2.4 \text{ cm}^2 \text{ V}^{-1} \text{ s}^{-1}$ and good ambient stability were observed for **N5**.^[120] PDI based semiconducting polymers constitute another important class of rylenediimide derivatives used for n-type applications. Zhan et al. studied a series of solution processable conjugated polymers, such as **N6a** and **N6b**, consisting of perylenediimide **A7** alternating with dithienothiophene or dithienopyrrole (DTP) units.^[121,122] As discussed earlier in the case of p-type polymers, the highly planar DTT units are known to promote highly ordered π -stacked structures which increase the charge carrier mobility. DTP on the other hand, which is more electron-rich offers the possibility of tuning the polymer solubility and ordering through N-substituents without disrupting the polymer's backbone. The electron affinities for **N6a** and **N6b** were found to be in the range of 3.8 eV to 4.0 eV. **N6a** is an electron-transport material with a charge carrier mobility in an OFET of $1.2 \cdot 10^{-2} \text{ cm}^2 \text{ V}^{-1} \text{ s}^{-1}$. Analogous devices with **N6b** resulted in a maximum electron mobility of $1.2 \cdot 10^{-3} \text{ cm}^2 \text{ V}^{-1} \text{ s}^{-1}$ after annealing under an inert atmosphere. Hüttner et al. highlighted the possibility of using a pendant approach by utilizing perylenediimide derivatives for the optimization of the electron transport properties. They synthesized a sidechain perylene bisimide homopolymer **N7a** and a block copolymer, polystyrene-b-poly(peryene bisimide acrylate) **N7b** and studied their transport characteristics in OFET devices. The polymers exhibited electron transport mobilities in the range of $10^{-3} \text{ cm}^2 \text{ V}^{-1} \text{ s}^{-1}$ under inert atmosphere.^[123] Energetically, conjugated polymers with backbones exclusively composed of electron-deficient units provide both low lying LUMOs and HOMOs and should, theoretically, be the best candidates for unipolar n-type transport. Poly(benzobisimidazobenzophenanthroline) (BBL) **N8** reported by Babel and Jenekhe, has a highly electron-deficient, rigid and planar backbone (**Figure 8**).

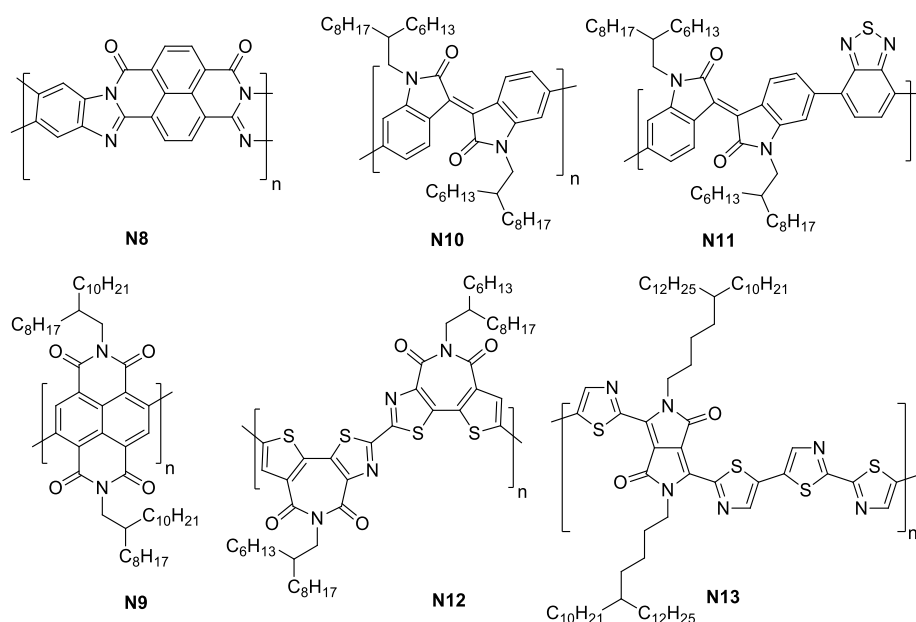


Figure 8. Examples of a ladder type BBL **N8**, and acceptor-acceptor semiconducting polymers PNDI-OTh **N9**, P(ii) **N10**, P(ii-BTD) **N11**, PDTzTI **N12**, P(DPP5DH-4Tz) **N13**.

N8 has a high electron affinity of about 4.0 eV to 4.4 eV and shows field-effect electron mobilities from 0.03-0.1 $\text{cm}^2 \text{V}^{-1} \text{s}^{-1}$ under atmospheric conditions.^[124] However, a lack of solubilizing groups limited its solubility in common organic solvents which is necessary for large area applications. An acceptor-acceptor (A-A) approach as principle design strategy has attracted a lot of attention for meeting the challenges in optimization of n-type semiconducting polymers. In this context, homopolymers obtained by polymerization of a single acceptor moiety or copolymers of different acceptor moieties were investigated for exclusive unipolar n-type transport. However, it is important to mention that the lack of donor units in the polymer backbone may negatively affect the interchain interactions and, hence, the crystallinity of the polymer due to a lack of favorable D-A interactions. Therefore, a careful tuning of the molecular structure, while keeping the effect on intermolecular chain-chain interactions in view is critical to obtain stable n-type polymers with high electron transport characteristics. Some examples of all acceptor polymers are shown in Figure 8 and they are discussed in light of the effect of the molecular structure on n-channel transport properties. A NDI based homopolymer PNDI-OTh **N1** was synthesized and the electron transport properties were compared with the corresponding thiophene containing D-A copolymers.^[104] The electron mobility of the homopolymer **N9** was found to be two orders of magnitude lower than the thiophene comonomers. From detailed XRD studies, it was found that **N9** has very little long-range order in solid state as compared to the D-A copolymers, which may explain the difference in charge carrier mobilities. Generally, an increased thiophene content leads to a higher crystallinity and order which subsequently improves the charge carrier mobilities.^[125] Stalder et al. introduced isoindigo **A5** as a novel acceptor and synthesized two conjugated polymers with backbones composed only of electron-deficient units.^[110] The homopolymer

N10 from monomer **A5** and a copolymer **N11** with 2,1,3-benzothiadiazole **A1** as a comonomer, are both thermally stable up to 380 °C, soluble and processable from common organic solvents. Both polymers can be reduced reversibly and have LUMO energy levels of -3.84 eV and -3.90 eV, respectively. Nevertheless, these isoindigo-based polymers were found to have extremely low electron mobilities with the highest value in the range of $10^{-7} \text{ cm}^2 \text{ V}^{-1} \text{ s}^{-1}$. Recently, Shi et al. addressed the need to synthesize new electron-deficient building blocks with good solubility, favorable geometry, and optimized electrical properties for high mobility n-type polymers.^[126] Using a new electron-deficient core 2,2'-bithiazolothienyl-4,4',10,10'-tetracarboxydiimide (DTzTI), containing thiazole units, an all acceptor homopolymer poly(2,2'-bithiazolothienyl-4,4',10,10'-tetracarboxydiimide) (PDTzTI) **N12** was synthesized. Thiazole, which is known to be electron deficient and has a low steric hindrance due to the elimination of the hydrogen at the 3-position, increases the planarity of the polymer backbone through intramolecular N··S interactions and can be considered as a good substitute for the commonly used thiophene in n-type D-A polymers.^[74] **N12** exhibits a LUMO level of -3.77 eV and unipolar electron transport with an electron mobility of $1.6 \text{ cm}^2 \text{ V}^{-1} \text{ s}^{-1}$ in OFETs. Yuan et al. reported poly-(diketopyrrolopyrrole-tetrathiazole) **N13**, containing the electron-deficient comonomers bithiazole and dithiazole-diketopyrrolopyrrole (DTzDPP). **N13** exhibits a field-effect electron mobility in the range of $0.2\text{--}0.7 \cdot 10^{-1} \text{ cm}^2 \text{ V}^{-1} \text{ s}^{-1}$ in OFET devices.^[127] From the discussion above, it can be seen that A-A polymers, either as homopolymers or as copolymers offer the advantage of a stable n-type charge transport and suppressed ambipolarity, which can offer unique opportunities for new n-type semiconducting polymers. However, the development of A-A-type polymers is curtailed by the limited choice of acceptor monomers. This restricts the available combinations for the synthesis of new n-type polymers severely. Furthermore, strong electron-withdrawing substituents, such as C=O, C≡N, etc., which are required to obtain n-type behavior, are usually bulky and exert significant steric hindrance on the neighboring flanking or comonomer units resulting in high torsional angles and twisted polymer backbones. Twisted polymer backbones are detrimental not only to the intrachain delocalization of charges, but also to the interchain transport as a result of poor molecular packing and low film crystallinity, which is reflected in low carrier mobilities. However, more research efforts are needed to establish fundamental relationships between molecular structures and the device performance of A-A n-type polymers.

3.2.3. The Effect of Electron-Withdrawing Substituents

Substituting hydrogen with electronegative atoms such as fluorine, chlorine, and bromine or a cyano group is an increasingly important approach to improve the electron mobility and the ambient stability of n-type polymers. These inductively electron-withdrawing substituents have been known to effectively lower the energy of both the HOMOs and the LUMOs. Fluorination, in particular, has turned out to be an extremely important strategy to improve transport properties of n-type polymers.^[128] Fluorine, is the most electronegative (electronegativity: 3.98) of all elements and the van der Waals radius of the fluorine atom (1.47 Å) is the second smallest, only slightly bigger than hydrogen. Therefore, a fluoro-substituent can be easily incorporated in hydrocarbons. The fluoro-substituent is known to affect the chemical structure of the polymer in the following ways:

- 1) Tuning of the frontier orbitals: the extreme electronegativity of fluorine pulls electrons from the backbone to stabilize the frontier molecular orbitals.
- 2) Ambient Stability: the hydrophobic nature of the fluorinated compounds can impart better air stability by reducing penetration by oxygen and water.
- 3) Non-bonding interactions: fluorine induced intermolecular interactions such as S...F, and H...F can promote backbone planarity and influence the packing motifs of the polymer chains.

Some selected examples of chemical structures which show a clear influence of halogenation on the material properties are given in **Figure 9**.

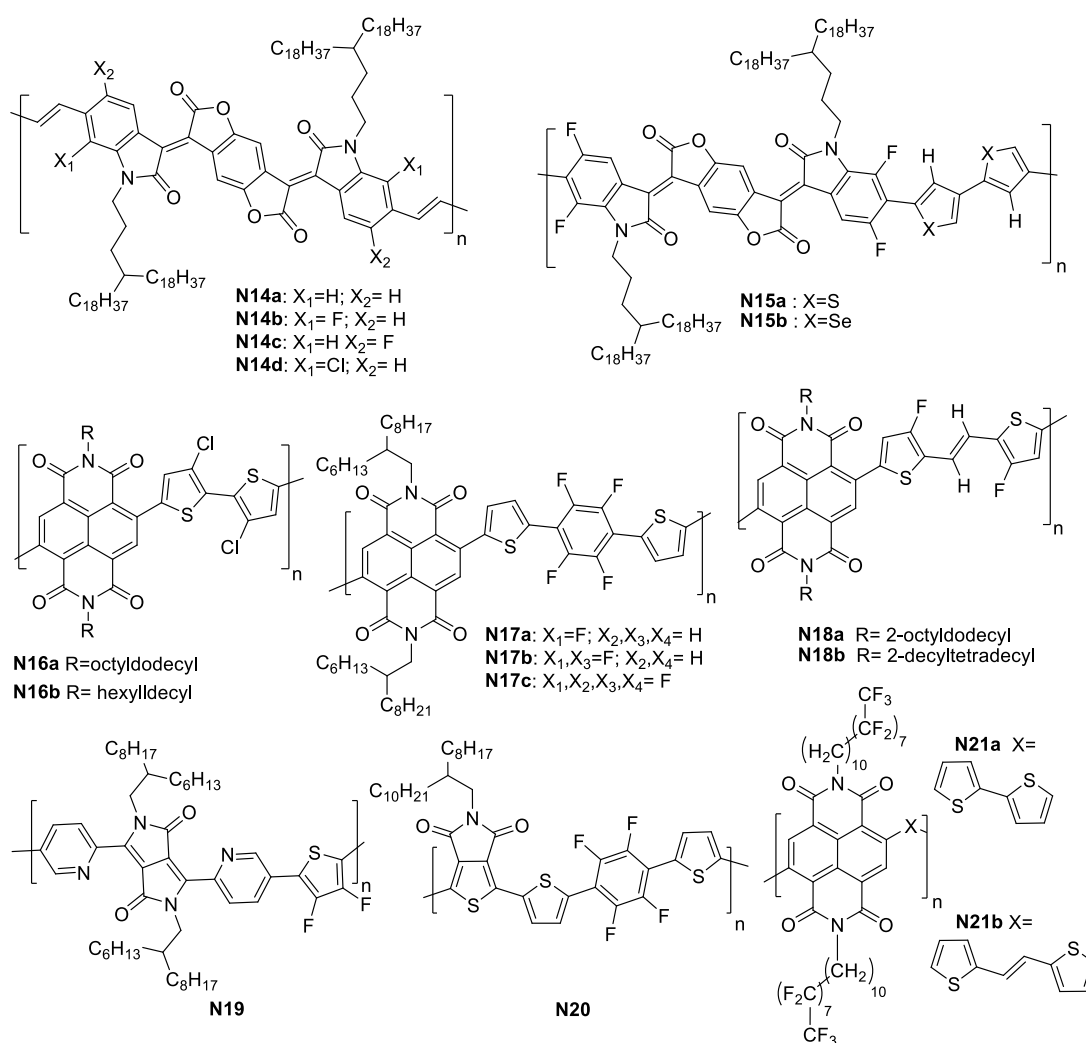


Figure 9. Examples of halogenated n-type semiconducting polymers: BDPPV **N14a**, FBDPPV1 **N14b**, FBDPPV2 **N14c**, ClBDPPV **N14d**, F₄BDPPV-2T **N15a**, F₄BDPPV-2Se **N15b**, P(NDI2OD-T2Cl2) **N16a**, P(NDI2HD-T2Cl2) **N16b**, NDI-T-1FP-T **N17a**, NDI-T-2FP-T **N17b**, NDI-T-4FP-T **N17c**, PNFD-TE1 **N18a**, PNFD-TE2 **N18b**, PDPP(Py)₂-TF₂ **N19**, P(TPD-TPF₄T) **N20**, PNDIFT2 **N21a**, PNDIFTVT **N21b**.

Lei et al. studied the effect of core substitution with fluorine and chlorine on the electron transport properties of BDOPV based polymers.^[129] They synthesized **N14b** and **N14c** by introducing fluorine and studied the electron transport properties of these n-type polymers in OFETs. The introduction of the fluorine atoms lowers the LUMO levels of **N14b** and **N14c** to -4.26 eV and -4.30 eV, respectively, which is 0.16 eV and 0.20 eV lower than that of the corresponding non-fluorinated polymer **N14a** (-4.10 eV). It was suggested that fluorination provides a more ordered packing in thin film, a smaller π - π stacking distance, stronger interchain interactions and that it locks the conformation of the polymer backbones. The maximum mobility of the **N14b** was determined to be 1.7 $\text{cm}^2\text{V}^{-1}\text{s}^{-1}$, which is one of the highest values in n-type conjugated polymers at ambient conditions. Surprisingly, the highest electron mobility of **N15c** was only 0.8 $\text{cm}^2\text{V}^{-1}\text{s}^{-1}$, which is even lower than that of the nonfluorinated polymer (1.0 $\text{cm}^2\text{V}^{-1}\text{s}^{-1}$). In order to further understand the effect of halogenation on the electron transport characteristics of BDPPV based systems, Lei et al.

extended their studies by substituting fluorine with chlorine as shown in **N14d**.^[130] The introduction of chlorine lowered the LUMO energy levels of **N14d** to -4.30 eV, which is very similar to those of **N14c**. Recently, Zheng et al. introduced two new copolymers **N15a** and **N15b** based on the highly electron-deficient building block F_4BDOPV , and 2,2'-bithiophene and 2,2'-biselenophene as donor units.^[131] These two copolymers, displayed low LUMO levels of about -4.32 eV and -4.34 eV and a n-type performance with electron mobilities of $14.9 \text{ cm}^2 \text{ V}^{-1} \text{ s}^{-1}$ and $6.14 \text{ cm}^2 \text{ V}^{-1} \text{ s}^{-1}$ respectively, at ambient conditions. The effect of backbone halogenation was also studied in halogenated substituted derivatives of PNDIODT2, such as the chlorinated polymers **N16a** and **N16b**.^[132] These polymers are based on N,N'-difunctionalized NDI and 3,3'-dichloro-2,2'-bithiophene (T2Cl2) moieties and exhibit electron mobilities in the range of $0.2\text{--}0.5 \cdot 10^{-1} \text{ cm}^2 \text{ V}^{-1} \text{ s}^{-1}$. This is about 5-10 times smaller than for the non-chlorinated polymers. However, both copolymers were far less ambipolar and exhibited excellent operational stabilities. In bias-stress tests $< 3\%$ degradations were observed.^[132] Kranthiraja et al. recently synthesized copolymers of NDI and thiophene-fluorophenylthiophene (T-FP-T) units.^[133] Polymer **N17c**, with four fluorine atoms at the TPT donor unit exhibited unipolar n-type transport as compared to the ambipolar charge transport in polymers with lower fluorine content. However, the electron mobility values were found to decrease with a higher fluorine content with 0.35 , 0.18 , and $0.16 \text{ cm}^2 \text{ V}^{-1} \text{ s}^{-1}$ in OFETs for 1, 2 and 4 fluorine atoms, respectively. The electrochemical properties of the copolymers **N18a** and **N18b**, with NDI as acceptor and fluorinated dithienylethenes as donor building blocks were reported by Chen et al.^[134] Both polymers exhibited deep-lying LUMO energy levels around -4.0 eV. The authors reported an impressive electron mobility of $3.2 \text{ cm}^2 \text{ V}^{-1} \text{ s}^{-1}$ in air for **N18a** in OFET devices. In comparison only $0.3 \text{ cm}^2 \text{ V}^{-1} \text{ s}^{-1}$ were observed for **N18b**. The authors suggest that the difference of the electron mobility arises because **N18a** thin films exhibit crystalline granular intercalating networks and crystallites with preferential edge-on orientation, whereas **N18b** thin films have smooth surfaces and smaller crystallites with mainly face-on orientation. Mueller et al. addressed the question of designing high electron mobility diketopyrrolopyrrole polymers based on DPP by varying the flanking aryl units between thienyl-, 2-pyridinyl-, or phenyl and choosing thiophene or 3,4-difluorothiophene as comonomer.^[75] They found that the aryl flanking units have a very pronounced influence on the type of charge carrier transport, as well as the charge carrier mobility values, with thienyl being highly suitable for hole transport and pyridyl for electron transport. 3,4-Difluorothiophene in combination with the electron-withdrawing pyridyl flanking unit leads to one of the best electron transport polymers (**N19**) with a bulk electron mobility (SCLC) of $4 \cdot 10^{-3} \text{ cm}^2 \text{ V}^{-1} \text{ s}^{-1}$ which is comparable to PCBM. Weller et al. recently studied the influence of the degree of fluorination on the electrochemical and the charge transport properties of a series of copolymers based on thieno[3,4-c]pyrrole-4,6-dione **A3** as electron-deficient monomer and thiophene-phenyl-thiophene (TPT) as donor.^[80] With increasing fluorination of the TPT unit, the ionization potential (E_{IP}) is lowered and therefore, the polymers become less oxidizable due to the decreased electron density along the polymer backbone. Difluorination

results in a lowering of the E_{IP} by 0.3 eV, but the electron affinity (E_{EA}) is not affected. However, by tetrafluorination (**N20**), the E_{IP} and E_{EA} are lowered even further by 0.3 eV. The electron transport behavior improves with increasing fluorination and tetrafluorination leads to exclusive n-type behavior with an OFET electron mobility of $3.7 \cdot 10^{-4} \text{ cm}^2 \text{ V}^{-1} \text{ s}^{-1}$ under nitrogen atmosphere. It is important to note that air-instability for typical n-type semiconductors is due to the trapping of the charge carriers in ambient conditions which seriously degrade the effective field-effect mobility. This can be generally reversed upon application of vacuum. Preventing the trapping species from reaching the charge-transporting area of the film can facilitate transport properties. The incorporation of long fluorocarbon sidechains into n-type polymers can provide many advantages, such as hydrophobicity, rigidity and thermal stability, as well as chemical and oxidative resistance.^[135–137] Although the incorporation of fluorinated sidechains does not significantly lower reduction potentials as compared to fluorine free analogues, OFETs fabricated with the fluorinated materials are reported to yield devices with higher air-stability as compared to their non-fluorinated counterparts.^[98,99,138] This behavior can be explained in terms of the high hydrophobicity of fluorinated sidechains and a substantial contraction of the channels between the fluoroalkyl chains due to better packing which presents a penetration-barrier for water and oxygen. Kang et al. designed **N21a** and **N21b** containing semifluorinated alkyl sidechains introduced to NDI-based copolymers.^[139] It was found that fluorinated sidechains induce a high degree of order in the polymer backbones by forming a superstructure composed of “backbone crystals” and “sidechain crystals”. These polymers exhibited unipolar n-channel transport in field-effect transistors with remarkably high electron mobility values of up to $6.5 \text{ cm}^2 \text{ V}^{-1} \text{ s}^{-1}$.

4. Conjugated Polymers for Thermoelectrics

4.1. General Introduction to Thermoelectrics

Thermoelectric generators (TEGs) are solid state energy converters, which work on the principle of the Seebeck effect and convert a heat flux (temperature difference) directly into electrical energy. Conversely, when an electric current is applied to the same type of device, the analogous Peltier effect can be used to convert electrical energy into thermal energy. As a result of the global energy crisis, these devices have attracted attention for applications such as waste-heat recovery from thermal power plants, automobile exhausts, solar heat utilization, and as miniature power sources for autonomous electronics.^[140]

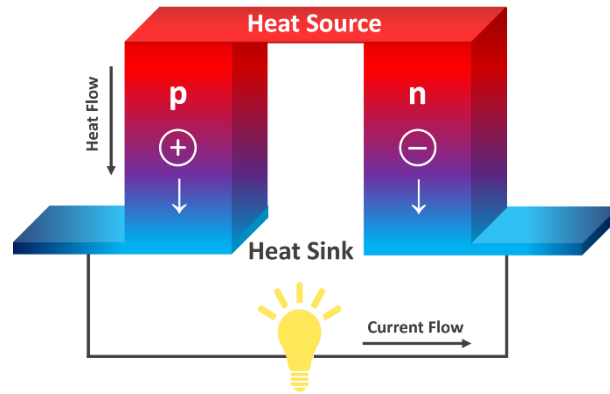


Figure 10. Schematic illustration of a thermoelectric couple for power generation, consisting of a p- and n-type leg aligned within a thermal gradient.

A TEG module consists of several pairs of p-type and n-type semiconductor legs (**Figure 10**), where each pair or thermoelectric (TE) couple represents the smallest unit of a thermoelectric generator. In a TE module, these legs are connected electrically in series and thermally in parallel. When a temperature gradient (ΔT) is applied to a TE couple, the mobile charge carriers (electrons and holes) with higher energy diffuse from the hot end to the cold end. This produces an electrostatic potential (ΔV), or a current in a closed circuit when the couple is used in power generation mode. The thermoelectric performance of a material is generally estimated in terms of a dimensionless thermoelectric figure of merit ZT , which is composed of the Seebeck coefficient S ($S = \Delta V/\Delta T$), the isothermal electrical conductivity σ , the thermal conductivity κ and the temperature T . The factor $S^2 \sigma$, is commonly known as the power factor PF, and the figure of merit is defined as:

$$ZT = S^2 \sigma T \kappa^{-1} \quad (4)$$

Thermoelectric generators with high efficiency require the constituent p- and n-type materials to have a high thermoelectric figure of merit, $ZT > 1$. For this, the materials must meet the following conditions: it needs to be a good electrical conductor (high σ), a poor thermal conductor (low κ) and the Seebeck coefficient S must be high.

The biggest challenges which have impeded the widespread use of TEGs up to now, are the intrinsically low thermoelectric efficiencies of available TE materials. These lead to very low power generation efficiencies η_p . The basic questions regarding TE as valid for metals or degenerate semiconductors (parabolic band, energy-independent scattering approximation) serves as a good starting point to introduce the topic. There are two reviews in this topic which address the interconnection of ZT parameters in terms of basic equations which are shortly described below.^[141,142] The power generation efficiency is related to the average value of the thermoelectric figure of merit ZT for both n-type and p-type legs as follows:

$$\eta_p = \frac{T_h - T_c}{T_h} \left[\frac{\sqrt{1 + ZT_{ave}} - 1}{\sqrt{1 + ZT_{ave}} + T_c/T_h} \right] \quad (5)$$

$$ZT_{ave} = \frac{1}{T_h - T_c} \int_{T_c}^{T_h} ZT dT \quad (6)$$

where ZT_{ave} is the average value of n-type and p-type legs. ZT_{ave} per leg is averaged over the temperature dependent ZT curve as a function of T between T_h and T_c , where T_h and T_c are the temperatures at the hot and cold ends. **Equation 5** and **6** show that a high value of ZT_{avg} and a large temperature difference (ΔT) are required to produce a high η_p . For example, a ZT value of the order 3 at a temperature difference of 400 K would result in a $\eta_p \approx 25\%$.^[143] However, even the best known commercialized TE materials only have ZT values close to 1. The fundamental reason which makes the optimization of ZT so challenging can be understood by re-examining **Equation 4**. In order to obtain a high ZT, both the electrical conductivity σ and the Seebeck coefficient S must be enhanced simultaneously, while the thermal conductivity κ must be minimized. However, these requirements cannot be satisfied simultaneously according to the Pisarenko-Relation and Wiedemann-Franz Law at least for solid-state inorganic semiconductors. The complex relationships for S, σ and κ are summarized as:

$$S = \frac{8\pi^2 k_B^2}{3eh^2} m^* T \left(\frac{\pi}{3n}\right)^{2/3} \quad (7)$$

$$\sigma = ne\mu = \frac{ne^2\tau}{m^*} \quad (8)$$

$$\kappa = \kappa_L + \kappa_E = \kappa_{lat} + L\sigma T \quad (9)$$

With k_B : Boltzmann constant, m^* : effective mass, h : Planck constant, n : charge-carrier concentration, e : elementary charge, μ : charge carrier mobility, τ : relaxation time, κ : total thermal conductivity, κ_L : lattice thermal conductivity, κ_E : electronic thermal conductivity, and L : Lorenz number.

These complex relationships suggest that if the carrier concentration n is increased to enhance the electrical conductivity, the Seebeck coefficient will decrease according to the Pisarenko-Relation. Additionally, the thermal conductivity will rise due to the increase in the electronic contribution to the thermal conductivity κ_E in accordance with the Wiedemann-Franz law ($\kappa_E = L \sigma T$), forbidding a simultaneous increase of S and σ , while keeping κ low. Therefore, the challenge to create high ZT thermoelectric materials lies in the optimization of three mutually contradictory properties (S, σ and κ) simultaneously. So far, the best thermoelectric materials have been inorganic compounds, such as bismuth telluride Bi_2Te_3 . Generally, mainly alloys or intermetallics based on elements like Bi, Te, Sb, Pb, Ge, Si etc. are used. However, a large scale commercialization and mass application of these inorganic systems is still not realized mainly because of the following limitations in the materials. Firstly, semiconducting elements such as Bi, Te, Sb and Pb are toxic and not earth-abundant. Secondly, the processing of inorganic materials by methods such as melt-spinning, ball milling, hot pressing etc. is costly in terms of energy and machinery. In addition to this, inorganic systems are severely limited regarding solution processing for large area applications. These challenges make organic materials, which are cheap, abundant, light-weight, flexible and solution-processable attractive

candidates to be explored along with current inorganic materials. Moreover, in case of organic semiconductors, it has been understood that only carriers close to Fermi level (E_F) participate in transport and therefore the Seebeck coefficient is more commonly defined as the average entropy per charge carrier weighted by the contribution of the carrier to conduction.^[144] Therefore, the fundamental equations derived for well-defined solid state semiconductors (**Equations 5 to 7**) need perhaps to be adopted to disordered soft matter semiconductors taking into account their ill-defined DOS, E_F and field and charge density dependent charge carrier mobility. However, there are many features of organic materials that justify a serious consideration and effort to exploit them for thermoelectric applications. The electronic structure of organic semiconductors is highly tunable through molecular design and synthetic approaches. The development of organic semiconducting materials in light emitting diodes, organic solar cells and field-effect transistors has also provided a large number of organic molecules and polymers with high field-effect mobilities.^[60] Considering the fact that the intrinsic electrical conductivity of organic semiconductors is not very high, many recent publications show that semiconducting polymers can be doped to increase their electrical conductivity to a level which is sufficient for practical TE purposes. Therefore, the efficiency of dopants, the mechanism of doping and the stability of the doped state are important fields of research.^[61,145] In addition to the above facts, a very important feature of organic semiconductors is that their thermal conductivity is very low, roughly around $0.3 \text{ W m}^{-1} \text{ K}^{-1}$ for amorphous, isotropic undoped materials.^[144] A good thermoelectric material is described as an electronic crystal and phonon glass^[146,147] and the thermal conductivity of organic semiconductors, particularly polymers, is closer to a phonon glass in many cases. The effect of this critical parameter for thermoelectrics, have been recently reviewed in detail by Segalman et al. and Crispin et al.^[144,148] However, the lower limits of thermal conductivity and how it changes with doping is not well understood so far in organic thermoelectric materials. These features suggest that organic materials are a very promising material class for thermoelectric applications. Recently, many excellent reviews about the potential of organic materials, for thermoelectric applications were published.^[144,148–154] In the following sections, we discuss the recent progresses in optimization of TE properties of conjugated polymers mainly from the point of view of general chemical design rules for polymers, dopants, doping methods and the chemical and physical features that are potentially correlated with their thermoelectric performance. We start with the TE performance of some of the best known p-type TE polymers and end with a limited number of preliminary studies conducted to evaluate TE performance of some well-known n-type polymers. Similar to the reporting on mobility values, we want to caution the reader when record values of TE parameters and conductivities are reported, we cannot verify these values in this review.

4.2. p-Type Organic Thermoelectric Polymers and Doping Strategies

The history of p-type organic thermoelectrics can be roughly traced back to the discovery of conducting polyacetylene in 1976, and subsequent development of many other conducting

polymers such as PAC, PPy, P3AT, PANI, and PEDOT, termed as first generation of conjugated polymers (see Figure 1). In the 1990s, Nogami et al. showed that iodine-doped, stretch-aligned polyacetylene was highly conductive, with a very high power factor of up to $1350 \mu\text{W m}^{-1} \text{K}^{-2}$, but the polymer suffered from poor environmental stability.^[155] Polyaniline, another very interesting p-type conducting polymer was studied by Mateeva et al. and Toshima et al.^[156,157] Stretch-aligned polyaniline doped with camphorsulfonic acid offers very good environmental stability, but low power factors.^[156] After these early studies, the progress of p-type polymers for TE applications remained modest for the next two decades, because of the lack of processable, environmentally stable doped materials with high power factors. However, tremendous advancements were made in developing new p-type polymers for LEDs, solar cells and OFETs. Some important examples of which are poly(3-alkylthiophenes) P3AT, and poly(3,4-ethylenedioxythiophenes) PEDOT. Additionally, copolymers employing the D-A strategy like poly(diketopyrrolopyrroles) PDPPs or poly(thieno[3,4-c]-pyrrole-4,6-dione) PTPDs led to novel second-generation p-type polymers. These p-type polymers offered a better solubility, stability, an improved microstructure, higher molecular weights and a good processability. At present, these are the most studied candidates for donor materials in the entire field of organic thermoelectrics. The recent advances for each class are reviewed and discussed below. PEDOT is one of the most important conjugated polymers regarding its practical use in semiconductor devices. It is solution processable from dispersions, environmentally stable, and conductivities beyond $6000 \text{ S} \cdot \text{cm}^{-1}$ can be achieved with optimized doping methods.^[16] Here, we discuss some of the important methods used to control the oxidation level in PEDOT systems leading to the highest thermoelectric performances. Doping in PEDOT systems is achieved by mixing the polymer with Brønsted-acids such as poly(styrene sulfonic acid) (PSS) or p-toluenesulfonic acid (Tos). For example, the monomer ethylenedioxythiophene (EDOT) can be polymerized oxidatively in water in the presence of PSS. In this case PEDOT:PSS forms a core-shell like particle structure, containing the conductive PEDOT in the core and the polyanionic PSS forming an isolating shell. Most researchers use commercial PEDOT:PSS where the ratio PEDOT and PSS is pre-set. In this case, the polymer's conductivity can be tuned by thinning out the isolating PSS shell, e.g. by dipping processed films in an appropriate solvent. Some of these approaches are described in the following, and the techniques are referred to as dedoping. Bubnova et al. tuned the oxidation level of PEDOT:Tos **P6** (see Figure 5) by exposing the polymer to the vapor of the reducing agent tetrakis(dimethylamino)ethylene TDAE for different times.^[158] TDAE can accept electrons from oxidized PEDOT and forms a salt with tosylate anions. The salt can be removed by rinsing the films with water. Thereby, the oxidation level was varied between 9 % and 36 %. At the optimal oxidation level of 22 %, a power factor of $3 \mu\text{W m}^{-1} \text{K}^{-2}$ was achieved, resulting in a ZT of 0.25 at room temperature. Park et al. produced highly conductive PEDOT films by the polymerization of EDOT, which were then used as electrodes.^[159] By applying a potential, the oxidation level of the deposited polymer could be adjusted. The optimized films exhibited

an electrical conductivity of $\sigma \approx 900 \text{ S cm}^{-1}$ and a Seebeck coefficient of $\alpha \approx 60 \text{ } \mu\text{V K}^{-1}$, leading to an unprecedented high power factor of $1270 \text{ } \mu\text{W m}^{-1} \text{ K}^{-2}$ and a record high ZT value of 1.02.

Similar to other conductive polymers, a large fraction of highly conducting domains is desirable in PEDOT. Kim et al. have shown that reducing the volume fraction of the dopant in PEDOT:PSS **P7** films leads to an increase in both the Seebeck coefficient and the electrical conductivity.^[160] By immersing spin-coated films in ethylene glycol, inactive (i.e. un-ionized) dopant molecules were extracted from the films. By that, the thickness of the insulating PSS shells around conducting PEDOT-islands is reduced, facilitating charge-tunneling between the conductive domains. Furthermore, by lowering the fraction of non-ionized dopant molecules within the matrix, the charge carrier mobility is increased, which further improves the electrical conductivity. Altogether, a maximum Seebeck coefficient of $S \approx 70 \text{ } \mu\text{V K}^{-1}$ and an electrical conductivity of 900 S cm^{-1} were achieved, which led to a PF of $470 \text{ } \mu\text{W m}^{-1} \text{ K}^{-2}$ in the optimized system. Therefore, a ZT value of 0.42 at room temperature, which is among the highest reported for this class of polymers could be reported. Similarly, Fan et al.^[15] used a sequential post-treatment of PEDOT:PSS films with sulphuric acid and sodium hydroxide solutions. PSS is removed with sulphuric acid in the first step, as evidenced by UV spectra. This decreased the fraction of insulating PSS-shells and improved the charge carrier mobility. The treatment with NaOH in the second step causes an ion exchange between PSS^- and OH^- anions and dedoping, leading to an increased Seebeck coefficient due to the decrease in the charge carrier density. A superposition of the observed effects leads to high thermoelectric figures, i.e. a Seebeck coefficient of $S = 39 \text{ } \mu\text{V K}^{-1}$, an electrical conductivity of $\sigma = 2170 \text{ S cm}^{-1}$, and a power factor of $334 \text{ } \mu\text{W m}^{-1} \text{ K}^{-2}$. This corresponds to a figure of merit of $\text{ZT} \approx (0.4 \pm 0.1)$. It is well known that the transport properties of semiconducting polymers are driven by the polymers structure formation. Polymers with a high crystallinity generally exhibit higher charge carrier mobilities and electrical conductivities. The addition of high boiling solvents (such as DMF or DMSO) as additives, leads to a slow evaporation of the solvent and gives the polymer more time to crystallize. Petsagkourakis et al. chose PEDOT:Tos, which showed higher Seebeck coefficients as compared to PEDOT:PSS, and studied the effect of several solvent additives on the thermoelectric properties of PEDOT:Tos thin films.^[161] They prepared PEDOT:Tos by in situ polymerization of EDOT with Iron(III)-4-toluenesulfonate in the presence of different co-solvents such as ethylene glycol, toluene, chlorobenzene, DMF, DMSO etc., based on a gradual increase of the boiling points. Depending on the boiling point of the chosen co-solvent which acts as a plasticizer, the co-solvent resides in the film for different times, allowing for longer or shorter reorganization times which have an impact on the crystallization. As the oxidation level of the polymer remains unaltered, the Seebeck coefficient was not affected by this method. However, the in-plane mobility and likewise the electrical conductivity increased with a higher boiling point of the co-solvent. Via this route, the electrical conductivity of pristine PEDOT (no co-solvent) was increased from $\sigma = 230 \text{ S cm}^{-1}$ to $\sigma = 640 \text{ S cm}^{-1}$ with DMF. With a Seebeck coefficient of $S = 35 \text{ } \mu\text{V K}^{-1}$, the power factor

increased threefold, from $25 \mu\text{W m}^{-1}\text{K}^{-2}$ to $78.5 \mu\text{W m}^{-1}\text{K}^{-2}$. Another widely used class of polymers are poly(3-alkylthiophene)s, which provide very good solubility in organic solvents. Due to the electron-rich nature of the thiophene unit, P3HT and the more rigid PBTBT **P18** have high HOMO energy levels, and form a well aligned redox combination with many dopants. The optimization of the PF of P3HT by doping with e.g. F_4TCNQ or Iron(III) salts is well studied and generally successful. Besides that, it is also known that the structural order and crystallinity of the polymer strongly influences the TE performance, i.e. more ordered systems show better TE properties.^[162] By utilizing doping, the structural order of the polymer film can be altered by the processing method of the dopant and polymer, or by modifying the sidechains of the respective polymer. It is accepted for P3HT, that mixing the polymer and the dopant in the casting-solution (“co-processing”), results in a lower electrical conductivity ($\sigma \approx 0.1\text{-}1 \text{ S cm}^{-1}$) compared to sequential doping, i.e. immersing a cast film into a dopant-solution or exposing the film to a dopant-vapor ($\sigma \approx 100 \text{ S cm}^{-1}$).^[163-165] Due to the formation of aggregates of the polymer and the dopant-anion, the molecular order of the polymer is disturbed, hence the charge transport is impeded. Hynynen et al. recently have shown that by increasing the degree of crystallinity in P3HT via processing from different solvents, the electrical conductivity is raised by one order of magnitude, while keeping the Seebeck coefficient almost constant ($\sigma = 0.7 \text{ S cm}^{-1} / S = 51 \mu\text{V K}^{-1}$ vs. $\sigma = 12.7 \text{ S cm}^{-1} / S = 46 \mu\text{V K}^{-1}$).^[166] This is explained by an increased fraction of crystalline domains within the film, where the charge carrier transport is improved compared to less ordered amorphous domains. Because of the relationship of $\sigma = \mu e N$, the electrical conductivity is improved due to higher mobility, and not an increased charge carrier density, which would deteriorate the Seebeck coefficient. An emerging tool to increase the dopants compatibility with the host polymer is by replacing of nonpolar alkyl sidechains with more polar oligoethylene glycol sidechains. This enhances the compatibility of semiconductor/dopant pairs.^[167] Kroon et al. could show, that by substituting solubilizing hexyl sidechains of a polythiophene with polar tetraethylene glycol sidechains (p(g₄2T-T) **P5**), two things were achieved:^[163] The polymer became processable from polar solvents, which also offers good solubility for common dopants like F_4TCNQ or 2,3-dichloro-5,6-dicyanobenzoquinone “DDQ”. The compatibility of the polymer and the dopant was increased, thus preventing aggregation in solution. Therefore, the electrical conductivity of the co-processed p(g₄2T-T) was as high as in the sequentially doped P3HT control-sample. Additionally, due to the enhanced compatibility of polymer and dopant, the thermal stability was claimed to be increased, i.e. the sublimation of the dopant out of the film was reduced.^[163] Regarding the long-term and thermal stability of doped films, the same group showed that acid doping of the same polymer results in equally high conductivity values, which were stable over time and at elevated temperatures.^[168] The sulfonic acid derivatives 4-toluensulfonic acid, 4-ethylbenzylsulfonic acid, 4-dodecylbenzyl-sulfonic acid, 1,3-propanedisulfonic acid and bis(trifluoromethane)sulfonimide were used to dope p(g₄2T-T). It was shown that the electrical conductivity was increased to $\sigma \approx 10^2 \text{ S cm}^{-1}$ regardless of the used acid, but the most stable doping was obtained for propanedisulfonic acid which retained its initial conductivity

for 20 h at 120 °C, or six months at ambient conditions. The decline of the conductivity upon heating was due to acid-mediated polymer degradation as no sublimation of the dopant was observed by TGA. This is substantially different from doping with molecular redox dopants like tetrafluorotetracyanoquinodimethane (F₄TCNQ). For the first time, Sun et al. demonstrated a simultaneous increase in both, the Seebeck coefficient and the electrical conductivity by modifying the materials density of states through adding a similar polymer poly(3-hexylthiophene) (P3HTT) **P2** to the matrix material P3HT **P1**.^[169] The additive P3HTT, exhibits a slightly lower oxidation potential (HOMO_{P3HT} = -5.2 eV, HOMO_{P3HTT} = -5.05 eV). With this strategy, they obtained a DOS-distribution, where the Fermi level is established by the minor component P3HTT and generated charges are transported via the major component P3HT. Charges were introduced via doping with F₄TCNQ. At P3HTT-concentrations of 8 wt.% and 20 wt.%, both, the Seebeck coefficient, and the electrical conductivity were increased simultaneously. The sample containing 20 wt.% of the additive exhibited the better performance. Similarly, Zuo et al. blended P3HT with PTB7 **P3** or TQ1 **P4**, both having lower lying HOMO levels compared to P3HT.^[170] Even though a regime where both, the Seebeck coefficient and the electrical conductivity increase was not found, they achieved extraordinarily high Seebeck coefficients. With the mixture P3HT_{0.1}:PTB7_{0.9} a Seebeck coefficient of 1100 μV K⁻¹ at an electrical conductivity of 0.3 S m⁻¹ was achieved, resulting in a PF of 0.3 μW K⁻². The mixture (P3HT_{0.05}:TQ1_{0.95}) has shown a Seebeck coefficient of 2000 μV K⁻¹ at an electrical conductivity of 0.03 S m⁻¹ and a PF of 0.1 μW K⁻². These results are remarkable for the reason that such high Seebeck coefficients are usually accompanied by a drastic decrease of the electrical conductivity. Semiconducting polymers other than P3HT and PEDOT are also offering new platforms for TE applications. The influence of solubilizing sidechains in polyfluorene derivatives **P8** was systematically studied by Liang et al.^[171] It was found that the sidechain length had little to no impact on the thermal, mechanical or photophysical properties, but the electrical conductivity decreased for longer sidechains. As the sidechain length does not affect the charge carrier density, the Seebeck coefficient also remains constant, resulting in an increased power factor upon shortening of the sidechain. This was explained by a disrupted interchain packing, leading to a reduced carrier mobility. The highest achieved thermoelectric power factor was PF ≈ 1.7 μW m⁻¹ K⁻². Even though this is not a very high value, the study underlines the importance of structural order.^[171] Jung et al. have shown that DPP-based polymers can be superior to P3HT, when doped with an Iron(III) chloride solution.^[172] Due to the high charge carrier mobility of the studied PDPP3T **P9**, a high conductivity was obtained. The lower amount of dopant which was used also assisted in maintaining a high Seebeck coefficient. A power factor of 276 μW m⁻¹ K⁻² was measured, which was five times higher than for P3HT (56 μW m⁻¹ K⁻²). Furthermore, for PDPP3T, the spectroscopically monitored doping response was linearly correlated with the dopant concentration, indicating that all introduced dopant molecules efficiently take part in doping. This is usually not observed in other polymers. Also, upon doping, the d-spacing in PDPP3T remained constant, whereas in P3HT it increased by 9 % and the crystallinity decreased, which

further impedes charge transport.^[172] Most prior studies have focused on p-type hole conducting materials with conductivities greater than 1000 S cm^{-1} .^[173–176] However, an all organic thermoelectric device requires, complementary n-type polymers which has been difficult due to intrinsic limitations of n-type materials.

4.3. n-Type Organic Thermoelectric Polymers

In the field of n-type conjugated polymers, the main challenge is to obtain stable doped systems with high ZT values. Moreover, the mechanism of doping is not fully understood in many cases. For the selected examples of n-doped n-type polymers here, all the relevant thermoelectric parameters are summarized in **Table 3**. Shi et al. investigated the relationship between the chemical structure and thermoelectric properties of polymers **N14a**, **N14b** and **N14d**, by doping with a hydride transfer dopant 4-(1,3-dimethyl-2,3-dihydro-1H-benzimidazol-2-yl)-N,N-dimethylaniline (N-DMBI) (**Figure 11**).

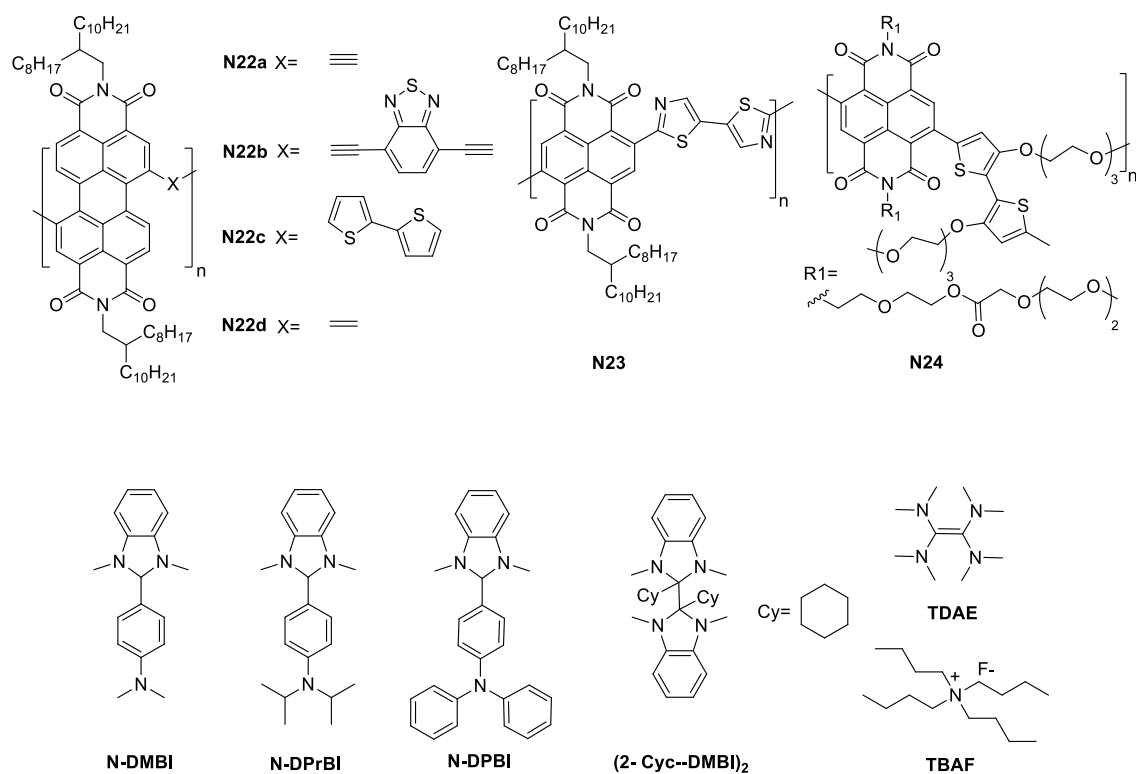


Figure 11. Chemical structures of some n-type TE polymers and some selected n-dopants.

Table 3. Thermoelectric parameters of selected p-type (P) and n-type (N) polymers.

#	Abbreviation	Dopant	σ at PF_{max} [S cm ⁻¹]	S at PF_{max} [$\mu V K^{-1}$]	PF_{max} [$\mu W m^{-1} K^{-2}$]	C_{Dopant} at σ_{max}	Ref.
P1	P3HT	F ₄ TCNQ	48	85 ± 10	0.3	-	[230]
P5	P(g ₄ 2T-T)	F ₄ TCNQ/DDQ	120	-	-	10	[154]
P6	PEDOT:Tos	Tos/TDAE	70	215	324	22 mol%	[158]
P7	PEDOT:PSS	PSS/EG	70	900	470	-	[160]
P8	F6BT	FeCl ₃	1.5	100	1.7	-	[171]
P9	PDPP3T	FeCl ₃	52 ± 3	217 ± 8	247 ± 21	-	[172]
N3	P(NDIODT2)	N-DMBI	0.008	-850 ± 90	0.6	9 mol%	[177]
N3	P(NDIODT2)	N-DPBI	0.004	-770 ± 80	0.2	9 mol%	[177]
N3	P(NDIODT2)	N-DiPrBI	7 · 10 ⁻³	-32 ± 15	1.1 · 10 ⁻³	-	[186]
N9	BBL	TDAE	0.42	-101	0.43	-	[187]
N14a	BDPPV	N-DMBI	0.26	-323	2	10 wt%	[130]
N14b	FBDPPV	N-DMBI	6	-213	28	7 wt%	[130]
N14b	FBDPPV	N-DMBI	6.23 ± 0.71	-210 ± 20	25.5 ± 2.0	5 wt%	[178]
N14d	CIBDPPV	TBAF	0.62	-	-	-	[179]
N14d	CIBDPPV	N-DMBI	3.5	-221	18	7 wt%	[130]
N22a	P(PDI2OD-A)	(2-CycDMBI) ₂	0.45	-	-	-	[181]
N22b	P(PDI2OD-DEBT)	(2-CycDMBI) ₂	0.07	-	-	-	[181]
N22c	P(PDI2OD-T2)	(2-CycDMBI) ₂	1 · 10 ⁻³	-	-	-	[181]
N22d	P(PDI2OD-E)	(2-CycDMBI) ₂	2 · 10 ⁻³	-	-	-	[181]
N23	P(NDI2OD-Tz2)	TDAE	0.06	-447 ± 15	1.5	-	[181]
N23	P(NDI2OD-Tz2)	N-DMBI	7 · 10 ⁻³	NA	NA	NA	[181]
N24	p(gNDI-gT2)	N-DMBI	0.1	-200	0.4	10 mol%	[185]

They revealed that all three polymers are capable of an effective doping with N-DMBI in solution. In conjugated polymers, the introduction of halogen atoms to the polymer backbones has a dramatic influence not only on the mobilities, but also on the doping levels. The highest conductivity of **N14a** is 0.26 S cm⁻¹, whereas **N14b** and **N14d** show much higher conductivities around 4 S cm⁻¹. Most notably, an efficient doping process in **N14b** leads to electrical conductivities of 14 S cm⁻¹ and power factors up to 28 $\mu W m^{-1} K^{-2}$, which is the highest PF that has been reported for solution processable n-type conjugated polymers.^[127] Currently, most research efforts in this field are directed towards reporting a high performance, or high TE parameters. However, the fundamental knowledge of the polymer structure, molecular packing, morphology evolution of film formation with added dopants and its impact on the free carrier concentration, conductivity and Seebeck coefficients etc. are in very early stages of understanding. In this context, **N14b** has been studied with GIWAXS to

probe the molecular packing and orientation in the pure film as well as those with different amounts of N-DMBI. Compared to the highly crystalline n-type conjugated polymer P(NDIOT2),^[177] the pure **N14b** film showed relatively weak diffraction peaks and thus lower a molecular packing. A small amount of N-DMBI induces a more ordered face-on molecular packing of **N14a**, which could be the reason for better charge carrier transport in doped films. Further, an AFM analysis showed that all films with small amounts of dopant (lower than 7 wt%) had a smooth surface morphology similar to the undoped film. When the amount of dopant exceeds 15 wt%, the film surface becomes rough, due to aggregation of the dopant. These results indicate that the miscibility threshold for N-DMBI in **N14b** must be between 7 wt% and 15 wt%. When the amount of the dopant exceeds 7 wt%, the dopant is negatively influencing the packing of the polymer chains and excess dopant-aggregates form on the top surface of the thin films.^[178] Recently, Zhao et al. demonstrated that small-anion salts such as tetrabutylammonium fluoride (TBAF), which is air-stable and solution-processable can also be employed as an effective n-dopant for BDPPV polymers such as **N14d** and enhances the conductivity up to 0.62 S cm^{-1} . They also measured a Seebeck coefficient of $-99.2 \text{ } \mu\text{V K}^{-1}$, and a power factor of $0.63 \text{ } \mu\text{W m}^{-1} \text{ K}^{-2}$ in air.^[179] Yao et al. have also reviewed some of these BDPPV polymers and other polymer composites.^[180] NDI based polymers, mainly **N3**, are the most studied n-type polymers for TE applications. Schlitz et al. examined the thermoelectric potential of this highly soluble, air stable, high mobility polymer by doping with the hydride transfer dopants N-DMBI and 4-(1,3-dimethyl-2,3-dihydro-1H-benzimidazol-2-yl)-N,N-diphenylaniline (N-DPBI).^[177] For **N3** with 9 mol% of N-DMBI mixed in solution, a Seebeck coefficient of $-850 \text{ } \mu\text{V K}^{-1}$ and a conductivity of $8 \cdot 10^{-3} \text{ S cm}^{-1}$ were measured, resulting in a PF of $0.6 \text{ } \mu\text{W m}^{-1} \text{ K}^{-2}$. Similarly, at the same concentration of N-DPBI, mixed in solution, a Seebeck coefficient of $-770 \text{ } \mu\text{V K}^{-1}$ and a conductivity of $4 \cdot 10^{-3} \text{ S cm}^{-1}$, and a PF of $0.2 \text{ } \mu\text{W m}^{-1} \text{ K}^{-2}$ were observed. From AFM, GIWAXS and TEM studies, the authors estimated that only one in a hundred molecules mixed with P(NDIOT-T2) **N3** in solution ultimately contribute a mobile electron to the conduction band of the polymer. The low conductivity is a result of the low solubility of N-DMBI and N-DPBI. Dopant aggregates are formed on the surface but the polymer morphology remains largely unchanged. Nonetheless, **N3** exhibits relatively high Seebeck coefficients, which indicate that novel doping strategies with a better polymer-dopant miscibility may significantly improve the carrier concentrations needed for most applications.^[177] It has been proposed that in order to obtain highly conducting n-type polymers, a good compatibility of the polymer with the dopant is required and, therefore, structural modifications of the polymer backbone or dopant are being looked upon as efficient strategies for increased miscibility. In an important contribution from Naab et al. the electrical conductivities of several conjugated copolymers based on PDI **A7** and NDI **A8** copolymerized with ethynylene, ethylene, or bithiophene and n-doped with the dimeric dopant (2-Cyc-DMBI)₂ have been reported.^[181] Their results indicate that n-doped polymers do not necessarily have to follow the same design rules as for OFET applications, where the regioregularity of the backbone and the crystallinity are beneficial for high charge carrier

mobilities. Amorphous polymers distinctly lacking donor–acceptor character can be highly conductive after solution n-doping, like in the cases of the ethynylene-linked polymers **N22a** (0.4 S cm^{-1}) and **N22b** (0.07 S cm^{-1}), rather than the donor-acceptor polymers **N22c** (0.001 S cm^{-1}) and **N3** (0.004 S cm^{-1}). **N22d**, only had a maximum conductivity of 0.002 S cm^{-1} , which suggested that polymers used for n-doping applications should be designed to have long polaron delocalization lengths in the doped phase. Wang et al. reported **N23** consisting of a 5,5'-di(1,3-thiazolyl) (Tz2) moiety linked to a NDI core at the C-2/C-2' positions which was n-doped with TDAE.^[182] A maximum PF of $1.5 \mu\text{W m}^{-1} \text{ K}^{-2}$ and a Seebeck coefficient of $-(447 \pm 15) \mu\text{V K}^{-1}$ ($\sigma \approx 0.06 \text{ S cm}^{-1}$) were observed. However, solution doping of **N23** with N-DMBI affords a conductivity of only 0.007 S cm^{-1} , which is ascribed to poor the miscibility of the DMBI in polymer matrix. The authors suggest that engineering of alkyl sidechains may enhance the miscibility and dopant-polymer crystallinity. An emerging tool to increase a dopant's compatibility is the replacement of nonpolar alkyl sidechains with more polar oligoethylene glycol sidechains, which enhances the compatibility of semiconductor/dopant pairs.^[167] This approach has shown an increased doping efficiency in P3HT^[163] and fullerenes^[183,184] for doping with F_4TCNQ and N-DMBI, respectively. Kiefer et al. studied the n-doping of the polar naphthalenediimide-bithiophene copolymer p(gNDI-gT2) **N24** with oligoethylene glycol-containing sidechains on both the NDI acceptor- and the bithiophene donor unit. A comparison with the non-polar P(NDIOD-T2) indicates that polar ethylene glycol sidechains largely suppress the aggregation of N-DMBI up to a concentration of 20 mol%, which indicates a better polymer-dopant miscibility. **N24** doped with 20 mol% of N-DMBI gives an electron mobility of $0.2 \text{ cm}^2 \text{ V}^{-1} \text{ s}^{-1}$, and a charge carrier density of about $1.0 \cdot 10^{19} \text{ cm}^{-3}$. This polymer doped with 10 mol% N-DMBI reaches an electrical conductivity of $10^{-1} \text{ S cm}^{-1}$, and a Seebeck coefficient of $-200 \mu\text{V K}^{-1}$, which results in a power factor of $0.4 \mu\text{W m}^{-1} \text{ K}^{-2}$.^[185] Saglio et al. recently studied the n-type doping of the NDI copolymer **N3** with a series DMBI derivatives with different linear and branched alkyl chains. They suggest that increasing the length and branching in the alkyl substituent, can improve the miscibility between the dopant and the polymer. 4-(1,3-dimethyl-2,3-dihydro-1H-benzo[d]imidazol-2-yl)-N,N-diisopropylaniline (DiPrBI) doped samples were reported to achieve an electrical conductivity of $7.2 \cdot 10^{-3}$, a Seebeck coefficient of $-32 \pm 15 \mu\text{V K}^{-1}$ and PF of $1.1 \cdot 10^{-3} \mu\text{W m}^{-1} \text{ K}^{-2}$ at 363 K.^[186] Wang et al. showed that ladder-type - "torsion-free" - conducting polymers (e.g., polybenzimidazobenzophenanthroline (BBL)) can outperform donor–acceptor polymers (e.g., P(NDI2OD-T2)), in terms of the conductivity and thermoelectric power factor. BBL was doped with TDAE and its thermoelectrics properties were studied. In the undoped state, the polymer shows an electrical conductivity of about $10^{-7} \text{ S cm}^{-1}$. After exposure to TDAE vapor, the electrical conductivity dramatically increases, reaching a value as high as $1.7 \pm 0.6 \text{ S cm}^{-1}$. This is almost seven orders of magnitude higher than for undoped BBL and about three orders of magnitude higher than for P(NDI2OD-T2). The reason for the higher electrical conductivity may be the larger polaron delocalization length of BBL in comparison to P(NDI2OD-T2). For BBL, a maximum PF of $0.43 \mu\text{W m}^{-1} \text{ K}^{-2}$ is obtained, which is one order of magnitude higher

than that of P(NDI2OD-T2) ($0.013 \mu\text{W m}^{-1} \text{K}^{-2}$). It is suggested that ladder-type conducting polymers, such as BBL, can reach conductivity values that are three orders of magnitude higher than those of distorted donor–acceptor polymer. This can be an important design rule for optimizing the thermoelectric properties of conducting polymers.^[187]

5. Conjugated Polymers for Bioelectronics

5.1. General Introduction to Bioelectronics: OFET vs. OECT

The term bioelectronics covers all kinds of electronic recording of interactions within biomolecular systems or between a biomolecular system and external stimuli. Even though many such interactions can be easily detected by optical methods, the electronic/electrical transducing of signals is very promising, especially using a transistor geometry. Since biosystems are soft matter, organic semiconductors which swell in aqueous ambient are more compatible with them than their inorganic counterparts as transducers and are even predestined for such applications. But there are some challenges in the structural design of highly efficient semiconductor polymers for bioelectronics applications, which will be discussed below. In order to sense biomolecules and their interactions, a classical OFET can be gated with an electrolyte. By applying a potential, the electrolyte is polarized and the transistor can be turned ON or OFF. If the semiconducting polymer cannot be penetrated by the electrolyte, such a so-called, electrochemically-gated organic field-effect transistor (EGOFET) behaves similarly to an OFET through the formation of a conducting channel at the interface between the electrolyte and the semiconductor. The comparably high capacitance of the electrolytes leads to high drain currents I_{DS} . This makes it possible to operate such a device at a potential below 1 V, which is within the potential window where water is stable.^[188] The EGOFET is distinguished from an organic electrochemical transistor (OECT) in which the semiconductor can be penetrated by the electrolyte.^[189,190] It is assumed in the Bernards model that in such a device the conductivity is changed in the whole volume of the channel due to penetration of the electrolyte into the semiconductor.^[191] This will lead to a higher amplification of the current in comparison to an EGOFET. The performance of an OECT is often measured by the transconductance, which is derived from the slope of the transfer characteristics:

$$g_m = \frac{\partial I_{DS}}{\partial V_G} \quad (10)$$

From this, the **Equation 11** can be derived for the transconductance in the saturation regime:^[192]

$$g_m = \frac{wd}{L} \mu C^* (V_{Th} - V_G) \quad (11)$$

This equation is similar to the transconductance of a classical FET; with the difference that the thickness of semiconductor d and the capacitance per volume C^* replace the capacitance of the dielectric. An optimal OECT material, therefore, fulfills several prerequisites. In a stable device the material must, firstly, be reduced/oxidized at low potential and form a stable

anion/cation. Secondly, it must be able to interact with the aqueous electrolyte or swell in its presence. The ion uptake follows an electrochemical doping of the conjugated polymer. Therefore, the voltage at the gate controls the redox state of the polymer and its conductivity.^[190] A high uptake of the electrolyte will lead to a higher volume and, therefore, according to Bernard's model, a large channel because the capacitance depends on the thickness of the active material. Consequently, a good material for OECTs must be a good swellable material which can be oxidized/reduced at voltages below 1V and has a high capacitance. The ionic conductivity, which facilitates a good interaction with the aqueous biological medium, requires polymers with high polarity and it could be shown that the hydrophilicity of a conjugated polymer's sidechains has a great influence on the performance of OECT. For hydrophobic sidechains the transistor is operated in the field-effect regime (EGOFET), whereas ethylene glycol sidechains facilitate the additional electrochemical regime (OECT).^[193] The semiconductor polymers should also exhibit an excellent charge carrier mobility in an aqueous medium or biological environment, since the product of the an electronic charge carrier mobility and the capacitance of the material determines the transconductance, which is used to benchmark new materials.^[194]

5.2. Conducting Polymers and Conjugated Polymers for Bioelectronics: OECTs in Depletion or Accumulation Mode

Depending on whether the semiconductor is already in a doped state (conducting) or in its pristine state (non-conducting), the OECT can be driven in depletion mode or in accumulation mode, respectively. Until now the most widely used polymer in OECT applications for depletion mode, is poly(3,4-ethylenedioxy-thiophene) (PEDOT) doped with the water-soluble polyelectrolyte poly(styrene sulfonic acid) (PSS).^[194,195] Due to the commercial availability of PEDOT:PSS and its very high conductivity, it can be considered the benchmark material for OECTs. However, PEDOT is insoluble in common organic solvents, making a controlled synthesis impossible – therefore limiting an insight into structure property relationships. PSS doping makes it possible to disperse PEDOT:PSS in water, which creates new problems. For one, the active material should be water compatible rather than soluble or the film stability has to be ensured by crosslinking with considerable amounts of an insulating material – e.g. 3-(glycidyloxypropyl)trimethoxysilane (GOPS) is frequently employed. Additionally, PSS is highly acidic which negatively influences the long-term stability of the devices.^[196,197] Different dopants have been used to counteract this, usually reducing the charge carrier mobility drastically without having a major effect on the capacitance.^[194] Only in PEDOT:Tos, a tosylate-doped, vapor-phase polymerized PEDOT, the mobility could be retained at an increased capacitance.^[198] A series of novel pristine conjugated polymers was tested in OECTs by Nielsen et al.^[199] In contrast to conducting PEDOT:PSS, these semiconducting materials can be used to fabricate accumulation mode OECTs which do not need to be crosslinked as they are not soluble in water. Different copolymers were synthesized from benzodithiophene, thiophene with tetraethylene glycol sidechains and thiophene. The influence on the device performance

basic hydrolysis a water soluble polyelectrolyte was formed which could be used to fabricate a thin film. A post-modification with dilute acids made the film resistant to aqueous electrolytes and the film could be repeatedly oxidized/reduced. In two subsequent publications it could be shown that water compatibility can be achieved by changing the sidechains without the need of any post-fabrication modifications ultimately leading to PProDot derivative **B4**.^[201,202] Recently, OECTs from PProDot derivatives were reported. The material exhibits a high capacitance and charge carrier mobility and also a high On/Off current ratio which leads to a current amplification that is equivalent to P(2gT-TT).^[203] In contrast to p-type semiconductors, materials for n-type OECTs are very rare and have only been introduced very recently. The challenges in this field – especially the problem of finding a suitable material which is stable in both the oxidized and the reduced form in aqueous medium – have been recently highlighted by Sun et al.^[204] The first electrolyte gated n-type transistor with a polymeric semiconductor was reported by Herlogsson et al.^[205] The authors used a naphthalene diimide bithiophene copolymer (PNDI-T₂) as n-type semiconductor. Due to the high capacitance of the used polyelectrolyte, the transistors could be operated at an extremely low voltage of 0.2 V. In the first report on water-gated OECTs by Giovannitti et al., stable OECTs could be fabricated through the incorporation of oligo ethylene glycol sidechains to a naphthalene diimide bithiophene copolymer P(NDI2OD-T₂) **B5** because the interaction of the glycol with the aqueous media lead to the formation of stable p- and n-doped states.^[206] At the same time Porazzo et al. independently reported the use of PNDI-T₂ and the corresponding biselenophene to fabricate a water-gated n-type OFET.^[207] Recently, the influence of the sidechains for PNDI-T₂ was studied in detail.^[208] Two monomers with either alkyl or glycol sidechains were copolymerized in different ratios leading to copolymers with different glycol contents. While a higher glycol content has a negative effect on the electron mobility there is a strong increase in the material's capacitance which ultimately leads to an increase of the OECTs transconductance. Additionally, a greater uptake of water in the polymer films showed the increased compatibility with the aqueous electrolyte. Aside from the PNDI-T₂ type copolymers there is only one other example of n-type polymers used as active material in an OECT. Sun et al. used the ladder-type BBL **B6** as active material in an OECT and reported a high transconductance and stability of the devices. Additionally, they are also the first to report a complementary circuit – incorporating n- and p-type – solely based on OECTs.^[209]

5.3. Conjugated Polyelectrolytes for Bioelectronics

A large number of conjugated polyelectrolytes mainly based on polyfluorenes have been reported.^[210–212] Here we focus mainly on conjugated polyelectrolytes which were successfully incorporated in electrochemical transistors. Carboxyl-functionalized polythiophene P3CPT **B7** was incorporated as active material in an electrolyte-gated transistor.^[213,214] Laiho et al. could show different modes of operation depending on the applied gate potential. At a low potential current modulation in the field-effect regime was observed. At a higher potential the

transistor operated in the electrochemical regime, i.e., the whole semiconductor layer was doped electrochemically.^[213] Brendel et al. synthesized another polythiophene-based polyelectrolyte with sulfonate groups and tetrabutylammonium (TBA) as counter ion in a controlled manner. By this they could obtain a material which aggregated in solution and subsequently exhibited a charge carrier mobility of $10^{-2} \text{ cm}^2 \text{ V}^{-1} \text{ s}^{-1}$ (measured by SCLC).^[215] This material can be used in accumulation mode OECTs but the device performance is limited by the high solubility of the polymer in water, which makes it necessary to add a high amount of a cross-linker.^[216] In these types of polymers, the importance of the counter ion on the device performance was shown by Schmidt et al. who exchanged the TBA with tetramethylammonium (TMA) and tetraethylammonium (TEA). They could show that for PTHS–TMA **B8** with the smallest cation a better aggregation, a fast interdiffusion of ions and a better recovery from the oxidized state could be observed. This led to an improvement of the transconductance by two orders of magnitude when compared to the TBA analogue. Again the necessary crosslinking in an OECT device negatively affects the performance because the aggregation of PTHS–TMA is reduced.^[217] The PEDOT derivative PEDOT-S **B9** with a sulfonate group attached to the end of an alkyl chain is a good candidate for OECTs due to the high conductivity (12 S cm^{-1}) in thin films.^[218] This was first shown by Hamedi et al., who could fabricate nanowire OECTs with a thin layer of PEDOT-S wrapped around amyloid fibrils.^[219] Similarly, it is also possible to coat silk fibers or DNA with **B9** and fabricate working OECTs.^[220,221] Zeglio et al. also made OECTs from **B9** and investigated the polythiophene derivative PTEBS **B10**.^[222] PEDOT-S is stable in the oxidized form and OECTs with this material function in the depletion mode. In contrast, OECTs fabricated with PTEBS as active material function in the more desired accumulation mode, but the material is not stable against electrochemical oxidation and its conducting properties are poor compared to PEDOT derivatives. The authors could show that by blending both materials they were able to fabricate devices with a transconductance comparable to pure PEDOT-S which functioned in accumulation mode and increased stability. Another interesting idea is the functionalization of a known high mobility donor-acceptor polymer with biocompatible polylysine isomers. Du et al. synthesized copolymers of dithienyl-diketopyrrolopyrrole and thiophene (PDPP3T) and functionalized them with oligolysine to obtain L_m TFA **B11**. Coatings with polylysine are already used to improve cell adhesion and very high charge transport has been observed in diketopyrrolopyrrole (DPP) based polymers. Stable OFETs could be made from the lysinated polymers exhibiting reasonable charge carrier mobilities while showing a good biocompatibility, which was tested by growing neuronal cells on the material.^[223]

6. Conclusion

We summarized the basic design principles of a new generation of conjugated polymers with a vision for novel and challenging applications in thermoelectrics and bioelectronics. The biggest challenge is to adapt the structures for the desired application with particular emphasis on the required ambient and simultaneously maintaining very high charge carrier mobilities. In both applications, the doped state of the polymers plays a crucial role. However,

in the field of doped semiconductor polymers, the efficiency of dopants and the doped structures as such are less broadly studied with respect to their structure, spectral features, uniformity, phase separation and long-term stability. The details of how doping improves charge transport in organic semiconductors is still not entirely understood.^[61,62] In some doped systems, the desired full charge transfer from dopant to organic semiconductor occurs indeed as intended. Often the π -system of the dopant interacts with the organic semiconductor to form a hybrid orbital, and the subsequent charge transfer is only partial.^[145] To avoid this, a steric shielding of the dopant with respect to the host is required while at the same time maintaining sufficient proximity to allow for charge transfer. Nevertheless, even when a full charge transfer via ion pair formation occurs, the probability for this remains below 50 %, requiring comparatively high dopant loadings up to 1 mol% (compared to conventional inorganic semiconductors). To enable good charge transport, even higher dopant loadings up to 50 mol% are used sometimes, even though the probability for the ion pair formation reduces to 1 mol% of the dopant. Additionally, the presence of the dopant has an impact on the film morphology, e.g. the crystallization of the host is often prevented or, in some cases, extended host-dopant aggregate phases are formed or phase segregation of the dopant and the host is induced. Moreover, the poorly shielded coulomb interaction of ionized dopant sites, as well as possibly employed counter-ions, can broaden the DOS, so that, for higher dopant loadings, the conductivity reduces after reaching a maximum. A judicious energy level engineering and selection of dopant-hole conductor pairs is therefore required. For this, the research focus must be to understand the doping mechanisms. Also the stability of the doped state must be improved and the amount of dopant should be decreased in order to create efficient materials for thermoelectrics as well as bioelectronics. The present tendency to incorporate more dopant can be avoided once the entire mechanism of efficient doping with very small amounts of dopant is understood and realized. Further, detailed theoretical descriptions of exact energetics of doped states and their evolution during doping requires more attention. For each kind of doping, the influence on the charge carrier mobility as such needs to be quantified and understood. In general, conjugated polymers, their doped counterparts and conjugated polyelectrolytes offer a big structural platform to tune and adapt polymers for diverse and challenging applications of future technological relevance. The broad property profile varying from high temperature stability (for thermoelectrics) up to stability and compatibility in aqueous media (for bioelectronics) combined with a tunability of the doping level to enable a wide range of conductivities makes these materials predestined for such applications. The feasibility and potential of these materials are already demonstrated, however a thoughtful tailoring of the chemical structures and their doping is necessary to exactly suit the profiles for future applications.

Acknowledgements

The authors acknowledge financial support for research by the Bavarian State Ministry of Sciences, Research and the Arts under “Solar Technologies Go Hybrid” (SolTech) and the Bavarian Polymer Institute (BPI).

Received: December 23, 2018

Revised: February 21, 2019

Published online: March 29, 2019

References

- [1] H. Shirakawa, E. J. Louis, A. G. MacDiarmid, C. K. Chiang, A. J. Heeger, *J. Chem. Soc. Chem. Commun.* **1977**, 0, 578.
- [2] N. Toshima, *Macromol. Symp.* **2002**, 186, 81.
- [3] N. Mateeva, H. Niculescu, J. B. Schlenoff, L. Testardi, *J. Appl. Phys.* **1998**, 83.
- [4] Y. W. Park, E. B. Park, K. H. Kim, C. K. Park, J.-I. Jin, *Synth. Met.* **1991**, 41, 315.
- [5] J. Reichenbach, M. Kaiser, S. Roth, *Phys Rev B* **1993**, 48, 14104.
- [6] A. Ali Benamara, M. Galtier, A. Montaner, *Synth. Met.* **1991**, 41, 45.
- [7] I. Y. Sapurina, M. A. Shishov, in *New Polymers for Special Applications*, Ed. A. De Souza Gomez, InTechOpen, London, UK, **2012**, Ch. 9.
- [8] J.-C. Chiang, A. G. MacDiarmid, *Synth. Met.* **1986**, 13, 193.
- [9] J. Li, X. Tang, H. Li, Y. Yan, Q. Zhang, *Synth. Met.* **2010**, 160, 1153.
- [10] S. P. Armes, *Synth. Met.* **1987**, 20, 365.
- [11] S. V. Lowen, J. D. V. Dyke, *J. Polym. Sci. Part Polym. Chem.* **1990**, 28, 451.
- [12] G. Qi, L. Huang, H. Wang, *Chem. Commun.* **2012**, 48, 8246.
- [13] L. Groenendaal, F. Jonas, D. Freitag, H. Pielartzik, J. R. Reynolds, *Adv. Mater.* **2000**, 12, 481.
- [14] Z. Yu, Y. Xia, D. Du, J. Ouyang, *ACS Appl. Mater. Interfaces* **2016**, 8, 11629.
- [15] Z. Fan, P. Li, D. Du, J. Ouyang, *Adv. Energy Mater.* **2017**, 7, 1602116.
- [16] X. Wang, X. Zhang, L. Sun, D. Lee, S. Lee, M. Wang, J. Zhao, Y. Shao-Horn, M. Dincă, T. Palacios, K. K. Gleason, *Sci. Adv.* **2018**, 4.
- [17] R. Søndergaard, M. Hösel, D. Angmo, T. T. Larsen-Olsen, F. C. Krebs, *Mater. Today* **2012**, 15, 36.
- [18] T.-C. Li, R.-C. Chang, *Int. J. Precis. Eng. Manuf.-Green Technol.* **2014**, 1, 329.
- [19] F. Ely, C. O. Avellaneda, P. Paredez, V. C. Nogueira, T. E. A. Santos, V. P. Mammana, C. Molina, J. Brug, G. Gibson, L. Zhao, *Synth. Met.* **2011**, 161, 2129.
- [20] L. Huang, Z. Hu, K. Zhang, P. Chen, Y. Zhu, *Thin Solid Films* **2015**, 578, 161.
- [21] J. H. Burroughes, D. D. C. Bradley, A. R. Brown, R. N. Marks, K. Mackay, R. H. Friend, P. L. Burns, A. B. Holmes, *Nature* **1990**, 347, 539.
- [22] D. Braun, A. J. Heeger, *Appl. Phys. Lett.* **1991**, 58, 1982.
- [23] N. Sariciftci, D. Braun, C. Zhang, V. Srdanov, A. Heeger, G. Stucky, F. Wudl, *Appl. Phys. Lett.* **1993**, 62, 585.
- [24] N. Sariciftci, L. Smilowitz, A. Heeger, F. Wudl, *Science* **1992**, 258, 1474.
- [25] Z. Bao, A. Dodabalapur, A. J. Lovinger, *Appl. Phys. Lett.* **1996**, 69, 4108.
- [26] H. Sirringhaus, N. Tessler, R. H. Friend, *Science* **1998**, 280, 1741.
- [27] J.-F. Chang, B. Sun, D. W. Breiby, M. M. Nielsen, T. I. Sølling, M. Giles, I. McCulloch, H. Sirringhaus, *Chem. Mater.* **2004**, 16, 4772.
- [28] R. J. Kline, M. D. McGehee, E. N. Kadnikova, J. Liu, J. M. J. Fréchet, *Adv. Mater.* **2003**, 15, 1519.
- [29] C. R. Singh, G. Gupta, R. Lohwasser, S. Engmann, J. Balko, M. Thelakkat, T. Thurn-Albrecht, H. Hoppe, *J. Polym. Sci. Part B Polym. Phys.* **2013**, 51, 943.
- [30] A. Yokoyama, R. Miyakoshi, T. Yokozawa, *Macromolecules* **2004**, 37, 1169.

- [31] E. E. Sheina, J. Liu, M. C. Iovu, D. W. Laird, R. D. McCullough, *Macromolecules* **2004**, *37*, 3526.
- [32] R. H. Lohwasser, M. Thelakkat, *Macromolecules* **2011**, *44*, 3388.
- [33] S. Ludwigs (Ed.), in *Advances in Polymer Science*, Vol. 265, Springer, Berlin-Heidelberg, Germany **2014**.
- [34] K. Yoshino, M. Onoda, Y. Manda, K. Sawada, R. Sugimoto, S. Inoue, *Jpn. J. Appl. Phys.* **1989**, *28*, L138.
- [35] Mahatsekake, C., J. M. Catel, C. G. Andrieu, M. Ebel Et, Y. Mollier, G. Tourillon, *Phosphorus Sulfur Silicon Relat. Elem.* **1990**, *47*, 35.
- [36] M. Heeney, W. Zhang, D. J. Crouch, M. L. Chabiny, S. Gordeyev, R. Hamilton, S. J. Higgins, I. McCulloch, P. J. Skabara, D. Sparrowe, S. Tierney, *Chem. Commun.* **2007**, *0*, 5061.
- [37] E. E. Havinga, W. ten Hoeve, H. Wynberg, *Polym. Bull.* **1992**, *29*, 119.
- [38] J. Roncali, *Macromol. Rapid Commun.* **2007**, *28*, 1761.
- [39] P.-L. T. Boudreault, A. Najari, M. Leclerc, *Chem. Mater.* **2011**, *23*, 456.
- [40] M. Svensson, F. Zhang, S. C. Veenstra, W. J. H. Verhees, J. C. Hummelen, J. M. Kroon, O. Inganäs, M. R. Andersson, *Adv. Mater.* **2003**, *15*, 988.
- [41] X. Guo, A. Facchetti, T. J. Marks, *Chem. Rev.* **2014**, *114*, 8943.
- [42] L. Dou, Y. Liu, Z. Hong, G. Li, Y. Yang, *Chem. Rev.* **2015**, *115*, 12633.
- [43] L. Lu, T. Zheng, Q. Wu, A. M. Schneider, D. Zhao, L. Yu, *Chem. Rev.* **2015**, *115*, 12666.
- [44] W. Li, K. H. Hendriks, M. M. Wienk, R. A. J. Janssen, *Acc. Chem. Res.* **2016**, *49*, 78.
- [45] R. Hildner, A. Koehler, P. Mueller-Buschbaum, F. Panzer, M. Thelakkat, *Adv. Energy Mater.* **2017**, *7*, 1700314.
- [46] A. Köhler, H. Bässler, *Electronic Processes in Organic Semiconductors*, Wiley-VCH, Weinheim, Germany **2015**.
- [47] V. Skrypnichuk, G.-J. A. H. Wetzelaer, P. I. Gordiichuk, S. C. B. Mannsfeld, A. Herrmann, M. F. Toney, D. R. Barbero, *Adv. Mater.* **2016**, *28*, 2359.
- [48] A. Troisi, *Org. Electron.* **2011**, *12*, 1988.
- [49] R. Noriega, J. Rivnay, K. Vandewal, F. P. V. Koch, N. Stingelin, P. Smith, M. F. Toney, A. Salleo, *Nat. Mater.* **2013**, *12*, 1038.
- [50] A. G. Dixon, R. Visvanathan, N. A. Clark, N. Stingelin, N. Kopidakis, S. E. Shaheen, *J. Polym. Sci. Part B Polym. Phys.* **2018**, *56*, 31.
- [51] A. Kokil, K. Yang, J. Kumar, *J. Polym. Sci. Part B Polym. Phys.* **2012**, *50*, 1130.
- [52] J. C. Blakesley, F. A. Castro, W. Kylberg, G. F. A. Dibb, C. Arantes, R. Valaski, M. Cremona, J. S. Kim, J.-S. Kim, *Org. Electron.* **2014**, *15*, 1263.
- [53] N. F. Mott, R. W. Gurney, *Electronic Processes in Ionic Crystals; 1st Edition*, Oxford University Press, Oxford, UK **1940**.
- [54] C. Tanase, E. J. Meijer, P. W. M. Blom, D. M. de Leeuw, *Phys Rev Lett* **2003**, *91*, 216601.
- [55] J. Zaumseil, H. Sirringhaus, *Chem. Rev.* **2007**, *107*, 1296.
- [56] Z. A. Lamport, H. F. Haneef, S. Anand, M. Waldrip, O. D. Jurchescu, *J. Appl. Phys.* **2018**, *124*, 071101.
- [57] J. Zaumseil, H. Sirringhaus, *Chem. Rev.* **2007**, *107*, 1296.
- [58] H. H. Choi, K. Cho, C. D. Frisbie, H. Sirringhaus, V. Podzorov, *Nat. Mater.* **2018**, *17*, 2.
- [59] I. McCulloch, A. Salleo, M. Chabiny, *Science* **2016**, *352*, 1521.
- [60] A. F. Paterson, S. Singh, K. J. Fallon, T. Hodsdon, Y. Han, B. C. Schroeder, H. Bronstein, M. Heeney, I. McCulloch, T. D. Anthopoulos, *Adv. Mater.* **2018**, *30*, 1801079.
- [61] I. Salzmann, G. Heimel, M. Oehzelt, S. Winkler, N. Koch, *Acc. Chem. Res.* **2016**, *49*, 370.
- [62] K. Walzer, B. Maennig, M. Pfeiffer, K. Leo, *Chem. Rev.* **2007**, *107*, 1233.

- [63] M. L. Tietze, J. Benduhn, P. Pahner, B. Nell, M. Schwarze, H. Kleemann, M. Krammer, K. Zojer, K. Vandewal, K. Leo, *Nat. Commun.* **2018**, *9*, 1182.
- [64] A. G. Macedo, C. F. N. Marchiori, I. R. Grova, L. Akcelrud, M. Koehler, L. S. Roman, *Appl. Phys. Lett.* **2011**, *98*, 253501.
- [65] S. Song, Y. Jin, S. H. Park, S. Cho, I. Kim, K. Lee, A. J. Heeger, H. Suh, *J Mater Chem* **2010**, *20*, 6517.
- [66] Y. Chen, H. Tian, D. Yan, Y. Geng, F. Wang, *Macromolecules* **2011**, *44*, 5178.
- [67] J.-H. Kim, J. B. Park, I. H. Jung, A. C. Grimsdale, S. C. Yoon, H. Yang, D.-H. Hwang, *Energy Environ. Sci.* **2015**, *8*, 2352.
- [68] Y. He, W. Wu, G. Zhao, Y. Liu, Y. Li, *Macromolecules* **2008**, *41*, 9760.
- [69] A. J. Moulé, A. Tsami, T. W. Bünnagel, M. Forster, N. M. Kronenberg, M. Scharber, M. Koppe, M. Morana, C. J. Brabec, K. Meerholz, U. Scherf, *Chem. Mater.* **2008**, *20*, 4045.
- [70] C.-C. Ho, C.-A. Chen, C.-Y. Chang, S. B. Darling, W.-F. Su, *J. Mater. Chem. A* **2014**, *2*, 8026.
- [71] J. Yuan, X. Huang, F. Zhang, J. Lu, Z. Zhai, C. Di, Z. Jiang, W. Ma, *J. Mater. Chem.* **2012**, *22*, 22734.
- [72] I. Kang, H.-J. Yun, D. S. Chung, S.-K. Kwon, Y.-H. Kim, *J. Am. Chem. Soc.* **2013**, *135*, 14896.
- [73] G. Conboy, H. J. Spencer, E. Angioni, A. L. Kanibolotsky, N. J. Findlay, S. J. Coles, C. Wilson, M. B. Pitak, C. Risko, V. Coropceanu, J.-L. Brédas, P. J. Skabara, *Mater. Horiz.* **2016**, *3*, 333.
- [74] N. E. Jackson, B. M. Savoie, K. L. Kohlstedt, M. Olvera de la Cruz, G. C. Schatz, L. X. Chen, M. A. Ratner, *J. Am. Chem. Soc.* **2013**, *135*, 10475.
- [75] C. J. Mueller, C. R. Singh, M. Fried, S. Huettner, M. Thelakkat, *Adv. Funct. Mater.* **2015**, *25*, 2725.
- [76] L. Chen, D. Deng, Y. Nan, M. Shi, P. K. L. Chan, H. Chen, *J. Phys. Chem. C* **2011**, *115*, 11282.
- [77] S.-Y. Liu, H.-Y. Li, M.-M. Shi, H. Jiang, X.-L. Hu, W.-Q. Li, L. Fu, H.-Z. Chen, *Macromolecules* **2012**, *45*, 9004.
- [78] C. Kanimozhi, M. Naik, N. Yaacobi-Gross, E. K. Burnett, A. L. Briseno, T. D. Anthopoulos, S. Patil, *J. Phys. Chem. C* **2014**, *118*, 11536.
- [79] J. H. Park, E. H. Jung, J. W. Jung, W. H. Jo, *Adv. Mater.* **2013**, *25*, 2583.
- [80] T. Weller, M. Breunig, C. J. Mueller, E. Gann, C. R. McNeill, M. Thelakkat, *J. Mater. Chem. C* **2017**, *5*, 7527.
- [81] C. Wang, C. J. Mueller, E. Gann, A. C. Y. Liu, M. Thelakkat, C. R. McNeill, *J. Polym. Sci. Part B Polym. Phys.* **2017**, *55*, 49.
- [82] C. J. Mueller, E. Gann, C. R. Singh, M. Thelakkat, C. R. McNeill, *Chem. Mater.* **2016**, *28*, 7088.
- [83] D. J. Crouch, P. J. Skabara, J. E. Lohr, J. J. W. McDouall, M. Heeney, I. McCulloch, D. Sparrowe, M. Shkunov, S. J. Coles, P. N. Horton, M. B. Hursthouse, *Chem. Mater.* **2005**, *17*, 6567.
- [84] D. J. Crouch, P. J. Skabara, M. Heeney, I. McCulloch, S. J. Coles, M. B. Hursthouse, *Chem. Commun.* **2005**, *0*, 1465.
- [85] J. W. Jo, J. W. Jung, H.-W. Wang, P. Kim, T. P. Russell, W. H. Jo, *Chem. Mater.* **2014**, *26*, 4214.
- [86] H. G. Kim, B. Kang, H. Ko, J. Lee, J. Shin, K. Cho, *Chem. Mater.* **2015**, *27*, 829.
- [87] Z. Chen, J. Fang, F. Gao, T. J. K. Brenner, K. K. Banger, X. Wang, W. T. S. Huck, H. Sirringhaus, *Org. Electron.* **2011**, *12*, 461.

- [88] Z. Fei, P. Pattanasattayavong, Y. Han, B. C. Schroeder, F. Yan, R. J. Kline, T. D. Anthopoulos, M. Heeney, *J. Am. Chem. Soc.* **2014**, *136*, 15154.
- [89] T. Weller, K. Rundel, G. Krauss, C. R. McNeill, M. Thelakkat, *J. Phys. Chem. C* **2018**, *122*, 7565.
- [90] P. Cai, Z. Chen, L. Zhang, J. Chen, Y. Cao, *J. Mater. Chem. C* **2017**, *5*, 2786.
- [91] Y. Lee, Y. M. Nam, W. H. Jo, *J. Mater. Chem.* **2011**, *21*, 8583.
- [92] D. M. de Leeuw, M. M. J. Simenon, A. R. Brown, R. E. F. Einerhand, *Synth. Met.* **1997**, *87*, 53.
- [93] T. D. Anthopoulos, G. C. Anyfantis, G. C. Papavassiliou, D. M. de Leeuw, *Appl. Phys. Lett.* **2007**, *90*, 122105.
- [94] T. D. Anthopoulos, F. B. Kooistra, H. J. Wondergem, D. Kronholm, J. C. Hummelen, D. M. de Leeuw, *Adv. Mater.* **2006**, *18*, 1679.
- [95] Z. Bao, A. J. Lovinger, J. Brown, *J. Am. Chem. Soc.* **1998**, *120*, 207.
- [96] H. E. Katz, A. J. Lovinger, J. Johnson, C. Kloc, T. Siegrist, W. Li, Y.-Y. Lin, A. Dodabalapur, *Nature* **2000**, *404*, 478.
- [97] B. A. Jones, M. J. Ahrens, M.-H. Yoon, A. Facchetti, T. J. Marks, M. R. Wasielewski, *Angew. Chem. Int. Ed.* **2004**, *43*, 6363.
- [98] R. Schmidt, M. M. Ling, J. H. Oh, M. Winkler, M. Könemann, Z. Bao, F. Würthner, *Adv. Mater.* **2007**, *19*, 3692.
- [99] J. H. Oh, S.-L. Suraru, W.-Y. Lee, M. Könemann, H. W. Höffken, C. Röger, R. Schmidt, Y. Chung, W.-C. Chen, F. Würthner, Z. Bao, *Adv. Funct. Mater.* **2010**, *20*, 2148.
- [100] M. Chikamatsu, A. Itakura, Y. Yoshida, R. Azumi, K. Yase, *Chem. Mater.* **2008**, *20*, 7365.
- [101] H. T. Nicolai, M. Kuik, G. a. H. Wetzelaer, B. de Boer, C. Campbell, C. Risko, J. L. Brédas, P. W. M. Blom, *Nat. Mater.* **2012**, *11*, 882.
- [102] T. Lei, J.-H. Dou, X.-Y. Cao, J.-Y. Wang, J. Pei, *J. Am. Chem. Soc.* **2013**, *135*, 12168.
- [103] Z. Yan, B. Sun, Y. Li, *Chem. Commun.* **2013**, *49*, 3790.
- [104] T. Lei, J.-H. Dou, X.-Y. Cao, J.-Y. Wang, J. Pei, *Adv. Mater.* **2013**, *25*, 6589.
- [105] J. D. Yuen, F. Wudl, *Energy Environ. Sci.* **2013**, *6*, 392.
- [106] F. Würthner, M. Stolte, *Chem. Commun.* **2011**, *47*, 5109.
- [107] H. A. M. van Mullekom, J. a. J. M. Venkemens, E. W. Meijer, *Chem. Commun.* **1996**, *0*, 2163.
- [108] W. Zhang, J. Smith, S. E. Watkins, R. Gysel, M. McGehee, A. Salleo, J. Kirkpatrick, S. Ashraf, T. Anthopoulos, M. Heeney, I. McCulloch, *J. Am. Chem. Soc.* **2010**, *132*, 11437.
- [109] J. D. Yuen, J. Fan, J. Seifert, B. Lim, R. Hufschmid, A. J. Heeger, F. Wudl, *J. Am. Chem. Soc.* **2011**, *133*, 20799.
- [110] R. Stalder, J. Mei, J. Subbiah, C. Grand, L. A. Estrada, F. So, J. R. Reynolds, *Macromolecules* **2011**, *44*, 6303.
- [111] F. Grenier, P. Berrouard, J.-R. Pouliot, H.-R. Tseng, A. J. Heeger, M. Leclerc, *Polym. Chem.* **2013**, *4*, 1836.
- [112] J. Lee, A.-R. Han, H. Yu, T. J. Shin, C. Yang, J. H. Oh, *J. Am. Chem. Soc.* **2013**, *135*, 9540.
- [113] M. J. Cho, J. Shin, S. H. Yoon, T. W. Lee, M. Kaur, D. H. Choi, *Chem. Commun.* **2013**, *49*, 7132.
- [114] B. Sun, W. Hong, Z. Yan, H. Aziz, Y. Li, *Adv. Mater.* **2014**, *26*, 2636.
- [115] X. Guo, M. D. Watson, *Org. Lett.* **2008**, *10*, 5333.
- [116] Z. Chen, Y. Zheng, H. Yan, A. Facchetti, *J. Am. Chem. Soc.* **2009**, *131*, 8.
- [117] H. Yan, Z. Chen, Y. Zheng, C. Newman, J. R. Quinn, F. Dotz, M. Kastler, A. Facchetti, *Nature* **2009**, *457*, 679.

- [118] K. Nakano, M. Nakano, B. Xiao, E. Zhou, K. Suzuki, I. Osaka, K. Takimiya, K. Tajima, *Macromolecules* **2016**, *49*, 1752.
- [119] J. T. E. Quinn, J. Zhu, X. Li, J. Wang, Y. Li, *J. Mater. Chem. C* **2017**, *5*, 8654.
- [120] M. J. Sung, A. Luzio, W.-T. Park, R. Kim, E. Gann, F. Maddalena, G. Pace, Y. Xu, D. Natali, C. de Falco, L. Dang, C. R. McNeill, M. Caironi, Y.-Y. Noh, Y.-H. Kim, *Adv. Funct. Mater.* **2016**, *26*, 4984.
- [121] X. Zhan, Z. Tan, B. Domercq, Z. An, X. Zhang, S. Barlow, Y. Li, D. Zhu, B. Kippelen, S. R. Marder, *J. Am. Chem. Soc.* **2007**, *129*, 7246.
- [122] X. Zhan, Z. Tan, E. Zhou, Y. Li, R. Misra, A. Grant, B. Domercq, X.-H. Zhang, Z. An, X. Zhang, S. Barlow, B. Kippelen, S. R. Marder, *J. Mater. Chem.* **2009**, *19*, 5794.
- [123] S. Huettner, M. Sommer, M. Thelakkat, *Appl. Phys. Lett.* **2008**, *92*, 093302.
- [124] A. Babel, S. A. Jenekhe, *J. Am. Chem. Soc.* **2003**, *125*, 13656.
- [125] M. M. Durban, P. D. Kazarinoff, C. K. Luscombe, *Macromolecules* **2010**, *43*, 6348.
- [126] Y. Shi, H. Guo, M. Qin, J. Zhao, Y. Wang, H. Wang, Y. Wang, A. Facchetti, X. Lu, X. Guo, *Adv. Mater.* **2018**, *30*, 1705745.
- [127] Z. Yuan, B. Fu, S. Thomas, S. Zhang, G. DeLuca, R. Chang, L. Lopez, C. Fares, G. Zhang, J.-L. Bredas, E. Reichmanis, *Chem. Mater.* **2016**, *28*, 6045.
- [128] J. Scheirs (Ed), in *Modern Fluoropolymers: High Performance Polymers for Diverse Applications*, Wiley, New York, USA **1997**.
- [129] T. Lei, X. Xia, J.-Y. Wang, C.-J. Liu, J. Pei, *J. Am. Chem. Soc.* **2014**, *136*, 2135.
- [130] K. Shi, F. Zhang, C.-A. Di, T.-W. Yan, Y. Zou, X. Zhou, D. Zhu, J.-Y. Wang, J. Pei, *J. Am. Chem. Soc.* **2015**, *137*, 6979.
- [131] Y.-Q. Zheng, T. Lei, J.-H. Dou, X. Xia, J.-Y. Wang, C.-J. Liu, J. Pei, *Adv. Mater.* **2016**, *28*, 7213.
- [132] G.-S. Ryu, Z. Chen, H. Usta, Y.-Y. Noh, A. Facchetti, *Mrs Commun.* **2016**, *6*, 47.
- [133] K. Kranthiraja, D. X. Long, V. G. Sree, W. Cho, Y.-R. Cho, A. Zaheer, J.-C. Lee, Y.-Y. Noh, S.-H. Jin, *Macromolecules* **2018**, *51*, 5530.
- [134] Z. Chen, W. Zhang, J. Huang, D. Gao, C. Wei, Z. Lin, L. Wang, G. Yu, *Macromolecules* **2017**, *50*, 6098.
- [135] T. Lei, J.-Y. Wang, J. Pei, *Chem. Mater.* **2014**, *26*, 594.
- [136] J. Mei, Z. Bao, *Chem. Mater.* **2014**, *26*, 604.
- [137] B. A. Jones, A. Facchetti, M. R. Wasielewski, T. J. Marks, *J. Am. Chem. Soc.* **2007**, *129*, 15259.
- [138] H. E. Katz, J. Johnson, A. J. Lovinger, W. Li, *J. Am. Chem. Soc.* **2000**, *122*, 7787.
- [139] B. Kang, R. Kim, S. B. Lee, S.-K. Kwon, Y.-H. Kim, K. Cho, *J. Am. Chem. Soc.* **2016**, *138*, 3679.
- [140] L. E. Bell, *Science* **2008**, *321*, 1457.
- [141] G. J. Snyder, E. S. Toberer, *Nat. Mater.* **2008**, *7*, 105.
- [142] X. Zhang, L.-D. Zhao, *J. Materiomics* **2015**, *1*, 92.
- [143] J. Yang, T. Caillat, *MRS Bull.* **2006**, *31*, 224.
- [144] B. Russ, A. Glauddell, J. J. Urban, M. L. Chabiny, R. A. Segalman, *Nat. Rev. Mater.* **2016**, *1*, 16050.
- [145] I. Salzmann, G. Heimel, S. Duhm, M. Oehzelt, P. Pingel, B. M. George, A. Schnegg, K. Lips, R.-P. Blum, A. Vollmer, N. Koch, *Phys. Rev. Lett.* **2012**, *108*, 035502.
- [146] A. Shakouri, *Annu. Rev. Mater. Res.* **2011**, *41*, 399.
- [147] M. Beekman, D. T. Morelli, G. S. Nolas, *Nat. Mater.* **2015**, *14*, 1182.
- [148] O. Bubnova, X. Crispin, *Energy Environ. Sci.* **2012**, *5*, 9345.
- [149] N. Dubey, M. Leclerc, *J. Polym. Sci. Part B Polym. Phys.* **2011**, *49*, 467.

- [150] T. O. Poehler, H. E. Katz, *Energy Environ. Sci.* **2012**, *5*, 8110.
- [151] Q. Zhang, Y. Sun, W. Xu, D. Zhu, *Adv. Mater.* **2014**, *26*, 6829.
- [152] X. Shi, L. Chen, *Nat. Mater.* **2016**, *15*, 691.
- [153] Y. Chen, Y. Zhao, Z. Liang, *Energy Environ. Sci.* **2015**, *8*, 401.
- [154] R. Kroon, D. A. Mengistie, D. Kiefer, J. Hynynen, J. D. Ryan, L. Yu, C. Müller, *Chem. Soc. Rev.* **2016**, *45*, 6147.
- [155] Y. Nogami, H. Kaneko, T. Ishiguro, A. Takahashi, J. Tsukamoto, N. Hosoi, *Solid State Commun.* **1990**, *76*, 583.
- [156] N. Mateeva, H. Niculescu, J. Schlenoff, L. R. Testardi, *J. Appl. Phys.* **1998**, *83*, 3111.
- [157] N. Toshima, *Macromol. Symp.* **2002**, *186*, 81.
- [158] O. Bubnova, Z. U. Khan, A. Malti, S. Braun, M. Fahlman, M. Berggren, X. Crispin, *Nat. Mater.* **2011**, *10*, 429.
- [159] T. Park, C. Park, B. Kim, H. Shin, E. Kim, *Energy Environ. Sci.* **2013**, *6*, 788.
- [160] G.-H. Kim, L. Shao, K. Zhang, K. P. Pipe, *Nat. Mater.* **2013**, *12*, 719.
- [161] I. Petsagkourakis, E. Pavlopoulou, G. Portale, B. A. Kuropatwa, S. Dilhaire, G. Fleury, G. Hadziioannou, *Sci. Rep.* **2016**, *6*, 30501.
- [162] S. Qu, Q. Yao, W. Shi, L. Wang, L. Chen, *J. Electron. Mater.* **2016**, *45*, 1389.
- [163] R. Kroon, D. Kiefer, D. Stegerer, L. Yu, M. Sommer, C. Müller, *Adv. Mater.* **2017**, *29*, 1700930.
- [164] E. Lim, K. A. Peterson, G. M. Su, M. L. Chabinyc, *Chem. Mater.* **2018**, *30*, 998.
- [165] D. T. Duong, C. Wang, E. Antono, M. F. Toney, A. Salleo, *Org. Electron.* **2013**, *14*, 1330.
- [166] J. Hynynen, D. Kiefer, C. Müller, *RSC Adv.* **2018**, *8*, 1593.
- [167] I. E. Jacobs, A. J. Moulé, *Adv. Mater.* **2017**, *29*.
- [168] A. I. Hofmann, R. Kroon, L. Yu, C. Müller, *J. Mater. Chem. C* **2018**, *6*, 6905.
- [169] J. Sun, M.-L. Yeh, B. J. Jung, B. Zhang, J. Feser, A. Majumdar, H. E. Katz, *Macromolecules* **2010**, *43*, 2897.
- [170] G. Zuo, X. Liu, M. Fahlman, M. Kemerink, *Adv. Funct. Mater.* **2018**, *28*, 1703280.
- [171] A. Liang, X. Zhou, W. Zhou, T. Wan, L. Wang, C. Pan, L. Wang, *Macromol. Rapid Commun.* **2017**, *38*, 1600817.
- [172] I. H. Jung, C. T. Hong, U.-H. Lee, Y. H. Kang, K.-S. Jang, S. Y. Cho, *Sci. Rep.* **2017**, *7*, 44704.
- [173] C. Y. Kao, B. Lee, L. S. Wielunski, M. Heeney, I. McCulloch, E. Garfunkel, L. C. Feldman, V. Podzorov, *Adv. Funct. Mater.* **2009**, *19*, 1906.
- [174] O. Bubnova, Z. U. Khan, H. Wang, S. Braun, D. R. Evans, M. Fabretto, P. Hojati-Talemi, D. Dagnelund, J.-B. Arlin, Y. H. Geerts, S. Desbief, D. W. Breiby, J. W. Andreasen, R. Lazzaroni, W. Chen, I. Zozoulenko, M. Fahlman, P. J. Murphy, M. Berggren, X. Crispin, *Nat. Mater.* **2014**, *13*, 190.
- [175] Y. Karpov, T. Erdmann, I. Raguzin, M. Al-Hussein, M. Binner, U. Lappan, M. Stamm, K. L. Gerasimov, T. Beryozkina, V. Bakulev, D. V. Anokhin, D. A. Ivanov, F. Günther, S. Gemming, G. Seifert, B. Voit, R. D. Pietro, A. Kiriy, *Adv. Mater.* **2016**, *28*, 6003.
- [176] S. N. Patel, A. M. Glauddell, K. A. Peterson, E. M. Thomas, K. A. O'Hara, E. Lim, M. L. Chabinyc, *Sci. Adv.* **2017**, *3*, e1700434.
- [177] R. A. Schlitz, F. G. Brunetti, A. M. Glauddell, P. L. Miller, M. A. Brady, C. J. Takacs, C. J. Hawker, M. L. Chabinyc, *Adv. Mater.* **2014**, *26*, 2825.
- [178] W. Ma, K. Shi, Y. Wu, Z.-Y. Lu, H.-Y. Liu, J.-Y. Wang, J. Pei, *ACS Appl. Mater. Interfaces* **2016**, *8*, 24737.
- [179] X. Zhao, D. Madan, Y. Cheng, J. Zhou, H. Li, S. M. Thon, A. E. Bragg, M. E. DeCoster, P. E. Hopkins, H. E. Katz, *Adv. Mater.* **2017**, *29*, 1606928.

- [180] H. Yao, Z. Fan, H. Cheng, X. Guan, C. Wang, K. Sun, J. Ouyang, *Macromol. Rapid Commun.* **2018**, *39*, 1700727.
- [181] B. D. Naab, X. Gu, T. Kurosawa, J. W. F. To, A. Salleo, Z. Bao, *Adv. Electron. Mater.* **2016**, *2*, 1600004.
- [182] S. Wang, H. Sun, T. Erdmann, G. Wang, D. Fazzi, U. Lappan, Y. Puttisong, Z. Chen, M. Berggren, X. Crispin, A. Kiriy, B. Voit, T. J. Marks, S. Fabiano, A. Facchetti, *Adv. Mater.* **2018**, *30*, 1801898.
- [183] J. Liu, L. Qiu, G. Portale, M. Koopmans, G. ten Brink, J. C. Hummelen, L. J. A. Koster, *Adv. Mater.* **2017**, *29*, 1701641.
- [184] L. Qiu, J. Liu, R. Alessandri, X. Qiu, M. Koopmans, R. W. A. Havenith, S. J. Marrink, R. C. Chiechi, L. J. A. Koster, J. C. Hummelen, *J. Mater. Chem. A* **2017**, *5*, 21234.
- [185] D. Kiefer, A. Giovannitti, H. Sun, T. Biskup, A. Hofmann, M. Koopmans, C. Cendra, S. Weber, L. J. Anton Koster, E. Olsson, J. Rivnay, S. Fabiano, I. McCulloch, C. Müller, *ACS Energy Lett.* **2018**, *3*, 278.
- [186] B. Saglio, M. Mura, M. Massetti, F. Scuratti, D. Beretta, X. Jiao, C. R. McNeill, M. Sommer, A. Famulari, G. Lanzani, M. Caironi, C. Bertarelli, *J. Mater. Chem. A* **2018**, *6*, 15294.
- [187] S. Wang, H. Sun, U. Ail, M. Vagin, P. O. Å. Persson, J. W. Andreasen, W. Thiel, M. Berggren, X. Crispin, D. Fazzi, S. Fabiano, *Adv. Mater.* **2016**, *28*, 10764.
- [188] S. H. Kim, K. Hong, W. Xie, K. H. Lee, S. Zhang, T. P. Lodge, C. D. Frisbie, *Adv. Mater.* **2013**, *25*, 1822.
- [189] J. Rivnay, S. Inal, A. Salleo, R. M. Owens, M. Berggren, G. G. Malliaras, *Nat. Rev. Mater.* **2018**, *3*, 17086.
- [190] E. Zeglio, O. Inganäs, *Adv. Mater.* **2018**, *0*, 1800941.
- [191] D. A. Bernards, G. G. Malliaras, *Adv. Funct. Mater.* **2007**, *17*, 3538.
- [192] J. Rivnay, P. Leleux, M. Ferro, M. Sessolo, A. Williamson, D. A. Koutsouras, D. Khodagholy, M. Ramuz, X. Strakosas, R. M. Owens, C. Benar, J.-M. Badier, C. Bernard, G. G. Malliaras, *Sci. Adv.* **2015**, *1*, e1400251.
- [193] A. Giovannitti, D.-T. Sbircea, S. Inal, C. B. Nielsen, E. Bandiello, D. A. Hanifi, M. Sessolo, G. G. Malliaras, I. McCulloch, J. Rivnay, *Proc. Natl. Acad. Sci.* **2016**, *113*, 12017.
- [194] S. Inal, G. G. Malliaras, J. Rivnay, *Nat. Commun.* **2017**, *8*, 1767.
- [195] S. Inal, J. Rivnay, A.-O. Suiu, G. G. Malliaras, I. McCulloch, *Acc. Chem. Res.* **2018**, *51*, 1368.
- [196] M. ElMahmoudy, S. Inal, A. Charrier, I. Uguz, G. G. Malliaras, S. Sanaur, *Macromol. Mater. Eng.* **2017**, *302*, 1600497.
- [197] A. Håkansson, S. Han, S. Wang, J. Lu, S. Braun, M. Fahlman, M. Berggren, X. Crispin, S. Fabiano, *J. Polym. Sci. Part B Polym. Phys.* **2017**, *55*, 814.
- [198] B. Winther-Jensen, K. West, *Macromolecules* **2004**, *37*, 4538.
- [199] C. B. Nielsen, A. Giovannitti, D.-T. Sbircea, E. Bandiello, M. R. Niazi, D. A. Hanifi, M. Sessolo, A. Amassian, G. G. Malliaras, J. Rivnay, I. McCulloch, *J. Am. Chem. Soc.* **2016**, *138*, 10252.
- [200] J. F. Ponder, A. M. Österholm, J. R. Reynolds, *Chem. Mater.* **2017**, *29*, 4385.
- [201] G. S. Collier, I. Pelse, A. M. Österholm, J. R. Reynolds, *Chem. Mater.* **2018**, *30*, 5161.
- [202] G. S. Collier, I. Pelse, J. R. Reynolds, *ACS Macro Lett.* **2018**, *7*, 1208.
- [203] L. R. Savagian, A. M. Österholm, J. F. Ponder, K. J. Barth, J. Rivnay, J. R. Reynolds, *Adv. Mater.* **2018**, *30*.
- [204] H. Sun, J. Gerasimov, M. Berggren, S. Fabiano, *J. Mater. Chem. C* **2018**, *6*, 11778.
- [205] L. Herlogsson, X. Crispin, S. Tierney, M. Berggren, *Adv. Mater.* **2011**, *23*, 4684.

- [206] A. Giovannitti, C. B. Nielsen, D.-T. Sbircea, S. Inal, M. Donahue, M. R. Niazi, D. A. Hanifi, A. Amassian, G. G. Malliaras, J. Rivnay, I. McCulloch, *Nat. Commun.* **2016**, *7*, 13066.
- [207] R. Porrazzo, A. Luzio, S. Bellani, G. E. Bonacchini, Y.-Y. Noh, Y.-H. Kim, G. Lanzani, M. R. Antognazza, M. Caironi, *ACS Omega* **2017**, *2*, 1.
- [208] A. Giovannitti, I. P. Maria, D. Hanifi, M. J. Donahue, D. Bryant, K. J. Barth, B. E. Makdah, A. Savva, D. Moia, M. Zetek, P. R. F. Barnes, O. G. Reid, S. Inal, G. Rumbles, G. G. Malliaras, J. Nelson, J. Rivnay, I. McCulloch, *Chem. Mater.* **2018**, *30*, 2945.
- [209] H. Sun, M. Vagin, S. Wang, X. Crispin, R. Forchheimer, M. Berggren, S. Fabiano, *Adv. Mater.* **2018**, *30*, 1704916.
- [210] A. Duarte, K.-Y. Pu, B. Liu, G. C. Bazan, *Chem. Mater.* **2011**, *23*, 501.
- [211] C. Zhu, L. Liu, Q. Yang, F. Lv, S. Wang, *Chem. Rev.* **2012**, *112*, 4687.
- [212] Y. Liu, V. V. Duzhko, Z. A. Page, T. Emrick, T. P. Russell, *Acc. Chem. Res.* **2016**, *49*, 2478.
- [213] A. Laiho, L. Herlogsson, R. Forchheimer, X. Crispin, M. Berggren, *Proc. Natl. Acad. Sci.* **2011**, *108*, 15069.
- [214] H. Toss, C. Suspène, B. Piro, A. Yassar, X. Crispin, L. Kergoat, M.-C. Pham, M. Berggren, *Org. Electron.* **2014**, *15*, 2420.
- [215] J. C. Brendel, M. M. Schmidt, G. Hagen, R. Moos, M. Thelakkat, *Chem. Mater.* **2014**, *26*, 1992.
- [216] S. Inal, J. Rivnay, P. Leleux, M. Ferro, M. Ramuz, J. C. Brendel, M. M. Schmidt, M. Thelakkat, G. G. Malliaras, *Adv. Mater.* **2014**, *26*, 7450.
- [217] M. M. Schmidt, M. ElMahmoudy, G. G. Malliaras, S. Inal, M. Thelakkat, *Macromol. Chem. Phys.* **2017**, *219*, 1700374.
- [218] R. H. Karlsson, A. Herland, M. Hamedi, J. A. Wiggenius, A. Åslund, X. Liu, M. Fahlman, O. Inganäs, P. Konradsson, *Chem. Mater.* **2009**, *21*, 1815.
- [219] M. Hamedi, A. Herland, R. H. Karlsson, O. Inganäs, *Nano Lett.* **2008**, *8*, 1736.
- [220] C. Müller, M. Hamedi, R. Karlsson, R. Jansson, R. Marcilla, M. Hedhammar, O. Inganäs, *Adv. Mater.* **2011**, *23*, 898.
- [221] M. Hamedi, A. Elfwing, R. Gabrielsson, O. Inganäs, *Small* **2013**, *9*, 363.
- [222] E. Zeglio, M. Vagin, C. Musumeci, F. N. Ajjan, R. Gabrielsson, X. T. Trinh, N. T. Son, A. Maziz, N. Solin, O. Inganäs, *Chem. Mater.* **2015**, *27*, 6385.
- [223] W. Du, D. Ohayon, C. Combe, L. Mottier, I. P. Maria, R. S. Ashraf, H. Fiumelli, S. Inal, I. McCulloch, *Chem. Mater.* **2018**, *30*, 6164.
- [224] H. Sirringhaus, P. J. Brown, R. H. Friend, M. M. Nielsen, K. Bechgaard, B. M. W. Langeveld-Voss, A. J. H. Spiering, R. A. J. Janssen, E. W. Meijer, *Synth. Met.* **2000**, *111–112*, 129.
- [225] Y. Liang, Z. Xu, J. Xia, S.-T. Tsai, Y. Wu, G. Li, C. Ray, L. Yu, *Adv. Mater.* **2010**, *22*, E135.
- [226] H. Zhang, Y. Wu, W. Zhang, E. Li, C. Shen, H. Jiang, H. Tian, W.-H. Zhu, *Chem. Sci.* **2018**, *9*, 5919.
- [227] G.-H. Kim, L. Shao, K. Zhang, K. P. Pipe, *Nat. Mater.* **2013**, *12*, 719.
- [228] Z. Liu, N. Wang, *J. Mater. Chem. C* **2018**, *6*, 9734.
- [229] Q. Zhang, Y. Sun, W. Xu, D. Zhu, *Macromolecules* **2014**, *47*, 609.
- [230] E. Lim, K. A. Peterson, G. M. Su, M. L. Chabinyk, *Chem. Mater.* **2018**, *30*, 998.

9. Eidesstattliche Versicherungen und Erklärungen

(§ 9 Satz 2 Nr. 3 PromO BayNAT)

Hiermit versichere ich eidesstattlich, dass ich die Arbeit selbstständig verfasst und keine anderen als die von mir angegebenen Quellen und Hilfsmittel benutzt habe (vgl. Art. 64 Abs. 1 Satz 6 BayHSchG).

(§ 9 Satz 2 Nr. 3 PromO BayNAT)

Hiermit erkläre ich, dass ich die Dissertation nicht bereits zur Erlangung eines akademischen Grades eingereicht habe und dass ich nicht bereits diese oder eine gleichartige Doktorprüfung endgültig nicht bestanden habe.

(§ 9 Satz 2 Nr. 4 PromO BayNAT)

Hiermit erkläre ich, dass ich Hilfe von gewerblichen Promotionsberatern bzw. –vermittlern oder ähnlichen Dienstleistern weder bisher in Anspruch genommen habe noch künftig in Anspruch nehmen werde.

(§ 9 Satz 2 Nr. 7 PromO BayNAT)

Hiermit erkläre ich mein Einverständnis, dass die elektronische Fassung meiner Dissertation unter Wahrnehmung meiner Urheberrechte und des Datenschutzes einer gesonderten Überprüfung unterzogen werden kann.

(§ 9 Satz 2 Nr. 8 PromO BayNAT)

Hiermit erkläre ich mein Einverständnis, dass bei Verdacht wissenschaftlichen Fehlverhaltens Ermittlungen durch universitätsinterne Organe der wissenschaftlichen Selbstkontrolle stattfinden können.

Ort, Datum, Unterschrift